ABSTRACT

HE, FENG. Novel Redox Processes for Carbonaceous Fuel Conversion. (Under the direction of Dr. Fanxing Li).

The current study investigates oxygen carrier development, process intensification, and oxygen carrier attrition behaviors for a number of novel, redox-based energy conversion schemes. These redox processes utilize oxygen carriers, a.k.a. redox catalysts, composed of first row transition metal oxides to indirectly convert carbonaceous fuels into clean energy carriers such as hydrogen, electricity, and/or syngas. More specifically, a chemical looping gasification (CLG) scheme for solid fuel conversion to hydrogen, a chemical looping combustion process (CLC) for indirect methane combustion, and a hybrid solar-redox process for methane and solar energy conversion are studied.

In order to address the slow reaction kinetics between the fuel and the oxygen carriers in CLG process, we propose to incorporate a secondary oxygen carrying metal oxide, i.e. CuO, to the iron-based oxygen carrier. Using the "oxygen-uncoupling" characteristics of CuO, gaseous oxygen is released at a high temperature to promote the conversion of both Fe_2O_3 and coal. Experiments and ASPEN Plus® simulations indicate that the incorporation of a small amount of copper improves coal char conversion, hydrogen yield and process efficiency.

Oxygen carrier attrition behaviors and particulate matter emissions of copper oxide based oxygen carrier from a methane CLC process are also investigated in a fluidized reactor It is observed that particulate attritions lead to increased CuO loss resulting from the chemical looping reactions, i.e. Cu is enriched in fine particles in the size range of 10-75 μm, which are generated primarily from fragmentation. It is determined that the cyclic reduction and oxidation reactions weakens the oxygen carrier particles, resulting in increased particulate emission rates when compared to oxygen carriers without redox reactions. The surface of the oxygen carrier is also found to be coarsened due to a Kirkendall effect, which also explains the surface enrichment of Cu. As a result, it is important to collect and reprocess fine particles generated from chemical looping processes to reduce copper oxide loss and to abate the environmental impact.

A hybrid solar-redox process is proposed based on the redox concept as a novel scheme that converts methane and solar energy into separate streams of liquid fuels and hydrogen at significantly lower temperature. Fixed and fluidized-bed experiments are conducted to evaluate the performances of the redox catalyst composed of iron oxide promoted with $La_{0.8}Sr_{0.2}FeO_{3-\delta}$ (LSF). Over 95% conversion in the methane oxidation step and 60% steam to hydrogen conversion in the water-splitting step are observed. Aspen Plus® simulation based on experimental data estimates the overall process efficiency to be 64.2 – 65.3% on a higher heating value (HHV) basis, which is 6.5 – 8% higher equivalent efficiency for liquid fuel and hydrogen co-production than the reforming-based methane reforming schemes.

Both experiments and a defect model indicate that the synergistic effect of reduced LSF and metallic iron phases is attributable to the exceptional steam conversion. . Using a proposed layered reverse-flow reactor concept, over 77% steam to hydrogen conversion is achieved at 930 °C, which more than triples the best performance reported to date and is 15% higher than the maximum conversion predicted by second law for unpromoted iron (oxides). The LSF-promoted iron oxide is demonstrated to be an exceptional redox material for methane partial oxidation and water-splitting. When applied to the hybrid solar-redox scheme, the process efficiency can increase by 15.1% (HHV) with up to 60% reduction in CO_2 emission for H_2 products. These aforementioned studies indicate that redox properties of first-row transition metal oxides can be used in redox processes for carbonaceous fuel conversion with high efficiency and low emissions. Effective utilization of such processes requires optimized oxygen carriers and process schemes as well as carefully designed particulate emission control and reprocessing systems.

Novel Redox Processes for Carbonaceous Fuel Conversion

by
Feng He

A dissertation submitted to the Graduate Faculty of
North Carolina State University
in partial fulfillment of the
requirements for the degree of
Doctor of Philosophy

Chemical Engineering

Raleigh, North Carolina

2015

APPROVED BY:

_____	_____
Dr. Fanxing Li Committee Chair	Dr. William Linak
_____	_____
Dr. Henry Lamb	Dr. Kirill Efimenko

DEDICATION

To my parents, Hancheng He and Xiuling Gu

BIOGRAPHY

Feng He was born in Nanjing, Jiangsu, China on July 15th, 1984. He graduated with a Bachelor of Science in Chemical Engineering from Tianjin University in July 2006. In 2008, he attended the Chemical and Biomolecular Engineering Department at North Carolina State University. Following completion of his Master of Science degree in 2011, he joined Dr. Fanxing Li's research group to pursuit a Ph.D degree.

ACKNOWLEDGMENTS

First and foremost, I would like to express my sincere gratitude to my advisor Dr. Fanxing Li. His patience, encouragement and support are essential to the completion of this dissertation. His expectations of excellence inspire me throughout my PhD study. I appreciate Dr. Li for guiding me in both research and personal matters with his extensive knowledge, sharp insight and personal integrity.

I would like to thank my committee members: Dr. William Linak, Dr. Henry Lamb, Dr. Kirill Efimenko, and Dr. Gregory Parsons. I am grateful for the guidance and insightful comments they provided me in the past four years. Special thanks goes to Dr. Linak, who helped me in my preparation of the particulates emission project and provided constructive advices on the experimental design and setup.

I also want to thank the members of the Dr. Li's research group, Dr. Luke Neal, Dr. Junshe Zhang, Dr. Yang Liu, Arya Shafiefarhood, Nathan Galinsky, Donny Bhuana, Amit Mishra, Vasudev Haribal, Seif Yusuf, and Yunfei Gao. My research would not have been possible without their assistance and suggestions.

I am very grateful to the undergraduate students, Grant Thomas, Shivalik Daga, Evan Scott, Joseph Hamill, Amy Stewart, Daniel Kim, and Patrick O'Shea, for their help on the equipment fabrication, conduction of experiments and data analysis.

Last but not the least, I would like to thank my family for their continuous encouragement and support.

TABLE OF CONTENTS

LIST OF TABLES

LIST OF FIGURES

CHAPTER 1 INTRODUCTION

1.1 Carbonaceous fuels

Carbonaceous fuels, including coal, crude oil, and natural gas, are the largest energy sources that power the modern society. Although renewable energy sources such as solar, wind, and biomass will likely to play an increasingly important role, carbonaceous fuels will still dominate the energy and chemical supply within the foreseeable future.[2] U.S. has vast coal and natural gas reserves. With rising concerns over the environmental impact of carbonaceous fuel utilization, new technologies in more cost-effective, efficient, and environmental friendly manners are highly desired.

1.1.1 Conventional coal conversion

Coal is composed mainly of carbon, hydrogen, nitrogen, oxygen, ash, and moisture. The exact composition is dependent upon the type and grade of coal. High-rank coals are high in carbon and heating value, while low-rank coals are low in carbon but high in hydrogen and oxygen content. An example of the Illinois No. 6 composition analysis is given in Table 1.1. In terms of proven reserve, coal is far more abundant than oil or gas, with more than 100 years of coal reserves remaining worldwide (assuming the current consumption rate).[2] Due to its ample availability and relatively low cost, coal has the potential to remain as an attractive option among the various energy sources.

Table 1.1. Coal analysis: Illinois No. 6[3]

Proximate Analysis Dry Basis (wt %)		Ultimate Analysis Dry Basis (wt %)		Heating Value (Btu/lb)	
Moisture	12.51	Ash	10.91	HHV (AR)	11,666
Ash	10.91	Carbon	71.72	HHV (dry basis)	13,126
Volatile Matter	39.37	Hydrogen	5.06		
Fixed Carbon	49.71	Nitrogen	1.41		
Total	100.00	Chlorine	0.33		
		Sulfur	2.82		
		Oxygen	7.75		
		Total	100.00		

Coal combustion

In a conventional coal fired power plant, coal is combusted with approximately 20% excess air. The following reaction generally represents the combustion of coal:

$$Coal + O_2 \rightarrow CO_2 + H_2O \qquad \text{Reaction 1.1}$$

Typical combustors types are pulverized coal (PC), stoker, and fluidized bed.[4] The heat generated in the boiler is used to heat up water into superheated steam. By driving a series of turbines at different pressures with regenerative-reheating cycles, the high temperature and high pressure steam is used to generate electricity. In 2013, 39% of the electricity in U.S. is generated from coal power plants.[2] The electricity generation from coal is predicted to be fairly stable until the 2040. The traditional PC power plants using a subcritical PC boiler produces steam with up to 550 °C and 24 MPa, which have 33%-37% (HHV) efficiency.[5] The ultra-supercritical (USC) power plant represents one recent advance in combustion technology, where steam can reach up to 760 °C and 35 MPa, greatly improving the thermodynamic advantage of the plant and allowing potential efficiencies of up to 46%.[6]

Flue gas pollutant control system is used to eliminate the hazard pollutant releasing from combustion, including NO_x, particulate matter (PM), SO_x and mercury. U.S. Federal regulations (2006 amended) on new fossil-fuel fired power plants have a limit on emissions of

NO_x 1.0 lb/MMBtu, PM 0.015 lb/MMBtu and SO_2 1.4 lb/MMBtu.[7] The NO_x control system is typically composed of low NO_x burners, staged overfire air, and selective catalytic reduction (SCR) which uses ammonia and a catalyst to reduce NO_x to N_2 and H_2O.[8] Fabric filter or electrostatic precipitator (ESP) can be used to effectively remove PM. SO_x is removed after the boiler. A typical flue gas desulfurization (FGD) process is wet limestone scrubbing. All these removal procedures would result in significant co-benefit capture of the mercury, where most of it is removed by the particulate removal and FGD.[8]

Coal gasification

A potentially cleaner and more versatile process for coal conversion is gasification. During gasification, preheated oxygen and/or steam are injected with pulverized coal or coal slurry into the gasifier. Instead of being fully oxidized to generate heat, coal is partially oxidized to a mixture of CO_2, CO, H_2O and H_2 under elevated pressures. Syngas obtained from coal gasification which is a combination of H_2 and CO, tends to have a H_2/CO ratio of 0.5-1. It is lower than the ideal ratio of ~2 for subsequent Fischer–Tropsch (F-T) or methanol synthesis. This ratio can be adjusted via the following water-gas-shift (WGS) reaction:

WGS: $H_2O + CO \rightarrow H_2 + CO_2$ Reaction 1.2

The generated syngas can also be used in combined cycle system for electricity generation, known as Integrated Gasification Combined Cycle (IGCC). The thermal efficiency of IGCC process can be more than 45%[9], which is comparable to the ultra-supercritical PC process. More details on the syngas utilization processes are given in Section 1.1.3. Despite advantages in product versatility and pollutant controllability, the main challenge of coal gasification is the high complexity and significant capital expenditure.

1.1.2 Natural gas and methane

Natural gas is an abundant carbonaceous fuel resource across the United States. Since 2007, shale gas has become a major source of natural gas in the United States and Canada with the development of unconventional gas reserves through hydraulic fracturing. Because of that,

recoverable reserves and supplies of natural gas have been significantly increased.[2] Most natural gas is currently used as a fuel for heat or electricity generation, with natural gas power plants in the U.S. accounting for 27% of the total national electricity generation.[2] The principal component of natural gas is methane, which represents 70-90 % of natural gas. Other major constituents of natural gas include ethane, propane, heavier hydrocarbons, carbon dioxide, and sulfur compounds. Methane molecule's inherently stable tetrahedral structure with four equivalent C-H bonds makes it difficult to activate. Although chemical processes based on direct activation of methane to value-added chemicals are being actively studied, low efficiency and poor product yield are still the key challenges.

The methane reforming processes are commercially used for methane conversion to synthetic fuels and chemicals. Commonly encountered reforming schemes include steam reforming, CO_2 reforming (dry reforming), and partial oxidation processes, whose characteristic reaction stoichiometry is given in Reactions 1.3 to 1.5:

Steam reforming:

$CH_4 + H_2O \rightarrow CO + 3H_2$, ΔH (298 K) = 206 kJ·mol^{-1} Reaction 1.3

CO_2 reforming:

$CH_4 + CO_2 \rightarrow 2CO + 2H_2$, ΔH (298 K) = 247 kJ·mol^{-1} Reaction 1.4

Partial oxidation:

$CH_4 + 0.5O_2 \rightarrow CO + 2H_2$, ΔH (298 K) = -36 kJ·mol^{-1} Reaction 1.5

Among these processes, steam methane reforming (SMR) process is a well-established process, as shown in Fig. 1.1. Over 90% of the world's total hydrogen production is derived from methane, a primary component of natural gas via the SMR process.[10,11] In the foreseeable future, natural gas will continue to be the major feedstock for hydrogen production.[12] Pre-treatment of the feedstock is necessary to remove sulfur, which can poison the reforming catalysts.[13] Following pretreatment, preheated and pressurized CH_4 is mixed with steam and introduced to the reformer, where methane reacts with steam to produce syngas. The WGS reaction in the reformer would make the H_2/CO ratio higher than stoichiometric ratio of 3. The

reformer converts CH_4 and steam into syngas with typical compositions shown in Table 1.2.[13] The syngas product exiting the reformer is cooled and introduced into WGS reactors. A high-temperature WGS reactor with iron catalyst and a low-temperature WGS reactor with copper catalyst are typically arranged in series to achieve over 95% CO conversion [13,14]. The shifted syngas is cooled further followed with a pressure swing adsorption (PSA) system to produce purified H_2. Through PSA, 90% of the H_2 is recovered as a product with 99.9% purity [3,13,14]. The reforming reactor is highly endothermic. To compensate the heat required, off-gas from the PSA system and additional methane is combusted with air in the reformer furnace. High temperature gases from the combustor as well as the reformer are introduced to a heat recovery steam generator (HRSG) to produce steam for reforming.

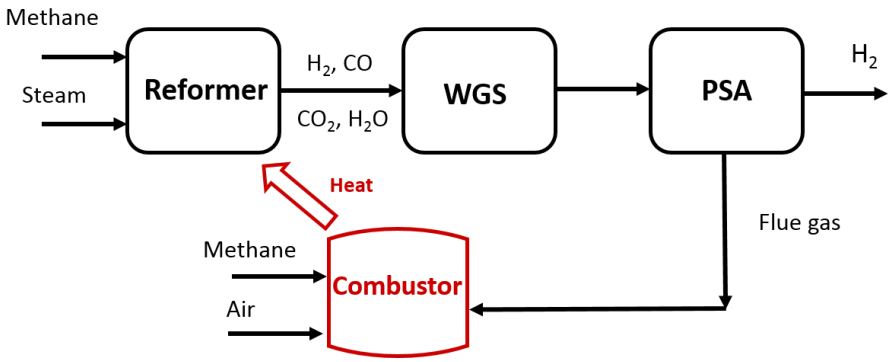

Fig. 1.1. Simplified schematic of conversional steam method reforming process

Table 1.2. Typical composition of the syngas leaving the methane reformer[13]

Component	Volume %
CH_4	2
CO	7
CO_2	6
H_2	44
H_2O	41
Total	100

Partial oxidation is a process would directly give the optimal composition syngas, but pure oxygen and the mixture of O_2 and CH_4 at high temperature required to drive the partial oxidation could be difficult to control, which inhibit the practical application. Different from endothermic steam reforming reaction, the partial oxidation is an exothermic reaction with large heat production. Therefore, a combination of steam reforming and partial oxidation reforming is developed and known as autothermal reforming (ATR). Steam and oxygen are injected along with methane into the reforming reactor. The overall heat of reaction depends on the ratio of steam and oxygen. A typical ATR process comprises a reformer, heat recovery systems, and gas separation units. Although additional gas separation units are incorporated in autothermal reforming, the combustor and heat exchange sections, leading to simpler process scheme compared to conventional steam reforming plants.[15] Moreover, the ATR is able to generate a syngas with the H_2:CO ratio of approximately 2, so it is often used in the gas to liquid (GTL) process.[16]

1.1.3 Syngas

A gas mixture of H_2 and CO called syngas, can be generated from the abovementioned coal gasification and steam reforming. Other solid fuels, such as biomass and coke, could also be used for gasification to generate syngas.[17,18] Fig. 1.3 summarizes the processes for syngas conversion. Electricity can be generated via combustion or fuel cell. Through the WGS reaction or separation such as pressure swing adsorption (PSA) and membrane-based processes, H_2 can be a final product. Furthermore, syngas could be converted into valuable chemicals by methanol and F–T synthesis.

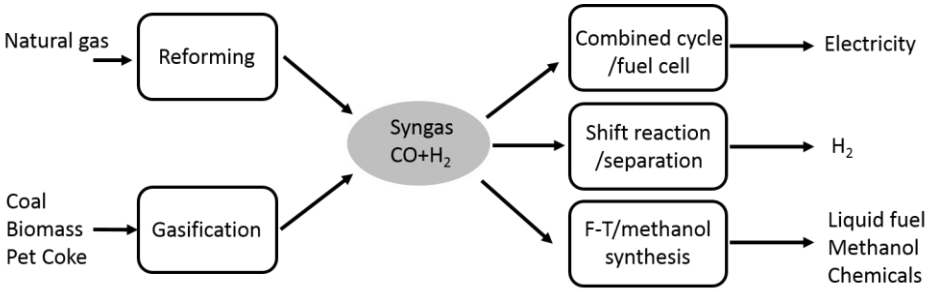

Fig. 1.2. Schematic of the use of syngas[4]

Fischer–Tropsch (F–T) synthesis

The F-T reaction utilizes syngas as the feedstock to produce hydrocarbons such as gasoline, diesel, jet fuel, or olefins. The F-T process involves a series of chemical reactions that produce a variety of hydrocarbons, ideally having the formula $C_nH_{(2n+2)}$. The reaction can be represented by:

$$(2n + 1)\ H_2 + n\ CO \rightarrow C_nH_{(2n+2)} + n\ H_2O \qquad \text{Reaction 1.6}$$

In general, the product distribution of hydrocarbons formed during the F-T process follows an Anderson–Schulz–Flory distribution, which can be expressed as:

$$W_n/n = (1 - \alpha)^2\alpha^{n-1} \qquad \text{Equation 1.1}$$

where W_n is the weight fraction of hydrocarbons containing n carbon atoms. α is the chain growth probability factor or the probability that a molecule will continue reacting to form a longer chain, which is largely determined by the catalyst and the reaction conditions. Most of the alkanes produced tend to be straight-chain, suitable as diesel fuel. In addition to alkane formation, competing reactions give small amounts of alkenes, as well as alcohols and other oxygenated hydrocarbons. The hydrocarbons at low molecular weight often would be combusted for heat.

A variety of catalysts can be used for the F-T process, but the most common are the transition metals cobalt and iron. For cobalt-based catalysts, the optimal H_2:CO ratio is around 1.8–2.1.

Iron-based catalysts promote the WGS reaction and thus can tolerate lower ratios. This reactivity can be important for syngas derived from coal or biomass, which tends to have relatively low H_2:CO ratios (<1). Higher pressures are favorable for the reaction but result in additional equipment costs and coke formation. Typical pressure ranges are 10 – 30 atm.[19–21]

Methanol synthesis

Methanol is another important chemical primarily produced from syngas. Natural gas derived syngas accounts for a majority of methanol synthesis, while coal/solid derived syngas is used to make 9% of the worldwide output of methanol.[9] Methanol is both a chemical feedstock for a range of important industrial chemicals and a fuel for combustion and fuel cell applications. The ideal H_2/CO ratio for menthol synthesis is approximately 2:1. The formation of methanol takes place via Reactions 1.7 to 1.9:

$2\ H_2 + CO \rightarrow CH_3OH$ Reaction 1.7

$CO_2 + 3\ H_2 \rightarrow CH_3OH + H_2O$ Reaction 1.8

$CO + H_2O \rightarrow CO_2 + H_2$ Reaction 1.9

The methanol synthesis reaction is exothermic. Therefore, higher methanol yields are obtained at lower temperatures. Higher pressures would favor the reaction equilibrium by promoting the CO and CO_2 conversion, but equipment and operation costs will increase. Cu-Zn based catalysts are commonly used for the synthesis at 5-15 MPa and 200-300 °C,[22] but are very sensitive to sulfur in the syngas. As a result, sulfur compounds are removed from the gaseous feedstock prior to the methanol synthesis reactor.

To summarize, coal and natural gas are important energy sources for electricity generation, which account for about 66% US electricity generation in 2013. The U.S. EIA estimates that demand for electricity will increase by approximately 24% in the U.S. from 2013 to 2040.[2] Therefore, it is important to find approaches to address the challenge of the CO_2 emission from the fossil fuel fired power plants. Not only producing electricity, coal and natural gas can also be converted into syngas and then used to produce valuable-add chemicals. However, coal

gasification and methane reforming are not able to directly provide syngas with 2:1 H_2/CO molar ratio for F-T or methanol synthesis. The additional conversation steps increase the process complexity and reduce the overall efficiency. Therefore, reliable processes for carbonaceous fuel conversion into F-T and methanol ready syngas with high efficiency and low emission are highly desirable.

1.2 CO_2 capture technologies

US EIA reports that over 80% of greenhouse gas emission in U.S. originate from the use of carbonaceous fuels. There are potential increase in the carbonaceous fuel consumption in the next 20 years.[2] Emission of CO_2 has been considered to be the largest contribution to the greenhouse gases-induced climactic warming, and has subsequently been realized as one of the fundamental problems of carbonaceous fuel conversion.[23] Therefore, developing efficient, reliable and low-cost technologies to mitigate this problem has received growing attention. One approach to control CO_2 emission is capturing CO_2 from carbonaceous fueled power plants, which typically includes three technological approaches: post-combustion capture, pre-combustion capture, and oxy-combustion.

In post-combustion capture, CO_2 is separated from the flue gas produced by combustion. Post-combustion capture is applicable to the majority of existing coal-fired power plants and serves as a retrofit technology option. This is a key advantage of the post-combustion technique. For typical combustion processes, the flue gas stream typically has a CO_2 concentration of less than 15%. Amine-based systems are based on the reactivity of amines with CO_2 to form water soluble compounds. The monoethanolamine (MEA) scrubbing technique is a well-established amine-based system for CO_2 capture.[24] The MEA technique is composed of an absorber with fresh amine solvent to remove the CO_2 and an absorber using high temperature steam to regenerate the solvent. Because of the large consumption of steam, the efficiency of the power plant could be reduced as much as 40%, nearly doubling the cost of electricity.[25] Additionally, carbonate, ammonia, membranes, metal organic frameworks, enzyme, and ionic liquids based

techniques are emerging technologies at the research stage in either laboratory or field that have shown promise for post-combustion capture.[26]

Oxy-combustion represents an approach to combust the fuel by using oxygen instead of air. As a result, a concentrated CO_2 steam is generated without the necessity to do further separation post-combustion. A cryogenic air separation unit (ASU) is most commonly used in the oxy-combustion process to supply the high purity (>95%) oxygen for the boiler. The oxygen is proposed to mix with recycled flue gas before the combustor, which enable the combustor to be operated under similar conditions to the conventional air fired configuration. The oxy-combustion processes have been studied in lab-scale setups and are transferring to pilot plant scale demonstration (up to 30 MW_{th}).[27–29] The energy intensive air separation and flue gas recirculation reduces the overall process efficiency by 20%-35%.[4,25] In order to reduce the cost, Praxair proposed to use an oxygen transport membrane within the boiler[30] and BOC Group developed ceramic autothermal recovery technology[31].

Pre-combustion capture is another method where the carbon is removed from the fuel before combustion, preventing the production of CO_2 during the combustion process. The integrated gasification combined cycle (IGCC) is one very promising approach to this concept. In the IGCC process, coal is first gasified with sub-stoichiometric amounts of oxygen and/or steam at elevated pressures to generate syngas. By passing through a series of catalyst beds with additional steam injection, CO in the mixture is converted into to CO_2 and additional H_2 by the water–gas shift reaction. After that, CO_2 is separated from the H_2, where high CO_2 partial pressure facilities the separation procedure. In the meantime, the high pressure gas stream may serve to reduce the size and cost of the capture equipment as well as utility cost associated with compression. However, IGCC can only be applicable to new plants. The requirement of extensive auxiliary processes, including air separation, WGS, and CO_2 separation makes the process very capital intensive.

1.3 Chemical looping

1.3.1 Chemical Looping combustion (CLC)

The chemical looping processes represent an alternative and potentially efficient strategy for power generation from fossil fuels with *in-situ* CO_2 capture. Though chemical looping presents challenges of its own, many of the issues associated with the abovementioned conversion/carbon capture techniques are inherently eliminated or drastically mitigated by the chemical looping scheme.

The CLC process utilizes a metal oxide based oxygen carrier particle to oxidize carbonaceous fuels into concentrated CO_2, allowing efficient CO_2 capture and storage, as seen in the process schematic (Fig. 1.3).[32–35] The reduced oxygen carrier resulting from the fuel oxidation step is subsequently combusted with air to release heat for power generation. Therefore, CO_2 can be captured from the reducer flue gas after water condensation, without the need for an expensive air separation unit or energy intensive sorbent regenerator. Moreover, chemical looping has the advantage of recuperating low-grade heat while producing a high-grade heat.[4] As a result, higher thermodynamic efficiency can be potential achieved in chemical looping processes. Additional environmental advantages are enjoyed by the CLC scheme, such as the lack of NO_x formation due to the separation of air and fuel reactors.

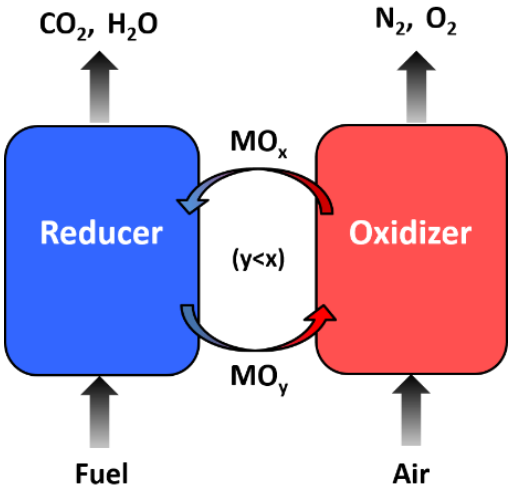

Fig. 1.3. Schematic of chemical looping combustion

The reactor system for the CLC process requires good contact between gas and solids as well as a flow of solid material between reducer and oxidizer. Circulating fluidized bed (CFB) has been extensively used for the CLC precesses.[4,36] In such a system, the reducer operates as a low velocity bubbling fluidized bed. Solids from reducer and air are introduced to the oxidizer where they are regenerated with air before being transported back to the reducer to close the loop. The moving bed is another reactor system for CLC, which has higher solid conversion for fuel and metal oxide conversions.[4,33] Moreover, several other representative reactor systems include spouted bed system,[37] double loop circulating fluidized bed reactor system,[38] rotating reactor system,[39] two-stage packed bed system[40]. Continuous testing of these oxygen carriers have been successfully carried out in circulating fluidized bed (CFB) reactors at scales up to 1 $MW_{th.}$[4,41–43] Besides the aforementioned experimental studies, the attractiveness of chemical looping as a novel power production process has been confirmed by both availability and process analyses.[44,45]

The efficiency of chemical looping processes strongly depends on the performance of the oxygen carrier. Generally speaking, desired properties of an ideal oxygen carrier include high oxygen capacity, high reactivity, long-term recyclability, good mechanical strength, high melting point, resistance to contaminates, low cost, minimal health and environmental impacts. Typical oxygen carrier is composed of a primary oxide which directly participates in the cyclic redox reactions. The oxides of transition metals such as iron, nickel, copper, manganese, and cobalt have been studied for chemical looping applications.[4,32,34,35] However, deactivation over multiple redox cycles has been reported, which is mainly attributed to the high temperature sintering (800 - 1000 °C).[35,46,47] A inert support is added to the primary oxide, forming the composite structure to improve sintering resistance and recyclability. The support is usually low-cost and stable ceramic materials, such as Al_2O_3, TiO_2, $MgAl_2O_4$, SiO_2, and ZrO_2.[35,47–49] Based on inert marker experiments and density function theory (DFT) calculations, Li et al.[50,51] proposed that the enhanced ionic diffusivity of oxygen anion within iron and its oxides are responsible for improved redox activity of the supported oxygen carrier. As a support, mixed

ionic and electronic conductive (MIEC) perovskites such as lanthanum strontium ferrite (LSF) have been shown to enhance the redox activity of iron oxides by 5−70 times when compared to oxygen carriers with conventional TiO_2, Al_2O_3, or yttria-stabilized zirconia (YSZ) support.[52] Good stability over 100 cycles and outstanding coke resistance are also achieved by the MIEC supported Fe_2O_3. Perovskites have the typical form of $ABO_{3-\delta}$, where A is a large cation of either the alkali earth or rare earth metal and B is a smaller transition metal cation.[53] More recently, perovskite structured oxygen carriers have received increasing attention as oxygen carriers for redox applications.[54–71] Similar to LSF, ceria is a frequently studied mixed-conductive support for the oxygen carrier with good reactivity and stability.[63,72,73]

Early research on chemical looping focused on the conversion of gaseous fuels such as methane/natural gas [74–77] and coal derived syngas [78–80]. Compared to gaseous fuels, solid fuels such as coal are cheaper on a same energy content basis. Therefore, direct conversion of solid fuels in chemical looping processes can be advantageous from a process economics standpoint. A key challenge for solid fuel conversion, however, resides in the slow solid-solid reaction kinetics between the fuel and the oxygen carriers. To address this challenge, a syngas chemical looping combustion system is proposed, where solid fuel is gasified into syngas by oxygen. The resulting syngas is then reacted with the oxygen carrier at a faster rate than direct solid-solid interactions.[81–86] However, the gasification step increases the process cost and complexity.

CLC with in-situ gasification

Another method to enhance solid fuel conversion is through in-situ gasification.[33,35] Under this approach, a gasification enhancer such as steam and/or CO_2 is introduced to the fuel reactor to gasify the fixed carbon via steam-carbon reaction and/or reverse Boudouard reaction, producing H_2 and/or CO. The H_2/CO generated will then react with the oxygen carrier at a faster rate than the solid fuel–oxygen carrier reactions. Reactions between the oxygen carrier and H_2/CO produce additional steam/CO_2 for in-situ solid fuel gasification. As a result, a chain reaction can be initiated. Although the in-situ gasification approach can enhance the solid fuel

conversion rate, steam-carbon and reverse Boudouard reactions are relatively slow at typical reducer operating temperatures. Hence a long fuel and metal oxide residence time is required in order to achieve satisfactory solid fuel conversions.[4] The residence time requirements may lead to large reducer volume and solids inventory.

Steam-carbon reaction: $C + H_2O \rightarrow CO + H_2$ Reaction 1.10

Reverse Boudouard reaction: $C + CO_2 \rightarrow 2CO$ Reaction 1.11

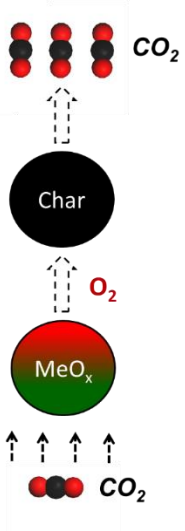

Fig. 1.4. Schematic of the chain reactions in CLOU

Chemical-Looping with Oxygen Uncoupling (CLOU) is an even faster approach to combust solid fuel while capturing CO_2. First proposed by Lewis and Gilliland [87] in the 1950s, the CLOU strategy uses gaseous oxygen released from metal oxide decomposition to convert solid fuels. As a result, solid fuel is able to react directly with molecular oxygen, which increases the activity for solid fuel conversion. Fig. 1.4 shows the reactions in CLOU. The CLOU concept has been tested over the past decade for the combustion of petroleum coke [88,89], and coal [90]. Using a laboratory scale fluidized bed reactor, Mattisson et al.[88] demonstrated 50-fold rate enhancement for petroleum coke conversion using CuO based CLOU when compared to an iron-based oxygen carrier in an in-situ gasification scheme.

The metal oxides which are suitable for the CLOU strategy include oxides of copper, manganese and cobalt.[24] Cobalt oxide it not commonly used, due to the low decomposition temperature and additional health and environmental concerns.[91] Mn_2O_3 decomposes at lower temperature, but re-oxidation of Mn_3O_4 tends to be slow.[92] CuO is the most frequently used oxygen carrier for the CLOU process, but faces challenges such as low meting point, sintering, and high cost.[35] In order to address these problems, various supports have been investigated, such as $MgAl_2O_4$, ZrO_2, Al_2O_3 and SiO_2.[93] Among them, $MgAl_2O_4$ is most promising as it increases sintering resistance and its performance has been tested in a continuously 1.5 kW_{th} unit.[94–96] Mixed metal oxides have also been investigated, since secondary metal addition can lead to enhanced structural and/or thermodynamic properties compared to their parent oxides. Mn-Fe oxides with 2:1 molar ratio show the best uncoupling properties with up to 0.5 wt.% oxygen uncoupling capacities.[97] Perovskites have also been tested for CLOU applications. $CaMnO_3$ based perovskites are currently the most studied perovskites, which can be synthesized from abundantly available Ca and Mn precursors. However, the loss of activity over long term cycles due to the irreversible phase change to $CaMn_2O_4$ and Ca_2MnO_4 phases limits the application of $CaMnO_3$.[93,98–100] Recent research focused on doping secondary metals into the A and B-sites in order to enhance the structure stability and CLOU properties of $CaMnO_3$ perovskites. By doping titanium on the B site,[58,61] the oxygen carrier exhibited good redox activity and stability for chemical-looping combustion of natural gas, based on 70 h of experiments in a circulating fluidized-bed reactor system.

1.4 Redox-based reforming

Chemical looping combustion is used for heat and power generation. The similar mode can also be directly or indirectly used to produce value-added chemicals and fuels from coal or natural gas.

1.4.1 Chemical looping reforming

Chemical looping reforming adopts the same redox principles as CLC by working under a cyclic redox mode. The CLR redox catalyst is similar to the oxygen carrier in CLC, carrying lattice oxygen between two reactors. The main difference is that the fuel is partially oxidized into syngas rather than fully oxidized into CO_2.[101] Therefore, the desired product from CLR is not heat but H_2 and CO. The reduced particle would be regenerated in the oxidizer by air, just as in CLC. Because the similar redox mode, most CLR redox catalysts investigated to date are similar to the oxygen carriers used in CLC processes. Instead of using an oxygen carrier to non-selectively oxidize fuels to CO_2 and steam, the CLR redox catalyst needs to selectively oxidize the fuel to syngas. Therefore, Ni-based redox catalysts are more attractive owing to their high activity and selectivity toward syngas.[63,102,103] The challenge of NiO based redox catalysts, however, resides in their high tendency for coke formation, high cost, and toxicity.[35] Because of the high particle inventory used in CLR, the relatively high cost and health concerns inhibit the Ni-based material's application.

1.4.2 Solar-thermal water-splitting

Solar-thermal water-splitting represents a potentially attractive and environmentally friendly option.[104,105] Typical solar-thermal water-splitting schemes involve the following cyclic redox reactions of transition metal oxides to indirectly convert solar energy and water into separate streams of hydrogen and oxygen.[106] By using the sustainable solar energy, H_2 is generated without CO_2 emission. In the first step, solar energy is used to decompose a metal oxide at high temperature. In the subsequent step, the decomposed metal/metal oxide is reoxidized with water, producing hydrogen.

$$M_xO_y \rightarrow M_xO_{y-\delta} + 0.5\delta O_2 \qquad \text{Reaction 1.12}$$

$$M_xO_{y-\delta} + \delta H_2O \rightarrow M_xO_y + \delta H_2 \qquad \text{Reaction 1.13}$$

Although a number of promising redox materials have been developed for this process,[107,108] the metal oxide reduction step in typical solar thermochemical water-splitting processes requires relatively high temperatures (> 1200 °C). Iron containing oxides are the most

commonly encountered redox materials, because they are effective for hydrogen production through the water-splitting reaction. A number of (supported) iron oxides[109], including Fe_3O_4-CeO_2-ZrO_2[110], Fe_3O_4-Al_2O_3[111,112], Fe_3O_4-$MgAl_2O_4$[113] and Fe_3O_4-$Ce_{0.5}Zr_{0.5}O_2$[114], have been investigated for steam-iron applications. In addition, perovskites have also been explored as redox catalysts for syngas generation and water-splitting.[115,116] However, the reported steam to hydrogen conversion is generally less than 20%. The high decomposition temperature and limited steam conversion are two key challenges. Therefore, novel solar-thermal schemes that can effectively promote metal oxide reduction at lower temperatures are highly desired in order to achieve improved efficiency and economic attractiveness for solar-thermal hydrogen generation.

1.5 Summary

A key challenge for solid fuel conversion in chemical looping resides in the slow solid-solid reaction kinetics between the fuel and the oxygen carrier. In Chapter 2, we investigate the effect of incorporating CuO into Fe_2O_3 based oxygen carrier to enhance the solid fuel conversion rate. The resulting bimetallic CLG process, enhanced by the CuO based oxygen uncoupling agent, has the potential to be effective for solid fuel conversion while maintaining the ability for hydrogen production at high efficiency. Thermal-Gravimetric Analyzer (TGA) experiments, ASPEN Plus® simulation, and mathematical modeling are carried out to validate the feasibility of this bimetallic CLG concept.

Attrition of oxygen carrier particles is another challenge for chemical looping technology. Potential issues associated with excessive attrition include instability in reactor operation, loss of oxygen carriers, and fine particulate emissions. Attrition inevitably occurs in chemical looping system especially under high temperature and alternating reducing/oxidizing environments in fluidized bed reactors. Despite various ongoing pilot-scale demonstrations and oxygen carrier particle research, little research has been conducted on characterizing particulate emissions from CLC processes. Chapter 3 represents an attempt to comprehensively evaluate attrition and particulate emission behaviors from CLC operations.

Besides chemical looping, novel applications based on the redox concept are explored for methane conversion. Hydrogen has been identified as an attractive, zero-emission fuel due to its high (weight-based) energy density, as well as an important feedstock for the petroleum and chemical industries. However, the steam-methane reforming process, accounting for over 90% H_2 produced, leads to notable greenhouse gas emissions from a life cycle standpoint. Chapter 4 investigates the feasibility of a hybrid solar-redox process for cogeneration of liquid fuels and hydrogen using methane and solar energy. The proposed process has the potential to produce transportation fuels and hydrogen at high efficiency with reduced carbon footprint. In Chapter 5, the novel hybrid solar-redox processes is compared to two other conventional and novel hydrogen production schemes, i.e. steam methane reforming (SMR), solar SMR. Based on a consistent set of process conditions and assumptions, H_2 (and liquid fuel) productivity, energy conversion efficiency, and associated CO_2 emissions are evaluated. Chapter 6 presents a further study on perovskite-promoted iron oxide as a highly effective redox catalyst in a hybrid solar-redox scheme for methane partial oxidation and water-splitting. Both experiments and a defect model indicate that the synergistic effect of reduced LSF and metallic iron phases is attributable to the exceptional steam conversion. A layered reverse-flow reactor concept is then proposed to promote the steam conversion and the process efficiency. Chapter 7 summarizes the abovementioned studies and discusses potential future research directions for redox based energy conversion processes.

REFERENCES

(1) Short-Term Energy Outlook. U.S. Energy Information Administration (EIA), June 9, **2015**.

(2) Annual Energy Outlook 2015. U.S. Energy Information Administration (EIA), April 14, **2015**.

(3) Gray, D.; White, C.; Salerno, S.; Plunkett, J.; Tomlinson, G. Production of High Purity Hydrogen from Domestic Coal: Assessing the Techno-Economic Impact of Emerging Technologies. DOE/NETL-2010/1432 August 30, **2010**.

(4) Fan, L.-S. Chemical Looping Systems for Fossil Energy Conversions; John Wiley & Sons, **2010**.

(5) Katzer, J.; Ansolabehere, S.; Beer, J.; Deutch, J.; Ellerman, A. D.; Friedmann, S. J.; Herzog, H.; Jacoby, H. D.; Joskow, P. L.; McRae, G.; others. The future of coal: options for a carbon-constrained world. *Mass. Inst. Technol.* **2007**.

(6) Bugge, J.; Kjær, S.; Blum, R. High-efficiency coal-fired power plants development and perspectives. *Energy* **2006**, *31* (10–11), 1437–1445.

(7) 40 CFR Part 60 – Standards of Performance for Electric Utility Steam Generating Units for Which Construction Commenced after September 18, **1978**, February 27, 2006.

(8) James. Cost and Performance Baseline for Fossil Energy Power Plants, Volume 1: Bituminous Coal and Natural Gas to Electricity. DOE/NETL-2010/1397 November **2010**.

(9) Higman, C.; Burgt, M. van der. *Gasification*; Gulf Professional Publishing, **2003**.

(10) Simpson, A. P.; Lutz, A. E. Exergy analysis of hydrogen production via steam methane reforming. *Int. J. Hydrog. Energy* **2007**, *32* (18), 4811–4820.

(11) T-Raissi, A.; Block, D. L. Hydrogen: automotive fuel of the future. *IEEE Power Energy Mag.* **2004**, *2* (6), 40–45.

(12) Skone, T. Power Generation Technology Comparison from a Life Cycle Perspective. DOE/NETL-2012/1567 March 15, **2013**.

(13) Chou, V.; Kuehn, N. Assessment of Hydrogen Production with CO_2 Capture, Volume 1: Baseline State of the Art Plants. DOE/NETL-2010/1434 August **2010**.

(14) Molburg, J.; Doctor, R. Hydrogen from Steam-Methane Reforming with CO_2 Capture. 20th Annual International Pittsburgh Coal Conference September 15, **2003**.

(15) Dybkjaer, I. Tubular reforming and autothermal reforming of natural gas — an overview of available processes. *Fuel Process. Technol.* **1995**, *42* (2–3), 85–107.

(16) Goellner, J.; Shuster, E. Analysis of Natural Gas-to-Liquid Transportation Fuels via Fischer-Tropsch. NETL/DOE **2013**/1597.

(17) Sutton, D.; Kelleher, B.; Ross, J. R. H. Review of literature on catalysts for biomass gasification. *Fuel Process. Technol.* **2001**, *73* (3), 155–173.

(18) Rezaiyan, J.; Cheremisinoff, N. P. Gasification Technologies: A Primer for Engineers and Scientists; CRC Press, **2005**.

(19) vanBerge, P. J.; Everson, R. C. Cobalt as an alternative Fischer-Tropsch catalyst to iron for the production of middle distillates. In *Natural Gas Conversion Iv*; **1997**; Vol. 107, pp 207–212.

(20) Sie, S. T. Process development and scale up: IV. Case history of the development of a Fischer-Tropsch synthesis process. *Rev. Chem. Eng.* **1998**, *14* (2), 109–157.

(21) Gray, D.; Klara, J.; Tomlinson, G.; White, C. Chemical-Looping Process in a Coal-to-Liquids Configuration. DOE/NETL, **2008**/1307.

(22) Suib, S. L. New and Future Developments in Catalysis: Hybrid Materials, Composites, and Organocatalysts; Newnes, **2013**.

(23) Advancing the Science of Climate Change, Climate Change at the National Academies, **2010**.

(24) Stiegel, G. J.; Ramezan, M. Hydrogen from coal gasification: An economical pathway to a sustainable energy future. *Int. J. Coal Geol.* **2006**, *65* (3–4), 173–190.

(25) Skone, T. Carbon Dioxide Capture from Existing Coal-Fired Power Plants. USDOE NETL November **2007**.

(26) Figueroa, J. D.; Fout, T.; Plasynski, S.; McIlvried, H.; Srivastava, R. D. Advances in CO_2 capture technology—The U.S. Department of Energy's Carbon Sequestration Program. *Int. J. Greenh. Gas Control* **2008**, *2* (1), 9–20.

(27) Strömberg, L.; Lindgren, G.; Jacoby, J.; Giering, R.; Anheden, M.; Burchhardt, U.; Altmann, H.; Kluger, F.; Stamatelopoulos, G.-N. Update on Vattenfall's 30 MWth oxyfuel pilot plant in Schwarze Pumpe. *Energy Procedia* **2009**, *1* (1), 581–589.

(28) Cameron, E. D.; Sturgeon, D. W.; McGhie, C.; Fitzgerald, F. D. Demonstration of the Doosan Babcock 40 MW_{th} oxycoal combustion system. In *The 35th International Technical Conference on Clean Coal & Fuel Systems Clearwater, FL*; **2010**.

(29) Kluger, F.; Monckert, P.; Back, A.; Wang, W. Oxy-Combustion Testing In 30MW_{th} Pilot Plant Schwarze Pumpe. In *2nd Oxyfuel Combustion Conference*, **2011**.

(30) Shah, M. M.; Christie, M. Oxy-fuel combustion using OTM for CO_2 capture from coal power plants. In *IEAGHG International OxyCombustion Network 2nd Workshop, Windsor, USA*; **2007**.

(31) Divyanshu Acharya, K. R. K. Development of a high temperature oxygen generation process and its application to oxycombustion power plants with carbon dioxide capture. *22nd Annu. Int. Pittsburgh Coal Conf. Pittsburgh PA* **2005**.

(32) Hossain, M. M.; de Lasa, H. I. Chemical-looping combustion (CLC) for inherent separations—a review. *Chem. Eng. Sci.* **2008**, *63* (18), 4433–4451.

(33) Li, F.; Fan, L.-S. Clean coal conversion processes – progress and challenges. *Energy Environ. Sci.* **2008**, *1* (2), 248.

(34) Moghtaderi, B. Review of the Recent Chemical Looping Process Developments for Novel Energy and Fuel Applications. *Energy Fuels* **2011**, *26* (1), 15–40.

(35) Adanez, J.; Abad, A.; Garcia-Labiano, F.; Gayan, P.; de Diego, L. F. Progress in Chemical-Looping Combustion and Reforming technologies. *Prog. Energy Combust. Sci.* **2012**, *38* (2), 215–282.

(36) Lyngfelt, A.; Leckner, B.; Mattisson, T. A fluidized-bed combustion process with inherent CO_2 separation; application of chemical-looping combustion. *Chem. Eng. Sci.* **2001**, *56* (10), 3101–3113.

(37) Shen, L.; Wu, J.; Xiao, J.; Song, Q.; Xiao, R. Chemical-Looping Combustion of Biomass in a 10 kWth Reactor with Iron Oxide As an Oxygen Carrier. *Energy Fuels* **2009**, *23* (5), 2498–2505.

(38) Bischi, A.; Langørgen, Ø.; Saanum, I.; Bakken, J.; Seljeskog, M.; Bysveen, M.; Morin, J.-X.; Bolland, O. Design study of a 150 kW_{th} double loop circulating fluidized bed reactor system for chemical looping combustion with focus on industrial applicability and pressurization. *Int. J. Greenh. Gas Control* **2011**, *5* (3), 467–474.

(39) Dahl, I. M.; Bakken, E.; Larring, Y.; Spjelkavik, A. I.; Håkonsen, S. F.; Blom, R. On the development of novel reactor concepts for chemical looping combustion. *Energy Procedia* **2009**, *1* (1), 1513–1519.

(40) Kooiman, R. F.; Hamers, H. P.; Gallucci, F.; van Sint Annaland, M. Experimental Demonstration of Two-Stage Packed Bed Chemical-Looping Combustion Using Syngas with CuO/Al_2O_3 and $NiO/CaAl_2O_4$ as Oxygen Carriers. *Ind. Eng. Chem. Res.* **2015**, *54* (7), 2001–2011.

(41) Lyngfelt, A.; Thunman, H. Chapter 36 - Construction and 100 h of Operational Experience of A 10-kW_{th} Chemical-Looping Combustor. In *Carbon Dioxide Capture for Storage in Deep Geologic Formations*; Elsevier Science: Amsterdam, **2005**; pp 625–645.

(42) Ryu, H.-J.; Jin, G.-T.; Yi, C.-K. Demonstration of inherent CO_2 separation and no NO_x emission in a 50 kW chemical-looping combustor: Continuous reduction and oxidation experiment. *Proceedings of the seventh international conference of greenhouse gas control technologies*, Vancouver, Canada, September; **2004**.

(43) Eide, L. I. Carbon dioxide capture for storage in deep geological formations : results from the CO_2 Capture Project. Volume 3, Advances in CO_2 capture and storage technology, results (2004-2009); CPL: Newbury, **2009**.

(44) Ishida, M.; Zheng, D.; Akehata, T. Evaluation of a chemical-looping-combustion power-generation system by graphic exergy analysis. *Energy* **1987**, *12* (2), 147–154.

(45) Anheden, M.; Svedberg, G. Exergy analysis of chemical-looping combustion systems. *Energy Convers. Manag.* **1998**, *39* (16–18), 1967–1980.

(46) Cuadrat, A.; Abad, A.; García-Labiano, F.; Gayán, P.; de Diego, L. F.; Adánez, J. The use of ilmenite as oxygen-carrier in a 500 W_{th} Chemical-Looping Coal Combustion unit. *Int. J. Greenh. Gas Control* **2011**, *5* (6), 1630–1642.

(47) Cho, P.; Mattisson, T.; Lyngfelt, A. Comparison of iron-, nickel-, copper- and manganese-based oxygen carriers for chemical-looping combustion. *Fuel* **2004**, *83* (9), 1215–1225.

(48) Jin, H.; Okamoto, T.; Ishida, M. Development of a novel chemical-looping combustion: Synthesis of a looping material with a double metal oxide of CoO-NiO. *Energy Fuels* **1998**, *12* (6), 1272–1277.

(49) Abad, A.; Adánez, J.; García-Labiano, F.; de Diego, L. F.; Gayán, P.; Celaya, J. Mapping of the range of operational conditions for Cu-, Fe-, and Ni-based oxygen carriers in chemical-looping combustion. *Chem. Eng. Sci.* **2007**, *62* (1–2), 533–549.

(50) Li, F.; Sun, Z.; Luo, S.; Fan, L.-S. Ionic diffusion in the oxidation of iron—effect of support and its implications to chemical looping applications. *Energy Environ. Sci.* **2011**, *4* (3), 876–880.

(51) Li, F.; Luo, S.; Sun, Z.; Bao, X.; Fan, L.-S. Role of metal oxide support in redox reactions of iron oxide for chemical looping applications: experiments and density functional theory calculations. *Energy Environ. Sci.* **2011**, *4* (9), 3661–3667.

(52) Galinsky, N. L.; Huang, Y.; Shafiefarhood, A.; Li, F. Iron Oxide with Facilitated O2– Transport for Facile Fuel Oxidation and CO_2 Capture in a Chemical Looping Scheme. *ACS Sustain. Chem. Eng.* **2013**, *1* (3), 364–373.

(53) Peña, M. A.; Fierro, J. L. G. Chemical Structures and Performance of Perovskite Oxides. *Chem. Rev.* **2001**, *101* (7), 1981–2018.

(54) Shafiefarhood, A.; Stewart, A.; Li, F. Iron-containing mixed-oxide composites as oxygen carriers for Chemical Looping with Oxygen Uncoupling (CLOU). *Fuel* **2015**, *139*, 1–10.

(55) Arjmand, M.; Hedayati, A.; Azad, A.-M.; Leion, H.; Rydén, M.; Mattisson, T. $Ca_xLa_{1-x}Mn_{1-y}MyO_{3-\delta}$ (M = Mg, Ti, Fe, or Cu) as Oxygen Carriers for Chemical-Looping with Oxygen Uncoupling (CLOU). *Energy Fuels* **2013**.

(56) Hallberg, P.; Jing, D.; Rydén, M.; Mattisson, T.; Lyngfelt, A. Chemical Looping Combustion and Chemical Looping with Oxygen Uncoupling Experiments in a Batch Reactor Using Spray-Dried $CaMn_{1-x}M_xO_{3-\delta}$ (M = Ti, Fe, Mg) Particles as Oxygen Carriers. *Energy Fuels* **2013**, *27* (3), 1473–1481.

(57) Leion, H.; Larring, Y.; Bakken, E.; Bredesen, R.; Mattisson, T.; Lyngfelt, A. Use of $CaMn_{0.875}Ti_{0.125}O_3$ as Oxygen Carrier in Chemical-Looping with Oxygen Uncoupling. *Energy Fuels* **2009**, *23* (10), 5276–5283.

(58) Rydén, M.; Lyngfelt, A.; Mattisson, T. $CaMn_{0.875}Ti_{0.125}O_3$ as oxygen carrier for chemical-looping combustion with oxygen uncoupling (CLOU)—Experiments in a continuously operating fluidized-bed reactor system. *Int. J. Greenh. Gas Control* **2011**, *5* (2), 356–366.

(59) Sundqvist, S.; Leion, H.; Rydén, M.; Lyngfelt, A.; Mattisson, T. $CaMn_{0.875}Ti_{0.125}O_3$ as an Oxygen Carrier for Chemical-Looping with Oxygen Uncoupling (CLOU)-Solid-Fuel Testing and Sulfur Interaction. *Energy Technol.* **2013**, *1* (5-6), 338–344.

(60) Källén, M.; Rydén, M.; Dueso, C.; Mattisson, T.; Lyngfelt, A. $CaMn_{0.9}Mg_{0.1}O_{3-\delta}$ as Oxygen Carrier in a Gas-Fired 10 kW_{th} Chemical-Looping Combustion Unit. *Ind. Eng. Chem. Res.* **2013**, *52* (21), 6923–6932.

(61) Pishahang, M.; Larring, Y.; McCann, M.; Bredesen, R. $Ca_{0.9}Mn_{0.5}Ti_{0.5}O_{3-\delta}$: A Suitable Oxygen Carrier Material for Fixed-Bed Chemical Looping Combustion under Syngas Conditions. *Ind. Eng. Chem. Res.* **2014**, *53* (26), 10549–10556.

(62) Moldenhauer, P.; Rydén, M.; Mattisson, T.; Hoteit, A.; Jamal, A.; Lyngfelt, A. Chemical-Looping Combustion with Fuel Oil in a 10 kW Pilot Plant. *Energy Fuels* **2014**, *28* (9), 5978–5987.

(63) Dai, X. P.; Li, J.; Fan, J. T.; Wei, W. S.; Xu, J. Synthesis Gas Generation by Chemical-Looping Reforming in a Circulating Fluidized Bed Reactor Using Perovskite $LaFeO_{3-\delta}$ Based Oxygen Carriers. *Ind. Eng. Chem. Res.* **2012**, *51* (34), 11072–11082.

(64) Mihai, O.; Chen, D.; Holmen, A. Chemical looping methane partial oxidation: The effect of the crystal size and O content of $LaFeO_3$. *J. Catal.* **2012**, *293*, 175–185.

(65) Murugan, A.; Thursfield, A.; Metcalfe, I. S. A chemical looping process for hydrogen production using iron-containing perovskites. *Energy Environ. Sci.* **2011**, *4* (11), 4639.

(66) Readman, J. E.; Olafsen, A.; Larring, Y.; Blom, R. $La_{0.8}Sr_{0.2}Co_{0.2}Fe_{0.8}O_{3-\delta}$ as a potential oxygen carrier in a chemical looping type reactor, an in-situ powder X-ray diffraction study. *J. Mater. Chem.* **2005**, *15* (19), 1931.

(67) Rydén, M.; Lyngfelt, A.; Mattisson, T.; Chen, D.; Holmen, A.; Bjørgum, E. Novel oxygen-carrier materials for chemical-looping combustion and chemical-looping reforming; $La_xSr_{1-x}Fe_yCo_{1-y}O_{3-\delta}$ perovskites and mixed-metal oxides of NiO, Fe_2O_3 and Mn_3O_4. *Int. J. Greenh. Gas Control* **2008**, *2* (1), 21–36.

(68) Sarshar, Z.; Sun, Z.; Zhao, D.; Kaliaguine, S. Development of Sinter-Resistant Core–Shell $LaMn_xFe_{1-x}O_3$@$mSiO_2$ Oxygen Carriers for Chemical Looping Combustion. *Energy Fuels* **2012**, *26* (5), 3091–3102.

(69) Zhao, K.; He, F.; Huang, Z.; Zheng, A.; Li, H.; Zhao, Z. Three-dimensionally ordered macroporous $LaFeO_3$ perovskites for chemical-looping steam reforming of methane. *Int. J. Hydrog. Energy* **2014**, *39* (7), 3243–3252.

(70) Sarshar, Z.; Kleitz, F.; Kaliaguine, S. Novel oxygen carriers for chemical looping combustion: $La_{1-x}Ce_xBO_3$ (B = Co, Mn) perovskites synthesized by reactive grinding and nanocasting. *Energy Environ. Sci.* **2011**, *4* (10), 4258–4269.

(71) Noorman, S.; Gallucci, F.; van Sint Annaland, M.; Kuipers, J. A. M. Experimental Investigation of Chemical-Looping Combustion in Packed Beds: A Parametric Study. *Ind. Eng. Chem. Res.* **2011**, *50* (4), 1968–1980.

(72) Bhavsar, S.; Najera, M.; Solunke, R.; Veser, G. Chemical looping: To combustion and beyond. *Catal. Today* **2014**, *228*, 96–105.

(73) Bhavsar, S.; Veser, G. Bimetallic Fe–Ni Oxygen Carriers for Chemical Looping Combustion. *Ind. Eng. Chem. Res.* **2013**, *52* (44), 15342–15352.

(74) Mattisson, T.; Lyngfelt, A.; Cho, P. The use of iron oxide as an oxygen carrier in chemical-looping combustion of methane with inherent separation of CO_2. *Fuel* **2001**, *80* (13), 1953–1962.

(75) Kronberger, B.; Lyngfelt, A.; Löffler, G.; Hofbauer, H. Design and Fluid Dynamic Analysis of a Bench-Scale Combustion System with CO_2 Separation−Chemical-Looping Combustion. *Ind Eng Chem Res* **2005**, *44* (3), 546–556.

(76) Johansson, E.; Mattisson, T.; Lyngfelt, A.; Thunman, H. Combustion of Syngas and Natural Gas in a 300 W Chemical-Looping Combustor. *Chem. Eng. Res. Des.* **2006**, *84* (9), 819–827.

(77) Consonni, S.; Lozza, G.; Pelliccia, G.; Rossini, S.; Saviano, F. Chemical-Looping Combustion for Combined Cycles With CO_2 Capture. *J. Eng. Gas Turbines Power* **2006**, *128* (3), 525.

(78) Abad, A.; Mattisson, T.; Lyngfelt, A.; Rydén, M. Chemical-looping combustion in a 300 W continuously operating reactor system using a manganese-based oxygen carrier. *Fuel* **2006**, *85* (9), 1174–1185.

(79) Mattisson, T.; García-Labiano, F.; Kronberger, B.; Lyngfelt, A.; Adánez, J.; Hofbauer, H. Chemical-looping combustion using syngas as fuel. *Int. J. Greenh. Gas Control* **2007**, *1* (2), 158–169.

(80) Xiang, W.; Wang, S.; Di, T. Investigation of Gasification Chemical Looping Combustion Combined Cycle Performance. *Energy Fuels* **2008**, *22* (2), 961–966.

(81) Lyngfelt, A. Chemical-looping combustion of solid fuels – Status of development. *Appl. Energy* **2014**, *113*, 1869–1873.

(82) Sorgenfrei, M.; Tsatsaronis, G. Design and evaluation of an IGCC power plant using iron-based syngas chemical-looping (SCL) combustion. *Appl. Energy* **2014**, *113*, 1958–1964.

(83) Tong, A.; Bayham, S.; Kathe, M. V.; Zeng, L.; Luo, S.; Fan, L.-S. Iron-based syngas chemical looping process and coal-direct chemical looping process development at Ohio State University. *Appl. Energy* **2014**, *113*, 1836–1845.

(84) Scott, S. A.; Dennis, J. S.; Hayhurst, A. N.; Brown, T. *In situ* gasification of a solid fuel and CO_2 separation using chemical looping. *AIChE J.* **2006**, *52* (9), 3325–3328.

(85) Leion, H.; Mattisson, T.; Lyngfelt, A. The use of petroleum coke as fuel in chemical-looping combustion. *Fuel* **2007**, *86* (12-13), 1947–1958.

(86) Luo, S.; Bayham, S.; Zeng, L.; McGiveron, O.; Chung, E.; Majumder, A.; Fan, L.-S. Conversion of metallurgical coke and coal using a Coal Direct Chemical Looping (CDCL) moving bed reactor. *Appl. Energy* **2014**, *118*, 300–308.

(87) Gilliland, E. R.; Gilliland, E. R. Production of Pure Carbon Dioxide. 2665971, January 12, 1954.

(88) Mattisson, T.; Lyngfelt, A.; Leion, H. Chemical-looping with oxygen uncoupling for combustion of solid fuels. *Int. J. Greenh. Gas Control* **2009**, *3* (1), 11–19.

(89) Mattisson, T.; Leion, H.; Lyngfelt, A. Chemical-looping with oxygen uncoupling using CuO/ZrO_2 with petroleum coke. *Fuel* **2009**, *88* (4), 683–690.

(90) Abad, A.; Adanez-Rubio, I.; Gayan, P.; Garcia-Labiano, F.; de Diego, L. F.; Adanez, J. Demonstration of chemical-looping with oxygen uncoupling (CLOU) process in a 1.5 kW_{th} continuously operating unit using a Cu-based oxygen-carrier. *Int. J. Greenh. Gas Control* **2012**, *6*, 189–200.

(91) Mattisson, T.; Lyngfelt, A.; Leion, H. Chemical-looping with oxygen uncoupling for combustion of solid fuels. *Int. J. Greenh. Gas Control* **2009**, *3* (1), 11–19.

(92) Zafar, Q.; Abad, A.; Mattisson, T.; Gevert, B.; Strand, M. Reduction and oxidation kinetics of Mn_3O_4/Mg–ZrO_2 oxygen carrier particles for chemical-looping combustion. *Chem. Eng. Sci.* **2007**, *62* (23), 6556–6567.

(93) Imtiaz, Q.; Hosseini, D.; Müller, C. R. Review of Oxygen Carriers for Chemical Looping with Oxygen Uncoupling (CLOU): Thermodynamics, Material Development, and Synthesis. *Energy Technol.* **2013**, *1* (11), 633–647.

(94) Arjmand, M.; Azad, A.-M.; Leion, H.; Lyngfelt, A.; Mattisson, T. Prospects of Al_2O_3 and $MgAl_2O_4$-Supported CuO Oxygen Carriers in Chemical-Looping Combustion (CLC) and Chemical-Looping with Oxygen Uncoupling (CLOU). *Energy Fuels* **2011**, *25* (11), 5493–5502.

(95) Gayán, P.; Adánez-Rubio, I.; Abad, A.; de Diego, L. F.; García-Labiano, F.; Adánez, J. Development of Cu-based oxygen carriers for Chemical-Looping with Oxygen Uncoupling (CLOU) process. *Fuel* **2012**, *96*, 226–238.

(96) Adánez-Rubio, I.; Abad, A.; Gayán, P.; de Diego, L. F.; García-Labiano, F.; Adánez, J. Performance of CLOU process in the combustion of different types of coal with CO_2 capture. *Int. J. Greenh. Gas Control* **2013**, *12*, 430–440.

(97) Azimi, G.; Leion, H.; Rydén, M.; Mattisson, T.; Lyngfelt, A. Investigation of Different Mn–Fe Oxides as Oxygen Carrier for Chemical-Looping with Oxygen Uncoupling (CLOU). *Energy Fuels* **2013**, *27* (1), 367–377.

(98) Bakken, E.; Norby, T.; Stolen, S. Nonstoichiometry and reductive decomposition of CaMnO. *Solid State Ion.* **2005**, *176* (1-2), 217–223.

(99) Mattisson, T. Materials for Chemical-Looping with Oxygen Uncoupling. *ISRN Chem. Eng.* **2013**, *2013*, 1–19.

(100) Arjmand, M.; Kooiman, R. F.; Rydén, M.; Leion, H.; Mattisson, T.; Lyngfelt, A. Sulfur Tolerance of $Ca_xMn_{1-y}M_yO_{3-\delta}$ (M = Mg, Ti) Perovskite-Type Oxygen Carriers in Chemical-Looping with Oxygen Uncoupling (CLOU). *Energy Fuels* **2014**, *28* (2), 1312–1324.

(101) Ortiz, M.; Abad, A.; de Diego, L. F.; García-Labiano, F.; Gayán, P.; Adánez, J. Optimization of hydrogen production by Chemical-Looping auto-thermal Reforming working with Ni-based oxygen-carriers. *Int. J. Hydrog. Energy* **2011**, *36* (16), 9663–9672.

(102) Rydén, M.; Lyngfelt, A. Using steam reforming to produce hydrogen with carbon dioxide capture by chemical-looping combustion. *Int. J. Hydrog. Energy* **2006**, *31* (10), 1271–1283.

(103) Johansson, M.; Mattisson, T.; Lyngfelt, A.; Abad, A. Using continuous and pulse experiments to compare two promising nickel-based oxygen carriers for use in chemical-looping technologies. *Fuel* **2008**, *87* (6), 988–1001.

(104) Nakamura, T. Hydrogen production from water utilizing solar heat at high temperatures. *Sol. Energy* **1977**, *19* (5), 467–475.

(105) Sibieude, F.; Ducarroir, M.; Tofighi, A.; Ambriz, J. High temperature experiments with a solar furnace: The decomposition of Fe_3O_4, Mn_3O_4, CdO. *Int. J. Hydrog. Energy* **1982**, *7* (1), 79–88.

(106) Perkins, C.; Weimer, A. W. Solar-thermal production of renewable hydrogen. *AIChE J.* **2009**, *55* (2), 286–293.

(107) Chueh, W. C.; Falter, C.; Abbott, M.; Scipio, D.; Furler, P.; Haile, S. M.; Steinfeld, A. High-Flux Solar-Driven Thermochemical Dissociation of CO_2 and H_2O Using Nonstoichiometric Ceria. *Science* **2010**, *330* (6012), 1797–1801.

(108) Muhich, C. L.; Evanko, B. W.; Weston, K. C.; Lichty, P.; Liang, X.; Martinek, J.; Musgrave, C. B.; Weimer, A. W. Efficient Generation of H_2 by Splitting Water with an Isothermal Redox Cycle. *Science* **2013**, *341* (6145), 540–542.

(109) Go, K. S.; Son, S. R.; Kim, S. D.; Kang, K. S.; Park, C. S. Hydrogen production from two-step steam methane reforming in a fluidized bed reactor. *Int. J. Hydrog. Energy* **2009**, *34* (3), 1301–1309.

(110) Yamaguchi, D.; Tang, L.; Wong, L.; Burke, N.; Trimm, D.; Nguyen, K.; Chiang, K. Hydrogen production through methane–steam cyclic redox processes with iron-based metal oxides. *Int. J. Hydrog. Energy* **2011**, *36* (11), 6646–6656.

(111) Kidambi, P. R.; Cleeton, J. P. E.; Scott, S. A.; Dennis, J. S.; Bohn, C. D. Interaction of Iron Oxide with Alumina in a Composite Oxygen Carrier during the Production of Hydrogen by Chemical Looping. *Energy Fuels* **2012**, *26* (1), 603–617.

(112) Kierzkowska, A. M.; Bohn, C. D.; Scott, S. A.; Cleeton, J. P.; Dennis, J. S.; Müller, C. R. Development of Iron Oxide Carriers for Chemical Looping Combustion Using Sol−Gel. *Ind. Eng. Chem. Res.* **2010**, *49* (11), 5383–5391.

(113) Rydén, M.; Arjmand, M. Continuous hydrogen production via the steam–iron reaction by chemical looping in a circulating fluidized-bed reactor. *Int. J. Hydrog. Energy* **2012**, *37* (6), 4843–4854.

(114) Galvita, V.; Hempel, T.; Lorenz, H.; Rihko-Struckmann, L. K.; Sundmacher, K. Deactivation of Modified Iron Oxide Materials in the Cyclic Water Gas Shift Process for CO-Free Hydrogen Production. *Ind. Eng. Chem. Res.* **2008**, *47* (2), 303–310.

(115) He, F.; Trainham, J.; Parsons, G.; Newman, J. S.; Li, F. A hybrid solar-redox scheme for liquid fuel and hydrogen coproduction. *Energy Environ. Sci.* **2014**, *7* (6), 2033.

(116) Mihai, O.; Chen, D.; Holmen, A. Chemical looping methane partial oxidation: The effect of the crystal size and O content of $LaFeO_3$. *J. Catal.* **2012**, *293*, 175–185.

CHAPTER 2 CHEMICAL LOOPING GASIFICATION OF SOLID FUELS USING BIMETALLIC OXYGEN CARRIER PARTICLES – FEASIBILITY ASSESSMENT AND PROCESS SIMULATIONS

Feng He, Nathan Galinsky, and Fanxing Li*

Department of Chemical & Bimolecular Engineering, North Carolina State University, Raleigh, North Carolina 27695, United States

CHAPTER 2 is a reprint of a manuscript published in *International Journal of Hydrogen Energy*, 2013, 38:7839. The supplementary information is in Appendix A.

* To whom the correspondence should be addressed. Telephone: +1 (919) 515-7328. Fax: +1 (919) 515-3465. E-mail: fli5@ncsu.edu.

Abstract

The chemical looping gasification (CLG) process utilizes an iron-based oxygen carrier to convert carbonaceous fuels into hydrogen and electricity while capturing CO_2. Although the process has the potential to be efficient and environmentally friendly, the activity of the iron-based oxygen carrier is relatively low, especially for solid fuel conversion. In the present study, we propose to incorporate a secondary oxygen carrying metal oxide, i.e. CuO, to the iron-based oxygen carrier. Using the "oxygen-uncoupling" characteristics of CuO, gaseous oxygen is released at a high temperature to promote the conversion of both Fe_2O_3 and coal. Experiments carried out using a Thermal-Gravimetric Analyzer (TGA) indicate that a bimetallic oxygen carrier consisting of a small amount (5% by weight) of CuO is more effective for coal char conversion when compared to oxygen carrier without copper addition. ASPEN Plus® simulations and mathematical modeling of the process indicate that the incorporation of a small amount of copper leads to increased hydrogen yield and process efficiency.

Nomenclature

$\%Conversion$	Conversion of the oxygen carrier/char mixture in the TGA test
$\Delta\dot{H}_1$	Energy carried by exhaust gas from the reducer
$\Delta\dot{H}_2$	Energy carried by exhaust gas from the oxidizer
$\Delta\dot{H}_3$	Energy carried by exhaust gas from the combustor
$\Delta\dot{H}_4$	Energy carried by exhaust gas from the turbines
$\Delta\dot{H}_{Reactor\_Loss}$	Rate of heat loss from reactor
$\Delta\dot{H}_{Loss}$	Rate of process energy loss
$\Delta H_{Vap,water}$	Latent heat of steam
ΔH_{R_j}	Heat of reaction for reaction *j*
$\Delta\dot{H}_{Turbine}$	Overall enthalpy of steam entering the steam turbine

K	Reaction equilibrium constant
m_c	Initial mass of the carbon
m_{int}	Initial mass of sample in the TGA test, including the oxygen carrier and the char
m_t	Mass of the sample at time t
MeO_x	Metal oxide
MW	Molecular weight
$\dot{n}_{i,reactor,in/out}$	Molar flow rate of stream i flowing into or out of a reactor, e.g. $\dot{n}_{H_2O,Oxidizer,in}$ refers to rate of H_2O feed into the oxidizer
O/C	Molar ratio between active oxygen in oxygen carrier and carbon in coal entering the reducer, $O/C = \frac{3\dot{n}_{Fe_2O_3,reducer,in} + \dot{n}_{CuO,reducer,in}}{\dot{n}_{C,reducer,in}}$
P	Pressure
$\dot{Q}_{Reducer}$	Rate of heat added in to the reducer
T_i	Temperature of a process unit (block) or stream denoted by i
T_0	Environmental temperature (25 °C)
T_1	Temperature of the reducer exhaust stream
T_2	Temperature of the oxidizer exhaust stream
T_3	Temperature of the combustor exhaust stream
T_4	Temperature of the turbines exhaust stream
x_{CuO}	CuO conversion in the reducer, $x_{CuO} = \frac{n_{CuO,reducer,in} - 2n_{Cu_2S,reducer,out} - n_{Cu_2O,reducer,out}}{n_{CuO,reducer,in} - 2n_{Cu_2S,reducer,out}}$
$x_{Fe_2O_3}$	Fe_2O_3 conversion in the reducer, $x_{Fe_2O_3} = \frac{3n_{Fe_2O_3,reducer,in} - 1.5(n_{Fe_{0.877}S,reducer,out})/0.877 - n_{Fe_{0.947}O,reducer,out}}{3n_{Fe_2O_3,reducer,in} - 1.5(n_{Fe_{0.877}S,reducer,out})/0.877}$
x_{steam}	Steam conversion in the oxidizer

y_{CO_2} CO_2 yield of a process, $y_{CO_2} = \frac{n_{CO_2,reducer,out}}{n_{C,reducer,in}}$

$\eta_{H_2,HHV}$ Hydrogen generation efficiency $\eta_{H_2,HHV} = \frac{\dot{m}_{H_2} E_{HHV,H_2}}{\dot{m}_{coal} E_{HHV,coal}}$

$\eta_{tot,HHV}$ Process efficiency $\eta_{tot,HHV} = \frac{\dot{m}_{H_2} E_{HHV,H_2} + \dot{W}_{Electricity}}{\dot{m}_{coal} E_{HHV,coal}}$

$\eta_{tot,LHV}$ Process efficiency $\eta_{tot,LHV} = \frac{\dot{m}_{H_2} E_{LHV,H_2} + \dot{W}_{Electricity}}{\dot{m}_{coal} E_{LHV,coal}}$

2.1 Introduction

Carbon dioxide emitted from fossil energy conversion accounts for roughly 20% of the greenhouse effect [1]. In order to mitigate the anthropogenic CO_2 emissions, effective carbon capture, utilization, and storage (CCUS) approaches need to be developed and adopted for fossil fuel conversions. Chemical looping processes, which include chemical looping combustion (CLC) and chemical looping gasification (CLG), utilize a novel, indirect strategy for fossil fuel conversion and CO_2 capture [2–5]. The CLC process uses an oxygen carrier particle to oxidize the carbonaceous fuel into concentrated CO_2. The reduced oxygen carrier resulting from the fuel oxidation step is subsequently combusted with air to generate heat/electricity [2,6]. CLG, on the other hand, uses an Fe_2O_3 based oxygen carrier particle to convert fuels into separate streams of sequestrable CO_2, heat/electricity, and hydrogen [7,8]. Both CLC and CLG use solid oxygen carriers to convert carbonaceous fuels through redox reactions. A key process unit common to both processes is the fuel reactor, also known as the reducer, where carbonaceous fuels react with oxygen carriers to form CO_2 [9,10].

Early research on chemical looping focused on the conversion of gaseous fuels such as methane/natural gas [11–14] and coal derived syngas [15–17]. These studies have resulted in various oxygen carriers with satisfactory reactivity, recyclability, and attrition resistance for

gaseous fuel conversions [18–20]. Continuous testing of these oxygen carriers have been successfully carried out in circulating fluidized bed (CFB) reactors at scales ranging from 300 W_{th} to 1 MW_{th} [9,21–23,45]. Besides the aforementioned experimental studies, the attractiveness of chemical looping as a novel power/hydrogen production process has been confirmed by both availability and process analyses [24,25]. Compared to gaseous fuels, solid fuels such as coal are cheaper on a same energy content basis. Therefore, direct conversion of solid fuels in chemical looping processes can be advantageous from a process economics standpoint. A key challenge for solid fuel conversion, however, resides in the slow solid-solid reaction kinetics between the fuel and the oxygen carriers. Over the past decade, extensive research has been performed on chemical looping conversion of solid fuels. These studies encompass oxygen carrier development [26–28], reactor system testing [26,29], and process evaluations [30,31]. Various types of coal and biomass were also used as the feedstock [32,33]. To date, one of the focal research areas for solid fuel CLC is still in the design of effective oxygen carriers and an operating scheme to achieve satisfactory solid fuel conversions.

A common method to enhance solid fuel conversion is through in-situ gasification [3,5]. Under this approach, a gasification enhancer such as steam and/or CO_2 is introduced to the fuel reactor to gasify the fixed carbon via steam-carbon reaction and/or reverse Boudouard reaction, producing H_2 and/or CO. The H_2/CO generated will then react with the oxygen carrier at a faster rate than the solid fuel–oxygen carrier reactions. Reactions between the oxygen carrier and H_2/CO produce additional steam/CO_2 for in-situ solid fuel gasification. As a result, a chain reaction can be initiated. Although the in-situ gasification approach can enhance the solid fuel conversion rate, steam-carbon and reverse Boudouard reactions are relatively slow at typical reducer operating temperatures. Hence a long fuel and metal oxide residence time is required in order to achieve satisfactory solid fuel conversions [9]. The residence time requirements may lead to large reducer volume and solids inventory.

The Chemical-Looping with Oxygen Uncoupling (CLOU) is another strategy to enhance solid fuel conversion. First proposed by Lewis and Gilliland [34] in the 1950s, the CLOU strategy uses gaseous oxygen released from metal oxide decomposition to convert solid fuels. CuO is

the most frequently used oxygen carrier for the CLOU processes. Other suitable metal oxides include oxides of manganese and cobalt, and certain mixed transition metal oxides [4,35,36]. The CLOU concept has been tested over the past decade for the combustion of petroleum coke [35,36], and coal [37]. Using a laboratory scale fluidized bed reactor, Mattisson et al. [35] demonstrated 50-fold rate enhancement for petroleum coke conversion using CuO based CLOU when compared to an iron-based oxygen carrier in an in-situ gasification scheme. Leion et al. [38] observed improved reaction rates for six different solid fuels using the CLOU strategy. Adánez-Rubio et al. [39] tested $MgAl_2O_4$ supported CuO in a batch fluidized-bed reactor. They reported complete conversion of the solid fuels. Although the CLOU scheme using CuO based oxygen carrier has distinct advantages for solid fuel conversion from a reaction kinetics standpoint, it has certain limitations including relatively low sintering resistance (when reduced to metallic copper) and high raw material cost when compared to Fe_2O_3. In addition, the CuO based oxygen carrier, in reduced forms, does not react with steam/water at any appreciable extent. Therefore, it is not suitable for the production of H_2, a value-added commodity chemical and clean fuel. To compare, iron based oxygen carrier can be utilized in the CLG schemes for hydrogen and power co-production. The rate for Fe_2O_3 solid fuel reactions, however, tends to be slow. Therefore, novel strategies that can take the advantage of the fast reaction kinetics of the CLOU strategy and the product-flexible nature of the CLG scheme are desired.

The use of iron-based oxygen carrier for chemical looping gasification of coal has been proposed and demonstrated by Fan et al. in the so called coal direct chemical looping (CDCL) gasification process [8,9,31]. Using an in-situ gasification strategy, 95% coal/coal char conversion was achieved in a 2.5 kW_{th} scale bench unit [3]. ASPEN Plus® CDCL process simulation performed by Zeng et al. [40] indicated that a high efficiency can potentially be achieved in the CDCL process. In the present work, we propose to incorporate CuO into the Fe_2O_3 based oxygen carrier to enhance the solid fuel conversion rate. The resulting bimetallic CLG process, enhanced by the CuO based oxygen uncoupling agent, has the potential to be effective for solid fuel conversion while maintaining the ability for hydrogen production at

high efficiency. To validate the feasibility of this bimetallic CLG concept, preliminary experiments are performed in a Thermal-Gravimetric Analyzer (TGA). ASPEN Plus® simulation and mathematical modeling are also carried out to evaluate the reactor and process performances.

2.2 Proposed approach and rationale

Addition of CuO to iron-based oxygen carrier is potentially beneficial for chemical looping gasification of coal since oxides of iron and copper have complementing chemical and physical properties. Table 2.1 summarizes the key chemical and physical properties of CuO and Fe_2O_3 for chemical looping applications. Several key property differences between CuO and Fe_2O_3 include:

- Ability to generate gaseous oxygen: CuO decomposes at high temperatures to generate gaseous oxygen, an effective gasifying agent for coal char gasification. In contrast, Fe_2O_3 is relatively stable. The equilibrium constants for the decomposition reactions of Fe_2O_3 and CuO are given in reactions 1 and 2.

$$6Fe_2O_3 \leftrightarrow 4Fe_3O_4 + O_2 \qquad K = 1 \times 10^{-6} \quad (900\ ^\circ C) \qquad (1)$$

$$4CuO \leftrightarrow 2Cu_2O + O_2 \qquad K = 1.2 \times 10^{-1} \quad (900\ ^\circ C) \qquad (2)$$

- Heat of reaction: oxidation of coal using CuO releases heat ($4CuO + C \leftrightarrow 2Cu_2O + CO_2$, ΔH = -132.8 kJ mol^{-1} at 900 °C). To compare, coal conversion using Fe_2O_3 is highly endothermic ($2Fe_2O_3 + C \leftrightarrow 4FeO + CO_2$, ΔH = 158.63 kJ mol^{-1} at 900 °C).
- Ability for water splitting/hydrogen generation: Fe_2O_3 can be reduced to FeO and Fe, both materials can readily react with steam to produce hydrogen. In contrast, neither Cu nor Cu_2O is active for hydrogen generation from water.

Table 2.1. Key properties of copper and iron oxides

	FeO_x	CuO_x
Group	VIIIB	IB
Oxidation States	4	3
Heat of Reaction with Coal	Positive	Negative
O_2 Uncoupling – Gasifying Agent Generation	N	Y
Reaction Rate with Coal/ Biomass without Gasifying Agent	Slow	Fast
Capable of Producing H_2	Y	N
Sintering Temperature	High	Low
Maximum Loading	High	Low
Cost	Low	Medium

According to the above mentioned characteristics of copper and iron, addition of small amount of CuO to iron based oxygen carrier can be attractive since an active oxygen carrier with relatively low cost for solid fuel conversion can potentially be obtained. With Fe_2O_3 being the primary oxide, the resulting bimetallic oxygen carrier particle can be used for the chemical looping gasification process. A schematic illustrating the enhancement effect of CuO is given in Fig. 2.1. The gaseous oxygen released by CuO decomposition can potentially enhance the coal conversion rate by a significant extent since a "chain reaction" can be initiated by a series of reactions including coal char gasification, syngas oxidation, and reverse Boudouard reaction. Such an enhancement effect can be achieved by intimately mixing or co-injecting bimetallic oxygen carrier and coal in the reducer. Addition of CuO also reduces the endothermicity of the oxygen carrier-coal reactions, thereby simplifying the energy integration scheme of the overall process. It is noted that oxides of iron or aluminum [41] and copper can form mixed metal oxides such as $CuFe_2O_4$ at typical chemical looping reaction conditions. This is undesirable for the proposed CLG system since the solid-state reactions between iron and copper oxides reduces the amount of CuO. As a result, O_2 generation from CuO uncoupling will be inhibited. Two approaches are proposed to limit the interactions between iron and copper oxides: (1) formation of composite copper-iron oxides spatially divided by a porous

support; (2) physically mixing copper and iron based oxygen carriers in the chemical looping reactors. Our experimental studies indicate that the solid-state reaction can be inhibited by the aforementioned strategies. Therefore, we will not consider the formation of mixed copper-iron oxides in our simulations.

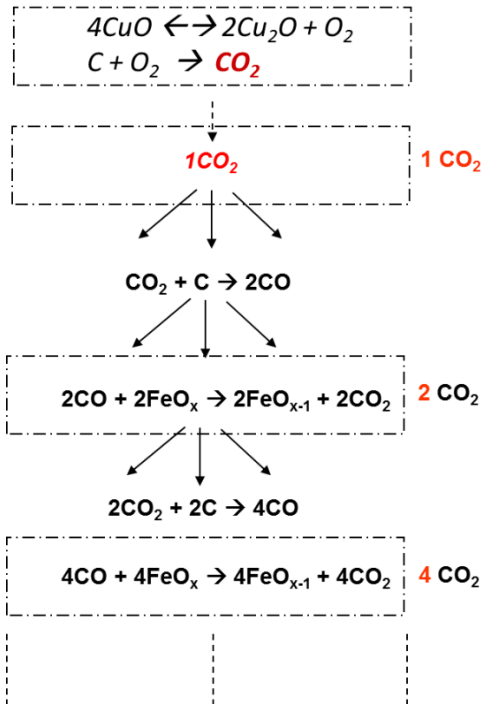

Fig. 2.1. (a) Overall material balances of the CLG process. (b) The flow chart of the mathematic model for the chemical looping process.

The proposed process configuration, similar to the chemical looping gasification scheme reported previously [9,40], is illustrated in Fig. 2.2. The key difference is that a small amount of CuO is added to the Fe_2O_3 based oxygen carrier. The representative reactions in the three-step reactors are summarized in Table 2.2. Further details regarding the chemical looping gasification process can be found elsewhere [9,42].

Table 2.2. Key reactions in the reducer, oxidizer, and combustor

Reducer	Oxidizer	Combustor
$4CuO \leftrightarrow 2Cu_2O + O_2$ $Cu_2O + C \leftrightarrow Cu + CO_2 / CO$ $C + O_2 \rightarrow CO_2$ $C + CO_2 \rightarrow CO$ $Fe_2O_3 + C \leftrightarrow Fe_3O_4 + CO_2 / CO$ $Fe_3O_4 + CO \rightarrow 3Fe_{0.947}O + CO_2$ $Fe_{0.947}O + CO \rightarrow Fe + CO_2$	$Fe + H_2O \leftrightarrow FeO + H_2$ $3FeO + H_2O \leftrightarrow Fe_3O_4 + H_2$	$4Fe_3O_4 + O_2 \rightarrow 6Fe_2O_3$ $4Fe_{0.947}O + O_2 \rightarrow 2Fe_2O_3$ $2Cu + O_2 \rightarrow 2CuO$ $2Cu_2O + O_2 \rightarrow 4CuO$
Endothermic	Exothermic	Exothermic

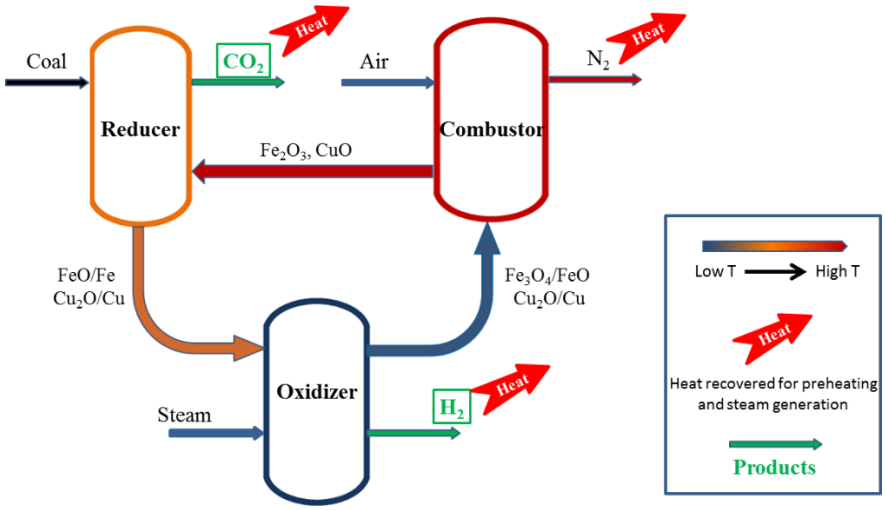

Fig. 2.2. Schematic of the bimetallic chemical looping gasification process.

2.3 Methodology

2.3.1 Materials and procedures

Two oxygen carriers, both containing 60 w.t.% Fe_2O_3, are synthesized via a solid state method. Fe_2O_3 supported on Al_2O_3 is used as a reference material. The reference material is prepared in which calculated amounts Fe_2O_3 (99.9%, Noah Chemical) and Al_2O_3 (99.9% anatase, Noah Chemical) precursors at a weight ratio of 60: 40 are used. The mixture is prepared in a planetary ball mill (XBM4X, Columbia International) for 3 hours at a rotation speed of 250 rpm. This is followed with pelletization in a tablet press (MTI). The pellets are then annealed in a tube furnace (OTF-1200X-S-VT, MTI) at 900 °C for 8 hours. A second oxygen carrier, which contains CuO promoter, is prepared using a similar approach. The oxygen carrier is prepared from Fe_2O_3 (99.9%, Noah chemical) and CuO supported on Al_2O_3 (13 w.t.% CuO, Sigma Aldrich) at a weight ratio of 60:40. Since CuO is impregnated into the porous structure of Al_2O_3, solid state reactions between iron and copper oxides are minimized. Coal char is prepared from bituminous coal (Asbury Carbons C3) through pyrolysis under an inert environment. All the reactivity studies are conducted in a SETARAM SETSYS Evolution TGA at 950 °C for 5 hours. Details regarding the TGA experiments are provided in the supplementary data section. Although the reaction environment in TGA is notably different from that in a moving bed or fluid bed reactor, the TGA experiments are designed to obtain preliminary confirmation for char conversion activity of the bimetallic oxygen carrier. It also serves to confirm whether the formation of mixed Fe-Cu oxide, which is undesirable for CLG, can be inhibited. The crystal structures of the post-experiment sample is tested using a Rigaku SmartLab X-ray diffractometer with Cu-Kα (λ=0.1542) radiation operating at 40 kV and 44 mA.

2.3.2 Simulation assumptions

ASPEN Plus® simulator [43] is used in the present study to determine the reactor and process performance and the process optimization strategy. Key simulation assumptions include: hydrogen is the desired product; electricity is co-generated mainly to meet parasitic power consumptions; Illinois #6 coal is used as the feedstock; coal processing capacity of the process

is 132.65 tonnes/hour (1000MWth, HHV). Table 2.3 specifies the key materials involved in the simulations. ASPEN Plus modules, property methods, and physical property databanks are summarized in Table 2.4. PR-BM is selected as the property method in all the simulation modules except for steam cycles, where STEAM-TA method is used. Table 2.5 lists the key operating assumptions and parameters used in the process simulations. Since the moving bed chemical looping gasification reactors are operated at high temperatures with relatively long residence time, it is assumed that thermodynamic equilibriums in the chemical looping reactors can be achieved in several simulation cases. A more conservative assumption of 95% coal conversion and 40% Fe_2O_3 conversion, which is achieved from moving bed reactor testing [9], is also used to evaluate kinetically limited cases. By comparing results obtained from the ideal, equilibrium assumptions with those from the conservative assumptions, the effects of the coal and metal oxide conversions on the overall process performance and efficiency can be revealed.

Table 2.3. Specifications of the materials

Feedstock to the CDCL system	
Coal (Illinois #6)	11.12% Moisture, 9.70% Ash, 63.75% C, 4.50% H, 1.25% N, 0.29% Cl, 2.51% S, 6.88% O, 0.0001% Hg by weight. HHV 27.113 MJ kg^{-1}, LHV 26.151 MJ kg^{-1}
Air	79% N_2, 21% O_2 by volume
Oxygen Carrier	Fe_2O_3, CuO, SiC (inert)
Water	H_2O
Process Output	
CO_2	>90% CO_2 capture efficiency; Purity: > 99% 15.3 MPa
H_2 product	Purity: >99.99% Pressure: 6 MPa
Flue gas	N_2, CO_2, NO_x (<300ppm), SO_x (<500ppm) 1 atm
Ash	Acting as inert
Sulfur	H_2S captured by acid gas removal process; SO_2 captured FGD process
Chlorine	Captured by wet/alkali scrubbing
Mercury	Captured by activated carbon

Table 2.4. ASPEN Plus® model setup

Stream class	MIXCINC
Databank	COMBUST, INORGANIC, SOLIDS, PURE
Solid components	Fe, $Fe_{0.947}O$, Fe_3O_4, Fe_2O_3, $Fe_{0.877}S$, Cu, Cu_2O CuO, CuS, Cu_2S,SiC
Nonconventional components	Coal, Ash
Property method	PR-BM, except STEAM-TA for steam cycles
Solution strategy	Sequential Modular
Unit operations Models	
Reducer	Multi-stage RGibbs (moving bed)
Oxidizer	Multi-stage RGibbs (moving bed); RYield
Combustor	RGibbs
Pressure changers	Pump, Compr, Mcompr
Heat exchangers	Heater, MheatX
Mixers/Splitters/Separators	Mixer/Fsplit/Sep/Flash2

Table 2.5. Key assumptions and simulation parameters

Ambient condition	T = 25 °C, P = 1 atm
Reaction assumptions	Unless specified, all reactions reach their equilibriums
Heat loss in the chemical looping reactors	1% of the total thermal input
Nominal pressure	30 atm
Pressure drop in the reducer and oxidizer	1 atm
Mechanical efficiency of pressure changers	1
Isentropic efficiency of steam turbines	0.85
Isentropic efficiency of air blowers and compressors	0.8
Heat Recovery Steam Generator	Pinch point: 15 ℃
Compressor specifications	4 stage with intercooler at 40°C, Isentropic efficiency is 0.8
Air Feed	10% excess at minimum (by mole)
Steam turbine conditions	3-level Steam Cycle 12.4 MPa (HP inlet)/3.1MPa(IP inlet)/0.45MPa(LP inlet)/0.01MPa(LP outlet)
Exhaust streams temperatures upon discharging to the environment	Reducer exhaust: 167 ℃ Oxidizer exhaust: 127 ℃ Combustor exhaust: 127 ℃
Pressure Swing Adsorption (PSA)	15 atm pressure drop in product gas steam; 95% H_2 recovery ratio unless specified

2.3.3 Reactor and process modeling

Prior to the comprehensive process analysis, key chemical looping reactors, i.e. the reducer and oxidizer, are simulated using a multi-stage RGibbs model reported earlier [31,40]. Combustor, which is a turbulent bed coupled with a riser operated at very high temperature (> 1000 °C) is simulated with a single RGibbs block. Since the key function of the reducer is to completely oxidize coal into H_2O and CO_2, simulations are carried out to determine the reducer operating parameters for complete coal oxidation. Steam conversion in the oxidizer, which is

a key parameter to characterize the oxidizer effectiveness, is also simulated. The effects of CuO addition on the coal and metal oxides conversions are also investigated.

After reactor modeling, process simulations are conducted. The ASPEN simulation model developed is shown in Fig. 2.S1. In the process simulation, pulverized coal as well as oxygen carrier particles are initially fed into the reducer. From the reducer, the reduced oxygen carrier particles are transported to the oxidizer. In the meantime, preheated steam is sent in the oxidizer for hydrogen generation via the steam-iron reaction. In the combustor, the reduced oxygen carrier is fully oxidized by excess air prior to recycling back to the reducer for another chemical loop. The high temperature gaseous product streams from the reactors are directed to a Heat Recovery Steam Generator (HRSG), where the sensible and latent heats of the product streams are captured. The HRSG has two important functions: (1) it preheats the gaseous reactants for the reactor; (2) it generates steam for steam turbines. The heat-exchanged products coming out of the HRSG, e.g. CO_2 from the reducer and H_2 from oxidizer, are cleaned and compressed for subsequent storage and transportation.

Four simulation cases with different operating conditions, as illustrated in Table 2.6, are investigated. Fe_2O_3 is used as the only oxygen carrier in Cases I and II. Case I assumes coal conversion of 99%. It further assumes that Fe_2O_3 equilibrates with the fuel and flue gases in the moving bed reducer, which corresponds to 56% Fe_2O_3 conversion. Case II considers a kinetically limited scenario of 95% coal conversion and 40% Fe_2O_3 conversion [3]. To validate the feasibility of the bimetallic CLG concept, CuO is incorporated with a 9:1 molar ratio (Fe_2O_3:CuO) in Case III and Case IV. Case III is consistent with Case I in assuming 99% coal conversion and equilibrium metal oxide conversion (64% for the bimetallic oxygen carrier). Similar to Case II, Case IV assumes 95% conversion of coal and 40% conversion of metal oxides. Sensitivity analyses are performed by varying key parameters including oxidizer temperature and inert support amount to determine the optimum operating condition.

Table 2.6. Operating conditions for the process simulation cases

	Case I	Case II	Case III	Case IV
Feedstock	Illinois #6 Coal, 1000 MW_{th}, 132.65 tonnes/hr			
Metal Oxide	Fe_2O_3	Fe_2O_3	Fe_2O_3:CuO (9:1)	Fe_2O_3:CuO (9:1)
Reducer	900 ℃			
Oxidizer	750 ℃			
Combustor	1170 ℃			
Coal conversion in Reducer	99%	95%	99%	95%
Metal oxide conversion in Reducer	56%	40%	64%	40%

2.3.4 Mathematical model for process energy loss calculation

Besides ASPEN Plus® simulations, a mathematical model is established to quantify the efficiency (loss) of the CLG process. The model can be used for process efficiency analysis and optimization. In the CLG process, as shown in the Fig. 2.3, the feedstock of the CLG process including coal, water to the oxidizer and air to the combustor. The products include CO_2, H_2, N_2, O_2, H_2O, etc. The following equations are used to quantify the process energy loss and process efficiency: equation 3a dictates the overall energy balance, where $\dot{m}_{coal}E_{HHV,coal}$ represents the total thermal input and $\Delta\dot{H}_{Loss}$ indicates the total energy loss. The process efficiency is given in equation 3b.

Overall energy balance and thermal efficiency:

$$\dot{m}_{coal}E_{HHV,coal} = \dot{m}_{H_2}E_{HHV,H_2} + \dot{W}_{Electricity} + \Delta\dot{H}_{Loss} \quad (3a)$$

$$\eta_{tot} = \frac{\dot{m}_{H_2}E_{HHV,H_2} + \dot{W}_{Electricity}}{\dot{m}_{coal}E_{HHV,coal}} = \frac{\dot{m}_{coal}E_{HHV,coal} - \Delta\dot{H}_{Loss}}{\dot{m}_{coal}E_{HHV,coal}} \quad (3b)$$

Total process energy loss:

$$\Delta \dot{H}_{Loss} = \sum_i \Delta \dot{H}_i = \Delta \dot{H}_1 + \Delta \dot{H}_2 + \Delta \dot{H}_3 + \Delta \dot{H}_4 + \Delta \dot{H}_{Reactor\_Loss} \quad (4)$$

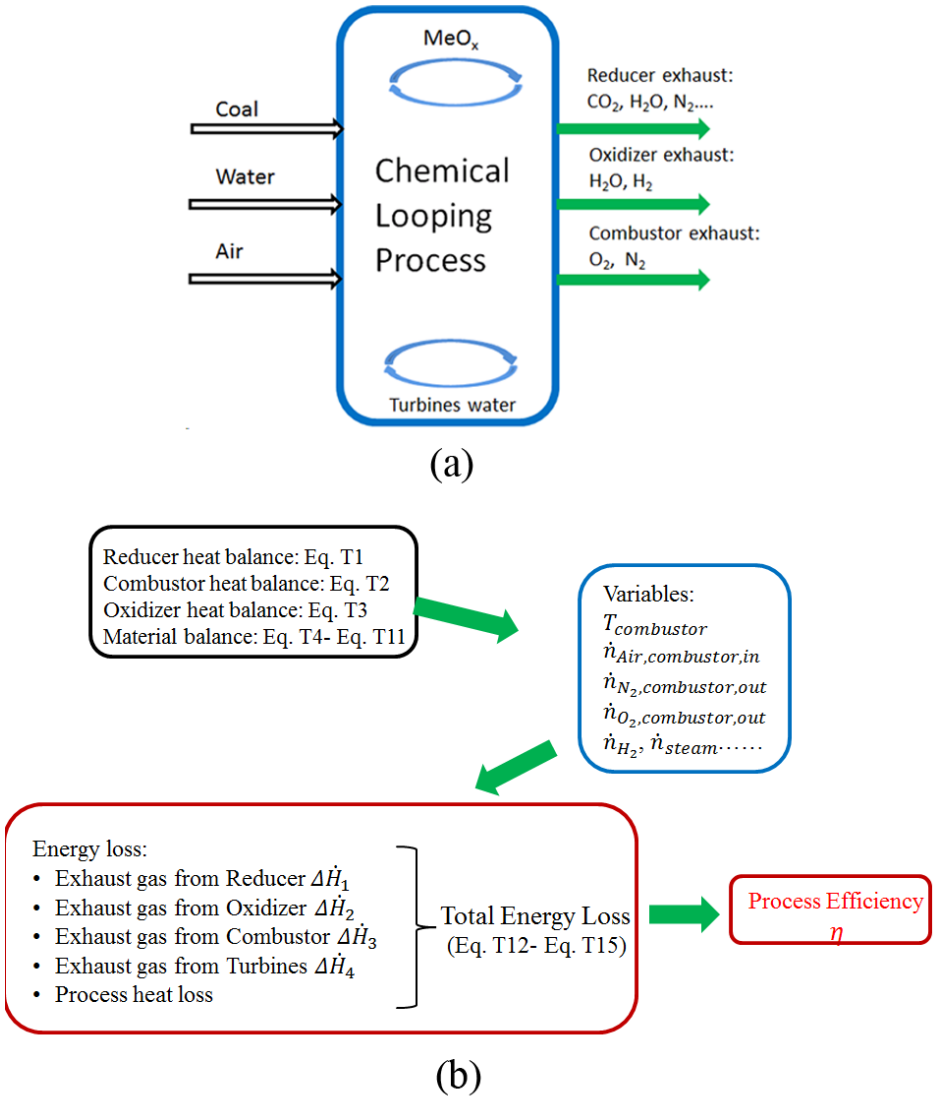

Fig. 2.3 (a) Overall material balances of the CLG process. (b) The flow chart of the mathematic model for the chemical looping process.

Equation 4 summarizes the various items included in the process heat loss ($\Delta \dot{H}_{Loss}$) including reactor heat loss and energy loss from residue heat carried by the exhaust gas streams after heat recovery operations. The heat loss from the exhaust streams is thus closely correlated with their flow rates (equations T12 to T15). Under given operating conditions, the material balances (equations T4 to T11) in the chemical looping system and energy balance for individual reactors (equations T1 to T3) directly determine the flow rate of each species. Therefore, it is feasible to calculate the product flow rates and overall energy loss by simultaneously solving the mass and energy balance equations. For consistency, assumptions identical to those in ASPEN simulations are used.

Fig. 2.3 illustrates the general modeling strategy. To summarize, $T_{combustor}$ is calculated first based on the reducer heat requirement using Eq. 3. The flow rates of $\dot{n}_{Fe_2O_3}$, $\dot{n}_{Fe_2O_3}$, $\dot{n}_{CuO}$, $\dot{n}_{Air}$, $\dot{n}_{N_2}$, $\dot{n}_{O_2}$ are then determined by the material and energy balances of the three looping reactors (equations T1 to T11). In a third step, the rates of the energy loss are obtained from equations T12 to T15. Finally, the overall process efficiency can be estimated based on the process energy input and energy loss (equtaions1-2). These equations are solved by multi-head linear algorithm using FORTRAN 95 language.

With the calculated flow rates in Table 2.7, the equations in Table 2.8 show the process heat loss by specific exhaust streams from chemical looping reactors and turbines. The overall heat loss of the process can be obtained by adding up the aforementioned heat losses.

Table 2.7. Energy and material balances in the chemical looping gasification process

Reducer heat balance:

$$-\dot{Q}_{\mathrm{Re}ducer} = \sum_i \dot{n}_i C_{p,i} (T_{combustor} - T_{reducer}) \quad \text{(T1)}$$

Oxidizer heat balance:

$$\dot{Q}_{\mathrm{oxidizer}} = \sum_i [\dot{n}_i C_{p,i} (T_{reducer} - T_{\mathrm{oxidizer}})] - \sum_j [\dot{n}_j \Delta H_{R,j,T_{\mathrm{oxidizer}}}] - \dot{n}_{steam,\mathrm{oxidizer},in} C_{p,steam} (T_{\mathrm{oxidizer}} - T_{steam}) \quad \text{(T2)}$$

Combustor heat balance

$$-\sum_i (\dot{n}_i \Delta H_{R,i,T_{combustor}}) = \dot{n}_{Air,combustor,in} C_{p,Air} (T_{oxidizer} - T_{Air}) + \sum_j [\dot{n}_j C_{p,j} (T_{combustor} - T_{oxidizer})] \quad \text{(T3)}$$

Material balances:

$$2\dot{n}_{Fe_2O_3,reducer,in} = 3\dot{n}_{Fe_3O_4,combustor,in} + 0.947\dot{n}_{Fe_{0.947}O,combustor,in} \quad \text{(T4)}$$

$$\dot{n}_{CuO,reducer,in} = \frac{\dot{n}_{Fe_2O_3}}{9} \quad \text{(T5)}$$

$$\dot{n}_{Air,combustor,in} = (0.25\dot{n}_{Fe_3O_4,combustor,in} + 0.21\dot{n}_{Fe_{0.947}O,combustor,in} + 0.5\dot{n}_{CuO,combustor,in}) \times \frac{1}{0.21} \times 1.1 \quad \text{(T6)}$$

$$\dot{n}_{N_2,combustor,out} = 0.79\dot{n}_{Air,combustor,in} \quad \text{(T7)}$$

$$\dot{n}_{O_2,combustor,out} = \frac{0.21}{11}\dot{n}_{Air,combustor,in} \quad \text{(T8)}$$

$$\dot{n}_{H_2,oxidizer,out} = \frac{1}{0.947}\dot{n}_{Fe,oxidizer,in} + \frac{0.788}{0.947}\dot{n}_{Fe_3O_4,oxidizer,out} \quad \text{(T9)}$$

$$\dot{n}_{steam,\mathrm{oxidizer},in} = \frac{1}{x_{steam}}\dot{n}_{H_2,\mathrm{oxidizer,out}} \quad \text{(T10)}$$

$$x_{steam} = f(T_{\mathrm{oxidizer}}) = 0.98 - 4\times10^{-4} T_{\mathrm{oxidizer}} \quad \text{(T11)}$$

Variables calculated:

$\dot{n}_{Fe_3O_4,combustor,in}$, $\dot{n}_{Fe_{0.947}O,combustor,in}$, $\dot{n}_{steam,\mathrm{oxidizer},in}$, $\dot{n}_{Air,combustor,in}$, $\dot{n}_{N_2,combustor,out}$, $\dot{n}_{O_2,combustor,out}$, $\dot{n}_{H_2,oxidizer,out}$

Table 2.8. Energy and material balances in the chemical looping gasification process

Energy carried by exhaust gas from reducer:

$$\Delta\dot{H}_1 = \sum_i \dot{n}_{i,reducer,out} C_{p,i} \times (T_1 - T_0) + \dot{n}_{H_2O,reducer,exhaust} \Delta H_{Vap,water} \quad \text{(T12)}$$

where *i* can be CO_2, H_2O, N_2 or H_2S from the reducer.

Energy carried by exhaust gas from oxidizer:

$$\Delta\dot{H}_2 = \sum_j \dot{n}_{j,\text{oxidizer},out} C_{p,j} \times (T_2 - T_0) + \dot{n}_{H_2O,Oxidizer,exhaust} \Delta H_{Vap,water} \quad \text{(T13a)}$$

where *j* can be H_2/H_2O from the oxidizer.

$$\dot{n}_{H_2,Oxidizer,exhaust} = 0.95\dot{n}_{H_2,\text{oxidizer,out}} \quad \text{(T13b)}$$

$$\dot{n}_{H_2O,Oxidizer,exhaust} = (1-x)\dot{n}_{steam,\text{oxidizer},in} \quad \text{(T13c)}$$

Energy carried by exhaust gas from Combustor:

$$\Delta\dot{H}_3 = \sum_k \dot{n}_{k,\text{combustor},out} C_{p,k} \times (T_3 - T_0) \quad \text{(T14a)}$$

where *k* can be N_2, O_2 or H_2O from the combustor.

$$\dot{n}_{O_2,\text{combustor},exhaust} = 0.021\dot{n}_{Air,combustor,in} \quad \text{(T14b)}$$

$$\dot{n}_{N_2,\text{combustor},exhaust} = 0.79\dot{n}_{Air,combustor,in} \quad \text{(T14c)}$$

$$\dot{n}_{H_2O,\text{combustor},exhaust} = 0.05\dot{n}_{H_2,\text{combustor},in} \quad \text{(T14d)}$$

Energy carrying by exhaust stream in the turbines:

$$\Delta\dot{H}_4 = \dot{n}_{H_2O,turbine,out} C_p \times (T_4 - T_0) + \dot{n}_{H_2O,turbine,out} \Delta H_{vap,H_2O} \quad \text{(T15a)}$$

$$\begin{aligned}\Delta\dot{H}_{Turbine} = & \sum_i [\dot{n}_{i,reducer,exhaust} C_{p,i} \times (T_{reducer} - T_1)] + \sum_j [\dot{n}_{j,oxidizer,exhaust} C_{p,j} (T_{oxidizer} - T_2)] \\ & + \sum_k [\dot{n}_{k,combustor,exhaust} C_{p,j} (T_{\exp ander} - T_3)] + \dot{Q}_{oxidizer} \\ & + (\dot{n}_{H_2O,reducer,out} + \dot{n}_{H_2O,oxidizer,out} + \dot{n}_{H_2O,combustor,out}) \Delta H_{Vap,water} \\ & - \dot{n}_{H_2,,\text{oxidizer},out} C_{p,H_2} (T_{H_2,Tail} - T_0) - \dot{n}_{Air,combustor,in} C_{p,Air} (T_{Air} - T_0) \\ & - \dot{n}_{H_2O,\text{oxidizer},out} C_{p,H_2O} (T_{H_2O} - T_0) - \dot{n}_{H_2O,\text{oxidizer},out} \Delta H_{Vap,water}\end{aligned} \quad \text{(T15b)}$$

$$\dot{n}_{turbine,H_2O} = 1.44158\Delta\dot{H}_{Turbine} \quad \text{(T15c)}$$

where $\Delta\dot{H}$ is in $\times 10^8$ Watt and $\dot{n}_{turbine,H_2O}$ is in mol s^{-1}.

Variables calculated:

$\Delta\dot{H}_1$, $\Delta\dot{H}_2$, $\Delta\dot{H}_3$, $\Delta\dot{H}_4$

2.4. Results and discussion

2.4.1 Experimental results

The experiments are carried out to provide preliminary confirmations on: (1) kinetic improvement for char conversion by oxygen uncoupling of bimetallic oxygen carrier; (2) the avoidance of mixed metal oxide (spinel) formation between Fe and Cu, which limits the oxygen uncoupling property of CuO. Details regarding the experiments are provided in the supplementary document. To summarize, TGA experiments indicate that the initial reduction temperature of the CuO containing sample is about 200°C lower than the reference oxygen carrier. In addition, copper enhanced sample converts coal at a significantly faster rate in the TGA. Although TGA does not provide a high fidelity environment comparable to moving bed or fluid bed reactors, the preliminary experimental results indicate that char conversion rate can potentially be enhanced by the bimetallic oxygen carrier. In addition, XRD analysis carried out on the post experiment bimetallic oxygen carrier sample did not indicate the formation of mixed Fe-Cu oxides, as shown in Fig. 2.4. The avoidance of mixed metal oxide formation will allow CuO to maintain its oxygen uncoupling properties.

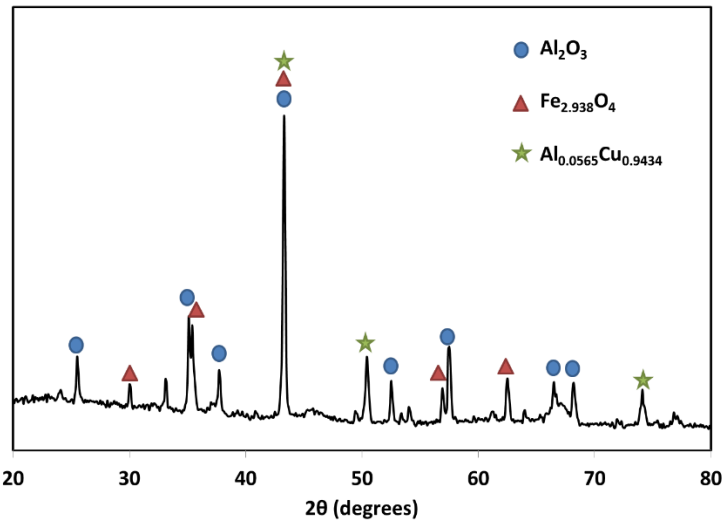

Fig. 2.4. XRD spectra of Al_2O_3 supported Fe_2O_3-CuO after reduction.

2.4.2 ASPEN Plus® simulation

The TGA experiments indicate that incorporating CuO into the Fe_2O_3 based oxygen carrier can enhance the reaction kinetics for coal conversion. In the following sections, ASPEN simulation is used to estimate the reactor and process performances of the bimetallic chemical looping concept. The effects of operating conditions such as CuO addition, oxidizer temperature and inert support amount are evaluated.

2.4.2.1 Reducer performance

2.4.2.1.1 Minimum *O/C* ratio

Reactor modeling is first conducted to evaluate reducer performance at 30 atm and 900 °C. The oxygen carrier particles, which have a Fe_2O_3:CuO molar ratio of 9:1, are introduced from the top of the reducer. Dry coal is injected in the middle stage of the reducer. One important parameter characterizing the effectiveness of an oxygen carrier is the minimum *O/C* ratio, which corresponds to the minimum amount of oxygen carrier required for complete coal conversion. Fig. 2.5 shows carbon distribution in the reducer product stream as well as metal oxide conversion at various *O/C* ratios. CH_4 formation is found to be negligibly low. As can be seen, more carbon in coal is converted to CO_2 with increasing *O/C* ratio. The simulation also indicates that a minimum (critical) *O/C* ratio of 3.37 is required for complete coal conversion.

The effect of copper content on CO_2 yield and Fe_2O_3 conversion in the reducer is summarized in Fig. 2.6. The CO_2 yield is enhanced with CuO addition. This is confirmed by the lowered critical *O/C* ratios after CuO addition. For instance, the critical *O/C* ratio of the 9: 1 (Fe_2O_3: CuO) bimetallic particles, which is equal to 3.37, is significantly lower that of pure Fe_2O_3, which is 4.42. Therefore, complete oxidation of coal can be achieved at the lower oxygen carrier circulation rate when bimetallic oxygen carrier is used. In addition, Fe_2O_3 conversion in reducer is increased with CuO addition.

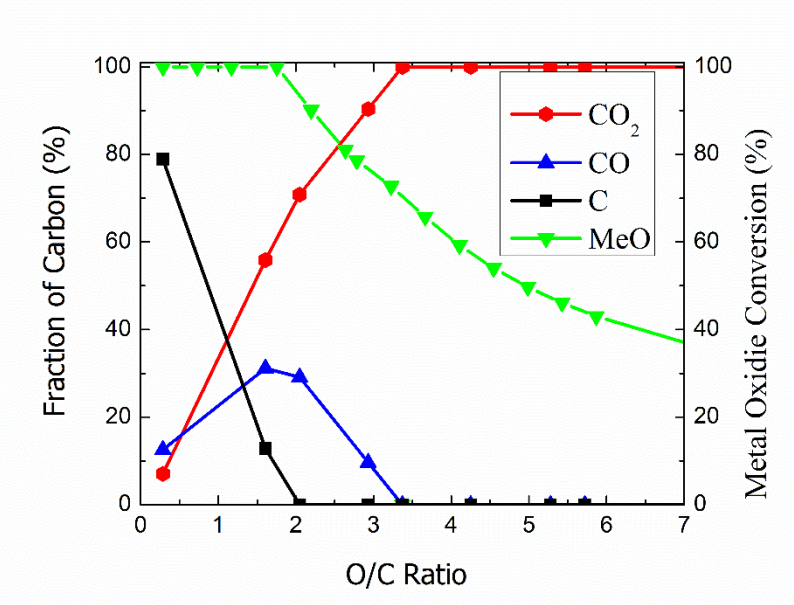

Fig. 2.5. Carbon distribution and metal oxides conversion under various O/C ratios. T = 900 °C; P = 30 atm. Solid line: Fe_2O_3:CuO = 9:1 (by mole).

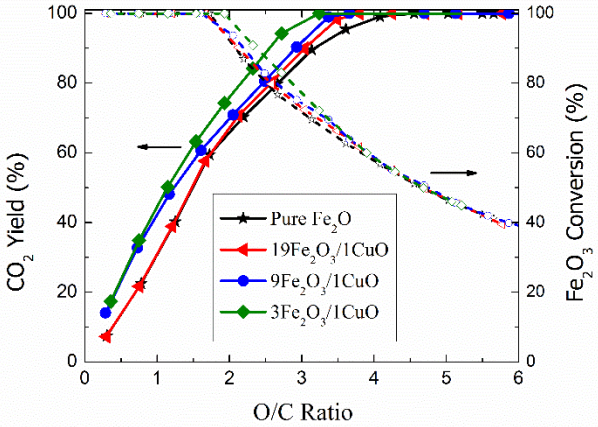

	Minimum O/C ratio	Corresponding Fe_2O_3 Conversion (%)
Pure Fe_2O_3	4.2	56%
19 Fe_2O_3/1 CuO	3.8	61%
9 Fe_2O_3/1 CuO	3.37	66%
3 Fe_2O_3/1 CuO	3.14	73%

Fig. 2.6. Effect of copper content on CO_2 yield and metal oxide conversion in the reducer. T = 900 °C; P = 30 atm. Table on the right side summarizes the key results from the diagram.

2.4.2.1.2 Effect of temperature and pressure

In order to investigate the effects of temperature and pressure on the reducer performance, sensitivity analyses are performed. Fig. 2.7 summarizes the key results. As can be seen from Fig. 2.7(a), high temperature enhances the endothermic coal conversion reaction. Since ultra-high operating temperatures can lead to potential challenges of high reactor costs, particle melting, and the ash softening, 900 °C is used as the standard operating temperature in the following sections. From Fig. 2.7(b), pressure higher than 35 atm will lead to incomplete coal conversion from a thermodynamic standpoint. Since the products of the process, i.e. CO_2 and hydrogen, need to be compressed for storage, a high operating pressure can reduce the energy consumption for gas compression. Therefore, 30 atm, which allows complete coal conversion, is selected as the standard operating pressure.

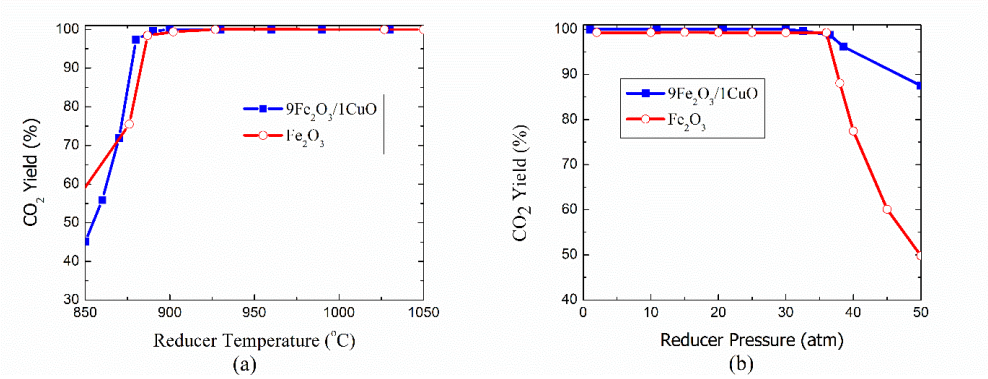

Fig. 2.7. (a) Effect of operating temperature on CO_2 yield in the reducer, P=30 atm. (b) Effect of operating pressure on CO_2 yield in the reducer, T = 900 °C. Legend shows the mole ratio between Fe_2O_3 and CuO. O/C = 3.37 for bimetallic oxygen carrier; O/C = 4.2 for Fe-based oxygen carrier.

2.4.2.1.3 In-situ char gasification via split injection

In the moving bed reducer, pulverized coal is injected into the middle stage in order to allow for coal devolatilization and coal char/volatile conversions. Although the gaseous O_2 released

from the CuO decomposition can enhance char gasification, introducing CuO/Fe_2O_3 on the top of the moving bed, as used in typical CLG schemes, may not provide sufficient contact between CuO and char. As a result, most of the gaseous O_2 from CuO is likely to be converted by gasified char (CO) and coal volatiles. By injecting a fraction of metal oxides to the middle stage of the reducer along with coal, intimate interaction between metal oxides and coal char can be expected, thereby improving the kinetics for char conversion more effectively. The effect of injecting metal oxides at the middle stage of the reducer is studied and the results are given in Fig. 2.8. At the critical *O/C* ratio of 3.37, the CO_2 yield starts to decrease with Fe_2O_3 splitting. For instance, CO_2 yield is predicted to decrease by 38% when 50% of the metal oxides are injected along with coal in the middle stage of the reducer. When the *O/C* ratio is increased to 5.15, CO_2 yield will remain at 100% up to a split ratio of 0.4. From Fig. 2.8, splitting of a portion of bimetallic oxygen carrier to the middle of the reducer can result in both high CO_2 yield and faster kinetics. In the meantime, a slightly decreased metal oxide conversion can be anticipated.

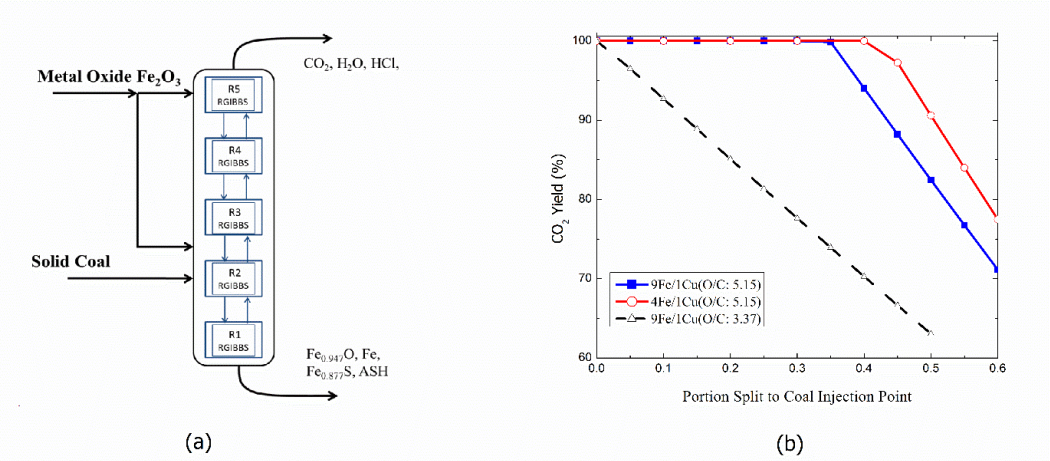

Fig. 2.8. (a) Schematic of the improved in-situ char gasification scheme. (b) Effect of splitting bimetallic oxygen carrier for middle-stage injection on CO_2 yield. T = 900 C; P = 30 atm.

2.4.2.2 Oxidizer simulation

The primary function of the oxidizer is to produce hydrogen from steam. Fig. 2.9 illustrates the steam conversion under different temperatures and metallic iron contents. As can be seen, the presence of CuO has no influence on steam conversion. This is understandable since copper does not react with steam to any significant extent.

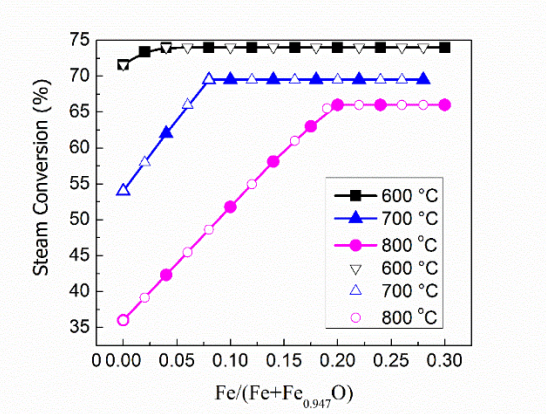

Fig. 2.9. Effect of temperature and oxygen carrier composition on steam conversion in the moving bed oxidizer. The x-scale is the molar flow rate ratio between Fe and the summation of Fe and $Fe_{0.947}O$ entering the oxidizer. Solid dots: bimetallic oxygen carrier with 10 mole% CuO; empty symbol: Fe-based oxygen carrier.

2.4.3 Process simulation

4.3.1 Process simulation with different particle and coal conversion

As discussed in Section 3.3, four process simulation cases are studied. Taking Case III as an example, the compositions and flow rates of the key process streams are summarized in Table 2.9. The simulation results provide useful information in terms of the process material balance as well as the fates of the pollutants: in the reducer, coal is oxidized to CO_2 and H_2O. Meanwhile, Fe_2O_3 is reduced to $Fe/Fe_{0.947}O$ and CuO to metallic Cu. In the oxidizer, the reduced $Fe/Fe_{0.947}O$ from the reducer is partially regenerated by steam, producing

$Fe_{0.947}O/Fe_3O_4$ and H_2. Metallic Cu remains unchanged in the oxidizer. Subsequently, the partially regenerated oxygen carrier is fully oxidized in the combustor, producing Fe_2O_3, CuO, and heat. In terms of pollutants, over 85% sulfur in coal is predicted to react with CuO in the reducer, forming Cu_2S. The remaining sulfur leaves the reducer in the form of gaseous H_2S at a concentration of 0.1%. The Cu_2S formed in the reducer is fully regenerated in the combustor. This leads to a combustor flue gas stream that containing 0.7% of SO_2. These sulfur containing flue gases can be easily conditioned using commercially available sulfur removal systems such as SELEXOL and flue gas desulfurization (FGD) process. The use of Fe_2O_3 as the primary oxygen carrier in a moving bed configuration results in a relatively reducing environment when compared to typical oxygen uncoupling reducers. This affects the fates of sulfur. For instance, experimental studies conducted by Forero et al. [44] using methane and H_2S indicate that the majority of the sulfur was released from reducer as SO_2 with low Cu_2S formation. The equilibrium based model also predicts that all the chlorine in the coal is converted into hydrogen chloride and mercury exits the reactor in its elemental form. NO_x formation is found to be insignificant in all three reactors. In general, these predictions are consistent with experimental studies on chemical looping processes [45].

The process simulation results are summarized in Table 2.10. Details regarding power generation/consumptions are illustrated in Fig. 2.10. In all cases, the CLG process produces hydrogen while coproducing adequate electricity for self-sustained operation. Compared to Cases I and II, the presence of copper in Case III and IV slightly improves the overall process efficiency even though copper does not contribute to steam generation in the oxidizer. The improved process efficiency results from the reduced exothermicity for reducer operation in the presence of copper. The simplified energy integration scheme of the bimetallic CLG leads to reduced gaseous reactant consumptions. This corresponds to reduced energy loss and higher process efficiency. Compared to Case IV, Case III leads to a slightly higher efficiency of 84.3%. The lowered efficiency of Case IV is due to the lower Fe_2O_3 and coal conversions in the reducer, which lead to higher solids circulation rate and increased air consumption in the combustor.

Table 2.9. Material flows (tonnes/hr) in bimetallic coal CLG system under Case III

Gaseous Stream Flow Rates (tonnes/hr)						Solid Stream Flow Rates (tonnes/hr)			
	Reducer flue gas	Steam feed	Oxidizer flue gas	Air feed	Combustor flue gas	From / To	Combustor / Reducer	Reducer / Oxidizer	Oxidizer / Combustor
T (°C)	900	191	750	550	1169	**T (°C)**	1169	900	750
P (atm)	30	31	30.5	31	30	**P (atm)**	30	30	30.5
H_2O	67.8	291.4	93.4	0	9.9	**Fe**	0	453.6	0
CO	0	0	0	0	0	**$Fe_{0.947}O$**	0	535.1	492.3
CO_2	306.7	0	0	0	0	**Fe_3O_4**	0	0	672.4
O_2	0	0	0	101.6	4.7	**Fe_2O_3**	1235.9	0	0
N_2	1.8	0	0	334.6	334.6	**SiC**	1368	1368	1368
H_2	0	0	22.2	0	0	**S**	0	0	0
Cl_2	0	0	0	0	0	**$Fe_{0.877}S$**	0	0	0
HCl	0.4	0	0	0	0	**CuO**	68.4	0	0
SO_2	0	0	0	0	5.6	**Cu_2O**	0	0	0
SO_3	0	0	0	0	0.2	**Cu**	0	43.1	43.1
H_2S	0.5	0	0	0	0	**Cu_2S**	0	14.4	14.4
NO	0	0	0	0	0.02	**ASH**	0	0	0
NO_2	0	0	0	0	1.2×10^{-3}				
Hg	1.3×10^{-4}	0	0	0	0				

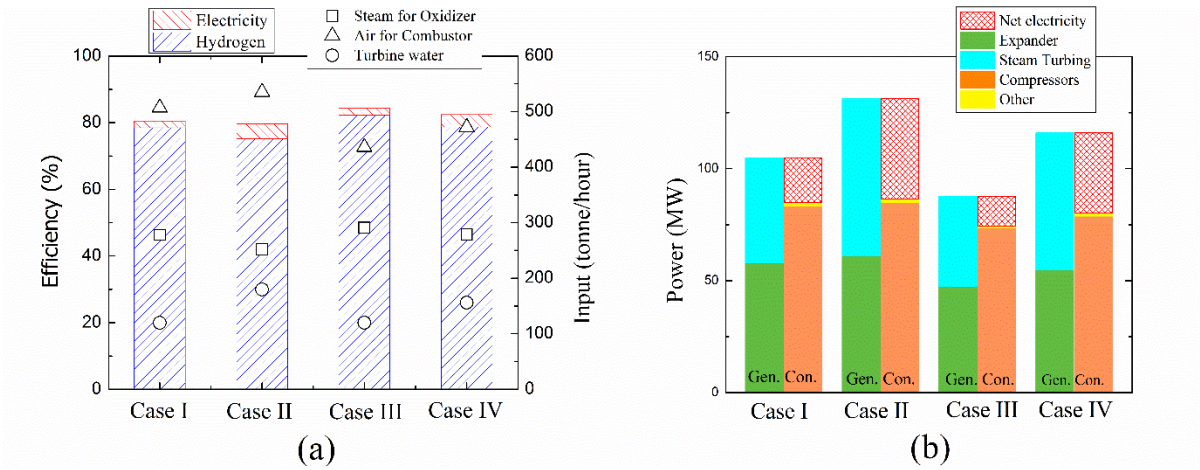

Fig. 2.10. Efficiency comparisons for the various CDCL cases: (a) Electricity and hydrogen coproduction; water and air consumptions. (b) Power generation and consumption balances in the four simulation cases.

Table 2.10. Process simulation results under different operating conditions

	Case I	Case II	Case III	Case IV
	Illinois #6 Coal, 1000 MW_{th}, 132.65 tonne/hr			
Coal conversion	99%	95%	99%	95%
Metal oxide composition Reducer	Fe_2O_3	Fe_2O_3	Bimetallic	Bimetallic
Solid circulating rate (tonne/hr)	3103	3287	2672	2727
Metal oxide loading wt%	50%	64%	49%	75%
Steam feed in oxidizer (tonne/hr)	278	252	291	279
Air feed in combustor (tonne/hr)	507	535	436	472
Fe_2O_3 conversion in Reducer	56%	40%	66%	40%
Steam conversion in Oxidizer	68%	68%	68%	68%
Carbon capture, %	99%	95%	99%	95%
H_2 Production Rate (tonne/hr)	19.9	19.09	20.9	19.97
H_2 Production Rate (MW_{th} of H_2/MW_{th} of coal in HHV)	0.785	0.752	0.823	0.787
Net Power (MW_e)	20.0	44.95	20.2	37.8
$\eta_{tot,HHV}$ %	80.5	79.7	84.3	82.5
$\eta_{tot,LHV}$ %	70.9	70.7	74.4	73.0

* Bimetallic refers to oxygen carrier with 9:1 molar ratio of Fe_2O_3 and CuO

2.4.3.2 Effect of oxidizer temperature on the process performance

Among the many operational parameters that may affect the overall efficiency of the CLG process, the oxidizer operating temperature is of critical importance since it not only affects the heat integration among the looping reactors but also affects the steam to hydrogen conversion. A decrease in oxidizer operating temperature ($T_{oxidizer}$) has two competing effects:

(i) at lower $T_{oxidizer}$, a larger fraction of the reduced Fe_2O_3 need to be combusted in order to maintain the desired combustor temperature. This leads to reduced H_2 yield and increased heat loss from combustor exhaust; (ii) lower $T_{oxidizer}$ leads to higher steam conversion in the oxidizer. Therefore, steam consumption and heat loss from oxidizer exhaust will be reduced. Based on the above discussions, the net impact of oxidizer operating temperature to the overall process efficiency is a non-obvious optimization issue. Using case III as the reference case, Table 2.11 summarizes the ASPEN simulation results at different oxidizer operating temperatures varying from 600°C to 900 °C. The mathematic model described in Section 3.4 is also used to quantify the process heat loss and efficiency (see Fig. 2.11). According to Table 2.11 and Fig. 2.11, the highest process efficiency can be expected when the oxidizer is operated at around 800 °C. A higher or lower oxidizer temperature will lead to excessive heat loss from either steam usage or combustor exhaust.

Table 2.11. Effect of oxidizer operating temperature on the process performance

Oxidizer Temperature (°C)	600	700	750	800	900
Illinois #6 Coal, 1000 MW_{th}, 132.65 tonne/hr 99% Coal conversion; Bimetallic					
Reducer Temperature (°C)	900	900	900	900	900
Combustor Temperature (°C)	1169	1169	1169	1169	1169
Steam feed in oxidizer (tonne/hr)	236	269	291	314	324
Air feed in combustor (tonne/hr)	548	475	436	396	317
Steam conversion in Oxidizer	74%	70%	68%	66%	62%
H_2 Production Rate (tonne/hr)	17.8	19.9	20.9	21.8	20.0
H_2 Production Rate (MW_{th} of H_2/MW_{th} of coal in HHV)	0.701	0.783	0.823	0.861	0.790
Net Power (MWe)	56.7	34.7	20.2	5.78	28.7
$\eta_{tot,HHV}$ %	75.8	81.8	84.3	86.7	81.85
$\eta_{tot,LHV}$ %	67.4	72.4	74.4	76.0	72.1

* Bimetallic refers to oxygen carrier with 9:1 molar ratio of Fe_2O_3 and CuO

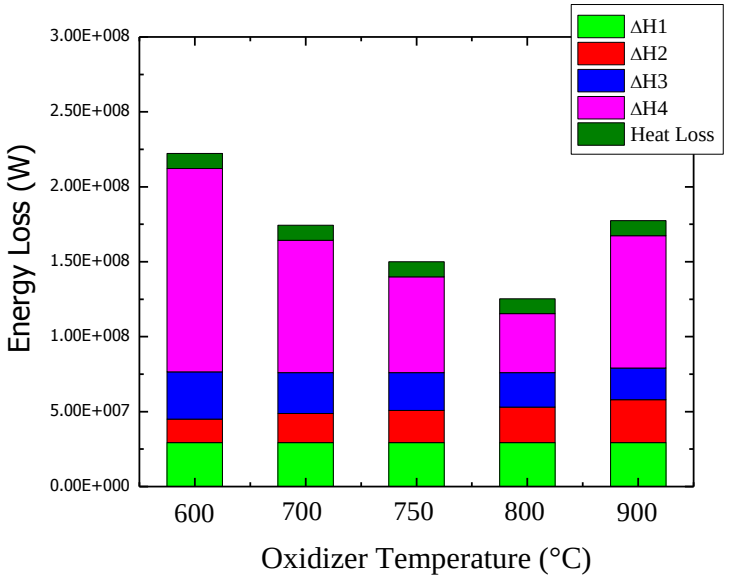

Fig. 2.11. Energy loss from the exhaust steams under various oxidizer temperatures.

2.4.3.3 Effect of support amount on the process performance

Another important operational parameter in the process is inert support percentage in the oxygen carrier. The inert support works as heat carrier and plays a crucial role in balancing the heat among the looping reactors. Again, using case III as the reference case, Table 12 and Fig. 2.12 summarize the simulation results using ASPEN Plus® and mathematically model. As we can see, process efficiency generally increases with decreasing support content. This is due to the decreased heat loss from the combustor (reduced air usage). On the flip side, decreasing support content leads to higher combustor operating temperature, which can impose serious challenges to the design of both looping reactors and oxygen carrier.

Table 2.12. Effect of solid inert loading on the process performance

SiC (tonne/hr)	720	1080	1368	1440	1800
Illinois #6 Coal, 1000 MW_{th}, 132.65 tonne/hr 99% Coal conversion; Bimetallic					
Metal oxide loading wt%	64%	53%	49%	44%	40%
Combustor Temperature (°C)	1274	1207	1169	1143	1127
Steam feed in oxidizer (tonne/hr)	299	295	291	287	285
Air feed in combustor (tonne/hr)	414	425	436	448	454
Steam conversion in Oxidizer	68%	68%	68%	68%	68%
H_2 Production Rate (tonne/hr)	21.5	21.2	20.9	20.6	20.4
H_2 Production Rate (MW_{th} of H_2/MW_{th} of coal in HHV)	0.846	0.834	0.823	0.817	0.805
Net Power (MW_e)	10.2	12.8	20.2	19.3	21.5
$\eta_{tot,HHV}$ %	85.6	84.7	84.3	83.6	82.6
$\eta_{tot,LHV}$ %	75.4	74.6	74.4	73.2	72.8

* Bimetallic refers to oxygen carrier with 9:1 molar ratio of Fe_2O_3 and CuO

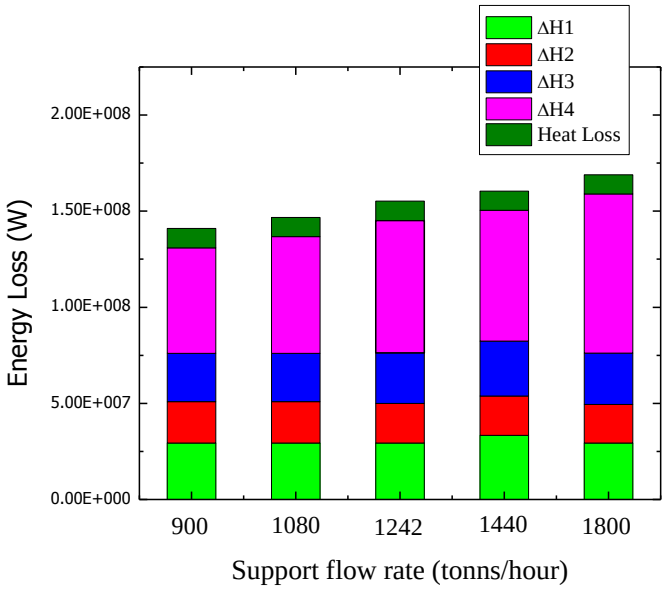

Fig. 2.12. Energy loss from the exhaust steams under various inert support amount.

2.4.3.4 Effect of heat loss on the process performance

The previous simulation is based on the assumption that the overall process heat loss is 1% of the total thermal input. Such a heat loss rate is suggested by National Energy Technology Laboratory (NETL) of the U.S. Department of Energy (USDOE) for coal gasification systems [46]. Using Case III as the reference case, we simulated the effect of an increased heat loss of 5%. The results are shown in Fig. 2.S3. The increased heat loss leads to a decreased process efficiency of 79.4%. Compared to conventional gasification based coal to hydrogen process which has a typical efficiency of ~60%, the bimetallic CLG system is far more efficient since the gasification of coal, a highly irreversible step, is decomposed into a series of less irreversible reactions by the oxygen carrier. Other factors that contribute to the high efficiency of CLG include reduced energy consumption for product separation; elimination of cooling and reheating of gaseous products; and improved heat integration scheme enabled by the circulating oxygen carrier.

2.5 Conclusions

The present study explores the feasibility of using CuO and its "oxygen-uncoupling" properties to promote Fe_2O_3 – coal reactions in the CLG process. Key findings from the current study include:

- Solid fuel conversion rate can potentially be enhanced by adding a small amount of CuO to Fe_2O_3 based oxygen carrier particle.

- Formation of mixed metal oxides of copper and iron in the oxygen carrier particle can be inhibited and/or avoided by segregating copper and iron atoms with an inert support. As a result, the CuO containing Fe_2O_3 oxygen carrier possesses oxygen uncoupling properties for coal and coal char conversions.

- From a thermodynamic standpoint, the presence of copper oxides enhances the conversions of both coal and Fe_2O_3 in the CLG reducer. In addition, copper does not affect the steam-iron reactions in the CLG oxidizer.

- Under a kinetically limited scenario of 40% Fe_2O_3 conversion and 95% carbon conversion, the bimetallic CLG process achieves 78.8% hydrogen generation efficiency, 82.5% (HHV) overall efficiency, and 95% CO_2 capture.

- Even though copper (oxides) does not directly participate in H_2 generation in the CLG oxidizer, the presence of copper leads to improved H_2 generation efficiency through simplified process heat integration scheme.

To summarize, incorporation of a small amount of CuO to an iron based oxygen carrier can result in an active composite oxygen carrier for solid fuel conversion. When used in the CLG processes, the composite oxygen carrier has the potential to enhance solid fuel conversion rate while improving the process efficiency for H_2 generation.

Acknowledgement

Authors would like to acknowledge the assistances from Dr. Yan Huang and Mr. Arya Shafiefarhood in oxygen carrier synthesis. This work is supported by the start-up funds provided by the Chemical and Biomolecular Engineering Department at the North Carolina State University.

REFERENCES

[1] Rodhe H. A comparison of the contribution of various gases to the greenhouse effect. Science 1990;248:1217–19.

[2] Hossain MM, de Lasa HI. Chemical-looping combustion (CLC) for inherent separations—a review. Chem Eng Sci 2008;63:4433–51.

[3] Li F, Fan L-S. Clean coal conversion processes–progress and challenges. Enegr Environ Sci 2008;1:248.

[4] Moghtaderi B. Review of the recent chemical looping process developments for novel energy and fuel applications. Energy Fuels 2011;26:15–40.

[5] Adanez J, Abad A, Garcia-Labiano F, Gayan P, de Diego LF. Progress in chemical-looping combustion and reforming technologies. Prog Energ Combust 2012;38:215–82.

[6] Ishida M, Jin H. A new advanced power-generation system using chemical-looping combustion. Energy 1994;19:415–22.

[7] Gupta, Velazquez-Vargas LG, Fan LS. Syngas redox (SGR) process to produce hydrogen from coal derived syngas. Energy Fuels 2007;21:2900–08.

[8] Fan L, Li F, Ramkumar S. Utilization of chemical looping strategy in coal gasification processes. Particuology 2008;6:131–42.

[9] Fan L-S. Chemical looping systems for fossil energy conversions. John Wiley & Sons, 2010.

[10] Lyngfelt A, Leckner B, Mattisson T. A fluidized-bed combustion process with inherent CO_2 separation; application of chemical-looping combustion. Chem Eng Sci 2001;56:3101–13.

[11] Mattisson T, Lyngfelt A, Cho P. The use of iron oxide as an oxygen carrier in chemical-looping combustion of methane with inherent separation of CO_2. Fuel 2001;80:1953–62.

[12] Kronberger B, Lyngfelt A, Löffler G, Hofbauer H. Design and fluid dynamic analysis of a bench-scale combustion system with CO_2 separation chemical-looping combustion. Ind Eng Che. Res 2005;44:546–56.

[13] Johansson E, Mattisson T, Lyngfelt A, Thunman H. Combustion of syngas and natural gas in a 300 w chemical-looping combustor. Chem Eng Res Des 2006;84:819–27.

[14] Consonni S, Lozza G, Pelliccia G, Rossini S, Saviano F. Chemical-looping combustion for combined cycles with CO_2 capture. J Eng Gas Turb Power 2006;128:525-34.

[15] Abad A, Mattisson T, Lyngfelt A, Rydén M. Chemical-looping combustion in a 300 w continuously operating reactor system using a manganese-based oxygen carrier. Fuel 2006;85:1174–85.

[16] Mattisson T, García-Labiano F, Kronberger B, Lyngfelt A, Adánez J, Hofbauer H. Chemical-looping combustion using syngas as fuel. Int J GreenhGas Cont 2007;1:158–69.

[17] Xiang W, Wang S, Di T. Investigation of gasification chemical looping combustion combined cycle performance. Energy Fuels 2008;22:961–66.

[18] Jin H, Okamoto T, Ishida M. Development of a novel chemical-looping combustion: synthesis of a looping material with a double metal oxide of CoO-NiO. Energy Fuels 1998;12:1272–77.

[19] Cho P, Mattisson T, Lyngfelt A. Comparison of iron-, nickel-, copper- and manganese-based oxygen carriers for chemical-looping combustion. Fuel 2004;83:1215–25.

[20] Abad A, Adánez J, García-Labiano F, de Diego LF, Gayán P, Celaya J. Mapping of the range of operational conditions for cu-, fe-, and ni-based oxygen carriers in chemical-looping combustion. Chem Eng Sci 2007;62:533–49.

[21] Lyngfelt A, Thunman H. Chapter 36 - construction and 100 h of operational experience of a 10 kw chemical-looping combustor. In: Carbon dioxide capture for storage in deep geologic formations. Amsterdam: Elsevier Science, 2005, p. 625–645.

[22] Ryu H-J, Jin G-T, Yi C-K. Demonstration of inherent CO_2 separation and no NO_X emission in in a 50kW chemical lopping combustor. Canada 2004: Proceeding of 7th Int Conf Greenhouse Gas Control Technology; 2004 Sep 5-9; Vancouver, Canada.

[23] Eide LI. Carbon dioxide capture for storage in deep geological formations: results from the CO_2 capture project. Newbury: CPL, 2009.

[24] Ishida M, Zheng D, Akehata T. Evaluation of a chemical-looping-combustion power-generation system by graphic exergy analysis. Energy 1987;12:147–54.

[25] Anheden M, Svedberg G. Exergy analysis of chemical-looping combustion systems. Energ Convers Manage 1998;39:1967–80.

[26] Shen L, Wu J, Xiao J, Song Q, Xiao R. Chemical-looping combustion of biomass in a 10 kwth reactor with iron oxide as an oxygen carrier. Energy Fuels 2009;23:2498–05.

[27] Shen L, Wu J, Gao Z, Xiao J. Characterization of chemical looping combustion of coal in a 1 kw_{th} reactor with a nickel-based oxygen carrier. Combust Flame 2010;157:934–42.

[28] Leion H, Jerndal E, Steenari B-M, Hermansson S, Israelsson M, Jansson E, johnsson M, Thunberg R, Vadenbo A, Mattisson T, Lyngfelt A. Solid fuels in chemical-looping combustion using oxide scale and unprocessed iron ore as oxygen carriers. Fuel 2009;88:1945–54.

[29] Berguerand N, Lyngfelt A. Design and operation of a 10 kw(th) chemical-looping combustor for solid fuels-testing with south african coal. Fuel 2008;87:2713–26.

[30] Cao Y, Pan W-P. Investigation of chemical looping combustion by solid fuels. 1. process analysis. Energy Fuels 2006;20:1836–44.

[31] Li F, Zeng L, Fan L-S. Biomass direct chemical looping process: process simulation. Fuel 2010;89:3773–84.

[32] Cao Y, Casenas B, Pan W-P. Investigation of chemical looping combustion by solid fuels. 2. redox reaction kinetics and product characterization with coal, biomass, and solid waste as solid fuels and CuO as an oxygen carrier. Energy Fuels 2006;20:1845–54.

[33] Gu H, Shen L, Xiao J, Zhang S, Song T. Chemical looping combustion of biomass/coal with natural iron ore as oxygen carrier in a continuous reactor. Energy Fuels 2010;25:446–55.

[34] Gilliland ER, Gilliland ER. Production Of Pure Carbon Dioxide. U.S. Patent 2665971, 1954.

[35] Mattisson T, Lyngfelt A, Leion H. Chemical-looping with oxygen uncoupling for combustion of solid fuels. Int J Greenh Gas Cont 2009;3:11–19.

[36] Mattisson T, Leion H, Lyngfelt A. Chemical-looping with oxygen uncoupling using CuO/ZrO_2 with petroleum coke. Fuel 2009;88:683–90.

[37] Abad A, Adanez-Rubio I, Gayan P, Garcia-Labiano F, de Diego LF, Adanez J. Demonstration of chemical-looping with oxygen uncoupling (CLOU) process in a 1.5 kw(th) continuously operating unit using a Cu-based oxygen-carrier. Int J Greenh Gas Cont 2012;6:189–00.

[38] Leion H, Mattisson T, Lyngfelt A. Using chemical-looping with oxygen uncoupling (CLOU) for combustion of six different solid fuels. Energy Procedia 2009;1:447–53.

[39] Adánez-Rubio I, Abad A, Gayán P, De Diego LF, García-Labiano F, Adánez J. Identification of operational regions in the chemical-looping with oxygen uncoupling (CLOU) process with a cu-based oxygen carrier. Fuel 2012;102:634–45.

[40] Zeng L, He F, Li F, Fan L-S. Coal-direct chemical looping gasification for hydrogen production: reactor modeling and process simulation. Energy Fuels 2012;26:3680–90.

[41] Adánez-Rubio I, Gayán P, García-Labiano F, De Diego LF, Adánez J, Abad A. Development of Cu-based oxygen-carrier materials suitable for chemical-looping with oxygen uncoupling (CLOU) process. Energy Procedia 2011;4:417–24.

[42] Fan L-S, Li F. Chemical looping technology and its fossil energy conversion applications. Ind Eng Chem Res 2010;49:10200–11.

[43] Aspen Technology Inc. ASPEN Plus v7.2 user guide. Aspen Technology, Inc. Cambridge, MA.

[44] Forero CR, Gayan P, Garcia-Labiano F, De Diego LF, Abad A, Adanez J. Effect of gas composition in chemical-looping combustion with copper-based oxygen carriers: fate of sulphur. Int J Greenh Gas Cont 2010;4:762–70.

[45] Proceedings of the 2nd International Conference on Chemical Looping, Sep 26-28 Germany: 2012.

[46] Matuszewski M, Woods M. QGESS: process modeling design parameters, Mar 2012. DOE/NETL.

CHAPTER 3 PARTICULATE EMISSIONS FROM COPPER OXIDE BASED OXYGEN CARRIERS IN CHEMICAL LOOPING COMBUSTION FOR *IN-SITU* CO_2 CAPTURE

CHAPTER 3 is a reprint of a manuscript in preparation.

Abstract

Oxygen carrier attrition behaviors and particulate emissions from a chemical looping combustion (CLC) process are investigated. Copper oxide based oxygen carrier is tested in a fluidized reactor for chemical looping combustion of methane. The aerodynamic diameters of most emitted particulates range between 2 and 5 μm. A notable amount of submicron particulates is also identified. It is also observed that oxygen carrier attritions lead to increased CuO loss resulting from the chemical looping reactions, i.e. Cu is enriched in small particles in the size range of 10-75 μm, which are generated primarily from fragmentation. It is determined that the cyclic reduction and oxidation reactions in CLC weakens the oxygen carrier particles, resulting in increased particulate emission rates when compared to oxygen carriers without redox reactions. The generation rate for particulates (< 10 μm) is found to decrease with progressive cycles over as-prepared oxygen carrier particles, and then reach a steady-state level of $2.48\pm0.72\times10^{-3}$ wt%/hr during the reduction step and $1.68\pm0.40\times10^{-3}$ wt%/hr in the oxidation step. The surface of the oxygen carrier is also found to be coarsened due to a Kirkendall effect, which also explains the enrichment of Cu on particle surfaces and in small particles. As a result, it is important to collect and reprocess small particles generated from chemical looping processes to reducer oxygen carrier loss and to mitigate the environmental impact.

3.1 Introduction

CO_2 emission reduction from fossil fuel combustion processes has received increasing attention due to concerns over global climate change related to the greenhouse effect.[1] Although efficiency improvements through advanced Rankine and combined cycles can reduce the carbon footprint of traditional combustion-based power generation processes, significant CO_2 emission reduction from fossil fuel conversion can only be achieved through carbon capture and sequestration (CCS).[2,3] Existing carbon capture technologies, which adopt oxy-fuel combustion, pre-combustion, or post-combustion approaches, are highly energy intensive, leading to decreased power generation efficiency and increased cost.[4] The chemical looping combustion (CLC) process represents an alternative, potentially efficient strategy for power generation from fossil fuels with *in-situ* CO_2 capture.[5–8] The CLC process utilizes a metal oxide based oxygen carrier particle to oxidize carbonaceous fuels into concentrated CO_2, allowing efficient CO_2 capture and storage. The reduced oxygen carrier resulting from the fuel oxidation step is subsequently combusted with air to release heat for power generation. For example, methane combustion with metal oxide (MO_x) as shown in Fig. 3.1 would involve the following two reactions that complete a redox cycle:

$MO_x + CH_4 \rightarrow MO_y + CO_2 + 2H_2O$ Reaction (1)

$MO_y + O_2 \rightarrow MO_x + \text{Heat}$ $(y<x)$ Reaction (2)

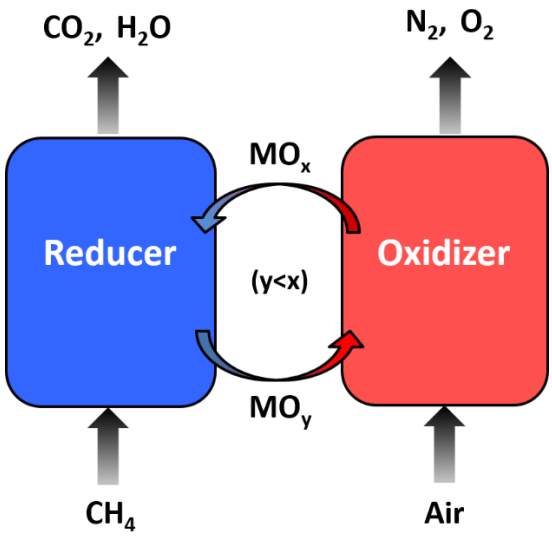

Fig. 3.1. Schematic of chemical looping combustion process

The aforementioned redox cycle of the oxygen carrier is exploited to transport oxygen from air to the fuel through a chemical loop. According to the US Department of Energy, chemical looping represents one of, if not the, most promising approaches for efficient CO_2 capture.[3,9] To date, the CLC concept has been investigated for both natural gas and solid fuel conversions.[5–8] Although the technology is not yet commercially mature, CLC processes have been operated at pilot scales (up to MW_{th}) through a number of demonstration projects.[10–12]

A critical consideration in all CLC processes is the performance of the oxygen carrier particle. An ideal oxygen carrier should possess the ability to store and transport significant amount of lattice oxygen while also being resistant to deactivation or physical degradation. A number of redox-active metal oxides have been investigated as the active material for oxygen storage and transport. Such metal oxides include those of Fe, Ni, Cu, Mn, and Co.[5,7,8,13] Mixed oxides containing these first row transition metals have also been investigated.[14–17] Among them, copper-based oxygen carriers are of interest due to their ability to release gaseous oxygen,

which promotes the conversion of solid fuel conversion.[8,18] Using a laboratory scale fluidized bed reactor, Mattisson et al.[19] demonstrated 50-fold rate enhancement for petroleum coke conversion using CuO when compared to an iron-based oxygen carrier. Leion et al.[20] reported improved reaction rates for six different solid fuels by using the gas-phase oxygen released by CuO. Adánez-Rubio et al.[12] tested $MgAl_2O_4$ supported CuO in a batch fluidized-bed reactor, with complete conversion of the solid fuels.

CLC reactors are typically designed with at least one fluidized bed reactor in the loop.[22] As a result, attrition from the oxygen carrier particles will inevitably occur in CLC processes due to mechanical, thermal, and/or chemical stresses originating from particle collisions at high temperature and alternating reducing/oxidizing environments.[18,23] Potential issues associated with excessive particle attrition include instability in reactor operation, loss of oxygen carriers, and small particulate emissions.[23] Specifically, particle attrition in the reactors can lead to loss of valuable oxygen carrier material, additional burden on the downstream particle separation systems, or emission of particulates that can cause health hazards.

Most studies on oxygen carriers reported to date focus on improving oxygen carrier formulation as well as characterizing their redox characteristics.[5–7] Among the several studies on attrition behavior of oxygen carrier particles, focus has been placed on the change in particle size distribution (PSD) within the chemical looping reactors.[24–26] Brown et al[27] studied attrition behavior of impregnated copper oxide from a bench-scale fluidized bed. It was found the rate of attrition of the CuO particles does not increase over the cycles. Garcia-Labiano et al[28] investigated the elutriated particles from a $10kW_{th}$ CLC operated during 100 h with a CuO-Al_2O_3 oxygen carrier. In addition to the PSD analysis, CuO content is found to be enriched in the small particles elutriated from both reducer and oxidizer. Rydén et al.[29] used a customized jet cup to evaluate the attrition resistance of 25 different material samples for chemical looping combustion in the absence of chemical reactions at room temperature. However, the analysis of fugitive particulate emissions (PM) was not performed in the aforementioned reports. Emission of particulate matter is an important consideration for all processes, particularly if

the particulates are less than 10 micron in diameter (PM_{10}).[30] It is difficult to be captured, but could cause health problems by passing through the throat and nose and then entering the lungs.[31] Investigation of PMs can also reveal the attrition mechanism in the chemical looping processes.

Despite various ongoing pilot-scale demonstrations and oxygen carrier particle research, little research has been conducted on characterizing particulate emissions from CLC processes. This study represents an attempt to comprehensively evaluate particulate emissions from CLC operations. With methane as the fuel, a Cu-based oxygen carrier particles, impregnated CuO-Al_2O_3, are tested in a laboratory fluidized bed apparatus by multi-cycle redox reactions (>1300 cycles). Particulate emissions of reduction/oxidation cycles were collected using a filter and fractionated into various particle sizes by an inertial cascade impactor. The morphology, crystal structure and chemical composition of these particles were determined using scanning electron microscope (SEM), Energy-dispersive X-ray spectroscopy (EDX), X-ray diffraction (XRD) and X-ray fluorescence (XRF). The effects of operating conditions including reducing or oxidizing environment, redox cycles, degree of reduction, etc. on particulate properties are investigated in order to obtain detailed understanding of particulate generation and attrition. It is observed that the chemical looping reaction causes higher attrition and particulates emission rates. The majority of the particulates are in the range of 2-5 μm aerodynamic diameters, while a notable amount of < 1 μm particulates is also found. The Cu loss is also found due to the Cu rich in small particles.

3.2 Experimental materials and methods

3.2.1 Materials and reactor system

Oxygen carrier used in this work is alumina supported copper oxide with 13 wt.% CuO loading (Sigma-Aldrich, prepared by impregnation). This CuO content is considered to be suitable since high loading of copper oxide can lead to significant sintering and defluidization.[32] A schematic of the reactor system is shown in Fig. 3.2. A separate gas mixing panel with multiple mass flow controllers (MFCs) is used to deliver mixtures of reducing and oxidizing reactant

gases including nitrogen, oxygen and methane to the bottom of the fluidized bed reactor. The reactor is constructed with a stainless tube of 0.88 inch inner diameter and 1 inch outer diameter. Gases and particles leaving the reactor would pass a horizontal tube with 0.21 cm inside diameter first and then goes through filter media (0.2 μm pore size) or cascade impactors (MOUDI Model 110). The diameter of the horizontal settling tube is selected such that the saltation diameter of particles are approximately 10 μm. A 3-way valve prior to the impactors (or filters) allows reactor emissions to be directed to different particle collection devices during oxidation and reduction steps, respectively. Composition of the gases exiting the system is determined by gas chromatography (Agilent CP-490) and a near-IR based gas analyzer (Emerson X-Stream) prior to exhaust.

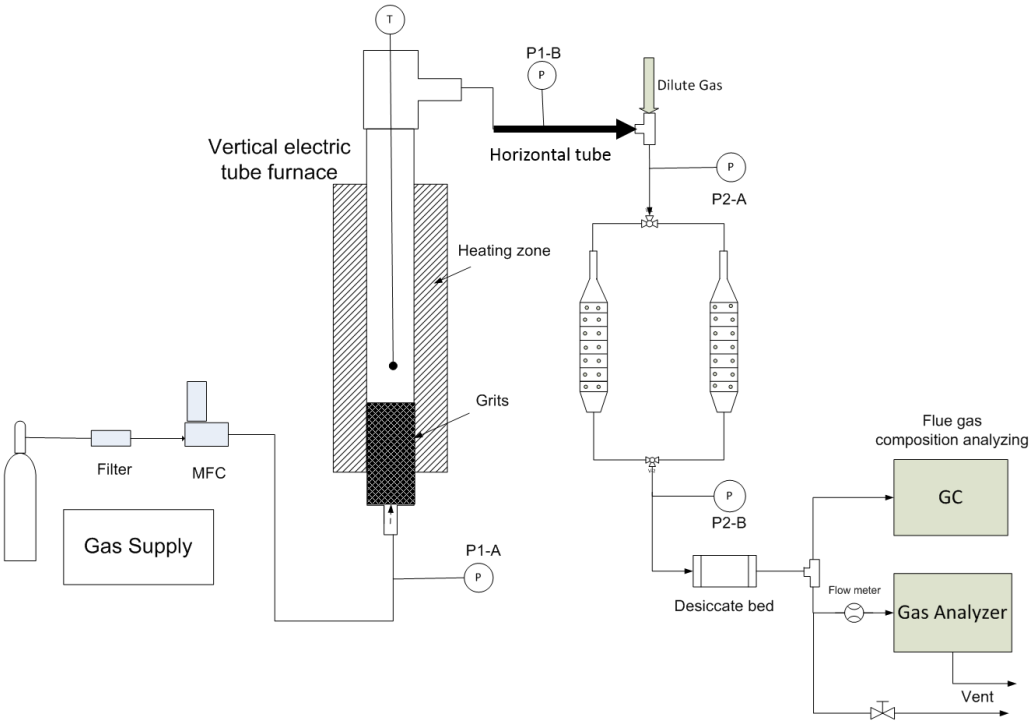

Fig. 3.2. Schematic of fluidized bed experimental setup with impactors

In a typical experiment, 25 grams of 90-300μm particles are used as the oxygen carrier. 16 mesh silicon carbide (SiC) grit is used to distribute gas across the reactor cross-section. The oxygen carrier particles are then added on top of the SiC grit layer before each experiment. A continuous flow of N_2 at 300 mL/min is used as the fluidization and purge gas during the experiments. To start the experiment, the reactor is first heated to 800°C, followed by the injection of methane (5.0 grade) at a flow rate of 50 mL/min for 4 minutes. Once methane is injected, it will be converted into a CO_2-rich stream, while oxygen carriers are reduced. Following the oxygen carrier reduction step, the reactor is purged with N_2 (5.0 grade) at a flow rate of 300 mL/min for 3 minutes. Air (5.0 grade, flow rate 75 mL/min) is subsequently injected into the reactor to regenerate the reduced oxygen carrier, thereby completing the redox cycle. The regenerate step is set at 10 minutes unless otherwise specified. This is followed with another 3 minutes purging step prior to initiating the next redox cycle. Gas flows of 350 - 375 mL/min are sufficient to maintain bed fluidization in the bubbling regime, but insufficient to carry normal bed materials out of the reactor. Such a cyclic operation is used to mimic CLC operations in a circulating fluidized bed. The operational parameters, such as reaction temperature, particle size and linear gas velocity, are adopted based on a 10 kW_{th} CLC demonstration unit reported in literature.[24,32,33] Detailed experimental conditions are given in Table 3.1. In addition, blank tests are conducted under the following two conditions: (1) 375 mL/min N_2 and (2) co-injection of 300 mL/min N_2 and 75 mL/min O_2. These conditions are chosen such that the predominant valence state of copper can be fixed at 1 (under condition 1) or 2 (under condition 2) in absence of redox reactions.

3.2.2 Particle size measurements

Two filters equipped with 0.2 μm pore size polycarbonate film are used after the horizontal tube to capture the particulates from reducing and oxidizing step respectively. Besides the filters, two sets of 8-stage 30 L/min micro-orifice uniform deposition impactors (MOUDI, MSP Inc.) are also used to separate and collect the elutriated particulates between 0.105 and 20 μm. The entire effluent from the reactor is diluted with nitrogen (30 L/min) after the settling

tube and directed to the MOUDI. With the dilution gas, the impactor inlet pressure is measured to be 2.2 PSIg. The slightly higher than atmospheric pressure condition is estimated to have <13% impact on the sizes of the particulates collected. Substrates used in the stages of MOUDI impactors are 47-mm polycarbonate film coated with Apiezon type L vacuum grease for particulate collection, which is ready for XRD analysis. Before the experiment, the films are placed in an 85°C oven for 1 hour and then measured the weight by an analytical balance (Mettler Toledo XA105DU). After collection, the polycarbonate films are measured again and stored in a desiccator until they are analyzed by XRF.

3.2.3 Characterization methods

X-ray powder diffraction (XRD) analysis is performed to identify the crystalline chemical species of the metal oxides by using a Rigaku SmartLab XRD with Cu-Kα radiation. The surface and structure morphology of the particles was determined by a SEM (Verios 460L). The same instrument is used for near surface elemental analysis using energy dispersive X-ray spectroscopy (EDS) under both spot and mapping modes (20 kV, 1.6nA). The particle metal analyses are determined by X-ray fluorescence (XRF) spectroscopy. The particle-size distributions (PSDs) for the bed materials are determined by sieve analysis. Carbon analysis is performed by oxidizing the samples using a thermogravimetric analyzer (TGA, SETARAM SETSYS Evolution) coupled with mass spectrometry (MS, MKS Sirrus 2). The total CO and CO_2 products are integrated from the calibrated MS signals.

Table 3.1. Experimental conditions

Fuel	CH_4 (99.9% pure)
Temperature	800 ^oC
Oxygen	CuO (13 wt%)-Al_2O_3 (Sigma-Aldrich)
Carrier	25 g; 90-300 μm, 0.73 g/cm^3 (bulk density)
Reactor	Diameter: 2.2 cm
	Minimum fluidization velocity: 0.04 m/s
	Fluidization regime: Bubbling regime
	Superficial gas velocity: 0.12 m/s
Reduction step	4 minutes
Oxidation step	10 minutes

3.3 Results and discussion

3.3.1 Oxygen carrier particle performance in CLC

Copper oxide based oxygen carriers can be used to convert both solid and gaseous fuels. In terms of solid fuel conversion, the so-called CLOU property of CuO is often utilized for improved combustion kinetics. Under such a scenario, CuO releases its lattice oxygen into the gas phase while being reduced primarily to Cu_2O. To convert gaseous fuels such as methane, CuO can be reduced to metallic copper in a facile manner. However, over-reduction of copper oxide is often avoided due to the low melting point of copper. This manuscript primarily investigates methane combustion with copper oxide based oxygen carriers. The fuel gas (CH_4) conversion, as well as the yield of CO, CO_2 and deposited carbon (mole percentage) with increasing experimental time are listed in Table 3.2. The amount of carbon decomposition is calculated based on CO and CO_2 produced in the subsequent oxidization reactions. The multi-cycle fluidized bed experiments show over 98% CH_4 conversion and 97% CO_2 yield after 1200 redox cycles, with minimal CO and carbon formation. XRD measurements of the reduced phase, as shown in Fig. 3.3, indicate that CuO is reduced to Cu_2O after reacting with CH_4.

$2CuO \rightarrow Cu_2O + 0.5O_2$ Reaction (3)

After 600 redox cycles, the oxidized oxygen carrier contains predominately $CuAl_2O_4$ phase, which is attributable to the solid-state reaction between copper-oxide and alumina at high temperatures.[32,34]

$CuO + Al_2O_3 \rightarrow CuAl_2O_4$ Reaction (4)

While the formation of $CuAl_2O_4$ mixed oxide negatively impacts the activity of the oxygen carrier to small extent, as evidenced by 1.5% decrease in methane conversion, it is fully reducible to $CuAlO_2$, Cu_2O, and elemental Cu. Therefore, loss in oxygen carrying capacity of the oxygen carrier was minimal. Based on the XRD results (Fig. 3.3), the following reversible reaction represents the reduction and oxidation reactions during the chemical looping combustion:

$2CuAl_2O_4 \leftrightarrow 2\ CuAlO_2 + Al_2O_3 + 0.5O_2$ Reaction (5)

Therefore, the CuO-Al_2O_3 based oxygen carrier in the present study exhibits satisfactory activity for methane combustion and is recyclable over continuous redox cycles. Moreover, its composition is comparable to typical copper oxide based oxygen carriers in previous studies,[32,35] making it a suitable reference material for attrition studies.

Table 3.2. Methane conversion and product yields (%) in the methane combustion step (water-free basis)

Mol.%	6^{th} cycle	600^{th} cycle	1200^{th} cycle
CH_4 Conversion	99.84	99.15	98.34
CO_2 Yield	99.6	98.34	97.3
CO Yield	0.25	0.31	0.35
C Deposition	0	0.50	0.60

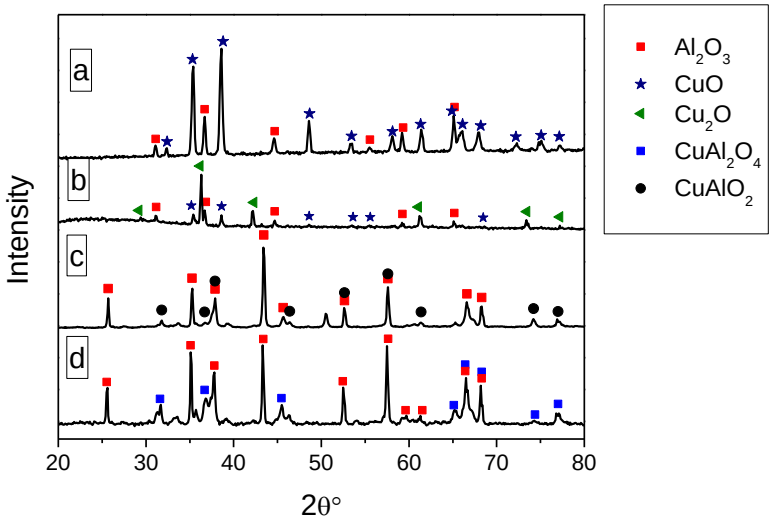

Fig. 3.3.XRD results of the bed particle (a) fresh, (b) reduced after 6 cycles, (c) reduced after 600 cycles, (d) oxidized after 600 cycles.

3.3.2 Rates of particulates emission and attrition

Particle attrition describes physical degradation in particle solids processing systems. Main factors impacting particle attrition rate can be divided into two categories[23]: (1) material properties, including particle structure, pretreatment and preparation history, particle size, shape and surface structure, particle size distribution; (2) process conditions, including gas and solid velocities, solids residence time, temperature, pressure, humidity, and chemical reaction. In CLC processes, oxygen carrier particles experience alternating reducing and oxidizing environments which are accompanied with loss and reincorporation of lattice oxygen in a cyclic manner. It is therefore important to study the impact of redox reactions on attrition behavior of oxygen carrier particles. From a mechanistic standpoint, small particles can be generated via[23,36]: (1) breakage or fragmentation, which produces coarse particles; (2) surface abrasion, which generates particulates. In addition, submicron particulates with aerodynamic diameters less than 0.5 μm are formed primarily through ash vaporization, nucleation, and coagulation/condensation mechanisms in coal combustion processes.[37]

Prior to the particle attrition and emission studies, it is important to categorize the particles generated in appropriate size ranges. Since the fresh particles are in the size range of 90-300 μm, the <90 μm particles in the reactor and the particles accumulated in the settling tube are defined as small particles, while the particles collected on the filter after the settling tube are identified as particulates in this paper. In addition, submicron particulates represents the particulates with < 1 μm aerodynamic diameter. It is noted that particulates collected on the filter, which are those escaping the horizontal settling tube, have a general aerodynamic diameter of < 10 μm, which is presented in Fig. 3.7. These particles are significantly smaller than typical CLC particle sizes and they are difficult to capture by cyclones, since the control efficiency range for conventional single cyclones would drop below 40% for such small particles.[38] Both the small particles and particulates are generated by attrition. The attrition rate of small particles at a given particle size range is calculated by the following equation and the results are shown in Fig. 3.4:

$$Attrition\ Rate = \frac{weight\ of\ particle}{initial\ bed\ particle\ weight \times reaction\ time} \qquad \text{Equation (1)}$$

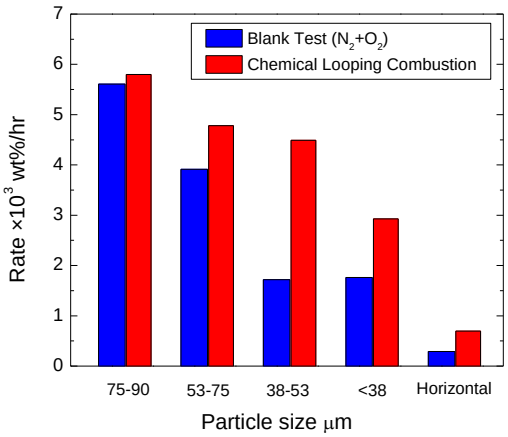

Fig. 3.4. Small particle attrition rate wt%/hr in various sizes (μm) with and without chemical looping reactions.

The attrition rate of small particles with sizes between 53-90 μm does not show much difference with or without chemical looping reactions. In contrast, particles with sizes <53 μm are generated at significantly faster rates under the chemical looping mode. For instance, particulates captured on the settling tube is 2.4 times higher under the chemical looping mode when compared to those under the blank test. As will be discussed in the following sections, the high generation rates for particulates can be attributed to enhanced surface abrasion resulting from surface property and phase changes of the oxygen carrier during redox reactions. In comparison, large particles generated from attrition are mainly caused by fragmentation or breakage.[23] The fact that generation rates of particles (53-90 μm) are not significantly affected by the chemical looping reactions indicate that such reactions have relatively low impact on the bulk properties of the oxygen carrier. This is understandable, as the primary component of the oxygen carrier is alumina support, which is largely unaffected by the redox reactions. It is also noted that particles of 38 – 53 μm range are generated at a notably higher rate under redox operation. This indicates that redox reactions indeed weaken the oxygen carrier but the impact of such reaction should be in the order of 50 μm or less. Further discussions of the consequences of the redox reactions are provided in later sections.

Fig. 3.5 shows the particulate emission rates of one batch of oxygen carrier particles over 1368 cycles. In such a continuous fluidized bed test, particulate samples are taken every 24 hours (72 cycles). In some cases, experimental conditions are adjusted after the 24 hour test. We altered the experimental conditions for the first 576 cycles (192 hours) among injecting N_2 (blank condition 1), injecting N_2+O_2 (20% O_2, blank condition 2), and chemical looping (CH_4 as the reducing gas and N_2+O_2 as the oxidizing gas). Since the fresh particles are prepared by crushing and sieving, their shapes are irregular and hence high attrition rates through both fragmentation and abrasion can be anticipated during the initial period of the test. It is also observed that the chemical looping condition generates more particulates comparing to the conditions with N_2 or N_2+O_2 injection. After the 576 cycles, the experiment is stopped by cooling down the reactor in order to analyze the bed particle size distribution, followed with reheating to restart the chemical looping reactions. An abnormally high particulate emission

rate is observed from 576-648 cycles. It is likely due to thermal stresses caused by temperature changes during cooling and reheating.[23]

It is noted that the particulate emission rate decreases with time, and then asymptotically approaches a steady-state value after around 948 cycles. Two more batches of particles are conducted using a similar experimental plan, where similar emission rate trends are observed. The average, steady-state particulates emission rates based on the three batches experiments are $(2.48 \pm 0.72)\times10^{-3}$ wt%/hr in reduction and $(1.68\pm0.4)\times10^{-3}$ wt%/hr in oxidation, respectively. In addition, two test conditions with N_2 or N_2+O_2 injection are investigated after steady-state emission rates are achieved, as shown in Fig. 3.5. The corresponding particulate amount, 1.3×10^{-3} wt%/hr, is smaller than chemical looping reactions, which again proves that chemical looping reactions induce increased particulate emissions. Another evidence of such an effect is that, when fresh oxygen carriers are tested in a fluidized bed without experiencing any redox reactions, a significantly lower emission rate of 0.24×10^{-3} wt%/hr is observed. Therefore, it is evident that that the chemical reactions weaken the oxygen carrier particles. It is also noted that the reducing step produces larger amount of particulates than the oxidizing step. This is partly because the time for the oxidation step is twice of the reducing step, and the longer non-reaction time during the oxidation step can lead to lowered time-averaged particulate emission rate.

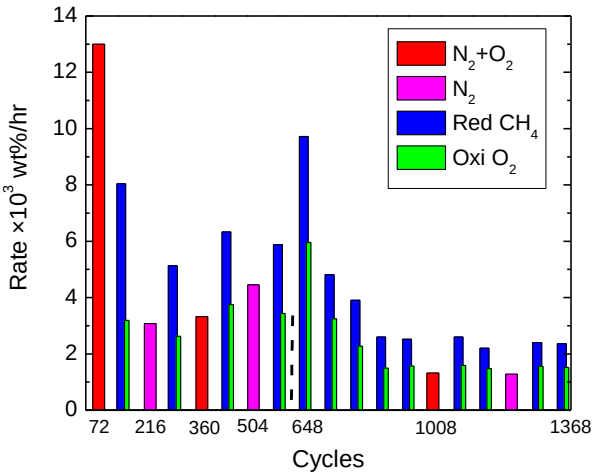

Fig. 3.5. Particulates collected on the filter over multi-cycle experiments. Each data point is based on 72 cycles. N_2+O_2: 300 mL/min N_2 and 75 mL/min O_2. N_2: 375 mL/min. Red. CH_4: reduction step with 50 mL/min CH_4 and 300 mL/min N_2. Oxi. O_2: oxidation step with 75 mL/min O_2 and 300 mL/min N_2. The experiment is continuous without stop after the dashed line.

While filters can effectively collect most, if not all, particulates escaping from the horizontal settling tube, further understanding of the particle size distributions and their compositions are desirable. In order to obtain such information, two sets of MOUDI cascade impactors are used to capture the elutriated particulates from the reducing and oxidizing reactions, respectively, after the emission rate reaches the steady-state value. The collected particulates are segregated by particle aerodynamic diameters, and the results are shown in Figure 6. The particulates from the reducing and oxidizing reactions show similar size distribution, while the reducing reaction lead to a higher emission rate. The majority of the particles have the size less than 5 μm, especially in the range of 2-5 μm. In addition, a notable amount of particulates is observed with the size less than 1 μm.

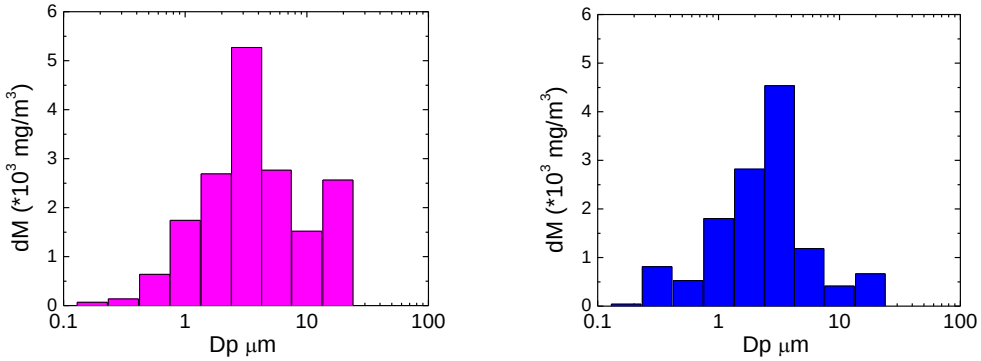

(a) (b)

Fig. 3.6. (a) Reducing and (b) oxidizing size distribution of the particulates after 1368 cycles. D_p: cut-off aerodynamic diameter.

3.3.3 Morphology and chemical compositions

The morphology of the bed particle, small particles and elutriated particulates are shown in Fig. 3.7. When comparing the fresh to cycled particles in the reactor, the bulk irregular shape of the fresh particles become more spherical since the edges are knocked off during the reactions. The initial particle surface which contains bumps and holes is smoothed. This supports the finding that high attrition rates are observed during the initial period of the test. Under a higher magnification, as shown in Fig. 3.7a, there are spherical or elliptical grains with sizes of <5 μm formed on the surface of the cycled particles. These grains are observed after 144 cycles of the chemical looping reactions. In addition, the settling tube is capable to capture the elutriated small particles with the size range of 10-50 μm by gravitational settling as shown in Fig. 3.7(b). These particles also show a porous, rough structure. The size of the particulates collected on the filter after the settling tube is typically smaller than 10 μm (Fig. 3.7(c)), which is consistent with the impactor results. The size of the particulates decreases with the number of looping cycles from 5-10 μm after 100 cycles to <5 μm after 1000 cycles, which is in a similar size range to the surface formed grains as mentioned earlier. This suggests that during

the initial period of the experiment, a wide size range of small particles and particulates are generated from a combination of fragmentation and surface abrasion. With increasing number of redox cycles, the primary mechanism for particulates generation seems to transit to surface abrasion. The images of particulates in Fig. 3.7(d) and (e) are collected from different impactor stages during reduction and oxidation steps. There is no obvious size and shape difference between reducing and oxidizing particulates. The particulates in Fig. 3.7(d) has a cut-off aerodynamic diameter of 3.2 μm, with a combination of porous and less porous particulates.

In the chemical looping reactions, oxygen carrier particles undergo reduction and oxidization in a cyclic manner. Due to the loss of oxygen, reduction results in the formation of a more porous structure. Oxidation causes swelling by adding the oxygen, which also creates local stresses. When this process is repeated, the porosity on the surface increases and leads to a rougher surface that is more susceptible to abrasion. Weak points, which can be broken by fragment or abrasion, are introduced by the reaction-induced local stress. By combining these two effects, the attrition and particulate emission rates are expected to be high with chemical looping reactions. The image of the porous small particles and particulates in Fig. 3.7 (b) and (d) serve as evidences for such an effect. A notable amount of less than 1 μm submicron particulates is also observed. Instead of porous structure, they are in bulk shape, which is very similar in size and morphology with the grains on the particle surface as shown in Fig. 3.7 (a). This suggests that the particulates are mainly formed from surface grains by abrasion or impact.

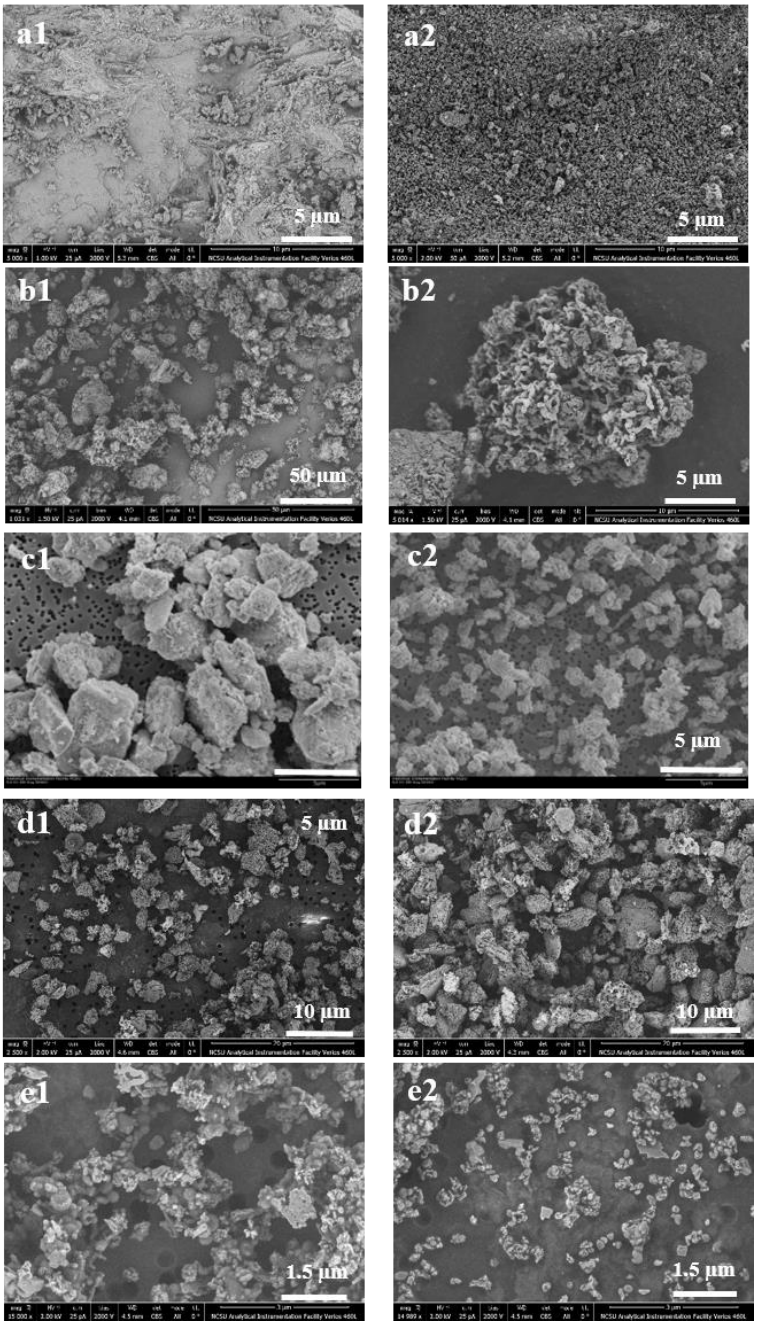

Fig. 3.7. SEM images of (a1): surface of fresh particle; (a2): surface of bed particle after 144 looping cycles; (b1) and (b2): small particle collected in the settling tube; (c1) and (c2): particulates collected by the filter with looping reactions after 100 and 1000 cycles; (d1) and (d2): reducing and oxidizing particulates collected by impactor with D_{50} = 3.2 µm; (e1) and (e2): reducing and oxidizing particulates collected by impactor with D_{50} = 0.17 µm.

Since the active material for the oxygen carrier is copper oxide, the small particle generated from attrition could lead to loss of valuable metal and hazardous emissions of particulate matters. Chemical compositions of the bed particles and elutriated particulates at different size ranges after over 1300 cycles of fluidized bed testing are examined by XRF (Fig. 3.8). The fresh particles in the size range of 90-300 μm contain CuO and Al_2O_3 with a Cu/Al molar ratio of 0.10. The Cu/Al ratio of the cycled particles with the same size as fresh particles is 0.093, which is slightly lower than the fresh particles. SEM-EDX results shows that Cu/Al ratio near particle surfaces (SEM penetration depth is < 5 μm at 20 kV) is 0.093 ± 0.07 on average. The Cu content in the small particles (<75 μm) generated from attrition is much higher than the fresh particles. For example, the Cu/Al ratios of the <38 μm bed particles and the small particles collected in the settling tube, are approximately four times more than that for the fresh particles. These results show Cu is depleted in the bulk and the surface of the bed particle after long-term redox reactions, and the small particles originating from attrition are rich in Cu.

The changes of the particulates Cu/Al ratios on the filter as a function of the progressing chemical looping cycles in the fluidized bed are shown in Fig. 3.9. A very high Cu/Al ratio is observed immediately following reloading of the reactor after 612 cycles. After that, the ratio Cu/Al then decreases steadily to be approximately 0.01 lower than the fresh particles. Garcia-Labiano et al.[28] observed similar CuO loss at the beginning of the combustion test, and subsequently, the rate decreased and stabilized at a lower value. The particulates generated from the reducing step show comparable but slightly higher Cu/Al ratios than the ones from the oxidizing step.

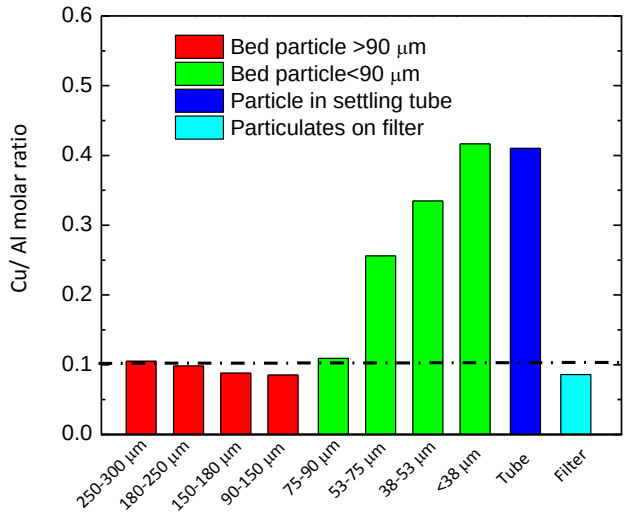

Fig. 3.8. XRF measured Cu/Al molar ratio of CuO/Al_2O_3 particle and particulates after more than 1300 cycles fluidized bed test

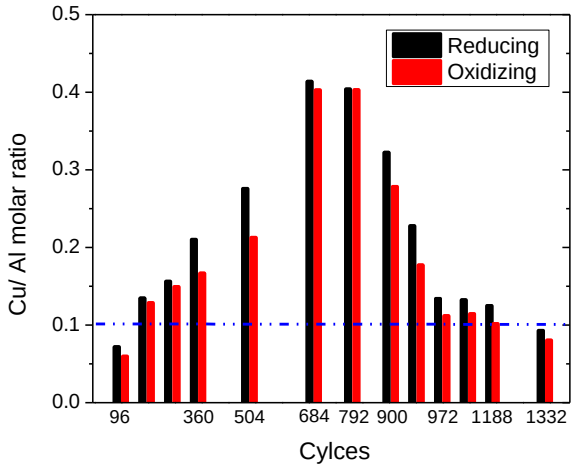

Fig. 3.9. XRF measured Cu/Al molar ratio of the particulates collected on the filter as a function of progressing reaction cycles. Blue dash dot line represents the Cu/Al molar ratio of the fresh CuO/Al_2O_3 particles.

Fig. 3.10 shows the SEM-EDX analysis on the element distributions of the collected particles. Cu was uniformly distributed on the elutriated particles collected in the settling tube, which is similar with the bed particles in all the size ranges. However, the particulates collected on the filter exhibit a Cu accumulation in relatively larger particulates. The results of XRF tests on the MOUDI samples in Figure 11 shows a maximum Cu/Al ratio of 0.23 for the particulates generated from reducing reaction and 0.22 for the particulates generated from oxidizing reaction. Both of these maximum Cu/Al ratios are corresponding to the particulates with approximately 3 μm diameter. When the particles are smaller than 1 μm, the Cu/Al ratio is significantly lower than the ratio of the fresh particles.

On the basis of the above investigations, the Cu components enriched in particle generated by attrition can be explained by the Kirkendall effect. According to the previous study[39], oxidation of Cu in the presence of air at high temperature proceeds through O diffusion. Kirkendall effect i.e. the motion of the Cu-CuO interface, was observed due to the difference in diffusion rate between Cu and oxygen. Outward diffusion of Cu ions is faster than inward diffusion of oxygen, which then leads to the out-diffusion of Cu. The oxidation will keep driving Cu to move outward and could create a porous core. Because of this, the Cu could be rich on the bed particle surface during the chemical looping reactions. The SEM-EDX tests on the bed particles, which shows 0.13±0.01 Cu/Al ratio of particles after 144 chemical looping cycles compared to 0.1 of the fresh ones, serve as an evidence for such an effect. By fragment and surface abrasion, the outer-layer is broken into small particles and particulates, which would be high in Cu ratio. With increasing number of cycles, the particulates Cu/Al ratio is steadily decreased to a value slightly lower than the fresh particles. The fact of the reduced near surface Cu/Al ratio on the bed particles after 1332 cycles, leads to two possible combined effects: (1) the Cu near the bed particles surface is continuously losing over reactions; (2) the amount of Cu being able to move to the surface is limited by the formation of $CuAl_2O_4$ and $CuAlO_2$ phases after redox reactions.

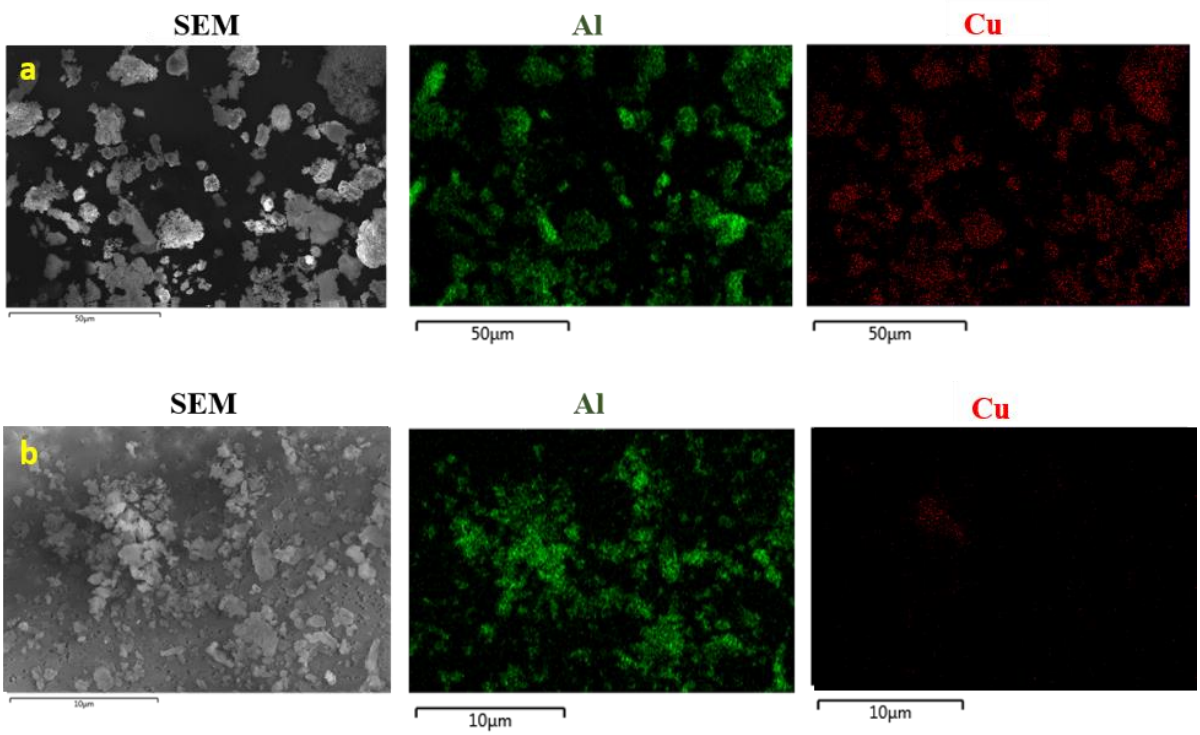

Fig. 3.10. Element mapping by SEM-EDX of elutriated small particles and particulates after chemical looping reactions. (a) Particles in the settling tube with the overall Cu/Al ratio of 0.42. (b) Particles collected on the filter with the overall Cu/Al ratio of 0.11. Green represents Al element and red represents Cu element.

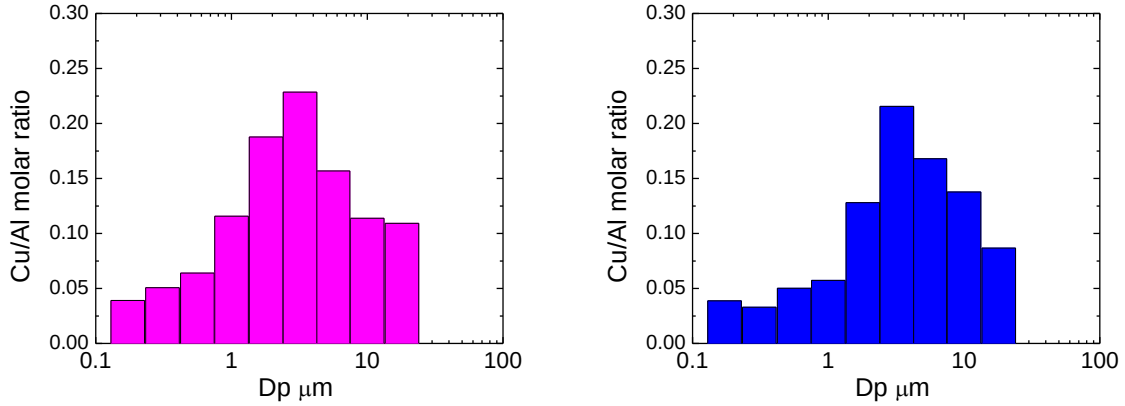

Fig. 3.11. Size distribution of Cu/Al molar ratio from XRF tests on the particulates collected by MOUDI impactors in reducing (a) and oxidizing (b) steps after 1332 cycles.

There are two potential challenges associated with attrition in the fluidized bed: (1) small particles and particulates generation which could cause defluidization and hazardous particulates emission; (2) loss of valuable metal by the elutriated small particles which deactivates the oxygen carrier and leads to health problems from emission. As can be seem from the experimental data, chemical looping reaction is a primary factor of increased particulate generation in fluidized reactors. As such, one would anticipate higher attrition rates of the oxygen carrier particles when used in CLC processes compared to non-reactive conditions. However, even under the chemical looping mode, the CuO-Al_2O_3 particle lifetime is estimated to be 5000 hours, which is based on amount of small particle with the size <90 μm. The CuO materials usually have low attrition resistance,[29] however, when incorporated with substantial Al_2O_3 matrix, the supported particles shows an acceptable attrition resistance, and then can be considered to be feasible for the real-world applications.

The attrition rate of the oxygen carrier particles decreases with time, starting from the first period of the operation, due to the irregularity and initial faults of the fresh particles. After reaching the steady-state region, the attrition rate of the tested impregnated CuO-Al_2O_3 is about

0.02 wt%/hr. Among the particles generated from attrition for 792 continuous cycles, over 85 wt% are small particles with 10-90 μm diameter, which can be captured practically in conventional cyclones.[40] The remaining 15 wt% is particulate, which contains 1.5 wt% submicron particulate with < 1 μm. The particulates (< 10 μm) generating rate is decreasing with progressive cycles, and then reach a steady-state level of $2.48 \pm 0.72\times10^{-3}$ wt%/hr in reduction and $1.68\pm0.40\times10^{-3}$ wt%/hr in oxidation. Assuming a typical solids inventory of 70 kg/MW_{th} in the reducer and 80 kg/MW_{th} in the oxidizer,[41] the particulate (PM_{10}) concentrations in from the reducer and oxidizer flue gases are estimated to be 0.048 g/MJ and 0.037 g/MJ respectively, in absence of additional particulate control systems downstream of the cyclones. It is noted that conventional methane combustion processes do not generate minimal particulates. When compared to the proposed U.S. regulations of 0.43×10^{-3} g/MJ for new coal fired power plants, the emission rates of particulates in CLC using the aforementioned oxygen carrier are higher. Therefore, the emission of the particulates is vital for chemical looping combustion, especially in the first period of the operation, because cyclones have relatively low collection efficiencies for particulates less than 10 μm. The additional options of the particulate control devices include fabric filter, bag house, wet scrubber and electrostatic precipitator (ESP). For example, fabric filter could achieve 99.8% particulate removal efficiency.[42]

In addition to emission, it is observed a total of 11 wt% Cu loss for 792 continuous cycles from the CuO-Al_2O_3 oxygen carriers during the chemical looping reaction. The small particles with 10-90 μm diameter account for approximately 10.7 wt% Cu or 97% of the overall Cu loss. Therefore, it is important to collect these small particles and reprocess them for reuse. The Cu concentration of the particulate decreases with time. Based on the results described above, the weight percentage Cu loss on the particulates as a function of the reaction time can be fitted into the following Equation (2) as shown in Figure 12, where *y* in wt% is the cumulative Cu loss and *t* is the particle residence time. Assuming the coarse particle also follows the same trend, with an residence time of 250 hours in the reactor and total solids inventory of 150

kg/MW_{th},[41] the Cu loss rate is estimated to be 9 kg/hr and the particulates emission rate is 4 kg/hr in a 1000 MW_{th} power plant without recovery.

$y = 5.5 \times t^{(-1.72)}$ Equation (2)

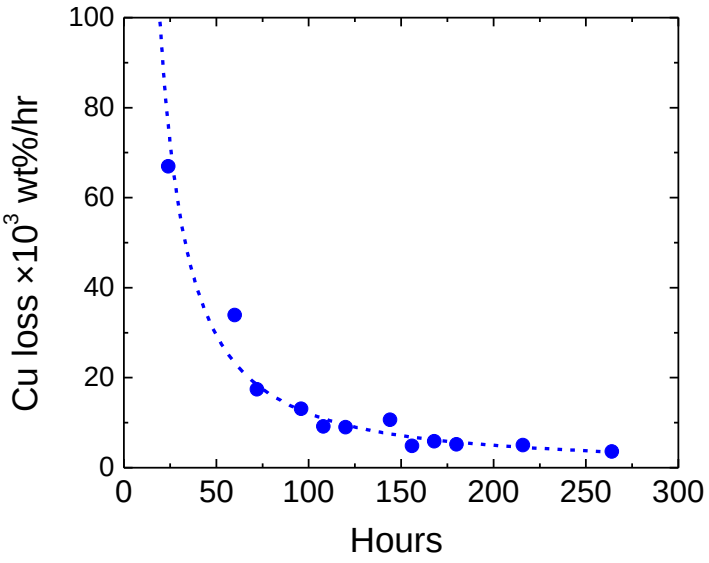

Fig. 3.12. The rate of Cu loss from particulates as a function of reaction time. Dots are the experiment data. Dashed line shows the fit curve based on Equation (3).

In conclusion, chemical looping reactions play an important role in particle attrition in the fluidized bed. Because of reaction-induced local stress, repeated reduction and oxidation of the CuO supported by Al_2O_3 lead to an increased small particle and particulates emission compared to the condition without redox reactions. Not only the small particles but also the particulates have a reduced emission rate over continuous chemical looping reactions. With substantial Al_2O_3 incorporated, the life time of the Cu-based oxygen carriers is estimated to be 5000 hours, which is based on amount of small particle with the size <90 μm. The particulate emission rates of particulates from the reducer and oxidizer in CLC using the aforementioned oxygen carrier are estimated to be over 80 times more than the proposed U.S. regulations for new coal fired power plants. Another result of attrition is Cu loss. The small particles

originating from attrition, especially in the size range of 10-75 μm, are rich in Cu, which can be explained by Kirkendall effect. The majority of the emitted particulates are in the range of 2-5 μm (aerodynamic diameter) with the maximum Cu/Al ratio. Based on these two facts, it could lead to an estimated 9 kg/hr Cu loss from the particles with 250 hours residence in a 1000 MW_{th} power plant without recovery. Therefore, the challenges of the particulates emission and the loss of valuable Cu, when using the $CuO-Al_2O_3$ as oxygen carrier, highlight the importance of a small particle and particulates control units for the practical application of the chemical looping combustion process. The capture of small particles could effectively reduce the emission and recover the majority of valuable metal.

REFERENCES

(1) US EPA, C. C. D. U.S. Greenhouse Gas Inventory Report: 1990-2013.

(2) Gibbins, J.; Chalmers, H. Carbon capture and storage. *Energy Policy* **2008**, *36* (12), 4317–4322.

(3) Figueroa, J. D.; Fout, T.; Plasynski, S.; McIlvried, H.; Srivastava, R. D. Advances in CO_2 capture technology—The U.S. Department of Energy's Carbon Sequestration Program. *Int. J. Greenh. Gas Control* **2008**, *2* (1), 9–20.

(4) DOE/NETL ADVANCED CARBON DIOXIDE CAPTURE R&D PROGRAM: TECHNOLOGY UPDATE. DOE/NETL May **2013.**

(5) Hossain, M. M.; de Lasa, H. I. Chemical-looping combustion (CLC) for inherent separations – a review. *Chem. Eng. Sci.* **2008**, *63* (18), 4433–4451.

(6) Li, F.; Fan, L.-S. Clean coal conversion processes – progress and challenges. *Energy Environ. Sci.* **2008**, *1* (2), 248.

(7) Moghtaderi, B. Review of the Recent Chemical Looping Process Developments for Novel Energy and Fuel Applications. *Energy Fuels* **2011**, *26* (1), 15–40.

(8) Adanez, J.; Abad, A.; Garcia-Labiano, F.; Gayan, P.; de Diego, L. F. Progress in Chemical-Looping Combustion and Reforming technologies. *Prog. Energy Combust. Sci.* **2012**, *38* (2), 215–282.

(9) DOE/NETL Advanced Combustion Systems: Chemical Looping Summary. DOE/NETL July 2013.

(10) Beal, C.; Epple, B.; Lyngfelt, A.; Adanez, J.; Larring, Y.; Guillemont, A.; Anheden, M. Development of metal oxides chemical looping process for coal-fired power plants. In *Proc 1st Int Conf on Chemical Looping. Lyon, France*; 2010.

(11) Dean, C. C.; Blamey, J.; Florin, N. H.; Al-Jeboori, M. J.; Fennell, P. S. The calcium looping cycle for CO_2 capture from power generation, cement manufacture and hydrogen production. *Chem. Eng. Res. Des.* **2011**, *89* (6), 836–855.

(12) Fan, L.-S.; Zeng, L.; Wang, W.; Luo, S. Chemical looping processes for CO_2 capture and carbonaceous fuel conversion – prospect and opportunity. *Energy Environ. Sci.* **2012**, *5* (6), 7254–7280.

(13) He, F.; Galinsky, N.; Li, F. Chemical looping gasification of solid fuels using bimetallic oxygen carrier particles – Feasibility assessment and process simulations. *Int. J. Hydrog. Energy* **2013**, *38* (19), 7839–7854.

(14) Galinsky, N. L.; Huang, Y.; Shafiefarhood, A.; Li, F. Iron Oxide with Facilitated O_2– Transport for Facile Fuel Oxidation and CO_2 Capture in a Chemical Looping Scheme. *ACS Sustain. Chem. Eng.* **2013**, *1* (3), 364–373.

(15) Shafiefarhood, A.; Stewart, A.; Li, F. Iron-containing mixed-oxide composites as oxygen carriers for Chemical Looping with Oxygen Uncoupling (CLOU). *Fuel* **2015**, *139*, 1–10.

(16) Galinsky, N. L.; Shafiefarhood, A.; Chen, Y.; Neal, L.; Li, F. Effect of support on redox stability of iron oxide for chemical looping conversion of methane. *Appl. Catal. B Environ.* **2015**, *164*, 371–379.

(17) Galinsky, N.; Mishra, A.; Zhang, J.; Li, F. $Ca_{1-x}A_xMnO_3$ (A = Sr and Ba) perovskite based oxygen carriers for chemical looping with oxygen uncoupling (CLOU). *Appl. Energy*, **2015**.

(18) Stiegel, G. J.; Ramezan, M. Hydrogen from coal gasification: An economical pathway to a sustainable energy future. *Int. J. Coal Geol.* **2006**, *65* (3–4), 173–190.

(19) Mattisson, T.; Lyngfelt, A.; Leion, H. Chemical-looping with oxygen uncoupling for combustion of solid fuels. *Int. J. Greenh. Gas Control* **2009**, *3* (1), 11–19.

(20) Leion, H.; Mattisson, T.; Lyngfelt, A. Using chemical-looping with oxygen uncoupling (CLOU) for combustion of six different solid fuels. *Energy Procedia* **2009**, *1* (1), 447–453.

(21) Adánez-Rubio, I.; Abad, A.; Gayán, P.; de Diego, L. F.; García-Labiano, F.; Adánez, J. Identification of operational regions in the Chemical-Looping with Oxygen Uncoupling (CLOU) process with a Cu-based oxygen carrier. *Fuel* **2012**, *102*, 634–645.

(22) Fan, L.-S. *Chemical Looping Systems for Fossil Energy Conversions*; John Wiley & Sons, **2010**.

(23) Yang, W. *Fluidization, Solids Handling, and Processing: Industrial Applications*; Noyes Publications, **1999.**

(24) Adanez, J.; Gayan, P.; Celaya, J.; de Diego, L. F.; Garcia-Labiano, F.; Abad, A. Chemical looping combustion in a 10 kW(th) prototype using a CuO/Al_2O_3 oxygen carrier: Effect of operating conditions on methane combustion. *Ind. Eng. Chem. Res.* **2006**, *45* (17), 6075–6080.

(25) Linderholm, C.; Mattisson, T.; Lyngfelt, A. Long-term integrity testing of spray-dried particles in a 10-kW chemical-looping combustor using natural gas as fuel. *Fuel* **2009**, *88* (11), 2083–2096.

(26) Li, F.; Kim, H. R.; Sridhar, D.; Wang, F.; Zeng, L.; Chen, J.; Fan, L.-S. Syngas Chemical Looping Gasification Process: Oxygen Carrier Particle Selection and Performance. *Energy Fuels* **2009**, *23* (8), 4182–4189.

(27) Brown, T. A.; Scala, F.; Scott, S. A.; Dennis, J. S.; Salatino, P. The attrition behavior of oxygen-carriers under inert and reacting conditions. *Chem. Eng. Sci.* **2012**, *71*, 449–467.

(28) García-Labiano, F.; Gayán, P.; Adánez, J.; De Diego, L. F.; Forero, C. R. Solid Waste Management of a Chemical-Looping Combustion Plant using Cu-Based Oxygen Carriers. *Environ. Sci. Technol.* **2007**, *41* (16), 5882–5887.

(29) Rydén, M.; Moldenhauer, P.; Lindqvist, S.; Mattisson, T.; Lyngfelt, A. Measuring attrition resistance of oxygen carrier particles for chemical looping combustion with a customized jet cup. *Powder Technol.* **2014**, *256*, 75–86.

(30) Dockery, D. W.; Pope, C. A. Acute Respiratory Effects of Particulate Air Pollution. *Annu. Rev. Public Health* **1994**, *15* (1), 107–132.

(31) III, C. A. P.; Dockery, D. W. Health Effects of Fine Particulate Air Pollution: Lines that Connect. *J. Air Waste Manag. Assoc.* **2006**, *56* (6), 709–742.

(32) De Diego, L. F.; Gayán, P.; García-Labiano, F.; Celaya, J.; Abad, A.; Adánez, J. Impregnated CuO/Al2O3 Oxygen Carriers for Chemical-Looping Combustion: Avoiding Fluidized Bed Agglomeration. *Energy Fuels* **2005**, *19* (5), 1850–1856.

(33) De Diego, L. F.; Garcı´a-Labiano, F.; Gayán, P.; Celaya, J.; Palacios, J. M.; Adánez, J. Operation of a 10 kWth chemical-looping combustor during 200 h with a CuO–Al_2O_3 oxygen carrier. *Fuel* **2007**, *86* (7–8), 1036–1045.

(34) Chuang, S. Y.; Dennis, J. S.; Hayhurst, A. N.; Scott, S. A. Development and performance of Cu-based oxygen carriers for chemical-looping combustion. *Combust. Flame* **2008**, *154* (1-2), 109–121.

(35) Arjmand, M.; Azad, A.-M.; Leion, H.; Lyngfelt, A.; Mattisson, T. Prospects of Al_2O_3 and $MgAl_2O_4$-Supported CuO Oxygen Carriers in Chemical-Looping Combustion (CLC) and Chemical-Looping with Oxygen Uncoupling (CLOU). *Energy Fuels* **2011**, *25* (11), 5493–5502.

(36) Scala, F.; Montagnaro, F.; Salatino, P. Attrition of Limestone by Impact Loading in Fluidized Beds. *Energy Fuels* **2007**, *21* (5), 2566–2572.

(37) Linak, W. P.; Yoo, J.-I.; Wasson, S. J.; Zhu, W.; Wendt, J. O. L.; Huggins, F. E.; Chen, Y.; Shah, N.; Huffman, G. P.; Gilmour, M. I. Ultrafine ash aerosols from coal combustion: Characterization and health effects. *Proc. Combust. Inst.* **2007**, *31* (2), 1929–1937.

(38) Cooper, C. D.; Alley, F. C. *Air Pollution Control: A Design Approach*; Waveland Press, **2011**.

(39) Qin, Y.; Yang, Y.; Scholz, R.; Pippel, E.; Lu, X.; Knez, M. Unexpected Oxidation Behavior of Cu Nanoparticles Embedded in Porous Alumina Films Produced by Molecular Layer Deposition. *Nano Lett.* **2011**, *11* (6), 2503–2509.

(40) US EPA. Air Pollution Control Technology Fact Sheet. July 15, **2003**.

(41) Abad, A.; Adánez, J.; García-Labiano, F.; de Diego, L. F.; Gayán, P.; Celaya, J. Maping of the range of operational conditions for Cu-, Fe-, and Ni-based oxygen carriers in chemical-looping combustion. *Chem. Eng. Sci.* **2007**, *62* (1–2), 533–549.

(42) James. Cost and Performance Baseline for Fossil Energy Power Plants, Volume 1: Bituminous Coal and Natural Gas to Electricity. DOE/NETL-2010/1397 November **2010**.

CHAPTER 4 A HYBRID SOLAR-REDOX SCHEME FOR LIQUID FUEL AND HYDROGEN COPRODUCTION

Feng He [a], James Trainham[b], Gregory Parsons[a], John S. Newman[b,c], and Fanxing Li*[a]

[a] Department of Chemical and Biomolecular Engineering, North Carolina State University, 911 Partners Way, Raleigh, NC 27695-7905, USA.

*Email: Fli5@ncsu.edu

[b] RTI International, 3040 E Cornwallis Road, Research Triangle Park, NC 27709-2194

[c] Department of Chemical Engineering, University of California, Berkeley, CA 94720-1462

CHAPTER 4 is a reprint of a manuscript published in *Energy & Environmental Science*, 2014, 7:2033-2042. The supplementary information is in Appendix B.

Graphical Abstract

A ferrite based oxygen carrier promoted with a mixed ionic-electronic conductor support is used in a hybrid solar-redox scheme for liquid fuel and hydrogen co-production from methane and solar energy. Compared to typical oxygen carriers for solar-thermal water-splitting, the oxygen carrier reported is 10 – 20 times more effective. Based on both experiments and simulations, the hybrid scheme has the potential to co-produce liquid fuels and hydrogen at high efficiency with near zero life cycle CO_2 emission for the hydrogen product.

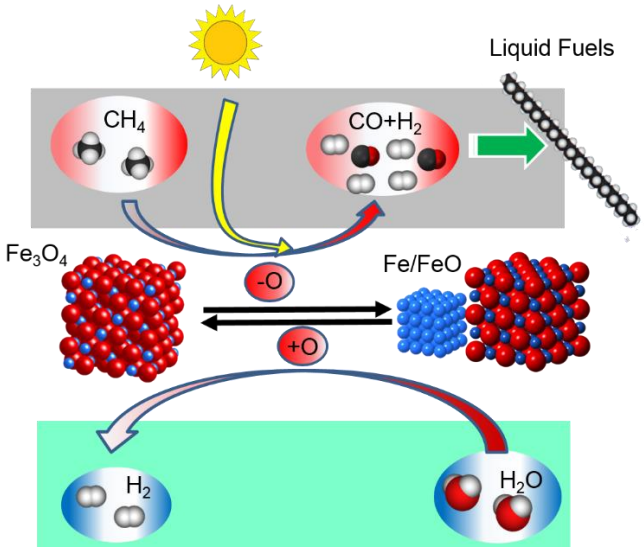

Abstract

The feasibility of a hybrid solar-redox process, which converts solar energy and methane into separate streams of liquid fuels and hydrogen through the assistance of an oxygen carrier, is investigated via both experiments and simulations. Fixed and fluidized-bed experiments are conducted to evaluate the redox performances of an oxygen carrier composed of iron oxide promoted with a mixed ionic-electronic conductor (MIEC) support. Over 95% conversion in the methane oxidation step and 60% steam to hydrogen conversion in the water-splitting step are observed. Aspen Plus® simulation based on experimental data and a comprehensive set of assumptions estimates the overall process efficiency to be 64.2 – 65.3% on a higher heating value (HHV) basis. Through the integration of solar energy, methane to fuel conversion efficiency can approach 100%. The proposed process has the potential to produce transportation fuels and hydrogen at high efficiency with reduced carbon footprint.

Efficient and cost-effective production of clean energy carriers such as hydrogen is of critical importance for sustained growth of the modern economy.[1] Among the various approaches for sustainable hydrogen generation, solar-thermal water-splitting represents a potentially attractive and environmentally friendly option.[2,3] Typical solar-thermal water-splitting schemes involve cyclic redox reactions of transition metal oxides to indirectly convert solar energy and water into separate streams of hydrogen and oxygen. In its simplest configuration, a solar-thermal water-splitting cycle involves two redox steps. In the first step, solar energy is used to decompose a metal oxide at high temperature. In the subsequent step, the decomposed metal/metal oxide is reoxidized with water, producing hydrogen. The key reactions involved in the aforementioned solar-thermal water-splitting cycle include:[4]

$$M_xO_y \rightarrow M_xO_{y-\delta} + \frac{\delta}{2}O_2 \quad (1)$$

$$M_xO_{y-\delta} + \delta H_2O \rightarrow M_xO_y + \delta H_2 \quad (2)$$

Of the two reactions above, Reaction 1 is particularly important from a process design standpoint due to the high temperature required for metal oxide decompositions. From a thermodynamic standpoint, solar-thermal processes have the potential to produce hydrogen at a higher efficiency than the combined power generation – electrolysis approach.[5]

Among the various metal oxide candidates, redox pairs consisting of Fe_3O_4/FeO[6,7] and ZnO/Zn[7–11] have received the most attention. Compared to the Fe_3O_4/FeO redox pair, decomposition of ZnO is more thermodynamically favored. Decomposition temperature of ZnO (~1700 °C) is lower than that of Fe_3O_4.[9] The ZnO/Zn redox pair, however, faces challenges including diffusion limitations in the redox reactions as well as the recombination of Zn vapor and gaseous oxygen during the cooling stage after decomposition (Reaction 1).[12] In addition, material integrity under the extremely high thermal and redox stresses represents another major challenge for the ZnO based redox scheme.[7,13] To date, extensive studies have been performed to address the aforementioned challenges. Although various creative strategies have been proposed and investigated, the economic feasibility of the ZnO based solar-thermal water-splitting cycle is still uncertain.[9,12,14]

Compared to zinc oxides, iron oxides are cheaper and more abundantly available.[6,7,9] In addition, unlike ZnO/Zn, Fe_3O_4 and FeO are nonvolatile and remain in condensed states during the operating cycles.[7] The key challenge of the FeO/Fe_3O_4 water-splitting cycle is the high reaction temperature required for Fe_3O_4 decomposition (2000 °C).[15] The high operating temperature poses significant challenges for reactor design as well as redox material development. Attempts to reduce the decomposition temperature of ferrite materials include the use of mixed oxides with general formula of $M_xFe_{3-x}O_4$[16–19] (M = Mn, Co, Ni, Zn, Mg, etc.). Of particular noteworthiness is the isothermal "hercynite cycle" reported by Muhich et al.[20] which utilizes solid state reactions between ferrite spinel and alumina to tailor the thermodynamic driving forces for the redox scheme. Although these approaches have led to notably lowered decomposition temperatures and/or reduced temperature swings in redox reactions, issues related to metal oxide sintering and deactivations as well as low steam

conversion still need to be addressed. To date, the endothermic decomposition reaction for most, if not all, solar-thermal water-splitting processes are conducted at temperatures above 1300 °C.[19] Therefore, novel solar-thermal schemes that can effectively promote metal oxide reduction at lower temperatures are highly desired in order to achieve improved efficiency and economic attractiveness for solar-thermal hydrogen generation.

The reduction or decomposition temperature of metal oxides can be effectively decreased through the introduction of reducing agents such as carbonaceous fuels. The presence of reducing agents significantly lowers the external partial pressure of oxygen (P_{O_2}), thereby enhancing the reduction/decomposition reactions. Among the various potential reducing agents, methane is particularly attractive since it is a clean, relatively cheap, and abundantly available (through natural gas) primary energy source.[21] The use of methane in conjunction with solar energy can notably reduce the carbon footprint of existing methane conversion processes. Moreover, the presence of methane can decrease the reduction temperature of iron oxides to well below 1000 °C.

Steinfeld[22] proposed several high temperature solar-thermal schemes to mitigate CO_2 emission from the metallurgical industry. These process schemes use a combination of methane and solar energy to reduce metal oxides, e.g. iron or zinc oxides, thereby abating the carbon footprint for metal oxide reduction process. It is further proposed that the metal oxides can serve as energy and oxygen carriers (OC) in a cyclic redox process for cogeneration of syngas (from methane oxidation) and hydrogen (from water-splitting).[23] In addition, methanol production using the syngas from solar-assisted methane oxidation has also been discussed.[22,24] Such a combined reduction-reforming approach is particularly attractive since it provides the potential to generate simultaneously hydrogen and methanol with a low carbon footprint. Moreover, the temperature for metal oxide reduction can be significantly lowered when compared to conventional solar-thermal water-splitting processes. Among the several potential metal oxides, iron oxide is considered to be effective, as confirmed by thermodynamic analyses.[23,25,26] To date, experimental studies for iron-oxide-based methane oxidation and

water-splitting are relatively limited. Steinfeld et al. studied methane oxidation using iron oxide powders in both a thermo-gravimetric analyzer (TGA) and a fluidized-bed reactor.[23,25] Successful syngas generation from methane was achieved. However, the reactivity of the iron oxide is relatively low, leading to low methane conversions (<35% average conversion).[23,25] In addition, carbon formation occurred when iron oxide is reduced to metallic iron phase. Besides pure iron oxides, a number of iron-containing mixed metal oxides such as ZrO_2-supported Ni-FeO_x[27], Cu−Cr−FeO_x[28], Ni-Cr-FeO_x[29], have been tested. These studies further confirm the reaction chemistry of the combined reduction-reforming scheme. Activities and syngas selectivity of these mixed oxides are nonetheless limited. Unless the reactions are carried out at temperatures significantly above 900 °C, methane conversion is generally below 60% with up to 50% CO selectivity. During the regeneration step, steam conversion is often limited to 25%. Another process of relevance is the so-called chemical looping gasification (CLG) process.[30–32] These processes, however, aim to produce carbon dioxide and hydrogen from methane conversion. Kim et al. comprehensively analyzed a number of novel "Sunshine to Petro" (S2P) process configurations to produce methanol or Fischer-Tropsch (F-T) liquids from solar-thermal CO_2 (and H_2O) splitting.[33,34] Their results indicate that the product costs from optimized S2P processes can be comparable to other renewable-based alternatives. The proposed CO_2/H_2O splitting is performed in absence of methane. Therefore, high operating temperature is likely to be necessary. To summarize, comprehensive experimental and simulation studies of the combined reduction-reforming approach are highly desired.

The current study investigates the feasibility of a hybrid solar-redox process for cogeneration of liquid fuels and hydrogen using methane and solar energy. Similar to the combined reduction-reforming concept[25], the Fe_3O_4/$FeO_{1-\delta}$ redox couple is used for methane (partial) oxidation and water-splitting. In this process, syngas from methane oxidation is used in a Fischer-Tropsch synthesis process for liquid fuel synthesis whereas H_2 from water-splitting is processed as a co-product. The current study reports the redox performances of a novel lanthanum strontium ferrite (LSF) supported iron oxide in a lab-scale tubular reactor. 95% conversion of methane is achieved in the iron oxide reduction step. Steam to hydrogen

conversion in excess of 60% is also observed. Results from experimental studies and/or thermodynamic analyses are then used in Aspen Plus simulation models to evaluate the proposed hybrid solar-redox process[35,36].

4.2 Proposed redox scheme:

A simplified schematic of the hybrid solar-redox scheme is given in Fig. 4.1. Solar energy assisted methane conversion is carried out in two interconnected redox steps. In the first step, oxidized ferrite material (Fe_3O_4) is used to convert methane into syngas in a reducer reactor, which reduces Fe_3O_4 to Fe/FeO (or $FeO_{1-\delta}$). The heat required in the reducer is compensated by solar energy. In the subsequent step, reduced ferrite material (Fe/FeO) from the previous step is re-oxidized with steam in an oxidizer, producing concentrated H_2. The syngas produced from Step 1 is then introduced into a Fischer-Tropsch (F-T) reactor to produce a hydrocarbon mixture, which is upgraded in refining units into naphtha and diesel. Hydrogen produced from Step 2 is compressed and purified using a pressure swing adsorption (PSA) system into a final product. A fraction of the hydrogen is used for fuel upgrading in the upgrader. Fuel containing byproducts from the F-T reactor, upgrader, and PSA are combusted for steam generation. A heat recovery steam generator (HRSG) and a series of steam turbines are used to recover process heat and to produce adequate electric power to satisfy parasitic energy requirements. Similar to the combined reduction-reforming approach, the proposed hybrid solar-redox scheme uses methane to supplement solar energy. Besides acting as an energy source, methane provides carbon atoms for liquid fuel synthesis and enables Fe_3O_4 decomposition/reduction at significantly lower temperatures. For instance, decomposition of Fe_3O_4 to FeO is not thermodynamically favored until over 2000 °C. In contrast, methane reduction of ferrites is feasible, both thermodynamically and kinetically, at below 1,000 °C. Besides the lowered operating temperature, the process is able to produce inherently separated liquid fuels and pure H_2. Since a large amount of solar energy is integrated to the methane conversion scheme, the life cycle CO_2 emission from the hybrid solar-redox process is expected to be much smaller than traditional methane-reforming processes.

4.2.1 Integration of solar energy

The experiments carried out in the present study do not involve direct input of solar energy. Instead, an equivalent form of thermal energy is provided by electric heating. It is noted that the proposed process scheme is very similar to the conventional solar-thermal water-splitting processes.[9,22] With significantly lowered operating temperatures and reduced thermal swings, the reactor design can be identical or much simpler for the proposed solar-redox process. A variety of reactor configurations have been investigated for conventional solar thermal water-splitting processes. Among them, the monolithic reactor[37], the foam reactor[38,39], the rotary-type reactor[40] and the volumetric gas–particle solar receiver-reactor[14,41,42] are frequently investigated. The proposed two-step solar-redox process can be carried out in either fixed beds or interconnected fluidized beds as validated in the current study. Therefore, the solar reactor configurations that are particularly suitable for the proposed redox scheme include the rotary-type reactor for fixed bed operation and the volumetric gas-particle solar reactor for fluidized bed operation. Compared to these reactors which have designed operating temperature of over 1400 °C, the reactors in the solar-redox process can be operated at 900 °C or lower. In addition, the MIEC promoted oxygen carrier in the proposed solar-redox process is estimated to be 10 – 20 times more effective (See Table 4.S4 in ESI) than that in conventional solar thermal water-splitting processes.[20,43] As a result, significantly reduced solids inventory and reactor size can be expected. Another potential advantage of the proposed concept is its ability to cope with the intermittency nature of solar energy with ease. Besides the various approaches disclosed in the literature,[35] heat required for methane reforming can be simply compensated by combusting a portion of the reduced iron oxides. Such a strategy allows for continuous process operation in absence of sunlight, at the expense of reduced hydrogen yield. Alternative approaches to ensure continuous operation include: (i) combustion of F-T off-gas and/or supplemental methane; (ii) use of thermal storage material, e.g. alumina sand.[44] As an exploratory study to investigate this novel concept, detailed solar reactor design is outside of the scope.

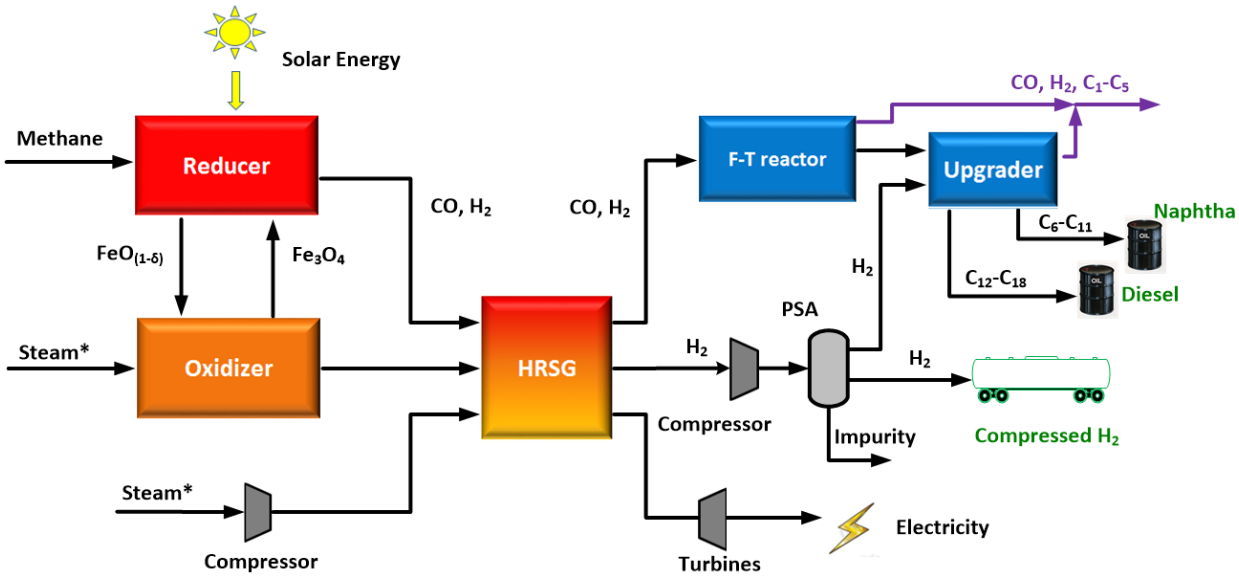

Fig. 4.1. Simplified schematic of the hybrid solar-redox process. To operate in absence of sunlight, steam* can be (partially) replaced with air to achieve auto-thermal operation.

4.3 Experimental and simulation methods

4.3.1 Experimental procedure

Lanthanum strontium ferrite ($La_{0.8}Sr_{0.2}FeO_{3-\delta}$ or LSF) supported Fe_3O_4 is used as the redox material, a.k.a. oxygen carrier, for water-splitting. The synthesis method has been reported earlier[45,46] and is described in ESI. Redox experiments are carried out in a tubular reactor (Fig. 4.S1) which can be operated under either fixed-bed or fluidized-bed mode. The quartz reactor tube has an inner diameter of 19 mm and an outer diameter of 25 mm. The reactor is externally heated with a tube furnace (MTI OTF-1200X-S-VT**)**. Temperature inside the reactor is measured using a type K thermocouple. A gas mixing panel with multiple mass flow controllers (MFCs) is used to deliver gaseous mixtures, e.g. nitrogen and methane, to the reactor. Steam is delivered to the reactor through water injection using a syringe pump (KD Scientific model 100) followed by vaporization in the preheating zone of the reactor. Prior to each experiment, 16 mesh silicon carbide (SiC) particles are loaded at the bottom of the reactor

to serve as a gas preheater and distributor. The SiC layer also supports the oxygen carrier particles. After loading the SiC particles, 7.5 to 20 grams of iron oxide particles are added on top of the SiC layer. In order to mimic the proposed hybrid redox scheme, the tests are carried out in two consecutive steps, i.e. methane partial oxidation and water-splitting. Both fixed-bed and fluidized-bed operation modes are tested. In typical fixed-bed experiments, the reactor is heated under N_2 flow of 15 ml/min. In fluidized-bed experiments, 600 ml/min of N_2 gas is provided during the heating stage to maintain fluidization of the Fe_3O_4-LSF particles. Once the desired temperature (900 °C unless otherwise specified) is reached, 15 ml/min of methane is introduced to the reactor. Corresponding gas residence times are 2.66 and 0.12 s for fixed-bed and fluidized-bed reactor, respectively. Compositions of the gases exiting the reactor are determined using a gas chromatograph (Agilent Micro GC 490) and a Near-IR gas analyzer (Emerson X-Stream gas analyzer). In order to inhibit excessive carbon formation from methane decomposition, methane injection is stopped when $H_2/(CO+CO_2)$ molar ratio exceeds 2. Water-splitting reaction is carried out after the residue gas from the methane oxidation step has been completely purged with N_2. The water-splitting reaction is initiated by steam injection. 15 ml/min (fixed-bed) or 600 ml/min (fluidized-bed) of N_2 is used as the internal standard. The reaction is stopped when H_2 concentration is below 0.1%. The aforementioned redox reactions are carried out for 5 cycles. The crystal phases of the metal oxides are analyzed using X-ray powder diffraction (XRD) (Rigaku SmartLab) with Cu-Kα (λ=0.1542 nm) radiation in the 20-80° angle range (2θ). The amount of carbon formation is quantified using a Thermal Gravimetric Analyzer (TGA) through combustion of 50 mg sample. The exhaust gas from the TGA is analyzed using a quadruple mass spectrometer (QMS, MKS Cirrus 2). The carbon content is calculated by integrating the CO and CO_2 peaks.

4.3.2 Reactor and process modeling

Aspen Plus[47] is used in the present study to determine the reactor and process performances. Detailed simulation assumptions with respect to materials, simulation modules, property methods, physical property databanks, and key operating parameters are summarized in ESI (Table 4.S1-4.S3). All the relevant reactions in the proposed reaction scheme are summarized

in ESI. Prior to comprehensive process analyses, key reactors, i.e. the reducer and oxidizer are simulated. Sensitive analysis is conducted to investigate the effect of reactor operating conditions using methods reported before.[48,49] F-T reactor is simulated using a RStoic model. The product distribution is determined using the Anderson–Schulz–Flory distribution: $W_n = n(1-\alpha)^2\alpha^{n-1}$. Based on a number of published experimental studies, the α value is assumed to be 0.873 with 80% CO conversion at 10 atm and 220°C.[50–52] After reactor modeling, process simulations are conducted based on specifications provided in Tables 4.S1-4.S3, where the Aspen Plus flowsheet is shown in Fig. 4.S6. A methane processing capacity of 8 t/hr (tonnes/hour) is assumed for all cases. Such a capacity, which requires solar input of approximately 60 MW_{th}, allows for integration with existing concentrated solar thermal systems,[8,53,38] In order to evaluate the effects of key process parameters, three simulation cases with different operating conditions are simulated. Since the reducer and oxidizer are operated at high temperatures, it is assumed that thermodynamic equilibrium in the two-step reactors can be achieved in two simulation cases (Cases I and II). A kinetically limited case (Case III) is also investigated using the results obtained from experiments. Key operating parameters for the three simulation cases are summarized in Table 4.1.

Table 4.4.1. Operating conditions for the process simulation cases

	Case I*	Case II*	Case III#
Input	8 t/hr CH_4 feedstock and 52-62 MW solar energy usage		
$\dot{n}_{Fe_3O_4} / \dot{n}_{CH_4}$	0.26	0.26	0.64
Reducer temperature and pressure	900 °C, 1 atm	950 °C, 10 atm	900 °C, 1 atm
Oxidizer temperature and pressure	750 °C, 1 atm	750 °C, 10 atm	750 °C, 1 atm
CH_4 conversion	97.6%	95.1%	95 %
Syngas yield	96.5%	93.2%	59%
Steam to H_2 conversion	68 %	68%	60%
Hydrogen purity	100%	100%	97%

***** Conversions calculated based on thermodynamic equilibrium

Experimentally obtained conversions (see Table 4.3). A conservative syngas yield of 59% is used since it is the lowest value observed in fixed bed experiments.

4.4 Experimental results

Feasibility of the proposed hybrid solar-redox scheme hinges upon satisfactory performance of the oxygen carrier particles for methane partial oxidation and water-splitting. In order to evaluate the performance of the Fe_3O_4-LSF oxygen carriers, cyclic redox operations are conducted to mimic the proposed reducer and oxidizer operations. Although Fig. 4.1 illustrates a circulating fluidized-bed type of reactor system where oxygen carriers are circulated between the reducer and oxidizer, the redox scheme can be carried out in fixed-bed reactors in which reactant gases are switched. To investigate the effect of operation modes, both fixed-bed and

fluidized-bed operations are investigated in the current study. Five redox cycles are performed under a fluidized-bed mode and five additional cycles are performed under a fixed-bed mode. Post experimental examination indicates that all the particulates are free flowing with no sign of agglomeration. In addition, no oxygen carrier deactivation is identified from the multi-cyclic experiments. Representative experimental data are discussed in the following section. Quantitative parameters for evaluating the redox experiments are summarized in Table 4.2, where $\dot{n}_i$ represents molar flow rate of component *i*.

Table 4.4.2. Summary of parameters used to characterize the redox reactions

Parameters	Equations
CH_4 Conversion	$(1-\frac{\dot{n}_{CH_4,out}}{\dot{n}_{CH_4,in}})\times 100\%$
H_2/CO ratio	$\frac{\dot{n}_{H_2,out}}{\dot{n}_{\mathrm{CO,out}}}$
Syngas yield	$\frac{\dot{n}_{H_2,out}+\dot{n}_{\mathrm{CO},out}}{3\dot{n}_{\mathrm{CH_4,in}}}\times 100\%$
Steam to H_2 Conversion	$\frac{\dot{n}_{\mathrm{H_2,out}}}{\dot{n}_{\mathrm{H_2O,in}}}\times 100\%$
H_2 Purity	$\frac{\dot{n}_{\mathrm{H_2,out}}}{\dot{n}_{\mathrm{H_2,out}}+\dot{n}_{\mathrm{CO,out}}+\dot{n}_{CO_2,\mathrm{out}}}\times 100\%$

4.4.1 Methane oxidation reaction

Methane conversion and syngas yield for typical fixed-bed and fluidized-bed CH_4 convention experiments are shown in Fig. 4.3. Further details with respect to the product gas compositions can be found in Fig. 4.S2 (ESI). CH_4 conversion is relatively low at the beginning of the

experiments and steadily increase over time. During fixed-bed operations, ~90% methane conversion was observed initially. The instantaneous methane conversion increases to nearly 100% as the reaction proceeds. A similar trend is observed for fluidized-bed operation, which has an initial methane conversion of ~20% and a final conversion of ~60%. The increase in methane conversion is likely to result from the higher activity for methane activation on metallic iron compared to iron oxides. As the reaction proceeds, more reduced iron is available to catalyze methane conversion. Excessive reduction of iron oxides, however, leads to coke formation from methane decomposition reaction. Syngas yield generally correlates with methane conversion at the initial stage of the reaction. Decrease in syngas yield, which corresponds to coke formation, is observed towards the end of the experiment. The average methane conversion under the fixed-bed mode is 95%. The corresponding syngas ($CO+H_2$) yield is 67% with a H_2/CO molar ratio of ~2. It is noted that both the fluidized-bed and fixed-bed experiments are carried out in a semi-batch mode. Therefore, steady-state gas and solid conversion profiles cannot be established. The very short gas residence time has contributed to the relatively low methane conversion in the fluidized-bed experiments. Improved gas and solids conversions can be expected with larger circulating fluidized-bed reactors. Another observation is the coexistence of notable amount of CO_2 and methane in the gaseous products, especially for the fluidized bed experiment (up to 10% CO_2 and 58% methane, N_2-free basis) as well as the initial stage of the fixed bed experiment (up to 11.5% CO_2 and 3.7% methane, N_2-free basis). This indicates that the Fe_3O_4-LSF oxygen carrier may not be very active for catalytic reforming of methane. Further enhancement of the catalytic activity of the oxygen carrier will likely improve syngas yield, especially for the fluidized bed operations. When compared to previously published experimental data, i.e. about 45% methane conversion and 15% syngas yield,[31] the use of Fe_3O_4-LSF based oxygen carrier has resulted in significantly improved methane conversion and syngas yield.

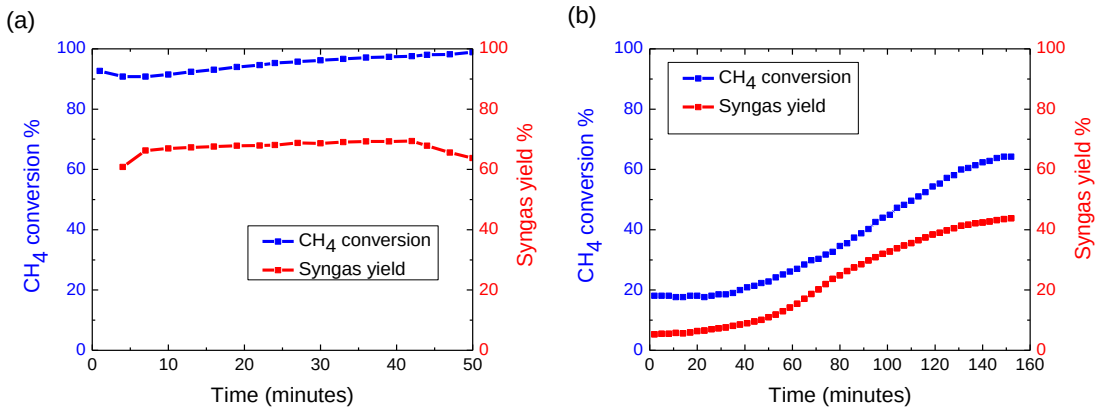

Fig. 4.2. Methane conversion and syngas yield as a function of time in the CH_4 oxidizing step. (a) 5th cycle fixed-bed (b) 5th cycle fluidized-bed.

4.4.2 Water-splitting reaction

Water-splitting or steam-iron reaction is initiated by introducing steam into the reactor after the methane conversion step. Besides H_2, small amounts of CO and CO_2 are detected, especially within the first 4 minutes of the experiment. This corresponds to the gasification of carbon deposited during the methane conversion step. Fig. 4.3 shows a representative H_2 purity profile (water-free basis) during the water-splitting step. The overall H_2 purity is 97.2 %. Small amount of the CO and CO_2 are detected at the beginning of the oxidization, which is resulted from coke formed in the methane conversion step. H_2 purity after the first 4 minutes is higher than 99%. A high steam conversion of 55 to 60% is achieved within the first 60 minutes of the oxidation step. Such a conversion is close to the 62.4% steam conversion predicted by thermodynamics. In order to confirm the phase and structural stabilities of the oxygen carrier particles, X-ray powder diffraction (XRD) and carbon analyses are carried out for spent oxygen carriers in both reduced and oxidized forms. XRD spectra of the samples are provided in Fig. 4.S4. Both wustite and metallic iron are observed in the reduced sample whereas the majority of the iron phase in the regenerated sample is magnetite. Iron carbide phases are not identified in the reduced sample, indicating that amorphous carbon and/or carbon fiber may represent the dominant forms of carbon. Post experiment carbon analyses indicate that steam is capable of

removing most of, if not all, the carbon formed on the sample during the methane conversion step. Table 4.3 further summarizes the key experimental data obtained from fixed and fluidized-bed experiments. Experimental data from the 5th redox cycles are shown since the data are quite reproducible among the various redox cycles. The comparisons of the redox performance among different redox cycles are shown in ESI (Fig. 4.S5).

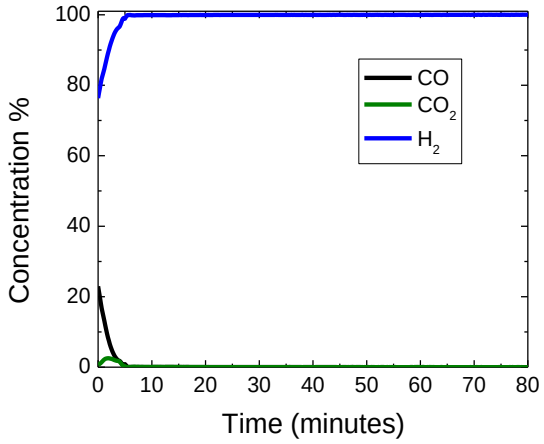

Fig. 4.3. H_2 concentration (water-free basis) during the water splitting step as a function of time at 900 °C (5th oxidation cycle under fixed-bed mode).

Table 4.4.3. Fixed-bed and fluidized-bed results of the redox reactions

	Fixed-bed 5^{th} cycle	Fluidized-bed 5^{th} cycle
Gas residence time (s)	2.66	0.12
Cumulative methane conversion (%)	95.3	38.0
Cumulative syngas yield (%)	67.7	23.0
Syngas production (mmol/gram of OC)	3.1	7.2
Cumulative H_2/CO molar ratio	1.9	2.6
Cumulative $(H_2-CO_2)/(CO+CO_2)$ molar ratio	0.97	1.13
Steam to hydrogen conversion in the first 60 min (%)	60	56.3
Overall steam to hydrogen conversion (%)	47.2	34.2
Cumulative hydrogen purity (%)	97.2	97.5
Carbon Formation (mmol/gram of OC)	0.18	0.24
H_2 yield first 60 min (mmol/gram of OC)	4.3	7.5
H_2 yield (µmol/gram of OC)	5.9	9.6

4.5 Aspen Plus® simulations

The experiments discussed in the previous section confirm the effectiveness of the Fe_3O_4-LSF based oxygen carrier particles for the proposed redox reactions. In the following sections, Aspen Plus simulation is used to estimate reactor and process performances of the hybrid solar-redox concept.

4.5.1 Reactor simulations

Reducer modeling is first conducted at 1 atm and 900 °C using the Aspen Plus RGibbs model. Methane and oxygen carrier particles (Fe_3O_4) are introduced to the reducer. An important

parameter characterizing the effectiveness of an oxygen carrier is the molar flow rate ratio between Fe_3O_4 and CH_4, i.e. $\dot{n}_{Fe_3O_4} / \dot{n}_{CH_4}$. Fig. 4.4 shows *$H_2$/CO* ratio, CH_4 conversion, and syngas yield at various $\dot{n}_{Fe_3O_4} / \dot{n}_{CH_4}$. As shown in Fig. 4.4a, the generation of solid C is inhibited when $\dot{n}_{Fe_3O_4} / \dot{n}_{CH_4}$ is higher than 0.25. In addition, the desired product, i.e. CO and H_2, shows a maximum yield when $\dot{n}_{Fe_3O_4} / \dot{n}_{CH_4}$ is around 0.25 (Fig. 4.4b), where the *H_2/CO* molar ratio is about 2. In the process simulations, $\dot{n}_{Fe_3O_4} / \dot{n}_{CH_4}$ equal to 0.26 is selected as the methane to oxygen carrier ratio. Table 4.4 compares the simulation predicted reducer performance under various temperature and pressure with the experimental data obtained in the fixed-bed. The syngas yield from experiments is significantly lower than that predicted from equilibrium based models. This results from the low catalytic activity of the oxygen carrier for dry reforming of methane. In addition, increase in reducer pressure generally inhibits methane conversion. Steam and/or CO_2 injection can be used to enhance methane conversion and to adjust the *H_2/CO* ratio to around 2 for Fischer-Tropsch synthesis using a cobalt based catalyst.

The primary function of the oxidizer is to produce hydrogen from steam. The oxidizer model is simulated by a multi-stage RGibbs model reported earlier[48,54]. For the exothermic steam iron reaction, equilibrium steam conversion decreases with increasing temperatures. While pressure has no effect on equilibrium steam conversion, higher molar ratio between reduced iron and wustite ($n_{Fe}/n_{Fe0.947O}$) generally leads to higher steam conversion. At 900 °C and 750 °C, equilibrium steam conversions are estimated to be 62.4% and 68%, respectively.

4.5.2 Process simulations

As specified in Table 4.1, three simulation cases of the hybrid solar-redox scheme are studied using Aspen Plus. The details of simulation parameters and assumptions are given in the experimental section. Cases I and II assume thermodynamic equilibrium in the redox steps. To evaluate the effect of operating pressure, Case II assumes a higher pressure of 10 atm for the reducer and oxidizer. Case III, a kinetically limited case using experimental data from the fixed-bed reactor, is also investigated using the experimental results presented previously. The

process simulation results are summarized in Table 4.5. Fig. 4.5 illustrates the energy balances of all three scenarios.

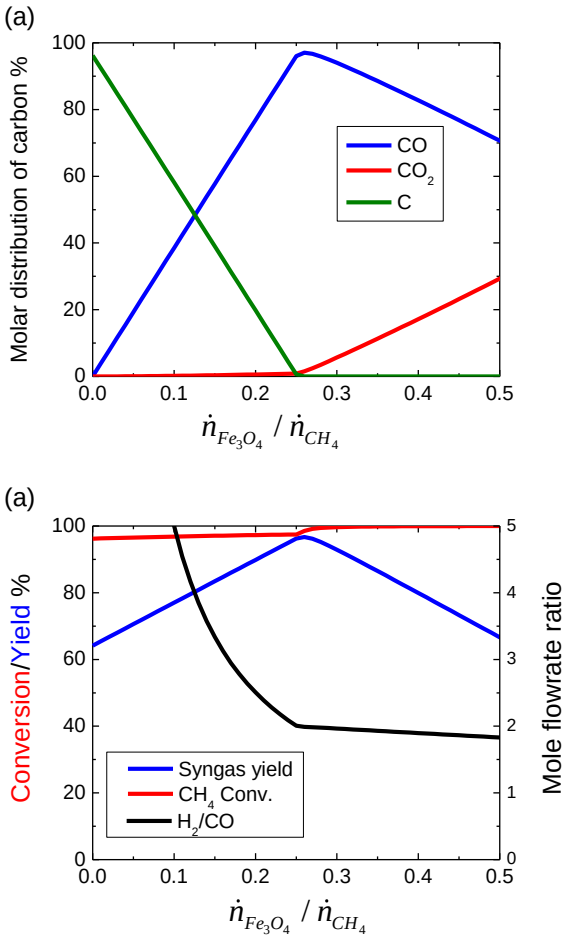

Fig. 4.4. Reducer performance under various n_{Fe3O4}/n_{CH4} molar flow rate ratios at 1 atm and 900 °C. (a) Carbon distribution; (b) syngas yield, CH_4 conversion and H_2/CO ratio.

Table 4.4. Reducer performance under various operating conditions from Aspen Plus simulation and fixed-bed experiments (CH4 molar flow rate is fixed at 1 kmol/hour)

	Condition A*	Condition B*	Condition C*	Fixed-bed experiment
Temperature	900 °C	900 °C	950 °C	900 °C,
Pressure	1 atm	10 atm	10 atm	1 atm
$\dot{n}_{Fe_3O_4} / \dot{n}_{CH_4}$	0.26	0.26	0.4	N/A
H_2O injection/CH_4	0	0	0.92	0
CO_2 injection/CH_4	0	0	0.27	0
C formation (mmol/g of OC)	0	0	0	0.18
H_2/CO	1.99	1.95	2	1.9
Syngas yield (%)	96.5%	83.0%	88.7%	59 %
CH_4 conversion (%)	97.6%	88.2%	99.3%	95.3%

* Thermodynamic equilibrium is assumed for the reducer under the given temperatures and pressures.

Taking Case I as an example, 8 t/hr CH_4 as well as 52.9 MW concentrated solar energy are converted into 2.0 t/hr naphtha, 3.2 t/hr diesel and 0.984 t/hr compressed hydrogen. As a result, the HHV efficiency of the overall process is 65.1 %. Without considering the solar energy input, the HHV efficiency for methane to fuel/hydrogen conversion is 93.7 %. Such an efficiency is significantly higher than those of conventional gas-to-liquids (GTL) processes, which are typically 57 to 63% efficient on an HHV basis.[55] Case II has hydrogen yields similar to those of Case I. Additional CO_2 and steam are injected into reducer to enhance the CH_4 conversion to 95.3%. Resulting from the reduced requirements for gas compressions, Case II, which operates at 10 atm, has more electricity produced. Therefore, in spite of its inhibition effects for methane conversion, higher operating pressure enhances the overall efficiency of the process. Compared to Cases I and II, Case III produces less liquid fuels and more hydrogen. The overall efficiency of Case III is slightly lower than those of Case I and Case II.

Consideration of kinetic limitations has two competing effects: (i) the lower syngas yield of 59% in the reducer leads to decreased liquid fuel production. (ii) Decreased syngas yield in the reducer leads to increased amount of oxygen deficient metal oxides available for water-splitting. This leads to increased hydrogen yield. On a methane conversion basis, the efficiencies of all three cases are significantly higher than those reported for reforming based approaches. Steinfeld et al.[6] evaluated solar-thermal water-splitting process based on Fe_3O_4/FeO redox couples. The maximum efficiency is estimated to be 61% without considering energy losses from product separation, quenching, purification, and F-T synthesis steps. Therefore, the proposed hybrid solar-redox scheme has the potential to utilize methane in a significantly more efficient manner. This corresponds to reduced life cycle greenhouse gas emissions (i.e., carbon footprint) and increased environmental sustainability.

The life-cycle carbon emission of the hybrid solar-redox process and conventional methane reforming processes without CO_2 capture are compared in Table 4.6. The calculation includes the estimated emission from construction, equipment, fuel transportation and process operation. Emissions from the upstream natural gas production activities are assumed to be 9.1 kg CO_2/mmBtu according to DOE reports.[56,57] As shown in Table 4.6, the CO_2 footprint of the hybrid solar-redox process (A) is roughly 22 kg CO_2/mmBtu less than hydrogen generation from methane-reforming (B) and 31 kg CO_2/mmBtu less than methane-reforming based liquid fuel generation process (C). When compared with a methane-reforming based hydrogen and liquid fuel co-generation process (D), the CO_2 emission reduction for the hybrid process is 28 kg CO_2/mmBtu less. This translates to 30% less carbon emission than conventional methane reforming for hydrogen and liquid fuel cogeneration. Since the life cycle CO_2 emissions for petroleum-derived gasoline and diesel are around 95 kg CO_2/ mmBtu,[58] a CO_2 emission quota for the liquid fuel products from the solar-redox process can be calculated assuming the synthetic fuels are identical to petroleum derived fuels. When such an emission quota is subtracted, life cycle CO_2 emissions from the H_2 product are estimated to be 4 kg CO_2/mmBtu of H_2 or 95% lower than the conventional scheme. To summarize, the proposed hybrid solar-redox process has the potential to reach high energy conversion efficiency and reduced carbon

footprint when compared to traditional approaches based on solar-thermal water-splitting and methane reforming.

Table 4.5. Process mass and energy balances of the Aspen Plus simulation on the three hybrid solar-redox

	Case I	Case II	Case III
Concentrated solar energy (MW)	52.9	56.9	61.6
CH_4 conversion	97.6%	95.3%	95.3%
Syngas yield	96.5%	93.2%	59%
Syngas (kmol/hr)/(t/hr)	1447/15.5	1399/14.9	878.7/9.66
H_2/CO Ratio	2.0	2.0	1.9
Naphtha (kmol/hr)/(t/hr)	17.4/2.0	15.3/1.8	10.9/1.2
Diesel (kmol/hr)/(t/hr)	15/3.2	13.2/2.8	9.4/2.0
Steam usage (reducer) (t/hr)	0	2.8	0
Steam usage (oxidizer) (t/hr)	13.5	13.5	30.4
Compressed H_2 (kmol/hr)/(t/hr)	487.8/1.0	487.8/1.0	965.6/2.0
Net power (MW)	13.2	3.0	3.5
Overall Efficiency (HHV) %	65.1	65.3	64.2
Efficiency based on methane (HHV) %	93.7	96.1	96.6

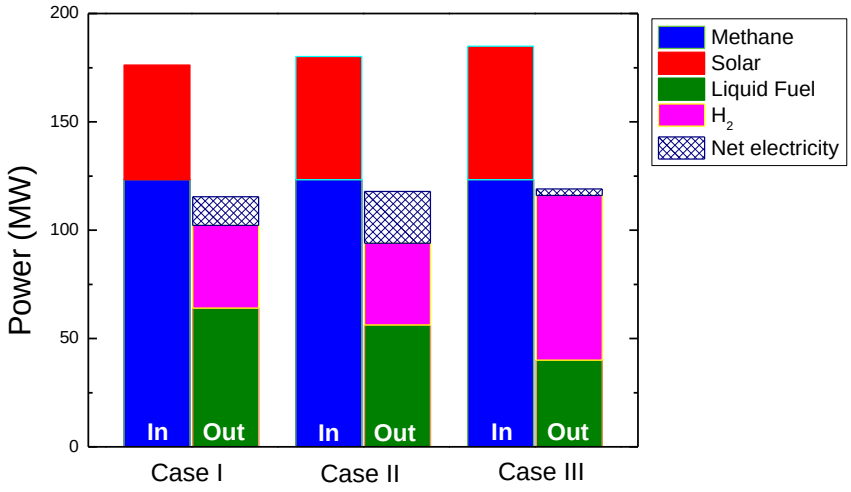

Fig. 4.5. Energy balances of the hybrid solar-redox processes based on Aspen Plus simulation. (In: energy input into the process; Out: energy output of the process.)

Table 4.6. Comparison of the process efficiency and life-cycle carbon emission

Process	A	B	C	D
Methane to fuel conversion efficiency	96.6%	70.2%	62.4%	NA
CO_2 footprint kg CO_2/mmBtu	63.9	85.5	95.0	91.7

A: Hybrid solar-redox process (Case III)

B: Methane-reforming for hydrogen generation[56,59]

C: Methane-reforming for liquid fuel generation (GTL)[57]

D: Methane-reforming for hydrogen and liquid fuel cogeneration

4.6 Conclusions

The current study investigates a hybrid solar-redox process for liquid fuels and hydrogen cogeneration from methane and solar energy with a mixed ionic-electronic conductor enhanced $Fe_3O_4/FeO_{1-\delta}$ redox couple. Methane is used in the reduction step to enhance iron oxide decomposition/reduction reactions at temperatures significantly lower than those in conventional solar-thermal water-splitting processes. Key findings from the current study are shown below.

The redox performance of a Fe_3O_4-LSF based oxygen carrier is tested in a lab-scale tubular reactor under both fixed and fluidized-bed modes. Repeatable experimental results are obtained over multiple redox cycles for syngas partial oxidation and water-splitting.

At 900 °C, 95% average methane conversion is achieved in the fixed-bed. Syngas with 2:1 H_2 and CO molar ratio, which is ideal for F-T synthesis, can be generated. Hydrogen with overall purity in excess of 97% is generated in the subsequent water-splitting step. The water-splitting step also exhibits high steam to hydrogen conversion. The MIEC enhanced oxygen carrier is 10 – 20 times more effective than those in conventional water-splitting processes, which are carried out at significantly higher temperatures.

Process simulations indicate that high energy conversion efficiencies can be achieved for the solar-redox process under both idealized and kinetically limited scenarios. Under a conservative set of assumptions, the overall process efficiency is estimated to be 64.2 HHV% when considering both methane and solar energy inputs. The methane to fuel efficiency is 96.6 HHV%.

These experimental and simulation studies confirm the feasibility of the proposed hybrid solar-redox scheme. Compared to conventional solar-thermal water-splitting processes, the proposed solar-redox scheme can be carried out at temperatures lower than 1,000 °C with significantly improved kinetics. The reduced operating temperature and simplified energy conversion

scheme can result in significantly higher efficiency and lowered carbon footprint when compared to conventional processes.

Acknowledgements

This work is supported by the U.S. National Science Foundation under Award (CBET-1254351), the DOD DURIP Project under Award (61607-CH-RIP), and North Carolina State University Start-Up Funds. We would like to acknowledge Evan Scott and Kit Yeung in their assistance to set-up the experimental apparatus.

REFERENCES

1. H. F. Abbas and W. M. A. Wan Daud, *Int. J. Hydrog. Energy*, 2010, **35**, 1160–1190.
2. T. Nakamura, *Sol. Energy*, 1977, **19**, 467–475.
3. F. Sibieude, M. Ducarroir, A. Tofighi, and J. Ambriz, *Int. J. Hydrog. Energy*, 1982, **7**, 79–88.
4. C. Perkins and A. W. Weimer, *AIChE Journal*, 2009, **55**, 286–293.
5. P. Charvin, S. Abanades, G. Flamant, and F. Lemort, *Energy*, 2007, **32**, 1124–1133.
6. A. Steinfeld, S. Sanders, and R. Palumbo, *Sol. Energy*, 1999, **65**, 43–53.
7. P. Charvin, A. Stephane, L. Florent, and F. Gilles, *Energy Conv. Manag.*, 2008, **49**, 1547–1556.
8. A. Steinfeld, *Int. J. Hydrog. Energy*, 2002, **27**, 611–619.
9. C. Perkins and A. W. Weimer, *Int. J. Hydrog. Energy*, 2004, **29**, 1587–1599.
10. K. Wegner, H. C. Ly, R. J. Weiss, S. E. Pratsinis, and A. Steinfeld, *Int. J. Hydrog. Energy*, 2006, **31**, 55–61.
11. A. Weidenkaff, A. W. Reller, A. Wokaun, and A. Steinfeld, *Thermochim. Acta*, 2000, **359**, 69–75.
12. N. Z. Muradov and T. N. Veziroğlu, *Int. J. Hydrog. Energy*, 2008, **33**, 6804–6839.
13. R. Palumbo, J. Léde, O. Boutin, E. Elorza Ricart, A. Steinfeld, S. Möller, A. Weidenkaff, E. A. Fletcher, and J. Bielicki, *Chem. Eng. Sci.*, 1998, **53**, 2503–2517.
14. J. K. Dahl, A. W. Weimer, A. Lewandowski, C. Bingham, F. Bruetsch, and A. Steinfeld, *Ind. Eng. Chem. Res.*, 2004, **43**, 5489–5495.
15. A. Steinfeld and E. A. Fletcher, *Energy*, 1991, **16**, 1011–1019.
16. Y. Tamaura, A. Steinfeld, P. Kuhn, and K. Ehrensberger, *Energy*, 1995, **20**, 325–330.
17. T. Kodama, N. Gokon, and R. Yamamoto, *Sol. Energy*, 2008, **82**, 73–79.

18. J. R. Scheffe, J. Li, and A. W. Weimer, *Int. J. Hydrog. Energy*, 2010, **35**, 3333–3340.

19. M. Roeb, M. Neises, N. Monnerie, F. Call, H. Simon, C. Sattler, M. Schmücker, and R. Pitz-Paal, *Materials*, 2012, **5**, 2015–2054.

20. C. L. Muhich, B. W. Evanko, K. C. Weston, P. Lichty, X. Liang, J. Martinek, C. B. Musgrave, and A. W. Weimer, *Science*, 2013, **341**, 540–542.

21. P. Setvens, "The 'Shale Gas Revolution': Developments and Changes", 2012. http://www.chathamhouse.org/sites/default/files/public/Research/Energy,%20Environment%20and%20Development/bp0812_stevens.pdf.

22. A. Steinfeld, *Energy*, 1997, **22**, 311–316.

23. A. Steinfeld, A. Frei, and P. Kuhn, *Metall. Mater. Trans. B*, 1995, **26**, 509–515.

24. Y. Katayama and Y. Tamaura, *Energy*, 2005, **30**, 2179–2185.

25. A. Steinfeld, P. Kuhn, and J. Karni, *Energy*, 1993, **18**, 239–249.

26. A. Steinfeld and G. Thompson, *Energy*, 1994, **19**, 1077–1081.

27. T. Kodama, T. Shimizu, T. Satoh, M. Nakata, and K. I. Shimizu, *Sol. Energy*, 2002, **73**, 363–374.

28. S. Takenaka, V. T. Dinh Son, and K. Otsuka, *Energy Fuels*, 2004, **18**, 820–829.

29. S. Takenaka, N. Hanaizumi, V. T. D. Son, and K. Otsuka, *J. Catal.*, 2004, **228**, 405–416.

30. P. Chiesa, G. Lozza, A. Malandrino, M. Romano, and V. Piccolo, *Int. J. Hydrog. Energy*, 2008, **33**, 2233–2245.

31. K. S. Go, S. R. Son, S. D. Kim, K. S. Kang, and C. S. Park, *Int. J. Hydrog. Energy*, 2009, **34**, 1301–1309.

32. L.-S. Fan and F. Li, *Ind. Eng. Chem. Res.*, 2010, **49**, 10200–10211.

33. J. Kim, C. A. Henao, T. A. Johnson, D. E. Dedrick, J. E. Miller, E. B. Stechel, and C. T. Maravelias, *Energy Environ. Sci.*, 2011, **4**, 3122–3132.

34. J. Kim, T. A. Johnson, J. E. Miller, E. B. Stechel, and C. T. Maravelias, *Energy Environ. Sci.*, 2012, **5**, 8417–8429.

35. F. Li and L.-S. Fan, *Energy & Environ. Sci.*, 2008, **1**, 248.

36. L.-S. Fan, *Chemical Looping Systems for Fossil Energy Conversions*, John Wiley & Sons, 2010.

37. M. Roeb, A. G. Konstandopoulos, A. Steele, P. Stobbe, C. Agrafiotis, C. Sattler, R. Klüser, V. T. Zaspalis, L. Nalbandian, N. Monnerie, and L. de Oliveira, *J. Sol. Energy Eng.*, 2005, **128**, 125–133.

38. T. Kodama, *Prog. Energy Combust.*, 2003, **29**, 567–597.

39. T. Kodama and N. Gokon, *Chem. Rev.*, 2007, **107**, 4048–4077.

40. R. B. Diver, J. E. Miller, M. D. Allendorf, N. P. Siegel, and R. E. Hogan, *J. Sol. Energy Eng.*, 2008, **130**, 041001–041001.

41. N. Gokon, S. Takahashi, H. Yamamoto, and T. Kodama, *Int. J. Hydrog. Energy*, 2008, **33**, 2189–2199.

42. A. Steinfeld, M. Brack, A. Meier, A. Weidenkaff, and D. Wuillemin, *Energy*, 1998, **23**, 803–814.

43. T. Kodama, Y. Nakamuro, and T. Mizuno, *J. Sol. Energy Eng.*, 2004, **128**, 3–7.

44. Support for Cost Analyses on Solar-Driven High Temperature Thermochemical Water-Splitting Cycles. 2011 TIAX LLC.

45. N. L. Galinsky, Y. Huang, A. Shafiefarhood, and F. Li, *ACS Sustainable Chem. Eng.*, 2013, **1**, 364–373.

46. A. Shafiefarhood, N. Galinsky, Y. Huang, Y. Chen, and F. Li, *ChemCatChem*, 2014, **6**, 790-799.

47. Aspen Technology Inc. ASPEN Plus v7.2 user guide. Aspen Technology, Inc. Cambridge, MA. 2006.

48. L. Zeng, F. He, F. Li, and L.-S. Fan, *Energy Fuels*, 2012, **26**, 3680–3690.

49. F. He, N. Galinsky, and F. Li, *Int. J. Hydrog. Energy*, 2013, **38**, 7839–7854.

50. P. J. vanBerge and R. C. Everson, *Natural Gas Conversion IV*, 1997.

51. S. T. Sie, *Rev. Chem. Eng.*, 1998, **14**, 109–157.

52. D. Gray, J. Klara, G. Tomlinson, and C. White, "Chemical-Looping Process in a Coal-to-Liquids Configuration", DOE/NETL-2008/1307. http://www.netl.doe.gov/energy-analyses/pubs/DOE%20Report%20on%20OSU%20Looping%20final.pdf.

53. S. Möller, D. Kaucic, and C. Sattler, *J. Sol. Energy Eng.*, 2005, **128**, 16–23.

54. F. Li, L. Zeng, and L.-S. Fan, *Fuel*, 2010, **89**, 3773–3784.

55. L. Bibber, J. Haslbeck, S. Kramer, and S. Olsen, "Technical and Economic Assessment of Small-Scale Fischer-Tropsch Liquids Facilities", DOE/NETL-2007/1253.

56. J. Ruether, M. Ramezan, and E. Grol, "Life-Cycle Analysis of Greenhouse Gas Emissions for Hydrogen Fuel Production in the United States from LNG and Coal", DOE/NETL-2006/1227.

57. E. Shuster and J. Goellner, "Analysis of Natural Gas-to-Liquid Transportation Fuels via Fischer-Tropsch", DOE/NETL-2013/1597.

58. K. Gerdes, T. Skone, NETL's Capability to Compare Transportation Fuels: GHG Emissions and Energy Security Impacts, DOE/NETL, 2009.

59. W. Feng, P. Ji, and T. Tan, *AIChE Journal*, 2007, **53**, 249–261.

CHAPTER 5 HYDROGEN PRODUCTION FROM METHANE AND SOLAR ENERGY – PROCESS EVALUATIONS AND COMPARISON STUDIES

Feng He and Fanxing Li*

Department of Chemical & Bimolecular Engineering, North Carolina State University, Raleigh, North Carolina 27695, United States

CHAPTER 5 is a reprint of a manuscript published in *International Journal of Hydrogen Energy*, 2014, 39, 18092. The supplementary information is in Appendix C.

* To whom the correspondence should be addressed. Telephone: +1 (919) 515-7328. Fax: +1 (919) 515-3465. E-mail: fli5@ncsu.edu.

Abstract

Three conventional and novel hydrogen and liquid fuel production schemes, i.e. steam methane reforming (SMR), solar SMR, and hybrid solar-redox processes are investigated in the current study. H_2 (and liquid fuel) productivity, energy conversion efficiency, and associated CO_2 emissions are evaluated based on a consistent set of process conditions and assumptions. The conventional SMR is estimated to be 68.7% efficient (HHV) with 90% CO_2 capture. Integration of solar energy with methane in solar SMR and hybrid solar-redox processes is estimated to result in up to 85% reduction in life-cycle CO_2 emission for hydrogen production as well as 99-122% methane to fuel conversion efficiency. Compared to the reforming-based schemes, the hybrid solar-redox process offers flexibility and 6.5 – 8% higher equivalent efficiency for liquid fuel and hydrogen co-production. While a number of operational parameters such as solar absorption efficiency, steam to methane ratio, operating pressure, and steam conversion can affect the process performances, solar energy integrated methane conversion processes have the potential to be efficient and environmentally friendly for hydrogen (and liquid fuel) production.

5.1 Introduction

Hydrogen is an intrinsically clean energy carrier and the enabling factor for the "hydrogen economy" [1]. Besides being combusted for heat generation, hydrogen can be converted into electricity in fuel cells at high efficiencies or used as a building-block chemical for oil refining, Fischer – Tropsch (F-T) synthesis, and ammonia and methanol productions [2]. As a secondary energy source, hydrogen is produced from hydrocarbons and/or water via reforming, electrolysis, or thermolysis [3]. These process schemes tend to be energy and/or capital intensive. In addition, H_2 production from fossil fuels can lead to significant CO_2 emission in absence of energy-intensive carbon capture and sequestration steps. Currently, over 90% of the world's total hydrogen production is derived from methane, a primary component of natural gas, via the well-known steam methane reforming (SMR) process [4,5]. In the foreseeable future, natural gas will continue to be the major feedstock for hydrogen production [6].

A typical SMR process is composed of a series of process steps including pretreatment, reforming, water-gas-shift (WGS), and product purifications. In the pretreatment step, impurities in natural gas such as sulfur compounds are removed to avoid catalyst poisoning. Subsequently, methane reforming is carried out by catalytically reacting methane with steam at high temperatures to produce syngas:

$$CH_4 + H_2O \leftrightarrow CO + 3H_2 \quad (1)$$

$$CO + H_2O \leftrightarrow CO_2 + H_2 \quad (2)$$

The overall reaction is endothermic. Over 75 % methane conversion is typically achieved under temperatures ranging between 800 and 900 °C and pressures up to 35 atm [7].

The product gas from the reformer, a mixture of CO, CO_2, CH_4, H_2, and H_2O, is then introduced into a WGS reactor system. In the WGS system, CO is reacted with H_2O in syngas to produce additional H_2 and CO_2 by the WGS reaction (Reaction 2). The WGS reaction is moderately exothermic. As a result, the equilibrium favors H_2 production at low reaction temperatures [8]. Kinetically, however, a high reaction temperature is desired. To address this challenge, typical

WGS system is comprised of a high temperature shift reactor for high reaction rates and a low temperature shift reactor for high CO conversions. After condensing out steam, the exit gas from the WGS system is predominantly hydrogen and CO_2 (~20%) as well as some residual CO and methane. To produce a high quality hydrogen product, the gas stream is further purified by absorption based acid gas removal (AGR) and pressure swing adsorption (PSA) operations. The purity of final H_2 product is typically 99.9% or higher [7,9].

As a benchmark process for hydrogen production from natural gas, the SMR process generates a significant amount of CO_2 by-product [10–12]. With the growing concerns over global warming, CO_2 capture and storage have been recognized as a necessity for SMR operations [13]. In commercial SMR processes, CO_2 removal is usually achieved by absorption based AGR processes using chemical or physical solvents such as monoethanolamine (MEA), methyldiethanolamine (MDEA), and dimethyl ethers of polyethylene glycol [7,14]. A large amount of steam is required for CO_2 desorption in these absorption based processes, lowering the overall process efficiency [6,14,15]. In addition, around 20-30% methane is typically combusted as a fuel in the reformer furnace to provide the heat for the endothermic reforming step, resulting in additional energy penalty. According to the studies performed by Simpson and Lutz [4], the majority (~30%) of the exergy destruction in the SMR process is attributable to the high irreversibility of combustion and heat transfer between reformer and furnace. Another challenge associated with methane combustion resides in the associated CO_2 emissions. The combustion flue gas contains CO_2 diluted by nitrogen in the air. As a result, CO_2 capture from the combustion exhaust gas, which has a low CO_2 partial pressure, can be particularly energy consuming [13,16]. Feng et al. investigated CO_2 capture on SMR via a number of configurations including burning H_2 instead of CH_4 in the furnace, using pure oxygen instead of air for fuel gas combustion, applying a pre-reformer to reduce the usage of pure oxygen, employing a H_2-membrane in the reformer to separate H_2 [13]. With a base case efficiency of 70% (exergy) in a traditional SMR system, the efficiency drop from these CO_2 capture steps are reported to range from 2% to 13%. To summarize, a hydrogen generation scheme with higher efficiency and lower emission is highly desired.

An alternative approach to reduce CO_2 emissions from methane reforming is to couple SMR with concentrated solar energy [17], since the latter is a clean energy source capable of providing heat directly to the reaction sites [3,18]. Becker and Funken investigated various cases for operating a solar reforming plant [19]. Although they share many similarities, the key differences between the solar SMR and conventional SMR are (i) use of solar heat for endothermic reforming reactor instead of CH_4 combustion; (ii) recycle of the off-gas from the PSA to the reformer. Möller et al. [8] performed techno-economic studies on the solar steam methane reforming process. In their model, natural gas consumption is reduced by up to 40% and H_2 product is 20% more expensive compared to the conventional SMR process. Besides theoretical studies, up to 500 kW large scale demonstrations of solar reforming have also been performed [17,20–22]. CO_2 emission is reduced in the solar SMR process by avoiding CH_4 combustion, which accounts for ~20% total CO_2 emissions from conventional SMR. The challenges of solar SMR reside in reactor design, solar facility cost and stability of the solar source. In addition, the complexity of WGS operations and acid gas removal steps impose energy penalties to the overall energy conversion scheme.

In addition to steam methane reforming, a so called two-step water-splitting or hybrid solar-redox process has been proposed to produce hydrogen with redox reaction of metal oxides. In such a process, methane and steam are introduced as the feedstock in two redox steps [18,23]:

$$M_xO_y + yCH_4 = xM + y(2H_2 + CO) \quad (3)$$

$$xM + yH_2O = M_xO_y + yH_2 \quad (4)$$

In the first step, methane is oxidized by the metal oxides to generate syngas, which can be used for methanol or F-T synthesis. The reduced metal oxides are then reacted with steam in the second step to generate H_2. Compared to SMR, the above mentioned hybrid solar-redox process produces F-T ready syngas and pure H_2 with lower CO_2 emission and simpler product separation steps. Such a scheme may offer a competitive alternative to conventional technologies.

A number of research efforts have been directed towards finding effective metal oxides for the two-step water-splitting process. Among the various options, iron oxide is abundant and relatively cheap [24–26]. However, limited experimental data is available with syngas yield and steam conversions generally limited to 25% and 30%, respectively [26–28]. Besides pure iron oxides, iron based mixed metal oxides such as ZrO_2-supported Ni(II)-ferrite [29], $Cu{-}Cr{-}FeO_x$ [30], Ni-Cr-FeOx [31], ZrO_2-supported Co(II)-ferrites [32], have also been tested. Up to 90% methane conversions have been reported for some of these mixed oxides. However, steam to hydrogen conversions are generally limited to about 25%. Kodama et al. [33] reported WO_3/W redox system to be a potential oxygen carrier for two-step methane reforming. While a relatively high methane conversion of 70% and a CO selectivity of 86% are reported, steam to H_2 conversion is limited to 30%. He et al. [23] reported the redox performance of Fe_3O_4 enhanced with a mixed ionic-electronic conductor (MIEC) support in a hybrid solar-redox process for liquid fuel and hydrogen co-production. Over 95% methane conversion in the methane oxidation step and up to 70% steam conversion in the water-splitting step are observed. Since the overall efficiency of the hybrid solar-redox process is hinged upon the metal oxide performance, the significantly improved methane and steam conversions achieved using the MIEC enhanced Fe_3O_4 may render a process with high efficiency and low CO_2 emissions. Since direct comparisons among the conventional SMR, solar SMR, and hybrid solar-redox process have not been performed, the present study attempts to compare these three process schemes under a consistent set of assumptions.

In the present work, three conventional and novel hydrogen (and liquid fuel) production schemes, i.e. conventional SMR, solar SMR, and hybrid solar-redox process are evaluated. H_2 productivity, process efficiency, and CO_2 emission are analyzed and compared. The advantages and disadvantages of these process schemes are also discussed.

5.2 Process and model descriptions

5.2.1 Conventional SMR

Fig. 5.1A illustrates a simplified flow diagram of a typical SMR process. Methane is used as the feedstock. Preheated and pressurized CH_4 is mixed with steam and introduced to the reformer. The reformer converts CH_4 and steam into syngas with typical compositions shown in Table 5.1 [7]. The syngas product exiting the reformer is cooled and introduced into WGS reactors. A high-temperature WGS reactor with iron catalyst and a low-temperature WGS reactor with copper catalyst are typically arranged in series to achieve over 95% CO conversion [7,9]. The shifted synthesis gas is cooled further for water condensation followed with an MDEA system for CO_2 removal. The MDEA system is 90% efficient for CO_2 removal [6,34]. CO_2 captured from MDEA is compressed to 151 atm for sequestration. A pressure swing adsorption (PSA) system is then used to produce purified H_2 at temperatures around 35–40°C. Through PSA, 90% of the H_2 is recovered as a product with 99.9% purity [7,9,35].

Table 5.1. Typical composition of the synthesis gas leaving the methane reformer [7]

Component	Volume %
CH_4	2
CO	7
CO_2	6
H_2	44
H_2O	41
Total	100

The reforming reactor is highly endothermic. To compensate the heat required, off-gas from the PSA system and additional methane is combusted with air in the reformer furnace. High temperature gases from the combustor as well as the reformer are introduced to the heat

recovery steam generator (HRSG) to produce steam for reforming. In addition, heat from exothermic WGS reactions is recovered to produce low temperature steam (at 4.4 atm and 149 °C) for CO_2 stripping.

5.2.2 Solar SMR

In the case of solar methane reforming, the heat required by methane reforming is directly provided by the solar energy, as shown in Fig. 5.1B. As a result, the off-gas from PSA is recompressed and introduced back to the reformer. This is the key difference between the solar and conventional SMR scheme. The remaining parts of the solar SMR process are similar, if not identical to conventional SMR.

5.2.3 Hybrid solar-redox

The hybrid solar-redox scheme adopts a two-step approach to convert methane into liquid fuel and hydrogen. As shown in Fig. 5.1C, syngas from reducer is used for F-T synthesis. Chain growth probability factor (α) for F-T is assumed to be 0.91 with 85% CO conversion at 22 atm and 249°C [37–40]. H_2 generated from the water-splitting step is cooled, cleaned, and compressed as the final product. To compensate the heat required for the endothermic methane oxidation reaction, solar energy is provided by direct irradiation. The fuel gas containing CH_4, CO and light hydrocarbons is combusted for heat generation. It is noted that many reactor designs for solar-thermal water-splitting can be directly utilized for solar energy integration in the current process. For instance, rotary-type and the volumetric gas-particle solar reactors will be directly applicable for the proposed solar-redox operations [32,41–43]. More detailed description of the process scheme can be found in supplemental file as well as an earlier report [23].

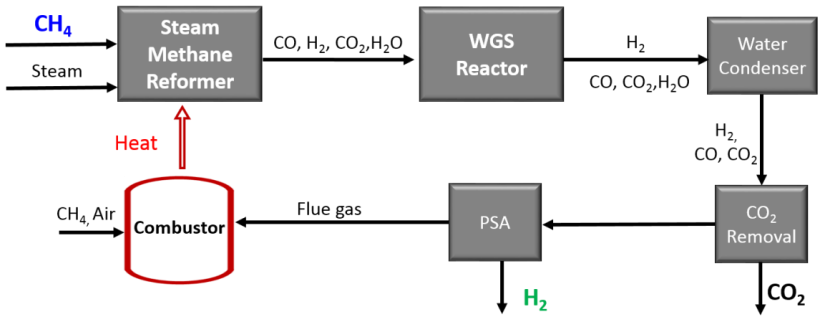

(A)

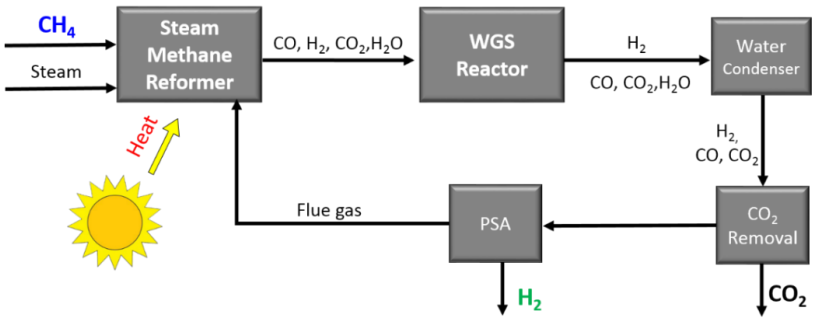

(B)

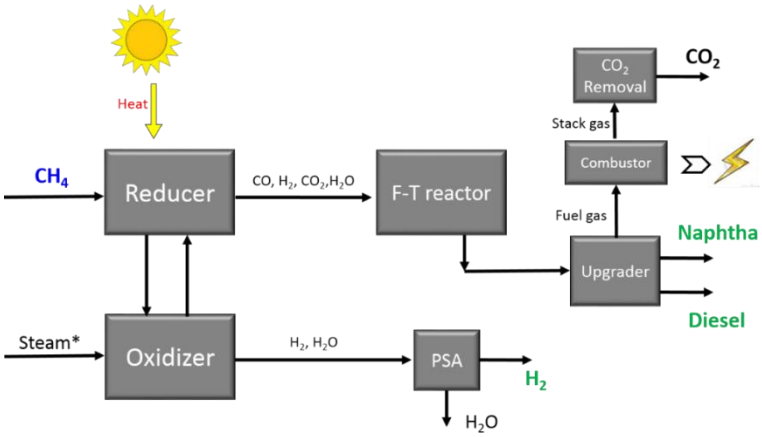

(C)

Fig. 5.1. Simplified schematic of the (A) conventional SMR; (B) solar SMR; (C) hybrid solar-redox process. To operate in the absence of sunlight, steam* (C) can be (partially) replaced with air to achieve auto-thermal operation.

5.2.4 Summary of simulation cases

In order to evaluate the different methane conversion schemes, three benchmark cases are studied in the present work followed with sensitivity analyses. Key operating parameters for these three simulation cases are summarized in Table 5.2. Case I and Case II are conventional and solar SMR process respectively, at a nominal pressure of 30 atm. The performance parameters of the key reactors described in Section 2.1 and 2.2 are applied in the Aspen models. The hybrid solar-redox process (Case III) is also investigated, which is based on the reported experimental results [23]. Key experimental data are summarized in Table 5.3. Syngas yield is defined as $(F_{H_2}+F_{CO})/3F_{CH_4}$, where F represents the molar flow rate.

Table 5.2. Operating conditions for the process simulation cases

	Case I	Case II	Case III
Process scheme	Conventional SMR	Solar SMR	Hybrid solar-redox
CH_4 feedstock	8 ton/h	8 ton/h	8 ton/h
Solar energy input	No	Yes	Yes
Reformer temperature	866 °C	866 °C	900 °C
Nominal reformer pressure	30 atm	30 atm	1 atm
Primary products	H_2	H_2	H_2 and liquid fuel

Table 5.3. Summary of reducer performance from experimental data [23]

Parameters	Unit	Value
Reducer		
Temperature	°C	900
Pressure	atm	1
CH_4 conversion	%	95.3
Syngas gas yield	%	59
H_2/CO molar ratio	mol/mol	1.9
Carbon formation*	mmol/g oxygen carrier	0.18

* Amount of coke formed, i.e. mmol of coke/gram of oxygen carrier, quantified during the experiments.

5.2.5 Simulation parameters and assumptions

ASPEN Plus® simulator [44] is used to evaluate reactor and process performances. CH_4 is used as the fuel and carbon source. A methane processing capacity of 8 ton/h ($123MW_{th}$, HHV) is assumed for all cases in order to match the solar reactor capacity reported in literature [8,21,45]. Table 5.4 specifies the materials involved in the simulations. For the case of hybrid solar-redox process, an oxygen carrier composed of Fe_3O_4 supported by lanthanum strontium ferrite ($La_{0.8}Sr_{0.2}FeO_{3-\delta}$ or LSF) is used. Since LSF is not available in the Aspen Plus® database, an alternative heat carrier, i.e. SiC, is used as the support for simulation purpose. The solar absorption efficiency is defined as the net solar energy absorbed by the reactor divided by solar power from the concentrator, which is given by

$$\eta_{absorption} = \frac{\alpha_S IC - \varepsilon\sigma T^4}{IC} \quad (5)$$

where I is the intensity of solar radiation with a typical value of 1 kW m^{-2}, T is the operating temperature, C is the concentration ratio which ranges from 2000 to 10000. α_S and ε are the effective absorptance and the emittance of the receiver respectively, and σ is the Stefan-Boltzmann constant [21,46]. Based on the equation above, the estimated absorption efficiency is calculated to be 94 – 98% at a reactor operating temperature of 900°C. Considering the energy loss at the reactor wall through radiation, conduction, and convection [47], the solar energy adsorbed by the redox catalyst is estimated to be 80%, which is consistent with previously reported numbers for the solar SMR process [8].

It is noted that such an absorption efficiency is notably higher than typical solar-thermal water-splitting processes considering the significantly lowered operating temperature. The effect of the solar absorption efficiency on the process performance is also discussed in Section 3.2.1.Hydrogen is the primary product from the reforming and hybrid solar-redox processes. The designed product purity is above 99.9%. Besides hydrogen, naphtha and diesel are co-produced in the hybrid solar-redox process. CO_2 is also captured, compressed (15.3 MP), and sequestered in all three processes. Aspen Plus modules, property methods, and physical property databanks are summarized in Table 5.S1. Table 5.S2 lists the key operating

assumptions and parameters used in the process simulations. More detailed information on the model of the hybrid solar-redox process can be find elsewhere [23].

Table 5.4. Specifications of the materials

Feedstock	
Methane	HHV (higher heating value) 55.5 MJ kg^{-1}, LHV (lower heating value) 50.0 MJ kg^{-1}
Concentrated solar energy input	55-90 MW [8,21,45]
Absorption efficiency for solar energy	80%
Air	79% N_2, 21% O_2 by volume
Oxygen carrier	Fe_3O_4, SiC (inert)
Water	H_2O
Output	
H_2 product	Purity: >99.9%, Pressure: 22 atm
Naphtha	C_6-C_{11}
Diesel	C_{12}-C_{18}
CO_2	Purity: >99.9%, Pressure: 151 atm

5.3 Results and discussion

5.3.1 Case study comparisons

Simulation results of the three benchmark cases are summarized in Table 5.5. Fig. 5.2 illustrates the energy generation/consumptions for these cases. Compared to Case I, Cases II and III exhibit higher energy conversion efficiencies after solar energy integration. Further discussions of these three cases are provided in the following sections.

Table 5.5. Process mass and energy balances for Cases I-III

	Case I	Case II	Case III
Material balance (kmol/h)			
CH_4	500	500	500
Supplemental (combustor) CH_4	201	NA	NA
Generated H_2	1561.8	2000.0	965.6
Captured CO_2	630.8	500.0	241.3
Liquid fuel	NA	NA	21.6
Energy in (MW)			
CH_4 (HHV/LHV)	174.1/155.7	123.3/111.1	123.3/111.1
Solar Energy	NA	90.5	58.4
Electricity	4.9	5.2	NA
Energy out (MW)			
Naphtha & Diesel (HHV/LHV)	NA	NA	41.0/39.2
H_2 (HHV/LHV)	123.0/104.1	157.6/133.3	76.1/64.4
Electricity	NA	NA	5.5
Efficiency (HHV)	68.7	71.9	67.5
Efficiency (LHV)	64.2	64.3	64.4

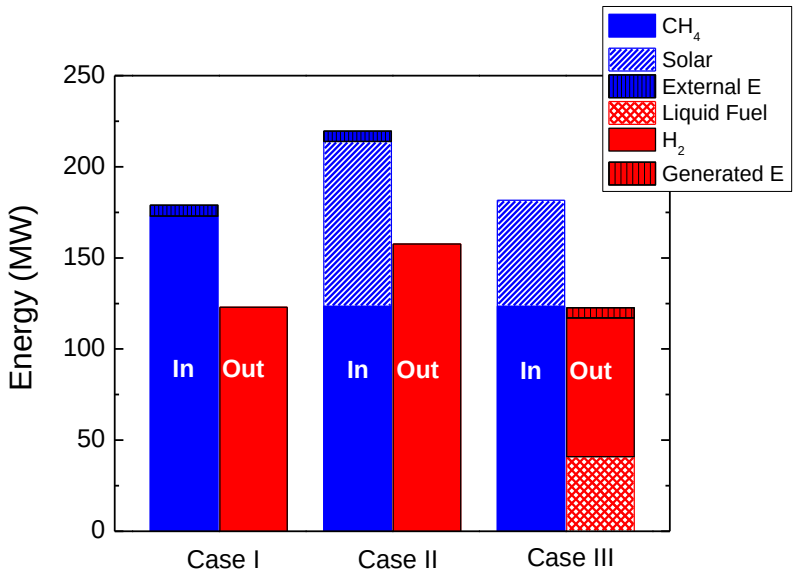

Fig. 5.2. Energy balances (HHV) of the four studied cases based on Aspen plus® simulation.

5.3.1.1 Conventional SMR

Case I mimics the conventional SMR process. The underlying assumptions are similar to those reported by DOE [7,9]. The scheme operates at a nominal pressure of 30 atm. Steam to CH_4 molar ratio for the reformer is 4.1 in order to ensure adequate steam for the WGS reactions. A 87% methane conversion is assumed in the reforming step with CO yield of ~47% and CO_2 yield of ~40%. With 8 ton/h CH_4 as the feedstock into the reformer, 3.5 ton/h H_2 with 99.9 % purity [48] are generated and compressed to 20 atm. In the meantime, 27.8 ton/h CO_2 is captured while 1.2 ton/h CO_2 is emitted to the atmosphere in the stack gas. The CO_2 capture consumes about 38 ton/h steam a 4.4 atm and 149°C. Overall, the efficiency of the conventional SMR process is 68.7 % and 64.2 % under HHV and LHV basis, respectively.

5.3.1.2 Solar SMR

Solar SMR is simulated in Case II. Similar to conventional SMR, the process is comprised of reforming, WGS, CO_2 removal, and H_2 purification steps. Despite the very similar simulation models, the main differences between Case II and Case I include solar energy integration and elimination of the combustor block for the SMR reaction. Resulting from 90.5 MW of solar energy input, the final H_2 product yield is 4 ton/h, which is 28% higher than Case I. Since no supplementary CH_4 is needed, the total methane consumption in Case II is 28.7% less than that in Case I. Overall, 22 ton/h CO_2 is captured from Case II. The overall efficiency of the solar SMR is estimated to be 71.9 % (HHV) and 64.3 (LHV). Compared to Case I, 2.2% increase in HHV efficiency is achieved from solar energy integration. However, only a slight (0.1%) increase in LHV efficiency is observed. This is because solar energy has identical HHV and LHV values whereas LHV of methane is 9% lower than its HHV. The lower HHV efficiency of Case I is largely resulted from the increased energy consumption for CO_2 capture and compression from the combustor flue gas. In addition, the larger amount of high temperature flue gas from Case I leads to energy loss in the form of sensible and unrecoverable latent heat.

5.3.1.3 Hybrid solar-redox process

Case III incorporates the experimental data summarized in Table 5.3. In the reducer, CH_4 conversion is 95.3% and syngas yield is 59 % [23]. 8.5 ton/h CO and 1.1 ton/h H_2 is generated from the reducer. F-T unit and upgrader generates liquid fuel containing 1.44 ton/h naphtha and 1.88 ton/h diesel. As a by-product, 11.7 ton/h CO_2 is captured. After purified by PSA, yield of H_2 product is 1.9 ton/h. With respect to heat integration, 58.4 MW concentrated solar energy is consumed for the endothermic methane-iron oxide reactions. The fuel gas after F-T is sent to the combustor to generate power for parasitic usage. Coupled with process heat recovered by the HRSG, the net electricity generation is 5.5 MW. The overall process efficiency is 67.5% (HHV) and 64.4% (LHV). Compared to Case II, solar energy consumption is reduced by 50% in Case III. One of the reasons is the heat recovered from F-T synthesis. The slightly exothermic steam-iron reaction simplifies the process heat integration. It is also noted that the amount of CO_2 generated in Case III is 47% less than Case II, which results in less steam consumption in the CO_2 capture step. Overall, Case III shows lower HHV efficiency due to the additional energy and exergy loss for the liquid fuel synthesis step. Under an LHV basis, however, hybrid solar-redox process (Case III) shows higher energy conversion efficiency than both conventional and solar SMR processes.

5.3.2 Sensitivity analyses

5.3.2.1 Effect of solar absorption efficiency

Cases II and III utilize concentrated solar energy to compensate the endothermic methane reforming reactions. As can be expected, solar absorption efficiency is of importance for the solar based processes. As shown in Fig. 5.3, process thermal efficiencies for solar SMR and hybrid solar-redox processes monotonically increase with increasing absorption efficiency. Efficiency of the conventional SMR is unaffected by absorption efficiency. A solar absorption efficiency of at least 72% is required in order for the solar SMR to be more efficient (HHV based) than conventional SMR. In addition, solar SMR is more sensitive to solar absorption efficiency than the hybrid solar-redox process since the latter consumes relatively less solar energy per mole of CH_4 converted (partially offset by exothermic F-T reactions and simpler

separation schemes). LHV efficiencies of the two solar processes are largely comparable when solar absorption efficiency is between 75 – 85%.

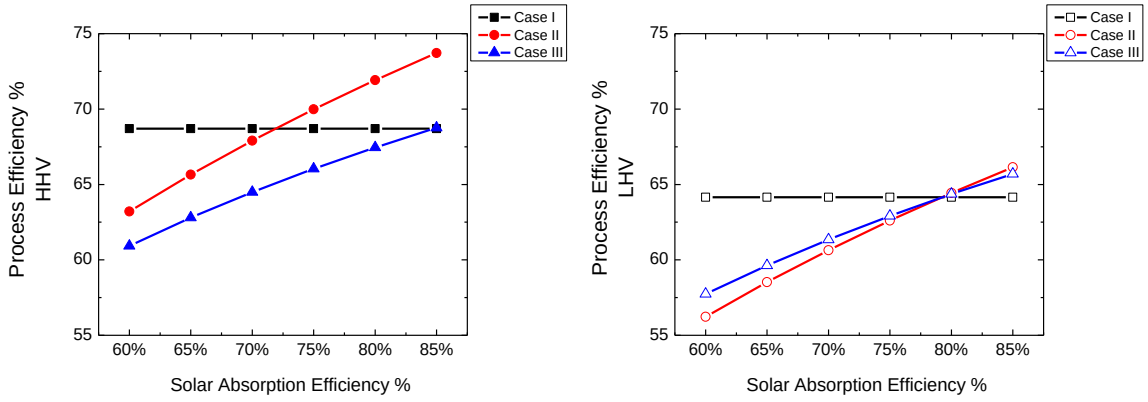

(A) (B)

Fig. 5.3. Effect of solar absorption efficiency on (A) HHV based and (B) LHV based process efficiency

5.3.2.2 Conventional and solar SMR: effect of steam to carbon ratio

The molar flow rate ratio between steam and CH_4 in the reformer inlet stream is defined as steam to carbon (H_2O/C) molar ratio. High H_2O/C ratios are typically used to enhance methane conversion and to reduce coke formation on the reforming catalyst. Sensitivity analysis is conducted to investigate the effect of H_2O/C ratio on the process performance. The reformer and WGS performances are assumed to be unchanged under the relatively narrow range investigated. The results are presented in Fig. 5.4. For conventional SMR, higher H_2O/C ratios lead to increased methane usage since more methane needs to be combusted to generate additional steam. Similarly, higher steam consumption leads to increased solar energy input for solar SMR. When H_2O/C ratio increases from 3.5 to 5, the process thermal efficiency is estimated to decrease by around 3% (HHV) for conventional SMR. And the efficiency of solar SMR process is estimated to decrease by around 4.5% (HHV). Under standard operating

conditions, solar SMR consumes more steam than conventional SMR since PSA flue gas is recycled to the reformer. It results in higher steam amount under same H_2O/C ratio compared to conventional SMR. As a results, when H_2O/C ratio increases, the decrease in efficiency is more significant in solar SMR case.

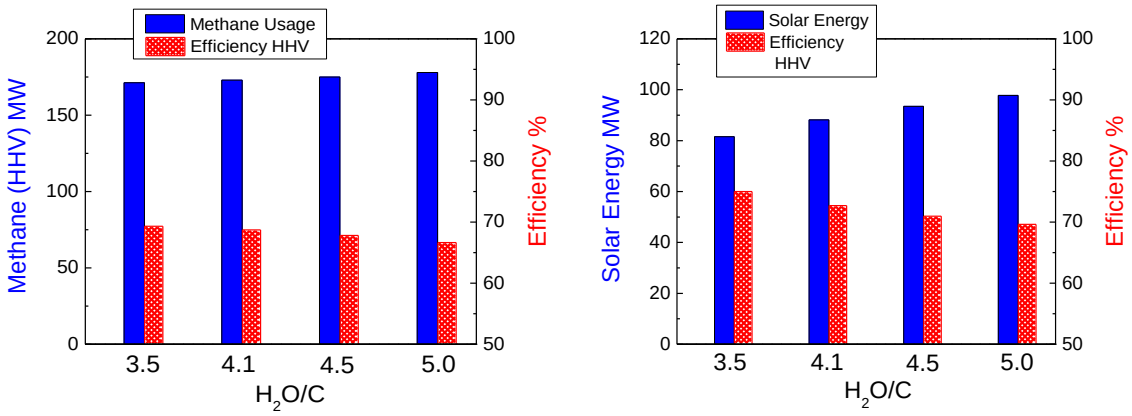

Fig. 5.4. The effect of steam to carbon molar ratio (H_2O/C) on the efficiency of (A) conventional SMR process; (B) solar SMR process

5.3.2.3 Hybrid solar-redox: effect of process pressure

From a thermodynamic standpoint, the reactions between CH_4 and metal oxides in the reducer are favored under low pressures. The effect of pressure on reducer performance is illustrated in Fig. 5.5A. While decrease in methane conversion and syngas yield at high pressures are undesirable, higher pressures offers the potential advantages to save energy on gas compressions. Fig. 5.5B shows the process performance under various process pressure from 1 to 30 atm. Under these simulations, thermodynamic equilibriums are assumed in both reducer and oxidizer, which is slightly different from that in Case III. In addition, the reducer temperature is fixed at 900°C and the oxidizer is at 750 °C. Pressure has no effect on equilibrium steam conversion in the oxidizer [49,50]. As shown in the Fig. 5.5B, hydrogen

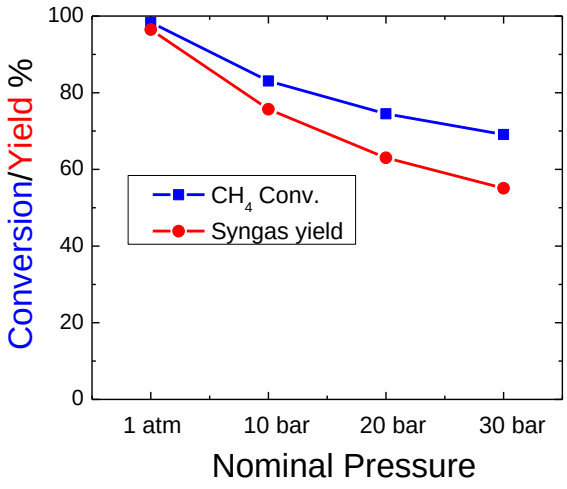

(A)

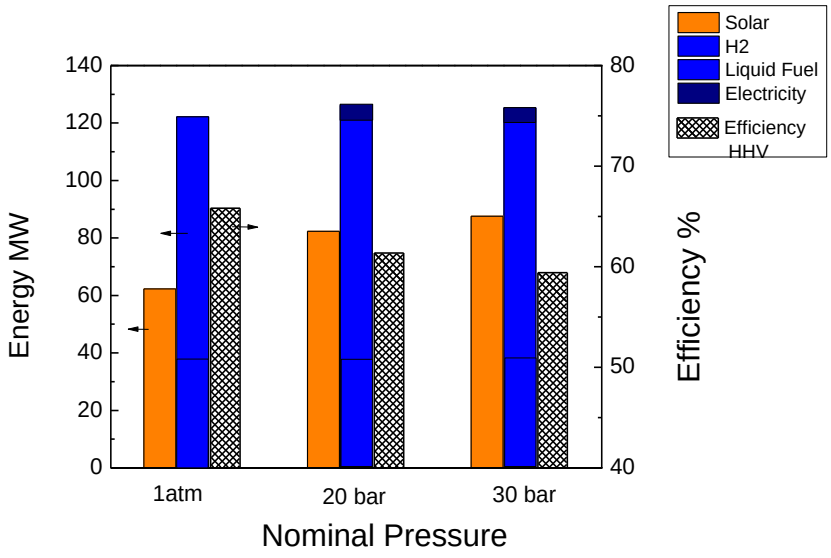

(B)

Fig. 5.5. Effect of the hybrid solar-redox process nominal pressure on the performance of (A) reducer; (B) process performance. Thermodynamic equilibriums are assumed in both reducer and oxidizer.

generation rates and liquid fuel yields are similar under different operational pressures. However, solar energy consumption increases with increasing pressure. The process efficiency (HHV) is projected to drop by about 6% when the system pressure is increased from 1 to 30 atm. The efficiency loss is mainly resulting from reduced CH_4 conversion and syngas yield at elevated pressure, which leads to a large amount of CO, H_2 and CH_4 for recycle. The cooling and reheating of these unconverted gases incur significant penalty for the process and outweighs the benefits in energy savings for compression operations.

5.3.2.4 Hybrid solar-redox: effect of steam to H_2 conversion in the oxidizer

While steam to H_2 conversion in the oxidizer does not impact the production rates of H_2 and liquid fuels from a mass balance standpoint, it significantly affects heat integration of the process. With lower steam to H_2 conversion, more steam is required for the oxidizer. In the meantime, the amount of power generated by the steam turbines may also vary. Taking Case III as the reference case, four conditions with steam to H_2 conversion from 50% to 80% are investigated, where the results are shown in Fig. 5.6. With increasing conversion, the solar energy consumption is decreased slightly since less steam is generated for oxidizer. Meanwhile, the electricity generation increases, which is attributable to the larger amount of heat carried by the steam exiting oxidizer. As a result, when the steam conversion in the oxidizer is increased from 50% to 80%, the process efficiency increases from 64.5% to 69.3%.

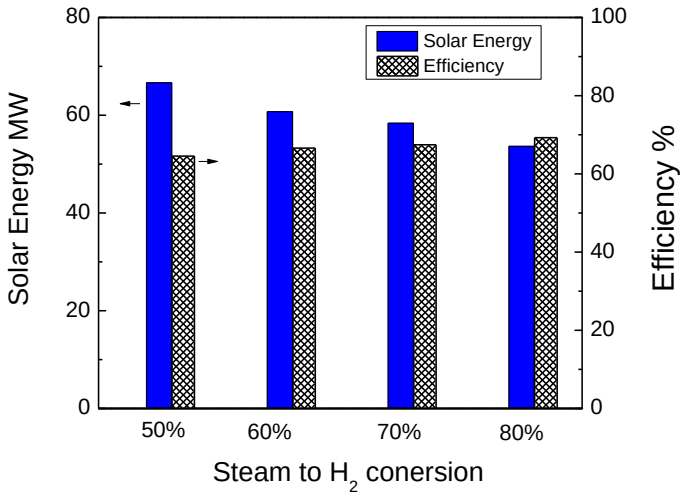

Fig. 5.6. Effect of the steam to H2 conversion in the oxidizer on the process performance

5.3.3 Hybrid solar-redox process: effects of flue gas separation and operating temperatures

5.3.3.1 F-T flue gas separation

As discussed in Section 3.2.3, the process efficiency is lower at elevated pressures due to lowered CH_4 conversion and the needs to increase recycle rates for unconverted fuels. One potential strategy is to separate H_2 from F-T flue gas using PSA. In the meantime, steam can be injected in the reducer to generate more H_2 to achieve 2:1 H_2/CO molar ratio for F-T synthesis. As a result, CH_4 conversion can be enhanced. The results for this alternative process configuration are shown in Table 5.6. Comparing with reference case where the flue gas is completely recycled, more H_2 is generated and less solar energy is required for reducer. As a result, the process thermal efficiency (HHV) is increased from 59.4% to 66.1%, which is comparable with the process operating at atmosphere pressure. The potential limitation of adding PSA is the increased process complexity.

5.3.3.2 Reducer temperature

Another alternative way to improve the process efficiency is to increase the reducer temperature. However, increasing reducer temperature will cause decrease in solar absorption

efficiency. Additional case with reducer operated under 1000 °C and 30 atm is studied. As can be seen in Table 5.6, with increasing reducer temperature, the CH_4 conversion is increased, leading to savings in solar energy consumption. The resulting process thermal efficiency is 68.9% or 2.8% higher than the case discussed in Section 3.3.1.Therefore, slight increase in reducer temperature can potentially improve the process performance.

Table 5.6. Strategy to improve the hybrid solar-redox process efficiency

	Reference Case*	H_2 separation from F-T flue gas – 1	H_2 separation from F-T flue gas – 2
Reducer T	900 °C	900 °C	1000 °C[#]
Solar Energy (MW)	87.5	73.9	67.8
Liquid fuel (MW)	82.1	79.1	79.7
H_2 (MW)	38.3	47.6	47.7
Process Efficiency (HHV)	59.4	66.1	68.9

* Equilibrium case with 30 atm nominal operating pressure as described in Section 3.2.3.

[#] The solar absorption efficiency at 1000 °C is assumed to be identical to that at 900 °C.

5.3.4 Comparisons of the three process schemes

Compared to the conventional and solar SMR processes, the hybrid solar-redox scheme offers an alternative approach to coproduce liquid fuel besides hydrogen. The previous discussion indicates that the solar based processes compare favorably, if not better, than conventional SMR from an energy conversion efficiency viewpoint. It is also noted that the HHV and LHV efficiencies can vary significantly for different processes, due mainly to the difference in product compositions and type of energy input. In order to directly compare the efficiencies of

all three processes, an equivalent efficiency assuming H_2 and liquid fuel co-production evaluated for both conventional and solar SMR. The equivalent efficiency is defined as:

$$\eta_{equ} = \eta_{H_2} R + \eta_{LF}(1-R) \quad (6)$$

In which the efficiency of H_2 production (η_{H2}) is obtained from the SMR Case studies. The liquid fuel production efficiency (η_{LF}) of a conventional gas to liquids (GTL) process is assumed to be 55.5% (HHV) based on literature reports [51]. R is the percent of H_2 product (HHV) to the sum of H_2 and liquid fuel products (HHV). As shown in Table 5.7, the equivalent efficiency of hybrid solar-redox process is 7.7% higher than conventional SMR and 8.6% higher than the solar SMR processes on an HHV basis. Therefore, the hybrid solar-redox process not only offers multiple products, it also has a higher efficiency than a simple combination of SMR and GTL (gas to liquids) processes.

Besides energy conversion efficiency, life cycle CO_2 emission is another important parameter for energy conversion processes. The life-cycle carbon dioxide emission considers emissions from mining, processing, fuel transportation, plant construction, process operation, and product utilization. According to DOE reports [36,52], emissions from the upstream natural gas production activities are about 8.6 g CO_2/MJ. Emissions associated with electric power generation are between 165-173 g CO_2/MJ [51]. Based on such data, the life cycle CO_2 emissions from the three cases are presented in Fig. 5.7A. With solar energy integration, CO_2 emission is reduced in solar based process without CO_2 capture. When CO_2 capture system is installed, the hybrid solar-redox process exhibits the highest overall CO_2 emission since significant amount of carbon in methane is converted into liquid fuel products.

An alternative approach to evaluate the emission data is to consider that the synthetic liquid fuels from the solar-redox process is as carbon intensive as petroleum based fuels. Under such an assumption, life cycle CO_2 emissions from the H_2 product are calculated by subtracting the emission quota from liquid fuel products. Since the life cycle CO_2 emissions for petroleum-derived gasoline and diesel are approximately 90 g CO_2/ MJ [53], the life cycle CO_2 emissions associated with H_2 products are estimated to be 2.8 g CO_2/MJ with CO_2 capture. This corresponds to roughly 15% of the CO_2 emission of H_2 produced from conventional SMR or

20% of solar SMR. To summarize, the hybrid solar-redox process has the potential to reach high energy conversion efficiency and reduced carbon footprint for H_2 production when compared to traditional and solar SMR processes. The challenges for the hybrid solar-redox process reside in the activity of the redox catalyst as well as the requirements for cyclic redox operations.

Table 5.7. Equivalent efficiency for H_2 and liquid fuel coproduction

	SMR (Case I)	Solar SMR (Case II)	Hybrid solar-redox (Case III)
Nominal efficiency (HHV)	68.7%	71.9%	67.5%
Nominal efficiency (LHV)	64.2%	64.3%	64.4%
Equivalent efficiency (HHV)	59.8%	60.9%	67.5%

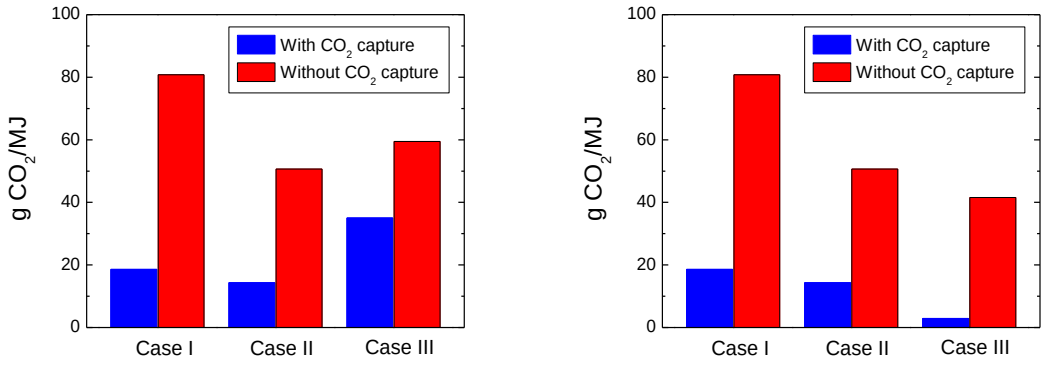

Fig. 5.7. Life-cycle CO_2 emission for (A) all the products, (B) H_2 product

Case I: conventional SMR; Case II: solar SMR; Case III: hybrid solar-redox.

5.4 Conclusion

Three methane to H_2 schemes, i.e. conventional steam methane reforming, solar steam methane reforming, and hybrid solar-redox processes, are evaluated using a consistent set of assumptions. Integration of solar energy with methane conversion is found to result in higher HHV efficiencies when compared to conventional SMR processes. Sensitivity analyses indicate that lower solar absorption efficiency adversely affect the efficiency of the two solar-based processes whereas efficiencies of SMR based processes can be affected by steam to methane ratio. The hybrid solar-redox process generally favors low operating pressure, under which CH_4 conversion and syngas yield in the reducer are high. Steam conversion in the oxidizer also plays an important role for the overall efficiency of the hybrid solar-redox process.

Compared to conventional and solar SMR processes, the hybrid solar-redox process offers an efficient yet flexible alternative to convert methane and solar energy into a combination of hydrogen and liquid fuels at high efficiency. Under a conservative set of assumptions using experimental data, the overall process efficiency is estimated to be 67.5 HHV% and 64.4 LHV% when considering both methane and solar energy inputs. The methane to fuel efficiency from the hybrid solar-redox process is estimated to be 99.4% on an HHV basis. As a novel process that co-produces liquid fuels and H_2, the hybrid solar-redox process is estimated to be 7.7% (HHV) more efficient than SMR based co-production processes. The efficiency increase is resulted from solar energy input and improved energy integration scheme. In addition, life cycle CO_2 emission associated with H_2 product for the solar-redox process is 85% lower than conventional approaches.

To summarize, use of solar energy to assist methane conversion represents a promising method that can potentially enhance the efficiency for methane conversion while reducing CO_2 emissions. Compared to the SMR based process schemes, the hybrid solar-redox process offers the flexibility to co-produce H_2 and liquid fuel with high efficiency. While the integration of solar energy can be capital intensive, the potential to improve process efficiency and reduce

CO_2 emission justifies continued research and development efforts for these advanced methane conversion schemes.

Acknowledgements

This work is supported by the U.S. National Science Foundation under Award (CBET-1254351), the DOD DURIP Project under Award (61607-CH-RIP), and North Carolina State University Start-Up Funds. We would like to acknowledge Evan Scott and Kit Yeung in their assistance to set-up the experimental apparatus.

REFERENCES

[1] Pregger T, Graf D, Krewitt W, Sattler C, Roeb M, Moeller S. Prospects of solar thermal hydrogen production processes. Int J Hydrogen Energy 2009;34:4256–67.

[2] Holladay JD, Hu J, King DL, Wang Y. An overview of hydrogen production technologies. Catalysis Today 2009;139:244–60.

[3] Muradov NZ, Veziroğlu TN. "Green" path from fossil-based to hydrogen economy: An overview of carbon-neutral technologies. Int J Hydrogen Energy 2008;33:6804–39.

[4] Simpson AP, Lutz AE. Exergy analysis of hydrogen production via steam methane reforming. Int J Hydrogen Energy 2007;32:4811–20.

[5] T-Raissi A, Block DL. Hydrogen: automotive fuel of the future. IEEE Power and Energy Magazine 2004;2:40–5.

[6] Skone T. Power Generation Technology Comparison from a Life Cycle Perspective. U.S. DOE/NETL 2013.

[7] Chou V, Kuehn N. Assessment of Hydrogen Production with CO_2 Capture, Volume 1: Baseline State of the Art Plants. U.S. DOE/NETL 2010.

[8] Möller S, Kaucic D, Sattler C. Hydrogen Production by Solar Reforming of Natural Gas: A Comparison Study of Two Possible Process Configurations. J Sol Energy Eng 2005;128:16–23.

[9] Molburg J, Doctor R. Hydrogen from Steam-Methane Reforming with CO_2 Capture. U.S. DOE/NETL 2003.

[10] Lutz AE, Bradshaw RW, Keller JO, Witmer DE. Thermodynamic analysis of hydrogen production by steam reforming. Int J Hydrogen Energy 2003;28:159–67.

[11] Lambert J, Sorin M, Paris J. Analysis of oxygen-enriched combustion for steam methane reforming (SMR). Energy 1997;22:817–25.

[12] Bargigli S, Raugei M, Ulgiati S. Comparison of thermodynamic and environmental indexes of natural gas, syngas and hydrogen production processes. Energy 2004;29:2145–59.

[13] Feng W, Ji P, Tan T. Efficiency penalty analysis for pure H_2 production processes with CO_2 capture. AIChE J 2007;53:249–61.

[14] Kuehn N, Woods. Current and Future Technologies for Natural Gas Combined Cycle Power Plants. U.S. DOE/NETL 2013.

[15] Improvement in Power Generation with Post-Combustion Capture of CO_2 2004. http://ccs101.ca/assets/Documents/iea-improvement-in-powe

[16] Dijkstra J., Jansen D. Novel concepts for CO_2 capture. Energy 2004;29:1249–57.

[17] Böhmer M, Langnickel U, Sanchez M. Solar steam reforming of methane. Solar Energy Materials 1991;24:441–8.

[18] Steinfeld A. High-temperature solar thermochemistry for CO_2 mitigation in the extractive metallurgical industry. Energy 1997;22:311–6.

[19] Becker M, Funken K-H. Solar Thermal Energy Utilization. Springer London, Limited; 1991.

[20] Muir JF, Hogan Jr. RE, Skocypec RD, Buck R. Solar reforming of methane in a direct absorption catalytic reactor on a parabolic dish: I—Test and analysis. Sol Energy 1994;52:467–77.

[21] Kodama T. High-temperature solar chemistry for converting solar heat to chemical fuels. Prog Energy Combust 2003;29:567–97.

[22] Solar Thermal Collector Manufacturing Activities. U.S. Energy Information Administration 2010. http://www.eia.gov/renewable/annual/solar_thermal/

[23] He F, Trainham J, Parsons G, Newman J, Li F. Investigation of a hybrid solar-redox scheme for liquid fuel and hydrogen coproduction. Energy Environ Sci 2013 DOI: 10.1039/C4EE00038B.

[24] Steinfeld A, Kuhn P, Karni J. High-temperature solar thermochemistry: Production of iron and synthesis gas by Fe_3O_4-reduction with methane. Energy 1993;18:239–49.

[25] Steinfeld A, Thompson G. Solar combined thermochemical processes for CO_2 mitigation in the iron, cement, and syngas industries. Energy 1994;19:1077–81.

[26] Steinfeld A, Frei A, Kuhn P. Thermoanalysis of the combined Fe_3O_4-reduction and CH_4-reforming processes. Metall Mater Trans B 1995;26:509–15.

[27] Rydén M, Lyngfelt A. Using steam reforming to produce hydrogen with carbon dioxide capture by chemical-looping combustion. Int J Hydrogen Energy 2006;31:1271–83.

[28] Go KS, Son SR, Kim SD, Kang KS, Park CS. Hydrogen production from two-step steam methane reforming in a fluidized bed reactor. Int J Hydrogen Energy 2009;34:1301–9.

[29] Kodama T, Shimizu T, Satoh T, Nakata M, Shimizu KI. Stepwise production of CO-RICH syngas and hydrogen via solar methane reforming by using a Ni(II)-ferrite redox system. Sol Energy 2002;73:363–74.

[30] Takenaka S, Dinh Son VT, Otsuka K. Storage and Supply of Pure Hydrogen from Methane Mediated by Modified Iron Oxides. Energy Fuels 2004;18:820–9.

[31] Takenaka S, Hanaizumi N, Son VTD, Otsuka K. Production of pure hydrogen from methane mediated by the redox of Ni- and Cr-added iron oxides. J Catal 2004;228:405–16.

[32] Dahl JK, Weimer AW, Lewandowski A, Bingham C, Bruetsch F, Steinfeld A. Dry reforming of methane using a solar-thermal aerosol flow reactor. Ind Eng Chem Res 2004;43:5489–95.

[33] Kodama T, Ohtake H, Matsumoto S, Aoki A, Shimizu T, Kitayama Y. Thermochemical methane reforming using a reactive WO_3/W redox system. Energy 2000;25:411–25.

[34] Cost and Performance Baseline for Fossil Energy Power Plants, Volume 1: Bituminous Coal and Natural Gas to Electricity. U.S. DOE/NETL 2010.

[35] Gray D, White C, Salerno S, Plunkett J, Tomlinson G. Production of High Purity Hydrogen from Domestic Coal: Assessing the Techno-Economic Impact of Emerging Technologies. U.S. DOE/NETL 2010.

[36] Shuster E, Goellner J. Analysis of Natural Gas-to Liquid Transportation Fuels via Fischer-Tropsch. U.S. DOE/NETL 2013.

[37] *Reedijk* J, *Poeppelmeier* K. Comprehensive Inorganic Chemistry II: from elements to applications. Newnes; 2013.

[38] vanBerge PJ, Everson RC. Cobalt as an alternative Fischer-Tropsch catalyst to iron for the production of middle distillates. Natural Gas Conversion Iv, vol. 107, 1997, p. 207–12.

[39] Sie ST. Process development and scale up: IV. Case history of the development of a Fischer-Tropsch synthesis process. Rev Chem Eng 1998;14:109–57.

[40] Gray D, Klara J, Tomlinson G, White C. Chemical-Looping Process in a Coal-to-Liquids Configuration. U.S. DOE/NETL 2008.

[41] Gokon N, Takahashi S, Yamamoto H, Kodama T. Thermochemical two-step water-splitting reactor with internally circulating fluidized bed for thermal reduction of ferrite particles. Int J Hydrogen Energy 2008;33:2189–99.

[42] Steinfeld A, Brack M, Meier A, Weidenkaff A, Wuillemin D. A solar chemical reactor for co-production of zinc and synthesis gas. Energy 1998;23:803–14.

[43] Diver RB, Miller JE, Allendorf MD, Siegel NP, Hogan RE. Solar Thermochemical Water-Splitting Ferrite-Cycle Heat Engines. J Sol Energy Eng 2008;130:041001–041001.

[44] Aspen Technology Inc. ASPEN Plus v7.2 user guide. Aspen Technology, Inc. Cambridge, MA. 2006.

[45] Steinfeld A. Solar hydrogen production via a two-step water-splitting thermochemical cycle based on Zn/ZnO redox reactions. Int J Hydrogen Energy 2002;27:611–9.

[46] Steinfeld A. Solar thermochemical production of hydrogen—a review. Solar Energy 2005;78:603–15.

[47] Charvin P, Stephane A, Florent L, Gilles F. Analysis of solar chemical processes for hydrogen production from water splitting thermochemical cycles. Energy Conv Manag 2008;49:1547–56.

[48] Matuszewski M, Woods M. QGESS: Process Modeling Design Parameters. U.S. DOE/NETL 2012.

[49] Li F, Zeng L, Fan L-S. Biomass direct chemical looping process: Process simulation. Fuel 2010;89:3773–84.

[50] Zeng L, He F, Li F, Fan L-S. Coal-Direct Chemical Looping Gasification for Hydrogen Production: Reactor Modeling and Process Simulation. Energy Fuels 2012;26:3680–90.

[51] Jaramillo P, Griffin WM, Matthews HS. Comparative Analysis of the Production Costs and Life-Cycle GHG Emissions of FT Liquid Fuels from Coal and Natural Gas. Environ Sci Technol 2008;42:7559–65.

[52] Ruether J, Ramezan M, Grol E. Life-Cycle Analysis of Greenhouse Gas Emissions for Hydrogen Fuel Production in the United States from LNG and Coal. U.S. DOE/NETL 2006.

[53] Gerdes K. NETL's Capability to Compare Transportation Fuels: GHG Emissions and Energy Security Impacts. U.S. DOE/NETL 2009.

CHAPTER 6 PEROVSKITE PROMOTED IRON OXIDE FOR HYBRID WATER-SPLITTING AND SYNGAS GENERATION WITH EXCEPTIONAL CONVERSION

Feng He and Fanxing Li*

Department of Chemical and Biomolecular Engineering, North Carolina State University
911 Partners Way, Raleigh, NC 27695-7905, USA.
*Email: Fli5@ncsu.edu

CHAPTER 6 is a reprint of a manuscript published in *Energy & Environmental Science*, 2015, 8:535-539. The supplementary information is in Appendix D.

Graphic abstract:

Under a cyclic redox mode, a perovskite promoted iron oxide exhibited 77% steam-to-hydrogen conversion in a layered reverse-flow reactor.

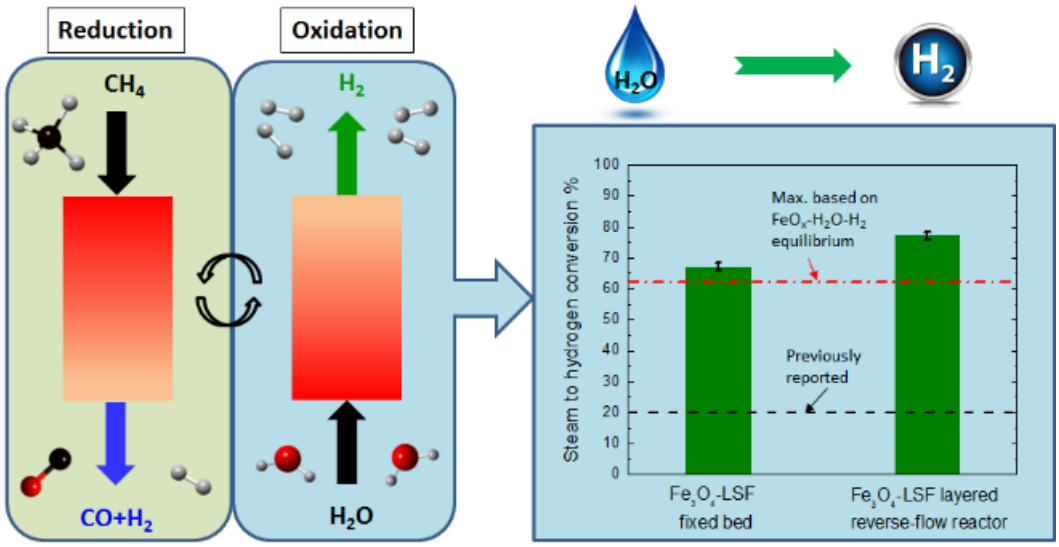

Abstract

We report a perovskite promoted iron oxide as a highly effective redox catalyst in a hybrid solar-redox scheme for methane partial oxidation and water-splitting. In contrast to previously reported ferrite materials, which typically exhibit 20% or lower steam to hydrogen conversion, $La_{0.8}Sr_{0.2}FeO_{3-\delta}$ (LSF) promoted Fe_3O_4 is capable of converting more than 67% steam with high redox stability. Both experiments and a defect model indicate that the synergistic effect of reduced LSF and metallic iron phases is attributable to the exceptional steam conversion. To further enhance such a synergistic effect, a layered reverse-flow reactor concept is proposed. Using this concept, over 77% steam to hydrogen conversion is achieved at 930 °C, which is 15% higher than the maximum conversion predicted by second law for unpromoted iron (oxides). When applied to the hybrid solar-redox scheme for liquid fuels and hydrogen co-generation, significant improvements in energy conversion efficiency can be achieved with reduced CO_2 emissions.

Besides being an important feedstock for petroleum and chemical industry, hydrogen is identified as an attractive, zero-emission fuel due to its high (weight-based) energy density.[1] At present, over 90% hydrogen is produced from fossil fuels, leading to notable greenhouse gas emissions from a life cycle standpoint. Unlike conventional reforming or gasification based approaches, water-splitting has the potential for hydrogen production with minimal environmental impacts. Extensive research has been conducted on H_2 generation using renewable resources.[2,3] Compared to photocatalytic water-splitting, thermochemical routes offer the potential to transform thermal energy to H_2 in a relatively simple yet effective manner. As an alternative to direct water thermolysis, which proceeds at extremely high temperatures (>3000 °C), two-step solar thermochemical water-splitting based on metal oxide reduction and oxidation (redox) cycles has emerged as a highly attractive approach.[4] Although a number of promising redox materials and schemes have been developed[4,5], the metal oxide reduction step in typical solar thermochemical water-splitting processes requires relatively high temperatures (> 1200 °C). In addition, steam conversion in the water-splitting step is often limited. An alternative redox-based approach for water-splitting is the steam–iron process.[5] In such a process, lattice oxygen in iron oxides is first removed by syngas, producing wüstite and/or metallic iron. The reduced ferrites are then used for water-splitting and hydrogen generation. A number of (supported) iron oxides[6], including Fe_3O_4-CeO_2-ZrO_2[7], Fe_3O_4-Al_2O_3[8,9], Fe_3O_4-$MgAl_2O_4$[10] and Fe_3O_4-$Ce_{0.5}Zr_{0.5}O_2$[11], have been investigated for steam-iron applications. The reported steam to hydrogen conversion is generally less than 20%. This, coupled with incomplete syngas conversion during the iron oxide reduction step, limits the process efficiency. We reported a hybrid solar-redox scheme for liquid fuel and hydrogen co-production from methane and solar energy.[12] Using a perovskite-supported iron oxide, high process efficiency and near zero CO_2 emissions for hydrogen generation are shown to be feasible. A key factor for the significantly improved efficiency resides in the high steam to hydrogen conversion for water-splitting.

Low steam conversion in the water-splitting step will exert inevitable energy penalty on the process, since the second law dictates that latent heat in the steam-H_2 product mixture cannot

be fully recuperated. A second law analysis (see ESI) indicates >3 kJ of exergy loss for every additional mole of unconverted steam. In practice, steam to hydrogen conversion for metallic iron and iron oxides is thermodynamically limited. For instance, at 930 °C, a maximum steam to hydrogen conversion of 62.3% is calculated by thermodynamic equilibrium of the FeO_x-H_2O-H_2 ternary system (see ESI). Many of the iron containing redox materials exhibit even lower affinity to oxygen, leading to lower equilibrium constants for the water-splitting reaction (Reaction 1). The present article reports a highly effective, ferrite-based redox material for combined methane partial oxidation and water-splitting. Using perovskite-promoted iron oxide coupled with a layered reverse-flow reactor concept, over 77% steam to hydrogen conversion is achieved at 930 °C. The exceptional conversion, which is 15% higher than the maximum conversion predicted by the second law for iron (oxides), is achieved through synergistic effects between iron oxide and its perovskite support as well as a novel, layered reverse-flow reactor concept.

$MeO_{x-1} + H_2O \leftrightarrow MeO_x + H_2$ Reaction 1

To validate their high efficacy for water-splitting, iron oxides with 25% and 40% $La_{0.8}Sr_{0.2}FeO_{3-\delta}$ (LSF) support are prepared and tested in a fixed-bed reactor. The primary role of LSF support is to provide ionic and electronic conduction pathways for effective removal and replenishment of active lattice oxygen in iron oxides. Such an effect has been confirmed through our recent studies.[12-15] A reduced iron phase is first created by contacting the redox material with hydrogen or CO. H_2 is used as reducing gas to rule out coke formation and its subsequent contribution towards H_2 generation through steam-carbon reaction. When re-oxidized, steam to H_2 conversion of these perovskite-supported redox materials (64±0.7% and 67±1.3%) as shown in Fig. 6.1 are consistently higher than those predicted by the FeO_x-H_2O-H_2 equilibrium (62.3%) at 930 °C. Excellent stability is also achieved over multiple redox cycles (see ESI). Similar steam conversions are observed for redox materials reduced with CO. The exceptional steam conversion with LSF-supported iron oxide, which is higher than the nominal thermodynamic limit of 62.3%, is certainly not unphysical. Rather, it can be explained by the high oxygen affinity of LSF precursors as well as the oxygen vacancies in reduced LSF.

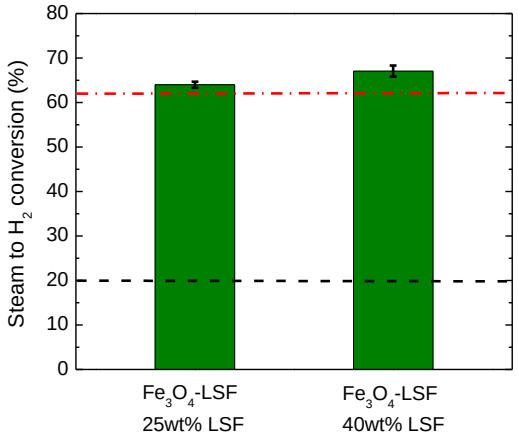

Fig. 6.1. Average steam conversion (%) of Fe_3O_4-LSF in the oxidation step at 930 °C (regenerated to an average composition of $FeO_{0.5}$). Error bars indicate 95% confidence interval for steam conversion form multi-cycle experiments (see ESI). Red dash-dotted line shows the maximum steam conversion for FeO_x-H_2O-H_2 ternary system based on thermodynamic equilibrium. Black dashed line shows the highest literature-reported steam conversion. [6-11]

In order to reveal the contribution of LSF to the overall water-splitting reaction, steam oxidation of reduced LSF-Fe_2O_3 is conducted in a thermal gravimetric analyzer (TGA). A H_2-steam mixture with decreasing H_2 concentrations is introduced into the TGA, and the sample weight change is recorded. Weight gain of the sample under a specific H_2 concentration, defined as $F_{H2}\ (F_{H2}+F_{H2O})^{-1}$, indicates that the sample is capable of achieving the corresponding or higher steam to H_2 conversion. In Fig. 6.2A, four regions are found under varying H_2 concentrations. The corresponding phases are analyzed by X-ray powder diffraction (XRD) (Fig. 6.2B). The reduced redox material is primarily composed of a composite of Fe, La_2O_3, and a very small amount of $LaSrFeO_{4-\delta}$. These reduced metallic iron and oxide species are stable under 100% H_2 (Region I). However, they are easily oxidizable even in the presence 95% H_2 balanced steam ($P_{O2}=5\times10^{-19}$ atm at 930 °C). Such a high affinity to oxygen is not observed in a pure Fe-O system, as iron is only oxidized to wüstite at P_{O2} = 6×10^{-17} atm or higher (equivalent to 62.3% steam conversion). The main driving force for the

exceptional steam conversion, as evidenced by XRD spectra of the partially oxidized sample in Region II, is the solid state reaction among iron, La_2O_3, and SrO in the presence of water as well as water-splitting reaction of defected LSF. Such reactions can be generalized as:

$$La_{0.8}Sr_{0.2}FeO_{3-\delta'} + (\delta' - \delta)\, H_2O \leftrightarrow La_{0.8}Sr_{0.2}FeO_{3-\delta} + (\delta' - \delta)\, H_2 \qquad \text{Reaction 2}$$

where $0 \le \delta < \delta' \le 1.6$. The specific reaction involved in Region II is:

$$0.4La_2O_3 + 0.2SrO + Fe + (1.6 - \delta)\, H_2O \leftrightarrow La_{0.8}Sr_{0.2}FeO_{3-\delta} + (1.6 - \delta)\, H_2 \qquad \text{Reaction 3}$$

Reaction 3 can be considered as a special case of Reaction 2, under which the oxygen defect concentration is too large to maintain a stable perovskite structure. The contribution of Reactions 2 and 3 to overall water-splitting reaction can be determined based on defect formation energies in LSF perovskites, which can accommodate significant oxygen non-stoichiometry resulting from acceptor (Sr) doping in its A-site cations and the variable valence states of its B-site (Fe) cations.[16] Using the defect model proposed by Mizusaki and Murugan et al[17-19], the relationship between oxygen vacancy (δ) and oxygen partial pressure is determined by:

$$\frac{\delta^{\frac{1}{2}}(2\delta - x + 1)}{(3-\delta)^{\frac{1}{2}}(2\delta - x)}\, p_{o_2}^{\frac{1}{4}} = \frac{K_{Fe}}{K_{Ox}} \frac{(1 + x - 2\delta)(3-\delta)^{\frac{1}{2}}}{\delta^{\frac{1}{2}}(2\delta - x)} \frac{1}{p_{o_2}^{\frac{1}{4}}} - \frac{1}{K_{Ox}^{\frac{1}{2}}} \qquad \text{Equation 1}$$

where $x = 0.2$ for $La_{0.8}Sr_{0.2}FeO_{3-\delta}$. Since the above model is suited for defected perovskites with very high steam conversions, it can accurately estimate steam conversions in both Reaction 2 and 3. As shown in Fig. 6.2A, the model predictions (see ESI for details) are in good agreement with TGA results. The slight over-prediction in Region II and III is partly due to incomplete reduction of the sample prior to steam oxidation, as confirmed by XRD in Fig. 6.2B.

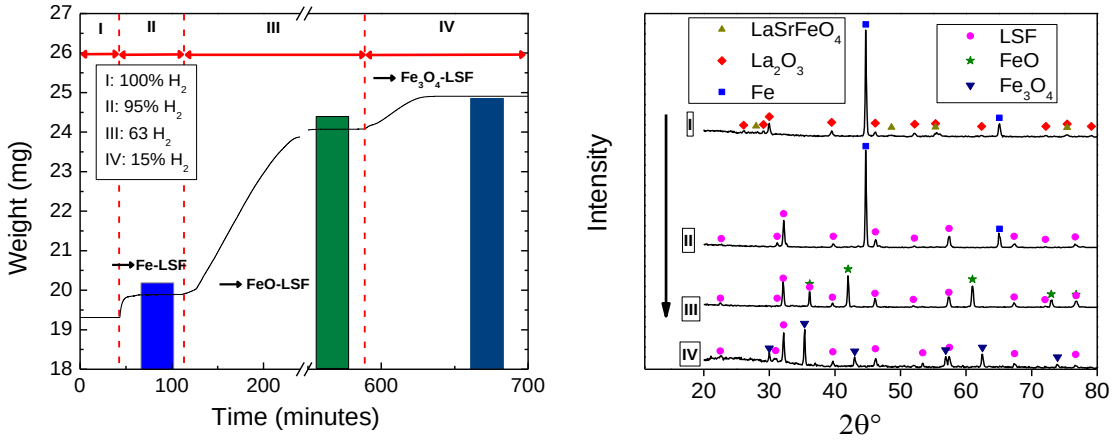

Fig. 6.2. (A) TGA profile of the reduced Fe_3O_4-LSF particle oxidized by steam and hydrogen mixture at 930°C. (I) in the presence of pure H_2; (II) oxidized by 95% H_2 (balance steam, N_2-free basis); (II) oxidized by 63% H_2; (IV) oxidized by 15% H_2. (B) XRD results of the particles when weight is stabilized in regimes (I), (II), (III) and (IV).

In the subsequent oxidation step in Region III, the main oxygen acceptor for water-splitting is metallic iron, forming wüstite. Oxygen vacancies in the LSF phase also contribute to a small fraction of the oxygen uptake. The corresponding steam to H_2 conversion in such a step is shown to be around 63%, which is in-line with equilibrium steam conversion between Fe to FeO (62.3%). As confirmed via TGA, iron (oxide), through phase transition from iron to wüstite, is responsible for 85.8% of the hydrogen generated from water-splitting with the LSF phase contributing the remaining 14.2%. The contribution from the LSF phase, albeit small, is essential for steam conversion (Fig. 6.3A). Based on the defect model, theoretical steam conversion for 25 wt% LSF promoted iron oxide is predicted to be 65.7% assuming iron and LSF phases act independently for water-splitting (additive effect). Besides the abovementioned additive effect, which is appropriate to describe composite LSF-iron oxide redox catalysts in a conventional fixed bed, one can also envision a scenario under which steam reacts with reduced iron (oxide) and LSF in a sequential manner. Such a configuration puts steam in sequential

contact with two redox materials with increasing oxygen affinity (or water-splitting efficacy). As a result, the overall thermodynamic driving force for water-splitting is maximized. As illustrated in Fig. 6.3B, further improvement in steam conversion can be anticipated under the sequential case.

In order to achieve the perceived advantage of the sequential reaction scheme, a layered reverse-flow reactor design using Fe_3O_4-LSF is proposed for combined syngas generation and water-splitting. As illustrated in Fig. 6.4, the reactor is composed of two layers. The bottom layer is iron (oxide) rich, whereas the top layer is primarily composed of LSF. A small amount of LSF at the bottom layer is necessary to prevent iron oxide sintering and deactivation. During the syngas generation stage, methane is introduced from the top of the reactor, producing syngas while removing the active lattice oxygen from both LSF and iron oxide-LSF layers. Since LSF has higher resistance towards coke formation,[15] injecting methane from the LSF end would be advantageous. Upon completion of the reduction reaction, steam is introduced from the bottom of the reactor to react with the reduced iron oxide-LSF layer and then the LSF layer. Such an arrangement maximizes the thermodynamic driving force for water-splitting while taking advantage of the unique properties of LSF for methane partial oxidation. As a result, high syngas yield and exceptional steam conversion can be achieved. The concept illustrated in Fig. 6.4 can be extended to general cases where concentration gradients of LSF and iron oxide are created along axial position of the fixed bed reactor.

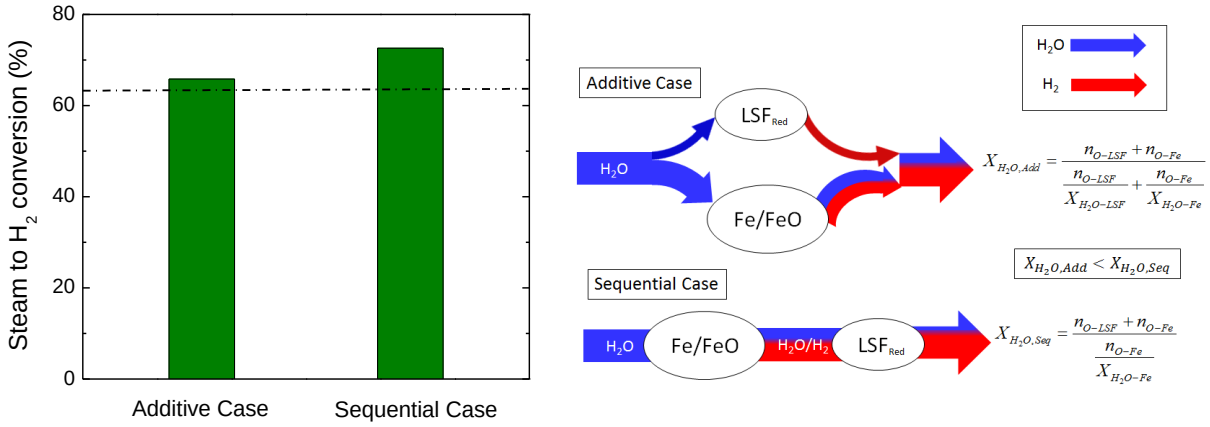

(A) (B)

Fig. 6.3. (A) Equilibrium steam conversion calculated based on an additive effect and sequential effect for iron oxide promoted with 25wt% LSF at 930 °C; (B) Schematic illustration of the additive and sequential cases. $n_{O\text{-}Fe}$ and $n_{O\text{-}LSF}$ represent the oxygen uptake by reduced iron oxide and LSF during water-splitting. $X_{O\text{-}Fe}$ and $X_{O\text{-}LSF}$ are equilibrium steam conversions for reduced iron oxide and LSF. $X_{H2O,Add}$ and $X_{H2O,Seq}$ refer to overall steam conversion in additive case and sequential case (equations shown are generally applicable to redox catalysts with <50 wt% LSF).

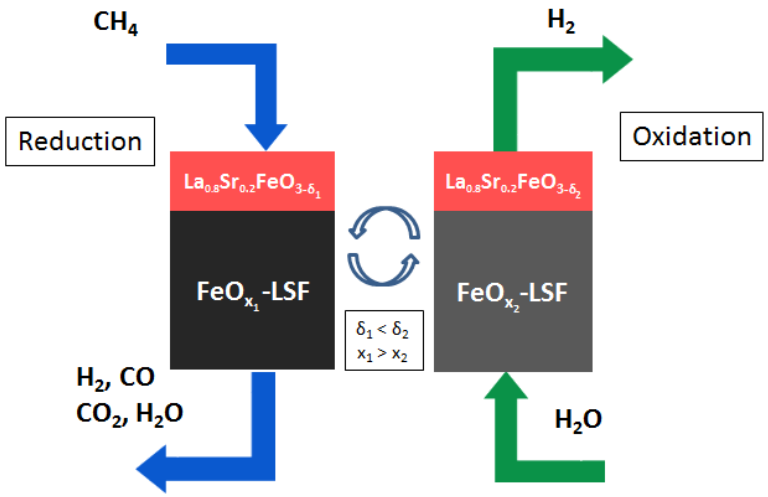

Fig. 6.4. Schematic of the proposed layered reverse-flow redox process with exceptional steam conversion and syngas yield.

Fixed bed testing is performed to validate the layered reverse-flow concept. The reactor is comprised of an LSF layer added on top of an LSF-iron oxide layer. Overall, the reactor is comprised of 55% iron oxide with a balance of LSF. Key results of the redox reactions are summarized in Table 6.1. 99% methane conversion and 62% (±3%) syngas yield was achieved in the reduction step. In the oxidation step, steam conversion in excess of 77% was achieved. A comparison of steam conversion is illustrated in Fig. 6.5. Using the layered reverse-flow concept, steam conversion was increased by over 10% when compared to a regular fixed bed. Such a conversion is also 15% higher than thermodynamically predicted conversion for pure iron oxides, which is the main contributor to water-splitting. An ASPEN Plus® model is used to simulate the performance of the layered reverse-flow concept in the hybrid solar-redox scheme.[12,20] Based on the experimental data, the overall process efficiency is determined to be 63.1% (HHV) or 15.1% higher than a case with 20% steam conversion (maximum steam conversion reported in literature). It is noted that steam conversion in excess of 77% is also feasible by adjusting the relative amounts of LSF and iron oxide in the reactor. Fig. 6.6

illustrates the relationships among La/Sr usage, H_2 generation capacity, and steam conversion. As can be seen, increase in La/Sr usage increases steam conversion. In the meantime, H_2 generation capacity of the redox catalyst is anticipated to decrease with increased catalyst cost. Overall, relatively low loading of La/Sr (~10 – 30 wt%) may result in a balance in terms of steam conversion (65-99%), H_2 generation capacity (12.3 – 9.4 mmol g^{-1}), and redox catalyst cost.

Table 6.1. Summary of the redox reactions performance

Syngas yield moles (mole of methane)$^{-1}$	1.78
H_2 yield moles (mole of methane)$^{-1}$	1.93
Methane conversion	99%
Steam conversion	77.2%
Hydrogen purity	98.5%
ASPEN simulated process efficiency	63.1% (HHV)

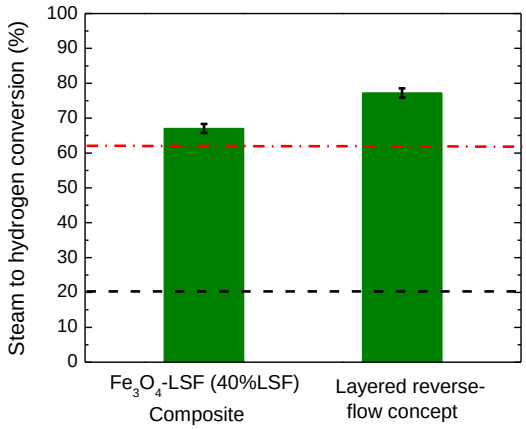

Fig. 6.5. Steam to hydrogen conversion in the oxidation step after CH_4 reduction at 930 °C. Red dash-dotted line displays thermodynamically predicted maximum steam conversion for FeO_x-H_2O-H_2 ternary system. Black dashed line shows the highest literature reported steam conversion.[6-11]

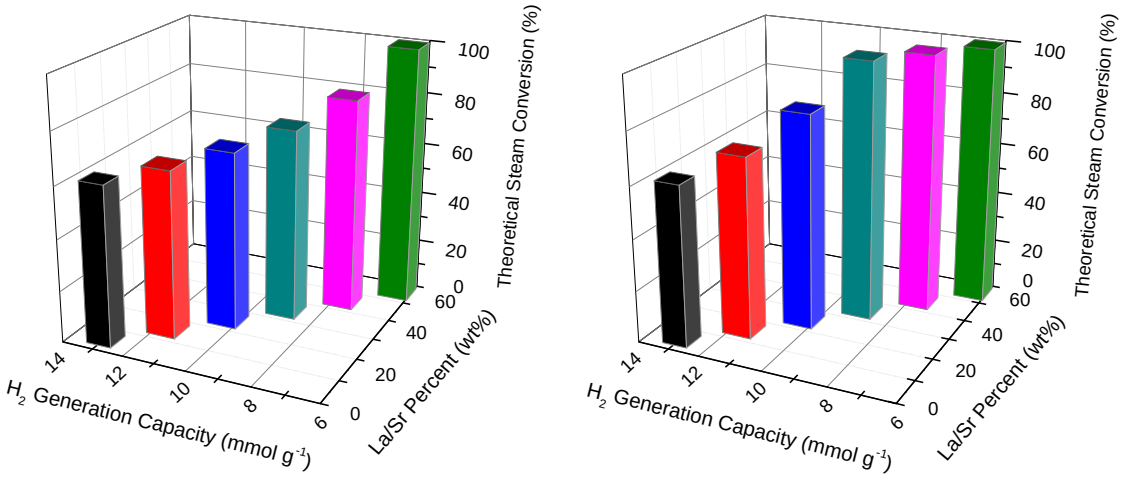

(A) (B)

Fig. 6.6. Theoretical conversion as a function of La/Sr content and H_2 generation capacity in (A) regular fixed bed; (B) layered reverse-flow reactor.

In summary, LSF-promoted iron oxide is demonstrated to be an exceptional redox material in a hybrid redox scheme for methane partial oxidation and water-splitting. Coupled with a novel layered reverse-flow reactor concept, the redox material is shown to be capable of converting over 77.2% steam into hydrogen. Such a conversion not only triples the performance of existing thermochemical based water-splitting processes, but also significantly exceeds the theoretical water-splitting efficiency for unpromoted iron oxides. When applied to the hybrid solar-redox scheme for liquid fuel and hydrogen co-generation, the process efficiency can increase by 15.1% (HHV) and CO_2 emission for H_2 product is reduced by up to 60%.

Acknowledgments

This work is supported by the U.S. National Science Foundation (CBET-1254351) and the Army Research Office DURIP program (61607-CH-RIP).

REFERENCES

1 J. M. Ogden, *Annu. Rev. Energy Environ.*, 1999, **24**, 227–279.

2 M. G. Walter, E. L. Warren, J. R. McKone, S. W. Boettcher, Q. Mi, E. A. Santori and N. S. Lewis, *Chem. Rev.*, 2010, **110**, 6446–6473.

3 J. Luo, J.-H. Im, M. T. Mayer, M. Schreier, M. K. Nazeeruddin, N.-G. Park, S. D. Tilley, H. J. Fan and M. Grätzel, *Science*, 2014, **345**, 1593–1596.

4 W. C. Chueh, C. Falter, M. Abbott, D. Scipio, P. Furler, S. M. Haile and A. Steinfeld, *Science*, 2010, **330**, 1797–1801.

5 C. L. Muhich, B. W. Evanko, K. C. Weston, P. Lichty, X. Liang, J. Martinek, C. B. Musgrave and A. W. Weimer, *Science*, 2013, **341**, 540–542.

6 K. S. Go, S. R. Son, S. D. Kim, K. S. Kang and C. S. Park, *Int. J. Hydrog. Energy*, 2009, **34**, 1301–1309.

7 D. Yamaguchi, L. Tang, L. Wong, N. Burke, D. Trimm, K. Nguyen and K. Chiang, *Int. J. Hydrog. Energy*, 2011, **36**, 6646–6656.

8 P. R. Kidambi, J. P. E. Cleeton, S. A. Scott, J. S. Dennis and C. D. Bohn, *Energy Fuels*, 2012, **26**, 603–617.

9 A. M. Kierzkowska, C. D. Bohn, S. A. Scott, J. P. Cleeton, J. S. Dennis and C. R. Müller, *Ind. Eng. Chem. Res.*, 2010, **49**, 5383–5391.

10 M. Rydén and M. Arjmand, *Int. J. Hydrog. Energy*, 2012, **37**, 4843–4854.

11 V. Galvita, T. Hempel, H. Lorenz, L. K. Rihko-Struckmann and K. Sundmacher, *Ind. Eng. Chem. Res.*, 2008, **47**, 303–310.

12 F. He, J. Trainham, G. Parsons, J. S. Newman and F. Li, *Energy Environ. Sci.*, 2014, **7**, 2033–2042.

13 N. L. Galinsky, Y. Huang, A. Shafiefarhood and F. Li, *ACS Sustain. Chem. Eng.*, 2013, **1**, 364–373.

14 A. Shafiefarhood, N. Galinsky, Y. Huang, Y. Chen and F. Li, *ChemCatChem*, 2014, **6**, 790–799.

15 L. M. Neal, A. Shafiefarhood and F. Li, *ACS Catal.*, 2014, **10**, 3560–3569.

16 M. A. Peña and J. L. G. Fierro, *Chem. Rev.*, 2001, **101**, 1981–2018.

17 J. Mizusaki, T. Sasamoto, W. R. Cannon and H. K. Bowen, *J. Am. Ceram. Soc.*, 1983, **66**, 247–252.

18 J. Mizusaki, M. Yoshihiro, S. Yamauchi and K. Fueki, *J. Solid State Chem.*, 1985, **58**, 257–266.

19 A. Murugan, A. Thursfield and I. S. Metcalfe, *Energy Environ. Sci.*, 2011, **4**, 4639–4649.

20 F. He and F. Li, *Int. J. Hydrog. Energy*, 2014, **39**, 18092–18102.

CHAPTER 7 CONCLUSIONS AND OUTLOOK

Two novel redox-based energy conversion processes, bimetallic chemical looping gasification (CLG) process and hybrid solar-redox process, are developed for coal and natural gas conversion respectively. These two processes provide promising approaches to convert carbonaceous fuel with improved kinetics, higher efficiency, and reduced CO_2 emission. A common feature of the redox based processes is the use of oxygen carrier or redox catalyst to transfer lattice oxygen between two reactors in a cyclic manner. The potential issues of attrition and particulate emission, caused by large solid inventory, vigorous solids-solids interactions, and intense thermal and redox stresses, are evaluated in a fluidized bed for chemical looping combustion.

A bimetallic chemical looping gasification process is developed based on the coal-direct chemical looping (CDCL) gasification process, which utilizes an iron oxide based oxygen carrier to indirectly gasify coal into separate streams of H_2 and CO_2. The CDCL process simplifies the conventional coal to hydrogen scheme by eliminating the gasifier, WGS, ASU, and CO_2 capture units, so that high process efficiency can potentially be achieved. However, a key challenge resides in the slow solid-solid reaction kinetics between the fuel and the oxygen carriers. To address this issue, a bimetallic oxygen carrier by incorporating small amount of CuO into the Fe_2O_3 based oxygen carrier is proposed. The resulting bimetallic CLG process is effective for solid fuel conversion by using the "oxygen-uncoupling" characteristics of CuO, which is validated by Thermal-Gravimetric Analyzer (TGA) experiments. Formation of mixed metal oxides of copper and iron in the oxygen carrier particle is inhibited by segregating copper and iron atoms with an inert support. ASPEN Plus® simulation and mathematical modeling are also conducted to evaluate the reactor and process performance. Under a kinetically limited scenario, 78.8% hydrogen generation efficiency, 82.5% (HHV) overall efficiency, and 95% CO_2 capture can be achieved by bimetallic CLG process. Although copper (oxides) does not directly participate in H_2 generation in the CLG oxidizer, the presence of copper leads to improved H_2 generation efficiency through simplified process heat integration scheme. To summarize, incorporation of a small amount of CuO to an iron based oxygen carrier can result

in an active composite oxygen carrier for solid fuel conversion. When used in the CLG processes, the composite oxygen carrier has the potential to enhance solid fuel conversion rate while improving the process efficiency for H_2 generation.

The hybrid solar-redox process is proposed to converted methane and solar energy into separate streams of liquid fuels and hydrogen with a novel lanthanum strontium ferrite (LSF) supported iron oxide. Methane is used in the reduction step to enhance iron oxide decomposition/reduction reactions at temperatures significantly lower than those in conventional solar-thermal water-splitting processes. Multiple redox cycle experiments using a lab-scale tubular reactor shows 95% conversion of methane with 2:1 H_2 and CO molar ratio syngas as the product. Over 97% pure hydrogen is generated with 60% steam to hydrogen conversion in the subsequent water-splitting step. Results from experimental studies and/or thermodynamic analyses are then used in ASPEN Plus® process simulator. Results indicate 64.2 HHV% process efficiency and 96.6 HHV% methane to fuel efficiency. These experimental and simulation studies confirm the feasibility of the proposed hybrid solar-redox scheme. The proposed process has the potential to produce transportation fuels and hydrogen at high efficiency with reduced steam usage and carbon footprint.

The performance of the hybrid solar-redox process is further compared with steam methane reforming (SMR) and solar SMR by ASPEN Plus® simulation using a consistent set of assumptions. Integration of solar energy with methane conversion is found to significantly reduce the life cycle CO_2 emissions. The efficiency of the process using solar energy can be largely affected by solar absorption efficiency. Under a conservative set of assumptions using experimental data, the hybrid solar-redox process is estimated to be 7.7% (HHV) more efficient than SMR based co-production processes. The efficiency increase is resulted from solar energy input and improved energy integration scheme. In addition, life cycle CO_2 emission associated with H_2 product for the solar-redox process is 85% lower than conventional approaches. To summarize, the hybrid solar-redox process offers an efficient yet flexible alternative to convert

methane and solar energy into a combination of hydrogen and liquid fuels at high efficiency, compared to conventional and solar SMR processes.

Sensitivity analysis by ASPEN process simulation and exergy analysis indicate that steam conversion in the oxidizer also plays an important role for the overall efficiency of the hybrid solar-redox process. In contrast to previously reported ferrite materials, which typically exhibit 20% or lower steam to hydrogen conversion, $La_{0.8}Sr_{0.2}FeO_{3-\delta}$ (LSF) promoted Fe_3O_4 is capable of converting more than 67% steam with high redox stability. Both experiments and a defect model indicate that the synergistic effect of reduced LSF and metallic iron phases is attributable to the exceptional steam conversion. The contribution from the LSF phase, albeit small, is essential for steam conversion. A layered reverse-flow reactor concept composed of two layers of redox catalysts with varying LSF content is proposed. The bottom layer is iron (oxide) rich, whereas the top layer is primarily composed of LSF. A small amount of LSF at the bottom layer is necessary to prevent iron oxide sintering and deactivation. During the syngas generation stage, methane is introduced from the top of the reactor, producing syngas while removing the active lattice oxygen from both LSF and iron oxide-LSF layers. Since LSF has higher resistance towards coke formation,[15] injecting methane from the LSF end would be advantageous. Using this concept, over 77% steam to hydrogen conversion is achieved at 930 °C, which is 15% higher than the maximum conversion predicted by second law for unpromoted iron (oxides). When applied to the hybrid solar-redox scheme for liquid fuels and hydrogen co-generation, significant improvements in energy conversion efficiency can be achieved with reduced CO_2 emissions.

Particles attrition is a common challenge for redox based processes. Attrition inevitably occurs in fluidized bed reactor especially under high temperature and cyclic reducing-oxidizing environments. It can lead to loss of valuable oxygen carrier material, additional burden on the downstream particle separation systems, or emission of fine particulates that can cause health hazards. The study on the CuO-Al_2O_3 oxygen carriers in a fluidized reactor for chemical looping combustion (CLC) of methane shows that the reducing and oxidizing reactions lead to

an increased emission rate of find particle and particulates. The particulates emission contains primarily of 2-5 μm sized particles. Notable amount of < 1 μm particulates are also observed. The surface of the oxygen carrier is also found to be coarsened due to a Kirkendall effect, which also explains the surface enrichment of Cu. The fine particles in the size range of 10-75 μm, generated primarily from fragmentation, are rich in Cu and lead to increased CuO loss. As a result, it is important to collect and reprocess fine particles generated from chemical looping processes to prevent oxygen carrier loss and to reduce the potential environmental impact.

The concept of the hybrid solar-redox process has been demonstrated by lab scale experiments and process simulations. A critical consideration for such a process is the performance of the redox catalyst. Optimization of the redox catalyst will further improve the attractiveness of the novel process. Perovskite such as $La_{0.8}Sr_{0.2}FeO_{3-\delta}$ (LSF) is a mixed ionic-electronic conductor, which could provide ionic and electronic conduction pathways for effective removal and replenishment of active lattice oxygen. Because of this, the LSF supported iron oxide has been reported with high reactivity and reasonable coke resistance as the redox catalyst. However, the rare earth elements contained in the particle, i.e. La significantly increase the cost and limit its application on the large–scale operation. Therefore, a perovskite composed of abundant, low-lost and environmental friendly element would be promising to be used as the redox catalyst for the hybrid solar-redox process. An economic analysis with assist of process simulation is useful to justify the feasibility of new redox catalysts.

A deep understanding of the reaction mechanisms of methane partial oxidation and water splitting using metal oxide based redox catalysts is highly desirable since such understanding will provide fundamental basis for rational design of novel redox catalysts. It has been reported that methane oxidation by LSF-supported iron oxides exhibits four distinct regions, i.e. deep oxidation; competing deep and selective oxidation; selective oxidation with auto activation; and methane decomposition. According to this finding, the reaction is suggested to be controlled within the region of competing deep and selective oxidation and selective oxidation with auto activation. A better understanding of the reaction mechanisms can also help to

optimize reactor design. The design of layered reverse-flow reactor in Chapter 6 is a good example. Fundamental knowledge guided redox catalyst and reactor design should be one of the crucial studies in the future, which can have a significant effect on particle conversion, product yields, and process efficiency.

In addition to catalyst and reactor design, studies on scale up demonstrations are of vital importance to the success of the redox process. Process scale-up and prototype demonstration is an important step to take conceptual technologies to commercial realization, which provides valuable data about reactions and catalyst properties at larger scale.

APPENDICES

Appendix A Supplementary Information for Chapter 2

This supporting information contains the following sections:

S1 The Aspen Plus process configuration

S2 TGA analysis

S3 Effect of heat loss on the process performance

S1 The Aspen Plus process configuration[1]

The ASPEN simulation model developed for the coal chemical looping gasification using bimetallic oxygen carrier particles is shown in Fig. 2.S1. It includes: the bimetallic looping section which has reducer, oxidizer and combustor; the power generation section which has steam turbines and HRSG; the product purification section. The process feedstock is coal and the final products from the gasification process are high purity compressed H_2 and CO_2.

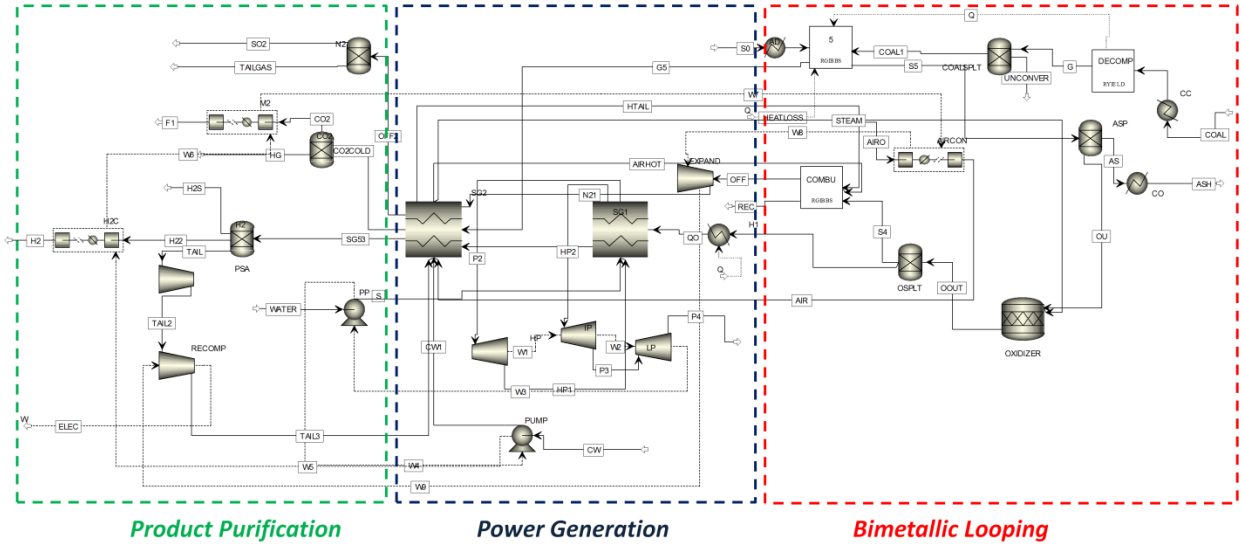

Fig. 2.S1. ASPEN Plus® flowsheet of the bimetallic chemical looping gasification process for hydrogen production from coal.

S2 TGA analysis

S2.1 Materials and procedures

Two oxygen carriers, both containing 60 w.t.% Fe_2O_3, are synthesized via a solid state method. Fe_2O_3 supported on Al_2O_3 is used as a reference material. The reference material is prepared in which calculated amounts Fe_2O_3 (99.9%, Noah Chemical) and Al_2O_3 (99.9% anatase, Noah Chemical) precursors at a weight ratio of 60: 40 are used. The mixture is prepared in a planetary ball mill for 3 hours at a rotation speed of 250 rpm. This is followed with pelletization in a

tablet press (MTI). The pellets are then annealed in a tube furnace at 900 °C for 8 hours. A second oxygen carrier, which contains cupric oxide promoter, is prepared using a similar approach. The oxygen carrier is prepared from Fe_2O_3 (99.9%, Noah chemical) and CuO supported on Al_2O_3 (13 w.t.% CuO, Sigma Aldrich) at a weight ratio of 60:40. Since CuO is impregnated into the porous structure of Al_2O_3, solid state reactions between iron and copper oxides are minimized. Coal char is prepared from bituminous coal (Asbury Carbons C3) through pyrolysis under an inert environment. All the reactivity studies are conducted in a SETARAM SETSYS Evolution TGA. Samples are prepared via hand-mixing of oxygen carriers with char at a 20:1 ratio by weight. During each experiment, approximately 50 mg oxygen carrier-char mixture is heated to 950 °C at a rate of 50 °C/min. The temperature is then held steady for 5 hours. 50 mL min^{-1} of He is used as the purge gas. Although the reaction environment in TGA is notably different from that in a moving bed or fluid bed reactor, the TGA experiments are designed to obtain preliminary confirmation for char conversion activity of the bimetallic oxygen carrier. It also serves to confirm whether the formation of mixed Fe-Cu oxide, which is undesirable for CLG, can be inhibited.

S2.2 TGA analysis

TGA does not provide a high fidelity environment comparable to moving bed or fluid bed reactors. It is most likely that all the CuO is converted by volatile and CO/H_2 produced by char gasification. Therefore, not much CuO remains at the coal feeding point. However, splitting the metal oxide flow to co-inject metal oxides and coal can allow direct contract between coal and CuO. The TGA results are shown in Fig. 2.S2. The reactivity of the oxygen carriers is characterized by two parameters, i.e. the initial reduction temperature and the coal char conversions after 5 minutes. Conversion of the oxygen carrier/char mixture is calculated using equation 1:

$$\%Conversion = \frac{(m_{\text{int}} - m_t)}{\frac{m_C}{MW_C} \cdot MW_{CO}} \quad (1)$$

where m_{int} is the initial mass of the oxygen carrier and the char, m_t is the mass of the sample at some time, m_c is the mass of the carbon inside the sample, MW_C and MW_{CO} are the molecular weights of carbon and carbon monoxide respectively. The results indicate that the initial reduction temperature of the CuO containing sample is about 200°C lower than the reference oxygen carrier. Comparing the conversion at 5 minutes after the temperature reaches 950°C shows that the copper enhanced sample achieved sixteen times as much conversion as the reference material. The TGA results confirm the kinetic improvement for char conversion by oxygen uncoupling.

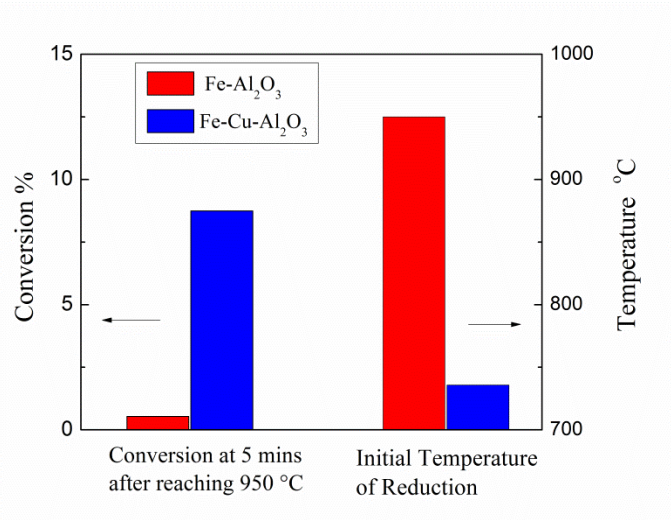

Fig. 2.S2: TGA results of pure Fe-based and bimetallic oxygen carrier particles.

S3 Effect of heat loss on the process performance

The simulation in Section 4.3.1 is based on the assumption that the overall process heat loss is 1% of the total thermal input. Such a heat loss rate is suggested by National Energy Technology Laboratory (NETL) of the U.S. Department of Energy (USDOE) for coal gasification systems. Using Case III as the reference case, we simulated the effect of an increased heat loss of 5%. The results are shown in Fig. 2.S3. The increased heat loss leads to a decreased process efficiency of 79.4%, which is about 5% less than the case with 1% heat loss.

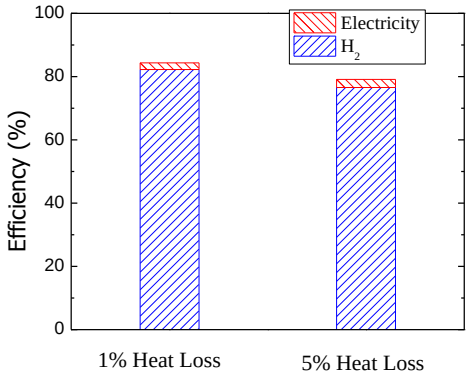

Fig. 2.S3: Effect of process heat loss on the overall process efficiency.

Appendix B Supplementary Information for Chapter 4

Metal Oxide Synthesis:

Lanthanum strontium ferrite ($La_{0.8}Sr_{0.2}FeO_{3-\delta}$ or LSF) supported Fe_3O_4 is used as the redox material, a.k.a. oxygen carrier, for water-splitting. The LSF support, which is an effective mixed ionic-electronic conductor, can inhibit the sintering of iron/iron oxides, thereby enhancing the redox activity and thermal stability of the iron oxide.[1,2] Fe_2O_3 is used as the precursor for Fe_3O_4. The oxygen carrier precursor contains 60 w.t.% Fe_2O_3 balanced with LSF. A solid-state reaction (SSR) method is used for oxygen carrier synthesis. Briefly speaking, a stoichiometric amount of precursors, i.e. iron oxide (Fe_2O_3, 99.9%, Noah Chemicals), La_2O_3 (99.9%, Aldrich), and $SrCO_3$ (99.9%, Noah Chemical), are weighed and mixed using a planetary ball-mill (XBM4X, Columbia International) for 6 hours. The solid mixture is then pelletized using a hydraulic press (YLJ-15T, MTI Corporation) under 7 to 8 MPa pressure. This is followed with annealing in air at 1200°C for 28 hours in a tube furnace (GSL-1500-X50, MTI Corporation). The resulting pellets are subsequently crushed and sieved into 75 to 300 μm for further characterization and testing. The as-prepared metal oxide obtained is composed of Fe_2O_3 and LSF. In order to obtain Fe_3O_4 phase, one cycle reduction with methane followed with steam regeneration is performed. Further details of the SSR method have been reported earlier.[1,2]

Experimental set up

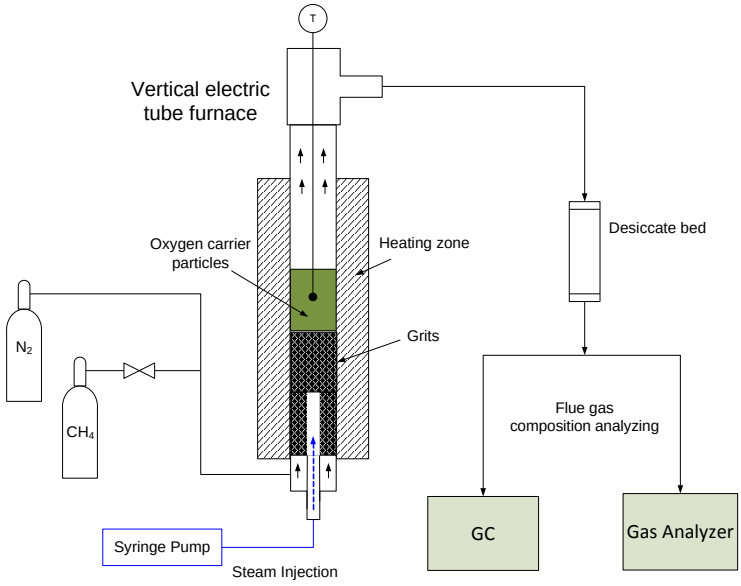

Fig. 4.S1 Experimental setup for hybrid redox process test with Fe_2O_3-LSF particle.

Simulation assumptions

Aspen Plus is used in the present study to determine the reactor and process performances. Table 4.S1 specifies the materials involved in the simulations. Since LSF is not available in the Aspen Plus database, SiC is used as the inert support in our simulations. It is noted that LSF support does not participate in the redox reaction to an appreciable extent. Replacement of LSF support with SiC will not affect the simulation results since the support material acts mainly as a heat carrier from a mass and energy balance standpoint. Aspen Plus modules, property methods, and physical property databanks are summarized in Table 4.S2. PR-BM is selected as the property method in all the simulation modules except for steam cycles, where STEAM-TA method is used. Table 4.S3 lists the key operating assumptions and parameters used in the process simulations.

Table 4.S1 Specifications of the materials

Methane	HHV (higher heating value) 55.5 MJ kg^{-1}, LHV 50.0 MJ kg^{-1}
Concentrated solar energy input	52-62 MW[3-5]
Absorption efficiency for solar energy	80%[3,4,6]
Air	79% N_2, 21% O_2 by volume
Oxygen carrier	Fe_3O_4, SiC (inert)
Water	H_2O
H_2 product	Purity: >99.99%, Pressure: 6 MPa
Naphtha	C_6-C_{11}
Diesel	C_{12}-C_{18}

Table 4.S2 Aspen Plus model setup

Overall setup	
Stream class	MIXCINC
Databank	COMBUST, INORGANIC, SOLIDS, PURE
Solid components	Fe, $Fe_{0.947}O$, Fe_3O_4, SiC, C
Property method	PR-BM, except STEAM-TA for steam cycles
Solution strategy	Sequential Modular
Unit operations models	
Reducer	Single-stage RGibbs; RGibbs
Oxidizer	Multi-stage RGibbs (moving bed); RGibbs
F-T Reactor	RStoic
Pressure changers	Pump, Compr, Mcompr
Heat exchangers	Heater, MheatX
Mixers/Splitters/Separators	Mixer/Fsplit/Sep/Flash2
Reducer	Single-stage RGibbs

Table 4.S3 Key assumptions and simulation parameters in the Aspen Plus simulation

Parameter	Value
Ambient condition	T = 25 °C, P = 1 atm
Reaction assumptions	Except for Case III, all reactions reach equilibrium
Heat loss in the reactors	1% of the total thermal input
F-T catalyst	Cobalt
F-T reactor temperature and pressure	220 °C; 10 atm
F-T α parameter	0.873
CO per-pass conversion in the F-T reactor	80% (10 atm)
Pressure drop in the reducer and oxidizer	0.5 atm
Mechanical efficiency of pressure changers	1
Isentropic efficiency of steam turbines	0.85
Isentropic efficiency of air blowers and compressors	0.8
Heat Recovery Steam Generator	Pinch point: 15 ℃
PSA	5 atm pressure drop, 95% H_2 recovery
Compressor specifications	4 stage with intercooler at 40°C, Isentropic efficiency is 0.8
Steam turbine conditions	3-level Steam Cycle 12.4 MPa (HP inlet)/3.1MPa(IP inlet)/0.45MPa(LP inlet)/0.01MPa(LP outlet)

Key reactions in the hybrid solar-redox scheme

Key chemical reactions are given below. It includes methane conversion reactions in the reducer (A) and water-splitting reactions in the oxidizer (B).

Table 4.S4 Key chemical reactions in the redox scheme

	Reactions	**Free energy@900 °C kJ/mol**
	Reducer (Methane conversion)	
A1.	$CH_4 + Fe_3O_4 \rightarrow CO + 2H_2 + 3FeO$	-78.3
A2.	$CH_4 + 4Fe_3O_4 \rightarrow CO_2 + 2H_2O + 12FeO$	-99.5
A3.	$CH_4 + 4FeO \rightarrow CO_2 + 2H_2O + 4Fe$	-49.9
A4.	$CH_4 + FeO \rightarrow CO + 2H_2 + Fe$	-65.9
A5.	$CO + Fe_3O_4 \rightarrow CO_2 + 3FeO$	-5.34
A6.	$CO + FeO \rightarrow CO_2 + Fe$	7.07
A7.	$H_2 + Fe_3O_4 \rightarrow H_2O + 3FeO$	-7.91
A8.	$H_2 + FeO \rightarrow H_2O + Fe$	4.49
A9.	$CO + H_2O \rightarrow CO_2 + H_2$	2.57
A10.	$CH_4 \rightarrow C + 2H_2$	-38.0
	Oxidizer (Water-splitting)	
B1.	$H_2O + Fe \rightarrow FeO + H_2$	-4.49
B2.	$H_2O + 3FeO \rightarrow Fe_3O_4 + H_2$	7.91
B3.	$H_2O + C \rightarrow CO + H_2$ (coke is formed in reducer)	-32.4
B4.	$2H_2O + C \rightarrow CO_2 + 2H_2$	-29.8

Product gas concentration from reducer as a function of time

While the real time methane conversion and syngas yield in the experiment are presented in the manuscript (Fig. 4.2), the corresponding product gases concentration as a function of time in the reducer is shown in Fig. 4.S2.

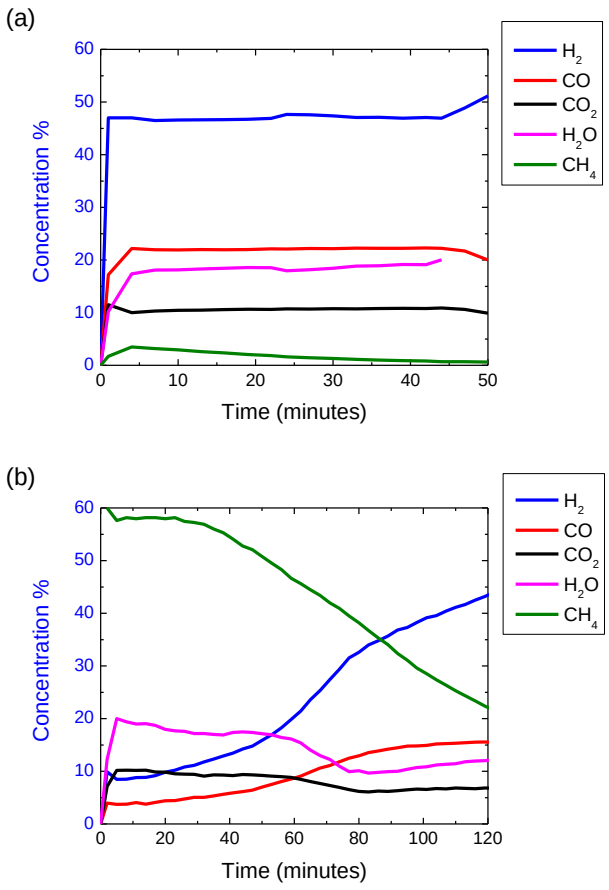

Fig. 4.S2 Product gases concentration (N_2-free) as a function of time in the CH_4 oxidizing step. (a) 5th cycle fixed-bed (b) 5th cycle fluidized-bed.

Fe_3O_4-LSF reactivity in the reducing step

Reactivity study on Fe_3O_4-LSF is also conducted in a differential bed reactor system composed of a computer-controlled panel for gas mixing and delivery, a TGA (STARAM SETSYS Evolution) for redox reactions, and a quadrupole mass spectrometer (QMS, MKS Cirrus 2) for gaseous product analyses. In the experiment, 50 mg Fe_3O_4-LSF is heated to 900 °C at a rate of 50 °C/min. And then the reacting gas in injected at the temperature of 900 °C for 10 minutes. Total gas flow rate is maintained at 300 ml/min. Concentrations of the reactive gases (CH_4) is fixed at 10%. Helium is used as the carrier gas. Product distributions and catalyst selectivity towards syngas are determined using the QMS. TGA experiments are designed to obtain confirmation for the Fe_3O_4-LSF particle activity to react with methane. At about 0.9 minutes during the experiment, the average phase of iron oxides is FeO. The methane conversion and syngas yield are relatively low at the beginning of the experiment. Then, methane conversion rate and syngas yield increase significantly with time or increasing degree of iron oxide reduction. At approximately 5 minutes of CH_4 injection, coke starts to form based on the carbon mass balance calculation. It causes the H_2/CO molar ratio to exceed 2, where methane should be stopped to inhibit the coke formation. Coke formation is found to stop at between 5.8 and 6 minutes. At that point, no further conversion of methane is observed due to lack of active lattice oxygen and lack of coke formation. In an actual process, constant reduction and regeneration of the oxygen carrier will be implemented as in fixed/fluidized bed experiments. Fig. 4.S3 summarizes the experimental results.

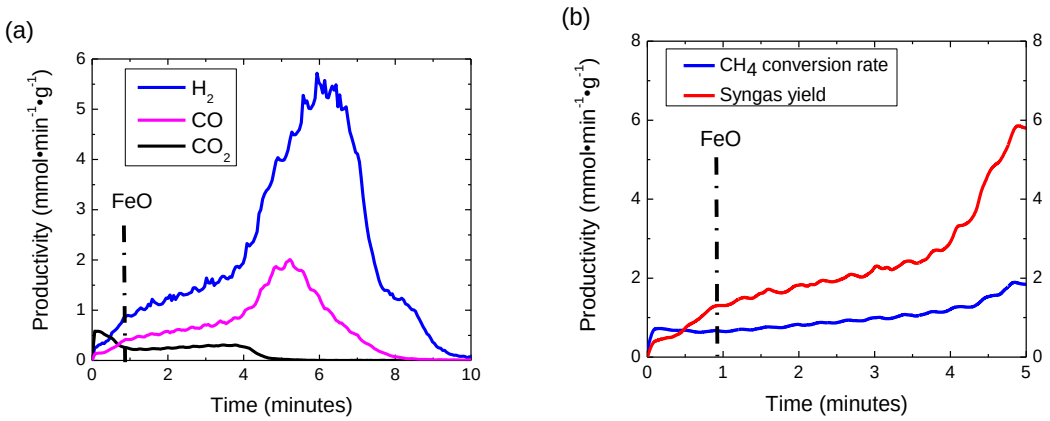

Fig. 4.S3 Flue gas analysis of Fe_3O_4-LSF and CH_4 reaction at 900 °C (a) flow rates of product gases (b) methane conversion rate and syngas yield.

X-ray powder diffraction results

X-ray powder diffraction (XRD) tests are carried out for spent oxygen carriers in both reduced and oxidized forms. The results are provided in Fig. 4.S4. Both wustite and metallic iron are observed in the reduced sample whereas the majority of the iron phase in the regenerated sample is magnetite. Iron carbide phases are not identified in the reduced sample, indicating that amorphous carbon and/or carbon fiber may represent the dominant forms of carbon.

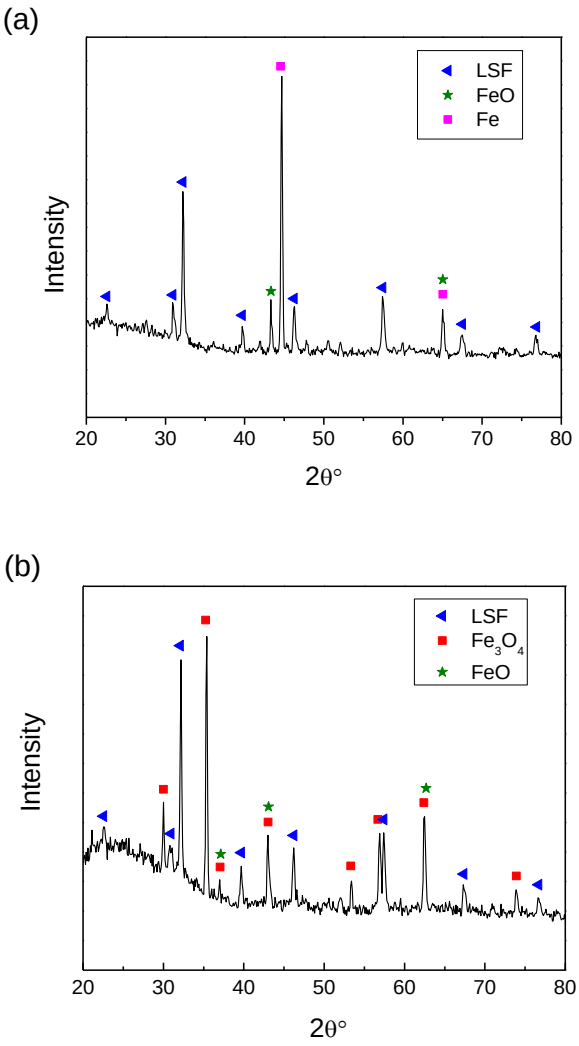

Fig. 4.S4 XRD results of the (a) reduced; (b) oxidized OC particles.

Experimental results on multi-cyclic studies

7.5 to 20 grams of iron oxide particles are added on top of the SiC layer in the tubular reactor. In order to mimic the proposed hybrid redox scheme, the tests are carried out in two consecutive steps, i.e. methane partial oxidation and water-splitting. Both fixed-bed and fluidized-bed operation modes are tested. In typical fixed-bed experiments, the reactor is heated under N_2 flow of 15 ml/min. In fluidized-bed experiments, 600 ml/min of N_2 gas is provided during the heating stage to maintain fluidization of the Fe_3O_4-LSF particles. Once the desired temperature (900 °C unless otherwise specified) is reached, 15 ml/min of methane is introduced to the reactor. In order to inhibit excessive carbon formation from methane decomposition, methane injection is stopped when $H_2/(CO+CO_2)$ molar ratio exceeds 2. Water-splitting reaction is carried out after the residue gas from the methane oxidation step has been completely purged with N_2. The water-splitting reaction is initiated by steam injection. 50 ml/min (fixed-bed) or 600 ml/min (fluidized-bed) of N_2 is used as the internal standard. The reaction is stopped when H_2 concentration is below 0.1%. The aforementioned redox reactions are carried out for 5 cycles. And the results are shown in the Fig. 4.S5. The CH_4 conversion, syngas yield and H_2/CO molar ratio is calculated for the reducing step, while the steam to H_2 conversion is calculated for the oxidizing step. Reproducible results are found among the various redox cycles.

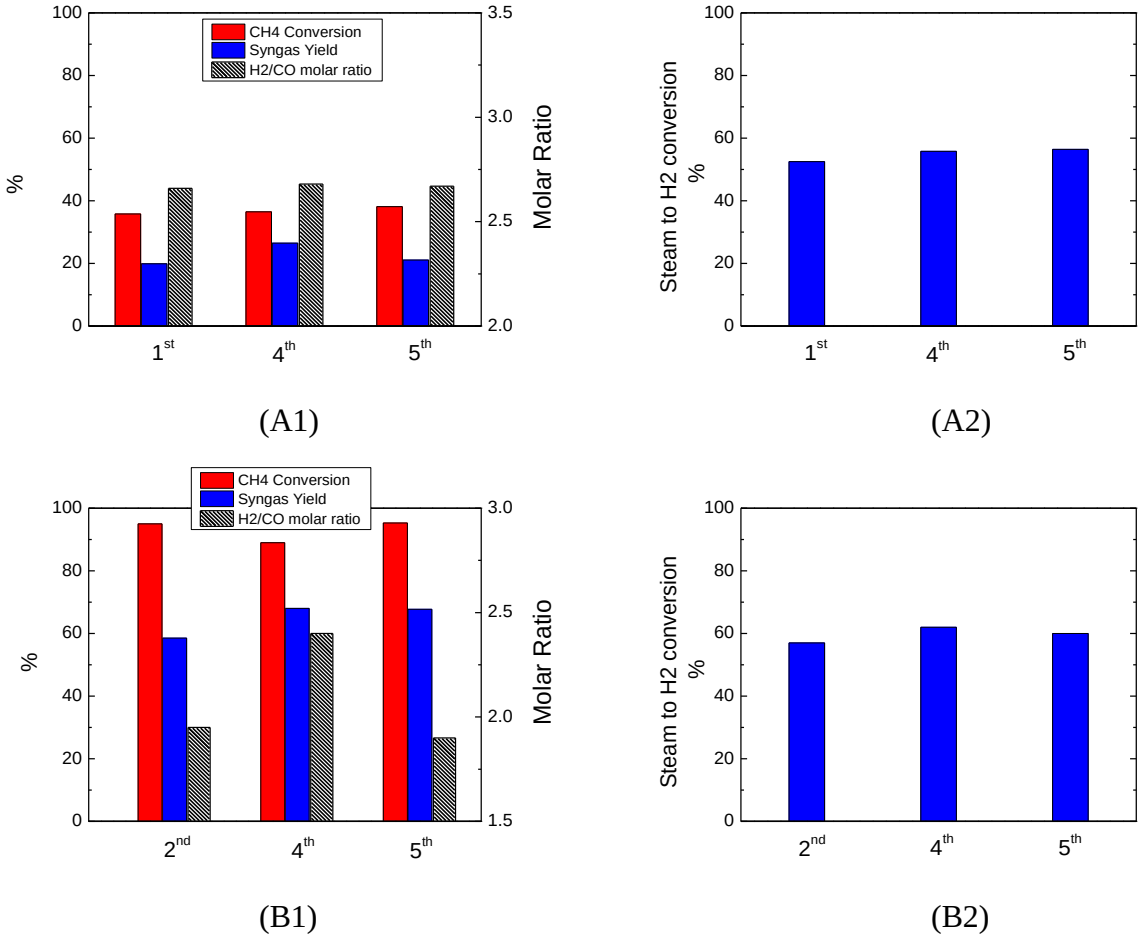

Fig. 4.S5 Experimental data from 5 redox cycles performance on (A) fluidized bed and (B) fixed bed.

Comparison of the oxygen carrier activity for energy conversion

The hybrid solar-redox process investigated in the current study represents an alternative scheme that converts methane and solar energy into separate streams of liquid fuels and hydrogen. Compared to the conventional solar water splitting scheme, solar-redox process has the advantages of multiple products and low reducing reaction temperature. In the present work, Lanthanum strontium ferrite ($La_{0.8}Sr_{0.2}FeO_{3-\delta}$ or LSF) supported Fe_3O_4 (60 wt%) is used as the redox oxygen carrier material. According to our experimental study, it is found 95% average methane conversion is achieved in the fixed-bed at 900 °C. Syngas with 2:1 H_2 and CO molar ratio, which is ideal for F-T synthesis, can be generated. Hydrogen with an overall purity in excess of 97% is generated in the subsequent water-splitting step. The water-splitting step also exhibits high steam to hydrogen conversion. In sum, the particle shows promising activity for solar redox process.

Kodama et al[7] studied an iron oxide supported on yttrium-stabilized zirconia (YSZ) at 1400 °C for the conventional solar water splitting scheme. Mixed oxides based ferrite materials with general formula of $M_xFe_{3-x}O_4$ (M = Mn, Co, Ni, Zn, Mg, etc.) has also been investigated as the alternative oxygen carrier.[8-11] $CoFe_2O_4$ and Al_2O_3 was tested in the isothermal redox cycles for H_2 generation.[12] The H_2 generation rates and oxygen carrier activities reported in their work are all in the same range. For comparison, we take the results of the Fe_3O_4/YSZ particle from Kodama et al., which is shown in Table 4.S5. The product generation rate is calculated by the energy of the product (HHV based) per gram of the oxygen carrier particle and per reaction time. As indicated in Table 4.S5, the Fe_3O_4/LSF used in the present work gives much higher H_2 generation rate. In addition, syngas is produced in the reducing step in the meantime. The total products generation rate is about 20 time more than conventional solar water splitting scheme by using the Fe_3O_4/LSF particle.

Table 4.S5 Comparison of Fe_3O_4 particle activity
in the hybrid solar-redox and water splitting scheme

	Peak H_2 generation rate J g^{-1} min^{-1}	Average H_2 generation rate J g^{-1} min^{-1}	Syngas generation J g^{-1} min^{-1}	Total product generation rate J g^{-1} min^{-1}
Ref[7]	6.3	3.2	NA	3.2
Our work	49.8*	49.8	12.9	62.7

* H_2 generation close to steady state achieved in our work

The Aspen Plus® process configuration

The ASPEN simulation model developed for the hybrid solar-redox process operating at low pressure for the redox reactions is shown in Fig. 4.S6. It includes: (1) the redox section which has reducer and oxidizer; (2) the F-T synthesis section where consists of the F-T reactor, upgrader and syngas compressor; (3) the power generation section which has steam turbines and HRSG; (4) the product purification section. As the process feedstock, methane is fed into the reducer, where it is partially oxidized by the oxygen carrier into syngas. In order to compensate the heat required for the endothermic methane oxidation reaction, solar energy is provided by direct irradiation. A methane processing capacity of 8 tonne/hr is assumed for all cases. Such a capacity, which requires solar input of approximately 60 MW_{th}, allows for integration with existing concentrated solar thermal systems,[1-3] Syngas produced by methane partial oxidation in the reducer is used as the feedstock for F-T synthesis. Byproducts from the F-T reactor, upgrader, and PSA units are recycled to the reducer to produce additional syngas. Besides syngas, the reducer generates reduced oxygen carrier particles which are transported to the oxidizer for water-splitting. The H_2 generated from the water-splitting or steam-iron reaction is cooled, cleaned, and compressed as the final product. The high temperature gaseous products from the reactors as well as the heat generated from the F-T reactor are directed to a Heat Recovery Steam Generator (HRSG) for (partial) heat reclamation. A 3-pressure level steam turbines system is used to generate power to satisfy parasitic energy requirements. The final products from the solar-redox process comprises high purity compressed H_2, liquid fuel and electricity.

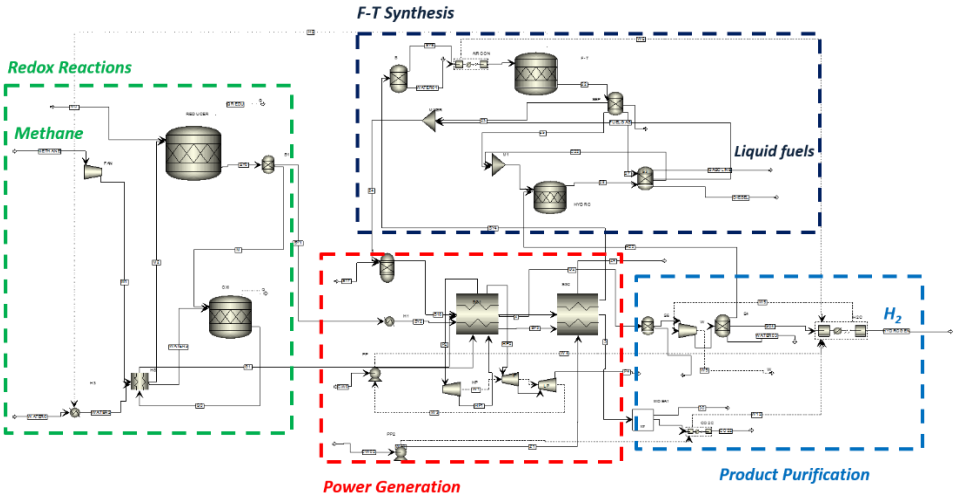

Fig. 4.S6 ASPEN Plus® flowsheet of the hybrid solar-redox process operating at low pressure for the redox reactions

Process material balance

Table 4.S6 shows the mass flow rate of the gaseous products from inlet and outlet of the key reactors in the hybrid solar-redox process. The results are exported from Aspen Plus simulation of Case III.

Table 4.S6 Key mass flow (kmol/hr) in the hybrid solar-redox process of Case III

	Feedstock of the reducer	After reducer	Fuel gas after F-T	Liquid fuel collector	After Oxidizer	After PSA
CO	0	304.0	65.9	0	4.8	0
CO_2	0	142.5	167.4	0	23.7	0
H_2	0	574.8	100.7	0	1016.4	965.6
H_2O	0	375.2	0	0	680.2	0
CH_4	500.0	25.0	26.7	0	0	0
C_2-C_4	0	0	3.9	0	0	0
C_5-C_{11}	0	0	0	10.9	0	0
C_{12}-C_{19}	0	0	0	9.4	0	0

Energy consumption in key unit operation steps

The energy consumption and generation from key unit operations in the hybrid solar-redox process are given in Table 4.S7. The results are exported from Aspen Plus simulation of Case III, where negative number represents energy consumption and positive number shows power generation.

Table 4.S7 Energy consumption and generation from key unit operations in the hybrid solar-redox process of Case III

	Energy (MW)
Syngas compression	-4.49
PSA	-2.6
H_2 compression	-4.12
Total consumption	***-11.21***
Heat recovery	2.83
Flue gas combustion	11.88
Total generation	***14.71***
Net Power	**3.5**

REFERENCES

1. N. L. Galinsky, Y. Huang, A. Shafiefarhood, and F. Li, *ACS Sustainable Chem. Eng.*, 2013, **1**, 364–373.
2. A. Shafiefarhood, N. Galinsky, Y. Huang, Y. Chen, and F. Li, *ChemCatChem*, 2014, **6**, 790-799.
3. A. Steinfeld, *Int. J. Hydrog. Energy*, 2002, **27**, 611–619.
4. T. Kodama, *Prog. Energy Combust.*, 2003, **29**, 567–597.
5. S. Möller, D. Kaucic, and C. Sattler, *J. Sol. Energy Eng.*, 2005, **128**, 16–23.
6. M. Roeb, A. G. Konstandopoulos, A. Steele, P. Stobbe, et al, *J. Sol. Energy Eng.*, 2005, **128**, 125–133.
7. T. Kodama, Y. Nakamuro, and T. Mizuno, *J. Sol. Energy Eng.*, 2004, **128**, 3–7.
8. Y. Tamaura, A. Steinfeld, P. Kuhn, and K. Ehrensberger, *Energy*, 1995, **20**, 325–330.
9. T. Kodama, N. Gokon, and R. Yamamoto, *Sol. Energy*, 2008, **82**, 73–79.
10. J. R. Scheffe, J. Li, and A. W. Weimer, *Int. J. Hydrog. Energy*, 2010, **35**, 3333–3340.
11. M. Roeb, M. Neises, N. Monnerie, F. Call, H. Simon, C. Sattler, M. Schmücker, and R. Pitz-Paal, *Materials*, 2012, **5**, 2015–2054.
12. C. L. Muhich, B. W. Evanko, K. C. Weston, P. Lichty, X. Liang, J. Martinek, C. B. Musgrave, and A. W. Weimer, *Science*, 2013, **341**, 540–542.

Appendix C Supplementary Information for Chapter 5

This supporting information contains the following sections:

S1. Hybrid solar-redox process description

S2. Simulation parameters and assumptions

S3. Process simulation results

S1. Hybrid solar-redox process description

The hybrid solar-redox scheme adopts a two-step approach to convert methane. In the first step, oxidized ferrite material (Fe_3O_4) is used to partially oxidize methane into syngas in a reducer. As shown in Fig. 5.1C, methane is fed into the reducer, where it is partially oxidized by the oxygen carrier into syngas. Syngas is then used as the feedstock for F-T synthesis. The Fischer–Tropsch process involves a series of chemical reactions that produce a variety of hydrocarbons: $(2n + 1)\ H_2 + n\ CO \rightarrow C_nH_{(2n+2)} + n\ H_2O$ [1]. Cobalt based F-T catalyst are often utilized in low temperature F-T synthesis (200-250 ºC) with a high chain growth probability factor (α) ranging between 0.85 and 0.95. This leads to increased liquid fuel and wax yields [2]. In the present work, F-T reactor is simulated using the RStoic model in ASPEN Plus®. The product distribution is determined using the Anderson–Schulz–Flory distribution: $W_n = n(1-\alpha)^2\alpha^{n-1}$. Based on a number of published experimental studies [3–5], α value in the current study is assumed to be 0.91 with 85% CO conversion at 22 atm and 249°C. After the F-T reactor, wax is introduced into the upgrader to generate diesel and naphtha. In the meantime, reduced ferrite material (Fe/FeO) is introduced to the second reaction step where it is regenerated with steam in an oxidizer reactor. H_2 generated from this water-splitting step is cooled, cleaned, and compressed as the final product. To compensate the heat required for the endothermic methane oxidation reaction, solar energy is provided by direct irradiation. The fuel gas containing CH_4, CO and light hydrocarbons is combusted for heat generation. In addition, the high temperature gaseous products from the reactors as well as the heat released by the F-T reactor are directed to a Heat Recovery Steam Generator (HRSG) for (partial) heat reclamation. The recovered heat is used for (i) preheating the gaseous reactants; (ii) generating power using a 3-pressure level steam turbines system to satisfy parasitic energy requirements. In addition, solar-hybrid redox scheme also has the capability to operate under solar-free conditions by switch to a chemical looping combustion mode as shown in Fig. 5.1C. Since the focus of this article is process evaluations and comparisons, detailed reactor design is not within the scope of the current study. It is noted that many reactor designs for solar-thermal water-splitting processes can be directly utilized for solar energy integration in the current

process. For instance, rotary-type and the volumetric gas-particle solar reactors will be directly applicable for the proposed solar-redox operations [6–9].

S2. Simulation parameters and assumptions

Aspen Plus is used in the present study to determine the reactor and process performances. Aspen Plus modules, property methods, and physical property databanks are summarized in Table 5.S1. Table 5.S2 lists the key operating assumptions and parameters used in the process simulations.

Table 5.S1. Aspen Plus® model setup

Stream class	MIXCINC
Databank	COMBUST, INORGANIC, SOLIDS, PURE
Solid components	Fe, $Fe_{0.947}O$, Fe_3O_4, SiC, C
Property method	PR-BM, except STEAM-TA for steam cycles
Solution strategy	Sequential Modular
Unit operations Models	
Reducer	RGibbs/ RStoic
Oxidizer	Multi-stage RGibbs (moving bed)/ RStoic
F-T Reactor	RStoic
Pressure changers	Pump, Compr, Mcompr
Heat exchangers	Heater, MheatX
Mixers/Splitters/Separators	Mixer/Fsplit/Sep/Flash2

Table 5.S2. Key assumptions and simulation parameters

	Parameters
Ambient condition	T = 25 °C, P = 1 atm
Heat loss in the key reactors	1% of the total thermal input
SMR Reformer	866 °C
Reducer	900-950 °C
Oxidizer	750-900 °C
F-T reactor temperature and pressure	249 °C; 22atm
F-T catalyst	Cobalt
F-T α value	0.91
CO per-pass conversion in the F-T reactor	85% @ 22atm
Pressure drop in the reducer and oxidizer	0.5 atm
Mechanical efficiency of pressure changers	1
Isentropic efficiency of steam turbines	0.85
Isentropic efficiency of air blowers and compressors	0.8
Heat Recovery Steam Generator	Pinch point: 10℃
CO_2 removal	90% [10,11]
Steam for CO_2 removal and solvent regeneration	1.32 kg steam /kgCO_2; steam conditions: 4.4 atm and 149°C [10,11]
PSA	1atm pressure drop for H_2 90% H_2 recovery
Compressor specifications	4 stage with intercooler at 40°C, Isentropic efficiency is 0.8
Steam turbine conditions	3-level Steam Cycle 12.4 MP (HP inlet)/3.1MP(IP inlet)/ 0.45MP (LP inlet)/0.1 (LP outlet)

S3. Process simulation results

S3.1 Conventional SMR

Case I mimics the conventional SMR process. The underlying assumptions are similar to those reported by DOE [10,11]. The scheme operates at a nominal pressure of 30 atm. Steam to CH_4 molar ratio for the reformer is 4.1 in order to ensure adequate steam for the WGS reactions. Table 5.S3 summarizes the flow rates of the key streams in Case I. 87% methane conversion is assumed in the reforming step with CO yield of ~47% and CO_2 yield of ~40%. With 8 ton/h CH_4 as the feedstock for the reformer, 6.6 ton/h CO and 3.0 ton/h H_2 are generated, along with 8.8 ton/h CO_2. After heat exchangers, CO in the gas mixture is further reacted with H_2O to generate H_2 in the two WGS reactors. The overall CO conversion is over 95% in the WGS system. As a result, 0.46 ton/h additional H_2 is produced in WGS. The gaseous stream from WGS is cooled down for water condensation. CO_2 is then removed by the MDEA system, which has 90% CO_2 capture efficiency [12]. The PSA downstream of MDEA operates at a considerably lower temperature and separates H_2 from CH_4, CO and CO_2 in the gaseous mixture. The final product is high purity (>99.9 %) H_2 at 20 atm. The off gas from PSA is sent to the combustor to generate heat for compensating the endothermic SMR reaction. 3.2 ton/h of supplemental CH_4 is also consumed in the combustor. CO_2 in the combustion flue gas is also captured by MDEA. Overall, 27.8 ton/h O_2 is captured at >99.9% purity. Around 1.2 ton/h CO_2 is emitted to the atmosphere in the stack gas.

Table 5.S3: Key mass flow rates (ton/h) in conventional SMR (Case I)

	After Reformer	After WGS	After CO_2 Removal	Flue gas After PSA	Combustor off-gas
CO	6.58	0.13	0.13	0.13	0
CO_2	8.80	18.94	1.89	1.89	13.8
H_2	3.03	3.50	3.50	0.35	0
H_2O	25.89	21.74	0.00	0.00	12.7
CH_4	1.04	1.04	1.04	1.04	0
T (°C)	866	204	40	38	886
P (atm)	30	28	27	1	1

S3.2 Solar SMR

Solar SMR is simulated in Case II. Similar to conventional SMR, the process is comprised of reforming, WGS, CO_2 removal, and H_2 purification steps. Despite the very similar simulation models, the main differences between Case II and Case I include solar energy integration and elimination of the combustor block for the SMR reaction. Since the off-gas from PSA is recycled to the reformer, approximately 20% additional steam is injected into reformer to maintain the desired steam to CH_4 ratio of 4.1. Table 5.S4 summarizes the mass flows of key process streams. Resulting from 90.5 MW of solar energy input, the final H_2 product yield is 4 ton/h, which is 28% higher than Case I. Since no supplementary CH_4 is needed, the total methane consumption in Case II is 28.7% less than that in Case I. Overall, 22 ton/h CO_2 is captured from Case II.

Table 5.S4: Key mass flow (ton/h) in solar SMR (Case II)

	After Reformer	After Shifter	After CO_2 Removal	Flue gas After PSA
CO	7.72	0.15	0.15	0.15
CO_2	12.56	24.45	2.44	2.44
H_2	3.94	4.48	4.48	0.45
H_2O	31.06	26.19	0.00	0.00
CH_4	1.20	1.20	1.20	1.20
T (°C)	866	204	40	38
P (atm)	30	28	27	1

S3.3 Hybrid solar-redox process

The hybrid solar-redox scheme studied in Case III uses methane and solar energy to co-produce hydrogen and liquid fuels in a two-step redox process with the assistance of MIEC enhanced iron oxide particles. The iron oxide particles serve as energy and oxygen carriers (OC). As a result, simpler product separation schemes can be achieved. Case III incorporates the experimental data summarized in Table 5.3. In the reducer, CH_4 conversion is 95.3% and

syngas yield is 59 % [13]. Key mass flow rates of the process are shown in Table 5.S5. As can be seen, 8.5 ton/h CO and 1.1 ton/h H_2 is generated from the reducer. F-T unit and upgrader generates liquid fuel containing 1.44 ton/h naphtha and 1.88 ton/h diesel. As a by-product, 11.7 ton/h CO_2 is captured. The reduced iron oxides are then introduced to the oxidizer to produce hydrogen via the steam-iron reaction. After purified by PSA, yield of H_2 product is 1.9 ton/h.

Table 5.S5: Key mass flow (ton/h) in the hybrid solar-redox process of Case III

	After reducer	Fuel gas after F-T	Liquid fuel collector	After Oxidizer
CO	8.51	0.3	0	0.14
CO_2	6.27	1.74	0	1.04
H_2	1.15	0.02	0	2.03
H_2O	6.75	0	0	7.86
CH_4	0.40	0.12	0	0
C_2-C_4	0	0.31	0	0
C_5-C_{11}	0	0	1.44	0
C_{12}-C_{19}	0	0	1.88	0
T (°C)	900	50	40	900
P (atm)	1	1	1	1

References:

[1] Shuster E, Goellner J. Analysis of Natural Gas-to Liquid Transportation Fuels via Fischer-Tropsch. U.S. DOE/NETL 2013.

[2] *Reedijk* J, *Poeppelmeier* K. Comprehensive Inorganic Chemistry II: from elements to applications. Newnes; 2013.

[3] vanBerge PJ, Everson RC. Cobalt as an alternative Fischer-Tropsch catalyst to iron for the production of middle distillates. Natural Gas Conversion Iv, vol. 107, 1997, p. 207–12.

[4] Sie ST. Process development and scale up: IV. Case history of the development of a Fischer-Tropsch synthesis process. Rev Chem Eng 1998;14:109–57.

[5] Gray D, Klara J, Tomlinson G, White C. Chemical-Looping Process in a Coal-to-Liquids Configuration. U.S. DOE/NETL, 2008.

[6] Dahl JK, Weimer AW, Lewandowski A, Bingham C, Bruetsch F, Steinfeld A. Dry reforming of methane using a solar-thermal aerosol flow reactor. Ind Eng Chem Res 2004;43:5489–95.

[7] Gokon N, Takahashi S, Yamamoto H, Kodama T. Thermochemical two-step water-splitting reactor with internally circulating fluidized bed for thermal reduction of ferrite particles. Int J Hydrogen Energy 2008;33:2189–99.

[8] Steinfeld A, Brack M, Meier A, Weidenkaff A, Wuillemin D. A solar chemical reactor for co-production of zinc and synthesis gas. Energy 1998;23:803–14.

[9] Diver RB, Miller JE, Allendorf MD, Siegel NP, Hogan RE. Solar Thermochemical Water-Splitting Ferrite-Cycle Heat Engines. J Sol Energy Eng 2008;130:041001–041001.

[10] Chou V, Kuehn N. Assessment of Hydrogen Production with CO_2 Capture, Volume 1: Baseline State of the Art Plants. U.S. DOE/NETL 2010.

[11] Molburg J, Doctor R. Hydrogen from Steam-Methane Reforming with CO_2 Capture. U.S. DOE/NETL 2003.

[12] Matuszewski M, Woods M. QGESS: Process Modeling Design Parameters. U.S. DOE/NETL 2012.

[13] He F, Trainham J, Parsons G, Newman J, Li F. Investigation of a hybrid solar-redox scheme for liquid fuel and hydrogen coproduction. Energy Environ Sci 2013 DOI: 10.1039/C4EE00038B.

Appendix C Supplementary Information for Chapter 6

This Supplementary information contains the following sections:

- Experimental method
- Second law analysis on the impact of steam conversion on process efficiency
- Steam conversion in the FeO_x-H_2O-H_2 ternary system under equilibrium conditions
- Non-stoichiometry within $La_{0.8}Sr_{0.2}FeO_{3-\delta}$ perovskite
- Steam to H_2 conversion in the fixed bed experiments
- Methane oxidation reaction in the layered reverse-flow reactor
- Water-splitting reaction in the layered reverse-flow reactor
- Process modeling of the hybrid solar-redox scheme

Experimental method

Redox Catalyst Synthesis

Lanthanum strontium ferrite ($La_{0.8}Sr_{0.2}FeO_{3-\delta}$ or LSF) supported Fe_3O_4 is used as the redox catalyst. We reported that LSF being an effective, mixed ionic-electronic conductive support to inhibit sintering of iron/iron oxides, thereby enhancing the redox activity and thermal stability of iron oxide based redox catalysts.[1] Fe_3O_4-LSF (25wt% LSF), Fe_3O_4-LSF (40wt% LSF), and pure LSF are synthesized by a solid-state reaction (SSR) method: a stoichiometric amount of precursors, i.e. iron oxide (Fe_2O_3, 99.9%, Noah Chemicals), La_2O_3 (99.9%, Aldrich), and $SrCO_3$ (99.9%, Noah Chemical), are weighed. This is followed by ball-milling, pelletization, and sintering at 1200°C for 12 hours. The resulting pellets are subsequently crushed and sieved into 75 to 150 μm. A reference redox catalyst, i.e. Fe_3O_4-$MgAl_2O_4$ (40wt% $MgAl_2O_4$), is prepared with an identical method. Since the as-prepared redox catalysts are composed of Fe_2O_3 and LSF support, one cycle reduction followed with steam regeneration is performed to obtain Fe_3O_4 phase. Crystallite phases of the resulting redox catalysts are confirmed using X-ray powder diffraction (XRD) (Rigaku SmartLab).

Fixed bed experiment

Redox experiments are carried out in a stainless steel tubular reactor with an inner diameter of 5 mm (Fig. 6.S1) under a fixed-bed mode. The reactor is externally heated with a tube furnace (MTI OTF-1200X-S-VT**)** with K type thermocouple measuring the temperature. A gas mixing panel with multiple Brooks mass flow controllers (MFCs) is used to deliver gaseous mixtures, e.g. nitrogen and methane, to the reactor. In each experiment, 2 to 3 grams of redox catalyst particles are added on top of the SiC layer which serves as a gas distributor. In order to mimic the hybrid redox scheme, the tests are carried out in two consecutive steps, i.e. methane partial oxidation (redox catalyst reduction) and water-splitting (redox catalyst oxidation). The redox reaction temperature is set at 930 °C. 15 ml min^{-1} (STP: standard temperature 0°C and pressure 1 atm) N_2 is used as the internal standard in both reduction and oxidation steps. 10 ml min^{-1} (STP) CH_4 is introduced along with N_2 from the top of the reactor. Water-splitting reaction is carried out after the residue gas from the methane oxidation step has been completely purged

with N_2. In the oxidation step, water is injected by a syringe pump (NE-300 Just Infusion^{TM}) from the bottom of the reactor at a rate of 0.278 mmol min^{-1}. Prior to entering the reactor, the water is vaporized and preheated. Compositions of the gases exiting the reactor are determined using a gas chromatograph (Agilent Micro GC 490) and a multi-gas analyzer (Emerson X-Stream gas analyzer). Parameters for evaluating the redox experiments are summarized in Table 6.S1, where $\dot{n}_i$ is the molar flow rate of component *i*, and in/out represents inlet/outlet steams of the reaction.

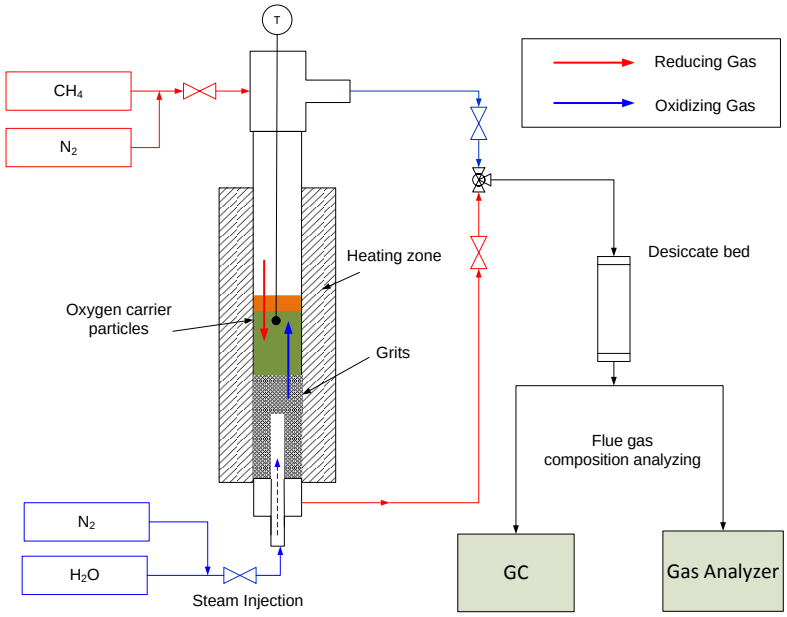

Fig. 6.S1: Experimental setup for hybrid redox process test with Fe_2O_3-LSF particle

Table 6.S1: Summary of parameters used to characterize the redox reactions

Parameters	Equations
CH_4 Conversion	$(1-\frac{\dot{n}_{CH_4,out}}{\dot{n}_{CH_4,in}})\times 100\%$
Syngas yield	$\frac{\dot{n}_{H_2,out}+\dot{n}_{CO,out}}{3\dot{n}_{CH_4,in}}\times 100\%$
Steam to H_2 Conversion	$\frac{\dot{n}_{H_2,out}}{\dot{n}_{H_2O,in}}\times 100\%$
H_2 Purity	$\frac{\dot{n}_{H_2,out}}{\dot{n}_{H_2,out}+\dot{n}_{CO,out}+\dot{n}_{CO_2,out}}\times 100\%$

H_2 analysis

The concentration of H_2 in the experiment is determined by an online micro-GC (Agilent CP-490) with a molecular sieve 5A *column.* The GC is calibrated to achieve the correlation coefficient of R>0.998 for H_2. Flow rate of H_2 generated is calculated by

$$V_{H_2}=\int(X_{H_2}F_{Total})dt=\int(X_{H_2}\frac{F_{N_2}}{X_{N_2}})dt \qquad \text{Equation S1}$$

where F is the flow rate, X is the mole fraction and V is the total volume of the gas. N_2 is used as an internal standard. When CO and/or CO_2 is detected in the oxidation step, H_2 generated from carbon deposition is excluded based on the stoichiometry of steam carbon reactions:

$C + H_2O \leftrightarrows CO + H_2$ Reaction S1

$C + 2H_2O \leftrightarrows CO_2 + 2H_2$ Reaction S2

Steam to H_2 conversion is then calculated by the amount of H_2 generated divided by the injected H_2O. The flow rate of the syringe pump is independently calibrated through a gravimetric method. All the gas flows in the experiment are controlled by Brooks 5850E mass

flow controllers (MFCs) which has 0.25% of rate in repeatability. Before each experiment, the gas flow rates are calibrated by a Bios Flow Calibrator (DryCal Definer 220 Primary) and a bubble flowmeter.

Steam Conversion Verification using a Thermal Gravimetric Analyzer (TGA)

Since steam conversion is an important parameter for the current study, a TGA (TA Instrument) with external reducing and oxidizing gas injection is used to independently verify steam conversion of the redox catalysts. A schematic of the TGA setup is shown in Fig. 6.S2. The aforementioned gas mixing panel with multiple mass flow controllers (MFCs) is used to deliver gaseous mixtures. The experiments are conducted with a sample weight of approximately 20 mg at a specific isothermal temperature. 200 ml min^{-1} N_2 and 50 ml min^{-1} H_2 is used as reducing gas, which is injected after the temperature reaches the setting. After 4 hours reduction or when the sample weight change is less than 0.01 mg ml min^{-1}, H_2 flow is stopped. This is followed with injection of oxidizing gas i.e. H_2 and steam mixture. To ensure accurate injection of steam, a gas mixture of N_2 and H_2 is injected into a bubbler at 50 °C to generate concentrated steam. The high concentration steam is then passed through another bubbler at 20 °C (5 ˚C below room temperature) to create a gaseous stream that contains 2.34 mol% steam prior to entering the TGA. The premixed H_2-steam allows for accurate verification of steam conversion. To determine the maximum steam conversion, H_2 flow rate is reduced by 1 ml min^{-1} until the sample weight in TGA start to increase. Provided that weight gain or oxidation of the redox catalyst is observed in the TGA at a given H_2 mole fraction X_{H2}, defined by $\frac{F(H_2)}{F(H_2)+ F(H_2O)} \times 100\%$, the redox catalyst is concluded to be capable of achieving steam conversion higher than X_{H2}. The crystalline phases of the post-experiment redox catalysts are analyzed using X-ray powder diffraction (XRD) (Rigaku SmartLab) with Cu-Kα (λ=0.1542 nm) radiation within the 20-80° 2θ angle range.

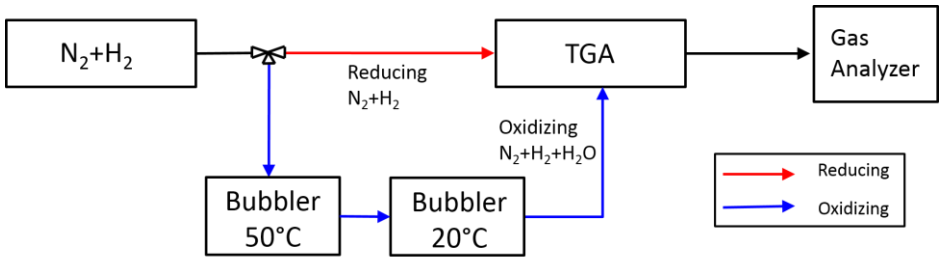

Fig. 6.S2: Schematic of TGA experimental setup with injection of reducing and oxidizing gases

Second law analysis on the impact of steam conversion on process efficiency

Fig. 6.S3 shows a simplified schematic for exergy analysis on the water-splitting reaction. *X* mole of H_2O is converted into 1 mol H_2, with the steam conversion of *1/X*. In order to obtain the minimum exergy loss, we optimistically assume that the sensible heat for water and steam preheating can be fully recovered from product cooling with no heat loss. The most irreversible step is then resided in the product condensation step. It is noted that the product stream would have a lower total pressure (P2) and steam mole fraction *(X-1)/X* than those in the feed stream. Therefore, steam partial pressure and hence dew point of the product is lower than those of the feedstock. As a result, latent heat from steam condensation in the product stream cannot be fully recoverable. In addition, a minimum temperature difference, typically >5 K, is required for effective heat exchange. This means that water-vaporization prior to water-splitting needs to be provided by external energy sources. If we further assume, optimistically, that a turbine is available to recover the latent heat from product steam condensation at 85% of Carnot efficiency with 40 ˚C discharge temperature[2,3], the exergy loss can be calculated using the following equation:

$$\Delta b = b_2 - b_1 = (1-\frac{T_o}{T_1})X\Delta\hat{H}_{evp} + 0.85(1-\frac{313}{T_r})5X\hat{C}_{P,steam} - 0.85(1-\frac{313}{T_2})(X-1)\Delta\hat{H}_{evp}$$

Equation S2

For each additional mole of water being heated and condensed, the minimal exergy loss is estimated to be:

$$\Delta\hat{b} = (1-\frac{T_o}{T_1})\Delta\hat{H}_{evp} + 0.85(1-\frac{313}{T_r})5\hat{C}_{P,steam} - 0.85(1-\frac{313}{T_2})\Delta\hat{H}_{evp} \qquad \text{Equation S3}$$

ΔH_{evp} is the mole heat of vaporization of water. T_o is the standard temperature of 298K and T_1 is steam boiling temperature of 398K at 1 atm. T_2 is the temperature at which latent heat from the unconverted steam is recovered (393K in this case). T_r is the temperature for the water-splitting reaction. Assuming a system pressure of 1 atm and water-splitting temperature of 1123K, minimum exergy loss is therefore estimated to be 3.05 kJ mol^{-1} of unconverted steam. Therefore, higher energy conversion efficiency can be anticipated with high steam to hydrogen conversion.

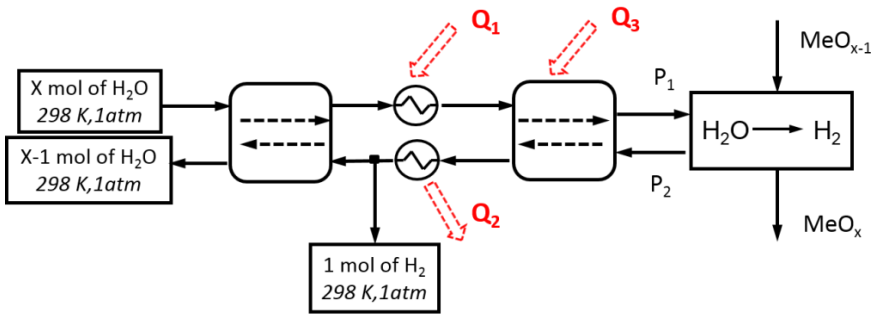

Fig. 6.S3: Exergy analysis on a simplified thermochemical water-splitting scheme

Steam conversion in the FeO_x-H_2O-H_2 ternary system under equilibrium conditions

Thermodynamic analysis can provide maximum steam to H_2 conversion in the steam-iron reactions under varying temperatures. When metallic iron is oxidized to wüstite, steam has the highest conversion as compared to steam reaction with other types of iron oxides, as shown in

the equilibrium phase diagram for the FeO_x-H_2O-H_2 ternary system (Fig. 6.S4).[4] At the reaction temperature of interest, wüstite typically exhibits cation deficiency with formula of $FeO_{0.947}$. As a result, water-splitting reaction: $0.947Fe + H_2O = Fe_{0.947}O + H_2$ should have the highest steam conversion for the FeO_x-H_2O-H_2 ternary system. Steam conversion (X) can be calculated by the following equation:

$$K = e^{-\frac{\Delta G}{RT}} = \frac{p_{H_2}}{p_{H_2O}} = \frac{X}{1-X} \qquad \text{Equation S4}$$

where K is the equilibrium constant, ΔG is the free energy change of the reaction at the given temperature. Using HSC Chemistry v7, the thermodynamic steam conversion as a function of temperature is calculated and the results are shown in Table 6.S2. Steam conversion decreases with increasing temperatures. At 930 °C, the steam to hydrogen equilibrium conversion is 62.3%. Such a conversion is confirmed using ASPEN Plus®.

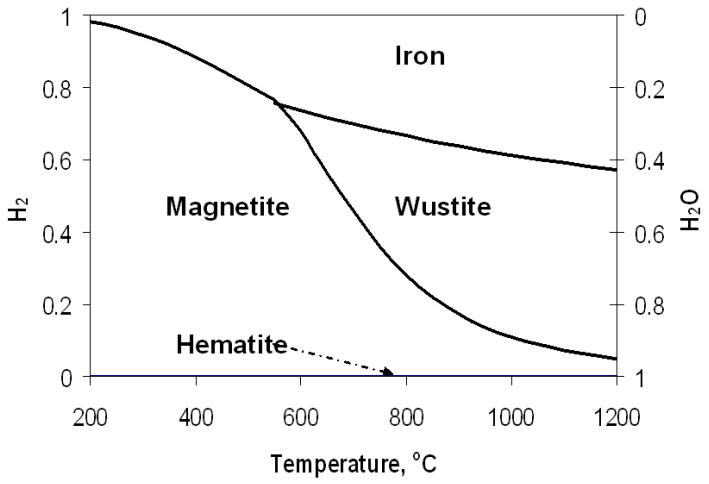

Fig. 6.S4: Phase diagram of the FeO_x-H_2O-H_2 ternary system

Table 6.S2: Maximum steam to hydrogen conversion calculated by thermodynamic equilibrium

T	Steam Conversion
750 °C	68.8%
800 °C	66.8%
850 °C	65.0%
900 °C	63.3%
930 °C	62.3%
1000 °C	60.2%

Non-stoichiometry within $La_{0.8}Sr_{0.2}FeO_{3-\delta}$ perovskite

Perovskite used in the present work has a general formula of $La_{0.8}Sr_{0.2}FeO_{3-\delta}$ (LSF). The Sr acceptor doped perovskite exhibits varying degree of oxygen non-stiochiometry at different oxygen partial pressures. A defect model[5,6] proposed by Mizusaki et al. is used to calculate the oxygen nonstoichiometry δ. Based on the model, the reaction between O_2 and oxygen defects in $La_{1-x}Sr_xFe_{3-\delta}$ is expressed as

$$\frac{1}{2}O_2(g) + V_O^{\bullet\bullet} + Fe_{Fe}^{x} = O_O^{x} + 2Fe_{Fe}^{\bullet} \qquad \text{Reaction S3}$$

The equilibrium constant K_{ox} is

$$K_{Ox} = \frac{\left[O_O^{\times}\right]\left[Fe_{Fe}^{\bullet}\right]^2}{p_{O_2}^{\frac{1}{2}}\left[V_O^{\bullet\bullet}\right]\left[Fe_{Fe}^{\times}\right]^2} = \frac{(3-\delta)\left[Fe_{Fe}^{\bullet}\right]^2}{p_{O_2}^{\frac{1}{2}}\delta\left[Fe_{Fe}^{\times}\right]^2} \qquad \text{Equation S5}$$

$$p_{O_2}^{\frac{1}{2}} = K_{wat}\frac{p_{H_2O}}{p_{H_2}} \qquad \text{Equation S6}$$

The concentration of iron with different charges is determined by disproportionation of Fe^{III} to Fe^{II} and Fe^{IV}:

$$2Fe_{Fe}^{\times} = Fe_{Fe}^{\bullet} + Fe_{Fe}^{'}$$ Reaction S3

The equilibrium constant K_{Fe} is

$$K_{Fe} = \frac{\left[Fe_{Fe}^{\bullet}\right]\left[Fe_{Fe}^{'}\right]}{\left[Fe_{Fe}^{\times}\right]^2}$$ Equation S7

For $La_{0.8}Sr_{0.2}FeO_{3-\delta}$

$$\left[Fe_{Fe}^{\times}\right] + \left[Fe_{Fe}^{\bullet}\right] + \left[Fe_{Fe}^{'}\right] = 1$$ Equation S8

$$x + \left[Fe_{Fe}^{'}\right] = 2\delta + \left[Fe_{Fe}^{\bullet}\right]$$ Equation S9

Combined Equations S5 to S9,

$$\frac{\delta^{\frac{1}{2}}(2\delta - x + 1)}{(3-\delta)^{\frac{1}{2}}(2\delta - x)} K_{wat}^{\frac{1}{2}} p_{o_2}^{\frac{1}{4}} = \frac{K_{Fe}}{K_{Ox}} \frac{(1 + x - 2\delta)(3-\delta)^{\frac{1}{2}}}{\delta^{\frac{1}{2}}(2\delta - x)} \frac{1}{K_{wat}^{\frac{1}{2}} p_{o_2}^{\frac{1}{4}}} - \frac{1}{K_{Ox}^{\frac{1}{2}}}$$ Equation S10

where x = 0.2 for $La_{0.8}Sr_{0.2}FeO_{3-\delta}$. P_{O2} is the oxygen partial pressure. $Fe_{Fe}^{'}$, $Fe_{Fe}^{\times}$ and $Fe_{Fe}^{\bullet}$ represents an Fe cation at the Fe site in the oxidation state of Fe^{II}, Fe^{III} and Fe^{IV}, respectively. The relationship of the $La_{0.8}Sr_{0.2}FeO_{3-\delta}$ oxygen deficiency (δ) with the steam conversion at 930 °C is given in Fig. 6.S5, by using the equilibrium constants reported by Mizusaki et al.[6]. The reduction of Fe^{IV} conversion to Fe^{III} and Fe^{III} to Fe^{II} occur in two separated stages $0 < \delta < 0.1$ and $0.1 < \delta < 0.6$. At the steam conversion of 62.3%, which is the thermodynamically maximum steam conversion for FeO_x-H_2O-H_2 ternary system, the δ is equal to approximately 0.107. When $\delta > 0.14$, steam conversion of the defected perovskite is greater than 99%. This contributes to the high steam conversion obtained by the LSF supported iron oxide.

Pure LSF tested in the TGA with H_2 reduction (Fig. 6.S6) shows a total of ~10.5% weight loss. A comparison of the weight gain during steam oxidation from TGA results and defect model calculation are shown in Table 6.S3. The weight gain under different steam conversion is normalized by fully oxidized sample weight. The data predicted by the defect model shows good consistency with experimental results. Based on the experimental results and theoretical

calculations, LSF could achieve a higher steam conversion than iron oxides. Therefore, LSF is partially oxidized before reduced metallic iron start to react with steam.

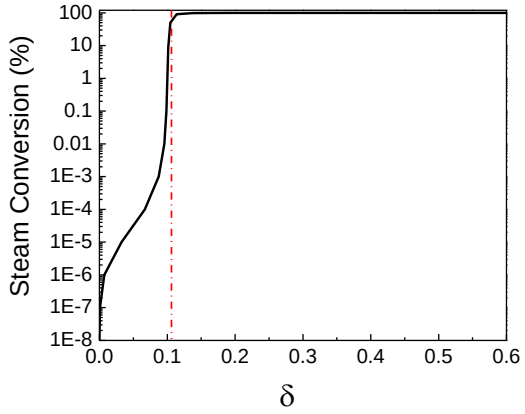

Fig. 6.S5: relationship between $La_{0.8}Sr_{0.2}FeO_{3-\delta}$ oxygen deficiency (δ) and steam conversion at 930 °C. Red dash-dotted line displays thermodynamically predicted steam conversion for Fe→FeO phase transition

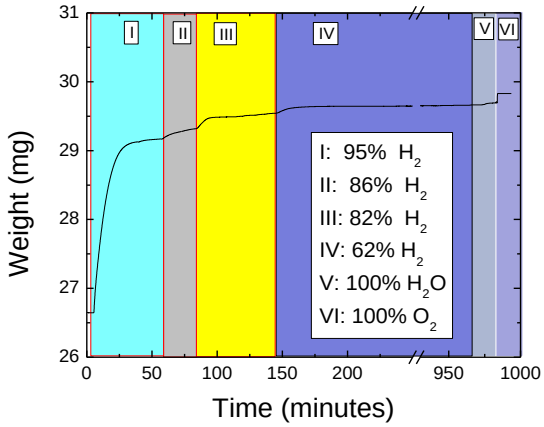

Fig. 6.S6: Pure LSF particle TGA test with steam and hydrogen mixture oxidation at 930°C.

Table 6.S3: Comparison on the normalized weight gain in the steam oxidation of the TGA results and defect model calculation

	Defect Model Calculation	Experimental Data
>95% conversion	10.0%	8.5%
>86% conversion	10.2%	9.0%
>62% conversion	10.2%	10.1%

The theoretical steam to H_2 conversion based on the defect model can be calculated under two idealized cases:

(i) Additive effect of iron oxide and LSF

Under the additive scenario, iron (oxides) and LSF are well mixed and act independently for steam conversion in a simultaneous manner. Assuming that iron (oxide) is the limiting reactant, parallel reactions will lead to the following conversion:

$$X_{H_2O} = \frac{n_{H_2O_{converted}}}{n_{H_2O_{initial}}} = \frac{n_{O-LSF} + n_{O-Fe}}{\frac{n_{O-LSF}}{X_{H_2O-LSF}} + \frac{n_{O-Fe}}{X_{H_2O-Fe}}}$$ Equation S11

(ii) Sequential effect of iron oxide (first) and LSF (second)

Under the sequential scenario, iron (oxides) and LSF are assumed to react with steam in a consecutive manner. In such a configuration, defect in reduced LSF will be able to further enhance steam conversion by reacting with the steam-hydrogen mixture resulted from steam-iron reaction. Assuming that iron (oxide) is the limiting reactant, sequential reactions will lead to the following conversion:

$$X_{H_2O} = \frac{n_{H_2O_{converted}}}{n_{H_2O_{initial}}} = \frac{n_{O-LSF} + n_{O-Fe}}{\frac{n_{O-Fe}}{X_{H_2O-Fe}}} \qquad (n_{O-LSF} < n_{O-Fe}(\frac{1}{X_{H_2O-Fe}} - 1)) \qquad \text{Equation S12}$$

$n_{O\text{-}Fe}$ and $n_{O\text{-}LSF}$ are the mole of oxygen gain in the water splitting reaction, and $X_{O\text{-}Fe}$ and $X_{O\text{-}LSF}$ are the corresponding steam conversion. The calculated results are shown in Fig. 6.2 and 6.3 in the main paper.

Steam to H_2 conversion in the fixed bed experiments

In order to demonstrate the high steam conversion, iron oxides with 25% and 40% $La_{0.8}Sr_{0.2}FeO_{3-\delta}$ support and reference Fe_3O_4-$MgAl_2O_4$ are tested in a fixed-bed reactor. Hydrogen is selected as the fuel in the reduction step for accurate initial assessment of steam conversion in the water-splitting step since no side reactions are likely to take place between hydrogen and the redox catalyst samples. The redox catalyst is reduced by H_2 for 30 minutes in the first step. After reduction, 6.8 ml min^{-1} steam with 15 ml min^{-1} N_2 is injected from the bottom of the reactor to oxidize the redox catalysts for 40 minutes. Then alternate reduction and regeneration of the redox catalyst will be implemented by the same procedure. The XRD pattern (Fig. 6.S7) indicates that redox catalyst is fully reduced to metallic iron in the reduction step. And in the oxidation step, it is regenerated into a mixture of Fe, FeO and Fe_3O_4, which has an average composition of $FeO_{0.5}$ by mass balance.

The impact of temperature on the steam to H_2 conversion is illustrated in Fig. 6.S8A for Fe_3O_4-LSF (40wt% LSF). There are two competing effects: (i) increasing temperature leads to lower steam conversion based on thermodynamics; (ii) increasing temperature enhances the reaction kinetics and hence increases steam conversion in the fixed bed. At a fixed space velocity of approximately 6 $minutes^{-1}$, the maximum steam to H_2 conversion of Fe_3O_4-LSF(40wt%) is archived at 930 °C, which is consistent with the results of Fe_3O_4-LSF(25wt%). Therefore, 930 °C is selected as the nominal temperature in the paper. After that, multi-cycle experiment is conducted at 930 °C in the fixed bed. As shown in Fig. 6.S8B, the average steam to H_2 conversion over 12 cycles of Fe_3O_4-LSF (25wt% LSF) and Fe_3O_4-LSF (40wt% LSF) is 64.0%

(±0.67%) and 67.1% (±1.27%) with 95% confidence, respectively. In comparison, $MgAl_2O_4$ spinel supported iron oxide shows a steam conversion of 39%, which is 25-28% lower than LSF promoted Fe_3O_4 particle.

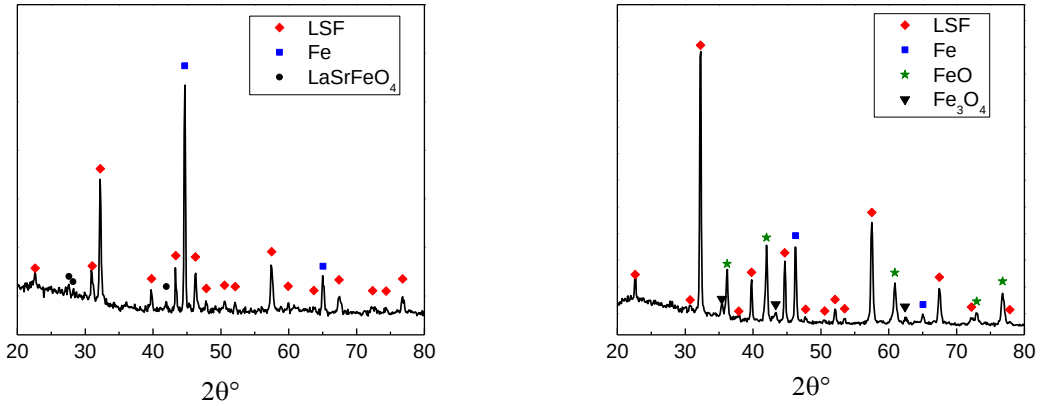

(A) (B)

Fig. 6.S7: XRD Pattern of Fe_3O_4-LSF redox catalyst in the fixed bed experiment at 930 °C (A) reduced by hydrogen and (B) regenerated by steam.

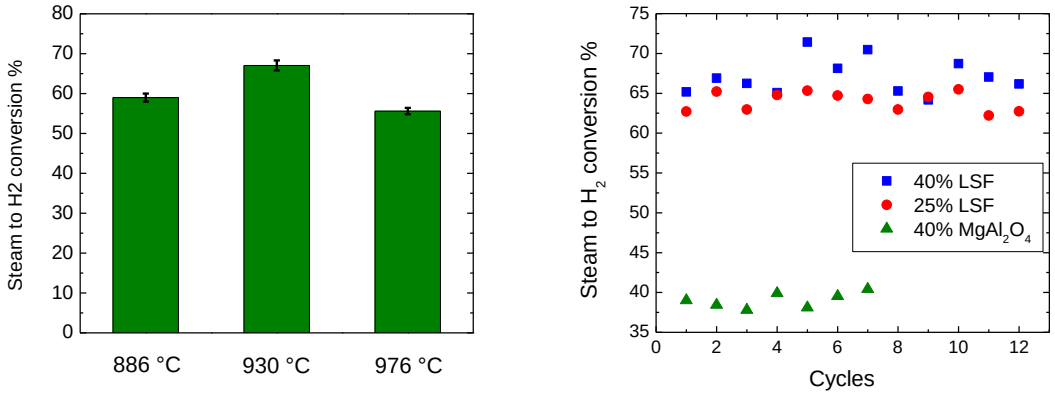

(A) (B)

Fig. 6.S8: (A) The temperature effects on the steam to H_2 conversion per cycle for Fe_3O_4-LSF (40wt% LSF). (B) Average steam to H_2 conversion per cycle over multi-cycle at 930 °C.

Methane oxidation reaction in the layered reverse-flow reactor

Redox study on Fe_3O_4-LSF is conducted in a layered reverse-flow reactor, where methane is injected from the top of the bed to reduce the redox catalyst. Neal et al.[8] reported that LSF has higher resistance towards coke formation compared to the iron oxides. In order to inhibit excessive carbon formation from methane decomposition, methane injection is stopped when $H_2/(CO+CO_2)$ molar ratio exceeds 2. The product gas concentration as a function of time in the reducer is shown in Fig. 6.S9. The average methane conversion under the fixed-bed mode is above 99%. The corresponding syngas ($CO+H_2$) yield is ~62% (±3%) with a H_2/CO molar ratio of ~2.2 (±0.1).

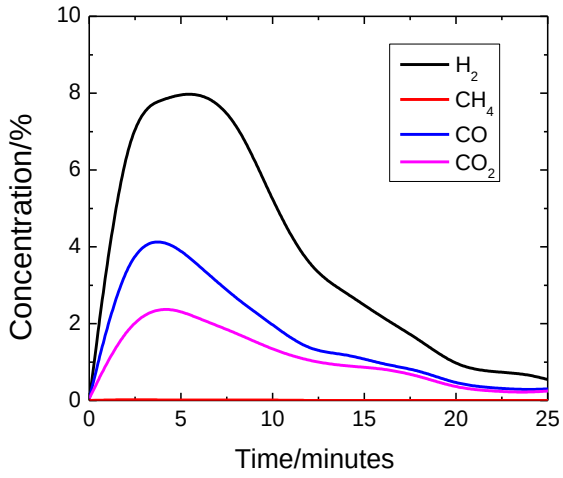

Fig. 6.S9: Product gases concentration (N_2 and H_2O-free basis) as a function of time in methane oxidation step.

Water-splitting reaction in the layered reverse-flow reactor

Water-splitting or steam-iron reaction is initiated by introducing steam into the reactor after the methane conversion step. Fig. 6.S10 shows a representative H_2 purity profile (water-free and N_2-free basis) as a function of time. At the beginning of the steam oxidation, small amounts of CO and CO_2 are detected, which corresponds to the gasification of carbon deposited in the methane oxidation step. Since it is well controlled to minimize the coke formation, an overall H_2 purity of 98.5% is achieved in the water-splitting step.

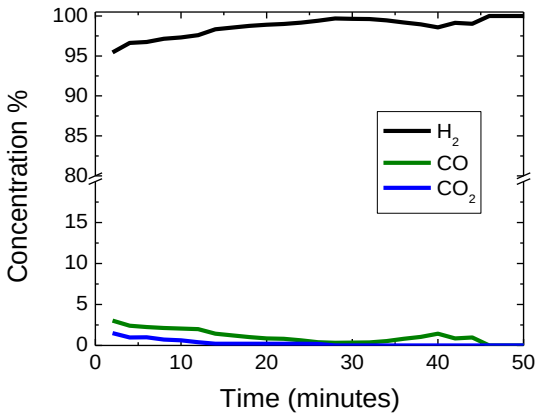

Fig. 6.S10: H_2 concentration (water-free) during the water splitting step as a function of time at 930 °C after the reduction step.

The layered reverse-flow reactor concept is proved in fixed bed experiments. Fig. 6.S11 shows a comparison of real time steam conversion between with and without layered reverse-flow. In the layered reverse-flow experiment, steam is going through the bottom Fe_3O_4-LSF bed with ~64.0% steam converted in the first place. And then the top layer of reduced LSF further converts part of the remaining steam into H_2, resulting in exceptional overall steam conversion of 77.2%. The average steam to H_2 conversion in the layered reverse-flow experiment is ~10% high than the one without reverse flow.

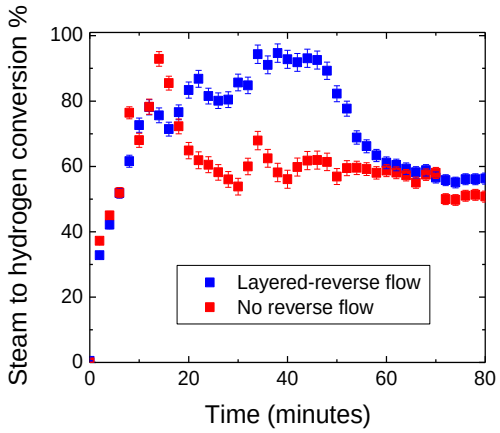

Fig. 6.S11: Real time steam conversion in oxidation with and without layered reverse-flow

Process modeling of the hybrid solar-redox scheme

In the hybrid solar-redox scheme (Fig. 6.S12A), liquid fuel and hydrogen are produced from methane and integrated solar energy in two redox steps.[8,9] In the first step (reducer), methane is partial oxidized by redox catalyst material (Fe_3O_4-LSF) into CO and H_2, which is then converted into naphtha and diesel in the Fischer-Tropsch (F-T) reactors. In the subsequent step (oxidizer), steam oxidizes the reduced redox catalyst material from the previous step, producing concentrated H_2. ASPEN Plus simulation (Fig. 6.S12B) is used to estimate reactor and process performances of the hybrid solar-redox concept. Detailed simulation assumptions with respect to materials, simulation modules, property methods, physical property databanks, and key operating parameters are summarized in our previous publication.[8] The temperature of the reducer and oxidizer is set at 930 °C, which matches the experimental conditions. Two simulation cases with different steam to hydrogen conversions in the oxidizer are simulated, and the results are shown in Table 6.S4. Case I is using the steam conversion of 77.2% which is achieved from the proposed layered reverse-flow reactor. Case II assumes steam conversion of 20%, which is the maximum reported conversion from literature. The incremental heat

requirement from the low steam conversion in Case II is provided by conventional methane combustion, so that the solar energy usage is identical in the two cases. All other simulation assumptions and parameters are assumed to be same.[9] Under the scenario of no CO_2 capture, case II uses 48% more methane to compensate the increased heat requirement through combustion. Therefore, with the benefit of exceptional steam to H_2 conversion, Case I has the overall process thermal efficiency of 63.1% (HHV), which is 15.1% higher than case II with lower steam conversion.

A life cycle greenhouse gas (GHG) footprint analysis is conducted, which considers the contributions from natural gas upstream and energy conversion facility. The estimated upstream natural gas emission based on US-DOE report is in the range of 6.1-9.1 g CO_2/MJ for various feedstocks.[10] The emission analysis from energy conversion facility is based on ASPEN model results. When calculating the emission on hydrogen, a CO_2 emission quota for the liquid fuel products is subtracted. The emission on liquid fuel products from the solar-redox process is assumed to be are identical to the one of petroleum derived fuels, which is reported at 90 g CO_2/ MJ[11]. Two scenarios are investigated for cases with and without CO_2 capture. 0.75 MJ/kg CO_2 energy consumption is assumed for the amine-based CO_2 capture.[2] The CO_2 footprint from the hybrid solar-redox scheme are shown in Table 6.S4.

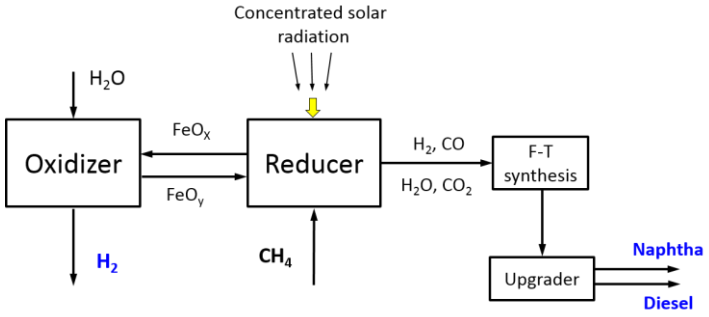

(A)

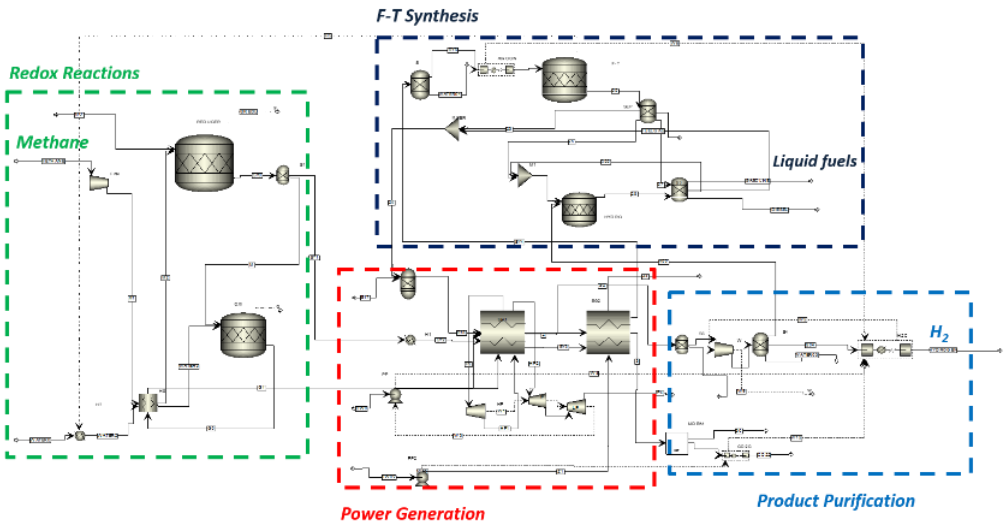

(B)

Fig. 6.S12: (A) Simplified schematic and (B) ASPEN flowsheet of the hybrid solar-redox scheme

Table 6.S4. Process simulation results on the hybrid solar-redox cases

		Case I		Case II	
		Without CO_2 Capture	With CO_2 Capture	Without CO_2 Capture	With CO_2 Capture
Steam to H_2 conversion	%	77.2%		20%	
Methane input	t hr^{-1}	8.0		11.9	
Overall process efficiency	HHV%	63.1	61.3	48.0	45.4
CO_2 footprint on all hydrogen	g CO_2/MJ H_2	44.4	9.0	96.7	29.0
CO_2 footprint on all product	g CO_2/MJ	65.5	38.8	97.3	45.7

References:

1. N. L. Galinsky, Y. Huang, A. Shafiefarhood and F. Li, *ACS Sustain. Chem. Eng.*, 2013, **1**, 364–373.
2. G. Rochelle, E. Chen, S. Freeman, D. Van Wagener, Q. Xu and A. Voice, *Chem. Eng. J.*, 2011, **171**, 725–733.
3. G. T. Rochelle, *Science*, 2009, **325**, 1652–1654.
4. D. R. Gaskell, *Introduction to metallurgical thermodynamics*, Hemisphere Pub. Corp., 1981.
5. A. Murugan, A. Thursfield and I. S. Metcalfe, *Energy Environ. Sci.*, 2011, **4**, 4639–4649.
6. J. Mizusaki, M. Yoshihiro, S. Yamauchi and K. Fueki, *J. Solid State Chem.*, 1985, **58**, 257–266.
7. L. M. Neal, A. Shafiefarhood and F. Li, *ACS Catal.*, 2014, **10**, 3560–3569.

8. F. He, J. Trainham, G. Parsons, J. S. Newman and F. Li, *Energy Environ. Sci.*, 2014, **7**, 2033–2042.
9. F. He and F. Li, *Int. J. Hydrog. Energy*, 2014, **39**, 18092–18102.
10. T. Skone, 2014, US DOE/NETL-2014/1646. http://www.netl.doe.gov/File%20Library/Research/Energy%20Analysis/Life%20Cycle%20Analysis/NETL-NG-Power-LCA-29May2014.pdf
11. K. Gerdes, T. Skone, 2009, US DOE/NET. http://www.netl.doe.gov/File%20Library/Research/Energy%20Analysis/Publications/CompTranspFuels-GHGEmisEnergySecImpacts---Pres.pdf